Wegener Center
SCIENTIFIC REPORT
98 | 2023

Diagnostics of tropospheric and stratospheric variability from radio occultation observations

Hallgeir Wilhelmsen

January 2023

Climate Change Graz
Field of Excellence
University of Graz

Wegener Center

UNI GRAZ

The Wegener Center for Climate and Global Change is an interdisciplinary, internationally recognized research and graduate education institute of the University of Graz that is pooling the University's expertise in Climate, Environmental and Global Change. It brings together research teams and scientists from fields such as geophysics and climate physics, meteorology, economics, geography, and social sciences. At the same time, close links are maintained and further developed with many national and international cooperation partners. The research interests range from monitoring, analysis, and modeling of climate and environmental change to the investigation of climate change impacts and the analysis of the human dimensions of these changes related to mitigation, adaptation, and loss & damage. More information at **www.wegcenter.at**.



Alfred Wegener (1880 – 1930), after whom the Wegener Center is named, was founding holder of the University of Graz Geophysics Chair (1924 – 1930). In his work in the fields of geophysics, meteorology, and climatology he was a brilliant scientist and scholar, thinking and acting in an interdisciplinary way, far ahead of his time with this style. The way of his ground-breaking research on continental drift is a shining role model. His sketch on the relations of continents based on traces of an ice age about 300 million years ago (left) as basis for the Wegener Center Logo is thus a continuous encouragement to explore equally innovative ways: paths emerge in that we walk them (motto of the Wegener Center).

This report is the result of a PhD thesis work completed in 2022.

SR 98 | 2023 Diagnostics of tropospheric and stratospheric variability from radio occultation observations
ISBN 978-3-9504700-7-9 January 2023

Suggested citation:
Wilhelmsen, H. (2023), Diagnostics of tropospheric and stratospheric variability from radio occultation observations, Wegener Center Scientific Report 98-2023, Wegener Center Verlag, University of Graz, Austria, January 2023. ISBN 978-3-9504700-7-9

(c) 2023 Wegener Center Verlag, University of Graz, Austria
The usage of images, tables, or texts of this Scientific Report is permitted for non-commercial purposes if appropriate credit is given.
For any other purposes, please contact: wegcenter@uni-graz.at

Publishing institution:
Wegener Center for Climate and Global Change, University of Graz
Brandhofgasse 5, 8010 Graz, www.wegcenter.at

Contact: Hallgeir Wilhelmsen
wilhelmsen@gmail.com

WILHELMSEN Hallgeir

Diagnostics of tropospheric and stratospheric variability from radio occultation observations

PhD thesis

to obtain the academic degree
Doctor of Natural Sciences

submitted to the
Faculty of Environmental and Regional Sciences and Education
University of Graz

First referee: Univ.-Prof. Dr.rer.nat. STEINER Andrea K.
Wegener Center for Climate and Global Change, University of Graz

Second referee: Univ.-Prof. Dr. De La TORRE Alejandro
Facultad de Ingeniería, Universidad Austral

Third referee: Univ.-Prof. Dr. HAIMBERGER Leopold
Department of Meteorology and Geophysics, University of Vienna

2022

Supervisor

Univ.-Prof. Dr.rer.nat. Andrea K. Steiner
University of Graz, Austria

Co-supervisor

Univ.-Prof. Dr.techn. Wilfried Winiwarter
International Institute for Applied Systems Analysis, Austria
University of Zielona Góra, Poland

Adviser

Dr.rer.nat. Florian Ladstädter
University of Graz, Austria

Abstract

Human-induced climate change reveals itself in many forms, one of which is long term changes in the atmospheric temperature. The atmospheric temperature is, however, also influenced by natural phenomena. This natural variability masks the underlying anthropogenic climate change.

The latest report of the Intergovernmental Panel on Climate Change clearly stated that the rise in temperature near the Earth's surface is caused by human activity. Higher up, in the Upper Troposphere–Lower Stratosphere (UTLS), the picture is more diffuse. There it is more difficult to detect the underlying trend emerging from natural variability.

This work aims at enhancing diagnostics of atmospheric temperature variability in order to reduce uncertainties, improve trend detection, and increase our understanding of the effects of atmospheric phenomena.

Radio Occultation (RO) observations are currently the only global measurements that properly resolve the vertical thermal structure. RO utilizes GPS signals to provide profiles of atmospheric parameters. These measurements are highly accurate in the UTLS and have a high vertical resolution.

In this thesis, I use RO observations to describe the variability in the UTLS as well as tropopause characteristics. Establishing vertically-resolved indices from RO temperature, the main modes of variability in the tropical UTLS are detected. These help to isolate the signals caused by volcanic aerosols and to detect stratospheric warming from even minor volcanic eruptions.

Moreover, analyzing double tropopauses reveals a connection to the El Niño–Southern Oscillation. A higher frequency of double tropopauses is observed during the cold La Niña phase as the tropical belt narrows, potentially enabling exchange of air between the troposphere and the stratosphere at lower latitudes than normal. Finally, a continuous rise of the tropopause over the Northern Hemisphere is detected, one of the fingerprints of climate change in the UTLS.

Zusammenfassung

Der vom Menschen verursachte Klimawandel zeigt sich in vielen Formen, eine davon ist die langfristige Veränderung der atmosphärischen Temperatur. Diese wird jedoch auch durch natürliche Variabilität beeinflusst welche die anthropogene Klimaänderung überlagert.

Der jüngste IPCC Bericht stellt eindeutig fest, dass der Temperaturanstieg an der Erdoberfläche durch menschliche Aktivitäten verursacht wird. In der oberen Troposphäre und unteren Stratosphäre (UTLS) ist es jedoch schwieriger den zugrunde liegenden Trend von der natürlichen Variabilität zu trennen.

Ziel dieser Arbeit ist eine verbesserte Diagnostik der atmosphärischen Variabilität um Unsicherheiten zu verringern, die Trenddetektion zu verbessern und unser Verständnis von atmosphärischen Phänomenen zu erweitern.

Radio-Okkultationsbeobachtungen (RO) sind derzeit die einzigen globalen Messungen, die die vertikale thermische Struktur auflösen. RO nutzt GPS-Signale, um Profile atmosphärischer Parameter zu erstellen. Diese Messungen haben eine hohe Genauigkeit in der UTLS und eine hohe vertikale Auflösung.

In dieser Arbeit verwende ich RO, um die Variabilität in der UTLS und die Eigenschaften der Tropopause zu beschreiben. Durch die Erstellung vertikal aufgelöster Indizes aus der RO-Temperatur werden die Hauptmoden der Variabilität in der tropischen UTLS ermittelt. Diese helfen, durch vulkanische Aerosole verursachte Signale zu isolieren und die Erwärmung der Stratosphäre selbst bei kleineren Vulkanausbrüchen zu detektieren.

Darüber hinaus zeigt die Analyse von doppelten Tropopausen einen Zusammenhang mit der El-Niño-Südlichen Oszillation. Während der kalten La-Niña-Phase wird eine größere Häufigkeit von doppelten Tropopausen beobachtet, da sich der tropische Gürtel verengt, was einen Luftaustausch zwischen Troposphäre und Stratosphäre in niedrigeren Breiten ermöglicht. Schließlich wird ein kontinuierlicher Anstieg der Tropopause über der Nordhemisphäre festgestellt, einer der Fingerabdrücke des Klimawandels im UTLS.

Acknowledgments

This work was not done without the help and sacrifice from a large number of people around me, not only in the scientific community.

A special thanks to Florian for moral, structural, organizational, technical, scientific, social, motivational, inspirational support, taking the role as an unofficial mentor and co-supervisor, and being a true friend! His role during this project has, to me, been crucial to reach the end goal. I cannot stress this enough.

Sanne, my wife, quit her job for 2 years, and moved to Graz with me. She organized my private life, so that I experienced more than just the daily walks between the apartment and the office at the Wegener Center for Climate and Global Change (WEGC). While I was in Graz alone, she raised our 3 children alone for the total of a year (the first and last half years of my 3 years long stay), including bringing them to sports, music lessons, and birthdays, while, at the same time, also working as a teacher. A special thanks to our children, Anton, Sne, and Billy, who have had long periods without their father, also after returning to Copenhagen. They were dragged along to Graz, left their friends, and went to school and kindergarten without previously knowing the German language. This was very hard for all of them in the beginning, but it ended exceptionally well. Thanks to GIBS, BIPS, and Wiki Kindergarten for that.

At the WEGC, I would like to thank Barbara ("die kleine"), for preparing the processed Radio Occultation (RO) data, and for friendship and taking me on hiking trips. I would like to thank the organization, Gottfried, Sabine, Betti, Verena, Lena, Wim, Armin, and Jürgen for running the WEGC house and infrastructure smoothly, facilitating a great workspace. Barbara ("die grosse"), Marc and Vroni, and everyone else at the WEGC for scientific help and discussions. Alejandro, Thomas, Harald and Matt for discussions on Paper I. Matthias and Patrik for discussions and critical questions, and letting me participate in their work, which e.g. resulted in Paper II. Thanks to Torsten for all the help on Paper III. My office colleagues Josef, Lukas, Clara, and Katha for creating a great work atmosphere. Therese for laying some of the ground work for Paper III.

Thanks to the Doctoral Programme Climate Change (DKCC) administration, Regina and Tina, and later Anna and Olivia, and all the supervisors for running the DKCC, and all my other great colleagues at the DKCC for discussions and great time at the workshops: Javier, Michael, Arijit, Matthias, Eike, Vincent, Silke, Stefan, Florian, Philipp, Sajeev, Johannes, Hannah, Kian, Yadira, Sungmin, Daniel, Christian and Nina. Also thanks to Austrian Science Fund (Fonds zur Förderung der wissenschaftlichen Forschung) (FWF) for providing the funding,

which made it all possible, and to the open source community (especially Linux and the projects funded by PyData).

A special thanks to Paul, Nina, Jörg, and Steffi for receiving me in Graz, for food, shelter, friendship, hikes, and making me feel home. Thanks to Dorit for letting me borrow the apartment. Thanks to fam. Benedikt for including us in their larger family and family traditions. Thanks to Gitti for lending out furniture.

I worked at the Danish Meteorological Institute (DMI) in Copenhagen in the RO field before I went to Graz. I would not have considered the project if it was not for the support from Stig, Kent, Hans, Joe, Kjartan, Georg, Kristian, and also Klub Kold. Moral support and PhD-student discount on clothing from my neighbor, Per. Lasse and Jonas in my current company, for giving me time and freedom to finalize Paper III and the thesis (after the stay in Graz). My own parents, Arne Brigt and Solfrid, for providing economical security if we needed it. We managed without, but it is hard to explain the value of having this option as safety. Also thanks to my parents in laws, Gunnar and Karen, who helped out when I was away.

Finally, lots of thanks to Andrea for making it all possible and being a great supervisor. Thanks for all the patience, freedom, and discussions, and guidance, pulling me back on the track, and not to forget, for believing in me in the first place, despite my somewhat unusual situation compared to the other students, with when it comes to age and children. I am sure there have been doubts, but now that the work is done, I hope it turned out OK at the end. I am truly grateful!

Contents

Preface 1

I. Synopsis 3

1. Introduction 5

2. Atmospheric structure and dynamics 9
2.1. The thermal structure of the Upper Troposphere–Lower Stratosphere 9
2.1.1. Troposphere . . . 9
2.1.2. Stratosphere . . . 10
2.1.3. Tropopause . . . 10
2.2. Global circulation patterns . . . 12
2.2.1. Troposphere . . . 12
2.2.2. Stratosphere . . . 15
2.3. Atmospheric variability patterns in the tropics . . . 15
2.3.1. The Quasi-Biennial Oscillation . . . 16
2.3.2. The El Niño–Southern Oscillation and the Walker circulation 19

3. Data 23
3.1. Global Navigation Satellite System Radio Occultation . . . 23
3.2. Radiosonde observations . . . 25
3.3. Reanalysis data . . . 25
3.4. Wind data for QBO indices . . . 26
3.5. Sea-surface temperature data for ENSO indices . . . 28
3.6. Aerosol data for volcanic impacts . . . 29
3.7. Solar activity index . . . 29

4. Diagnostics of atmospheric variability 31
4.1. Characterizing atmospheric variability modes in the UTLS . . . 31
4.1.1. Multivariate linear regression . . . 31
4.1.2. Variability indices from Empirical Orthogonal Function analysis 32
4.2. Characterizing the tropopause, its variability and trends . . . 36
4.2.1. Cold Point Tropopause . . . 36
4.2.2. Tropopause proxy at 100 hPa . . . 38
4.2.3. Lapse rate tropopause - implementation and results . . . 38
4.2.4. Double tropopauses - implementation and results . . . 47
4.2.5. Zero lapse rate tropopause . . . 50

4.3. Characterizing the tropopause region 52
4.3.1. Tropopause Inversion Layer 53
4.3.2. Tropical Tropopause Layer 55
4.3.3. Tropical belt width - cluster analysis 60

5. Summary and conclusions **69**

II. Published papers **71**

Paper I: Atmospheric QBO and ENSO indices with high vertical resolution from GNSS radio occultation temperature measurements **73**
1. Introduction 73
2. Data 74
3. Methods 75
4. Results 77
5. Summary and conclusions 83

Paper II: Quantifying Stratospheric Temperature Signals and Climate Imprints From Post-2000 Volcanic Eruptions **87**
1. Introduction 87
2. Data and method 89
3. Results and Discussion 91
4. Conclusions 94

Paper III: Double Tropopauses and the Tropical Belt Connected to ENSO **97**
1. Introduction 97
2. Data 98
3. Methods 98
4. Results 99
5. Conclusions 104

Paper IV: Continuous rise of the tropopause in the Northern Hemisphere over 1980–2020 **107**
1. Introduction 107
2. Results 108
3. Discussion 111
4. Materials and methods 111

Supplementary Materials for Paper IV **117**

Acronyms **127**

List of Figures **131**

List of Tables **135**

Bibliography **137**

Preface

This thesis is based on the following peer-reviewed publications:

Wilhelmsen, H., F. Ladstädter, B. Scherllin-Pirscher, and A. K. Steiner (2018)."Atmospheric QBO and ENSO indices with high vertical resolution from GNSS radio occultation temperature measurements". *Atmos. Meas. Tech.* 11.3, pp. 1333–1346. DOI: 10.5194/amt-11-1333-2018

Contributions: H.W. collected the data, performed the computational implementation and the analysis, created the figures, and wrote the first draft of the paper, and revised the manuscript. All authors contributed to the study design. F.L. provided advice on the analysis design and made major contributions to the text. B.S.-P. provided advice on the method and interpretation of the results, and contributed to the text. A.K.S. provided guidance and advice on all aspects of the study, and contributed to the text. All co-authors helped on the manuscript revisions and gave their final approval of the paper to be published.

Stocker, M., F. Ladstädter, **H. Wilhelmsen**, and A. K. Steiner (2019). "Quantifying Stratospheric Temperature Signals and Climate Imprints From Post-2000 Volcanic Eruptions". *Geophys. Res. Lett.* 46.21, pp. 12486–12494. DOI: 10.1029/2019GL084396

Contributions: M.S. collected and prepared the data, performed the computational implementation and analysis, created the figures, and wrote the manuscript. H.W. helped with the computational implementation on the use of the Empirical Orthogonal Function analysis, provided technical guidance, guidance on the programming language, and contributed to the text. F.L. and A.K.S. provided guidance on all aspects of the study, helped on the interpretation of the results, and contributed to the text. A.K.S. advised the work. All co-authors helped on the manuscript revisions and gave their final approval of the paper to be published.

Wilhelmsen, H., F. Ladstädter, T. Schmidt, and A. K. Steiner (2020). "Double Tropopauses and the Tropical Belt Connected to ENSO". *Geophys. Res. Lett.* 47.14, e2020GL089027. DOI: 10.1029/2020GL089027

Contributions: H. W. collected and prepared the data, performed the computational implementation and the analysis, created the figures, and wrote the first draft of the paper, and revised the manuscript. F.L., T.S., and A.K.S. provided advice on the analysis design and interpretation of the results. F.L. and A.K.S. provided guidance on all aspects of the study and made major contributions to the text. All

co-authors helped on the manuscript revisions and gave their final approval of the paper to be published.

Meng, L., J. Liu, D. W. Tarasick, W. J. Randel, A. K. Steiner, **H. Wilhelmsen**, L. Wang, and L. Haimberger (2021). "Continuous rise of the tropopause in the Northern Hemisphere over 1980–2020". *Sci. Adv.* 7.45, eabi8065. DOI: 10.1126/sciadv.abi8065
Contributions: J.L. and L.M. conceived the study. L.M. developed the methodology and conducted data analysis under the supervision of J.L. W.J.R. provided critical guidance and advice. A.K.S., D.W.T., and L.W. contributed significantly to the work overall. A.K.S., H.W., and L.H. provided the GPS, RICH, and RAOBCORE data and guided application and interpretation of the data. J.L. and L.M. wrote the manuscript with valuable input from all coauthors. All co-authors helped on the manuscript revisions and gave their final approval of the paper to be published.

This thesis is structured in two parts. It starts with a synopsis in Part I which includes an introduction and motivates the research questions and aims of this thesis. A scientific background and an overview on the datasets is given. A detailed description of methods is provided and interpretation of results is discussed in context of the resulting papers. The papers are listed in Part II. Finally, a list of acronyms, figures, and tables and a bibliography are included at the end of the thesis.

Part I.

Synopsis

1. Introduction

> "It is very likely that global mean stratospheric cooling will be larger by the end of the 21st century in a pathway with higher atmospheric CO_2 concentrations. It is likely that upper tropospheric warming will be larger than at the tropical surface, but with an uncertain magnitude owing to the effects of natural internal variability and uncertainty in the response of the climate system to anthropogenic forcing." (IPCC 2021)

The Earth's climate system is constantly changing. When the changes happen over long time periods, plants and animals relocate, adapt, evolve, and even become extinct. No one is hurt. Nobody notices. Since the last ice age the Earth's climate has been remarkable stable, which has nourished an incredible growth in the human population. In recent years, however, the temperature on the Earth's surface has been rising, and it has been rising fast. With the number of people currently living on the planet, it will not happen unnoticed.

The atmospheric temperature is influenced by several phenomena. E.g., the tilt of the Earth's axis of rotation with respect to the sun creates the seasons, with varying solar influx at different locations during the year. Volcanic aerosols, ozone and water reflect and absorb solar radiation prohibiting parts of it to reach the Earth's surface. There are internal effects like e.g. wind systems that carry cold air from the poles, or naturally occurring oscillations in temperature that have wide-reaching impact around the world, like the major modes of variability in the tropics, the El Niño–Southern Oscillation (ENSO) and the Quasi-Biennial Oscillation (QBO). All these effects, and many others, naturally influence the global temperature.

The atmospheric temperature is also influenced by human activity. Increased emissions of greenhouse gases into the atmosphere, from e.g. burning fossil fuels, enhance the greenhouse effect. More outgoing long-wave radiation from the Earth is absorbed in the lower parts of the atmosphere, so that it no longer reaches the upper parts. A signature of the human influence on the atmospheric temperature may therefore be observed by rising temperatures in the lower part of the atmosphere, and falling temperatures higher up.

Both the natural and anthropogenic effects paint a messy picture of a rather complex system. In the last couple of decades, therefore, there has been much debate about whether the changing climate is caused by humans or not. I.e., whether or not e.g. the observed changes in temperature are just part of naturally

occurring internal dynamics of the complex and chaotic atmosphere. Despite extensive evidence in the scientific literature there have been economical, political and ideological interest in keeping doubt about cause and effect in the human population. In the latest Intergovernmental Panel on Climate Change (IPCC) assessment report, however, it was made absolutely clear that the underlying warming of the Earth's global temperature is anthropogenic. It is now well established that human activity has resulted in increased greenhouse gas emissions, which has led to rising temperatures, and that it is still ongoing (IPCC 2021). The changes in temperature near the Earth's surface is, in other words, well known, due to e.g. observations and models. The source of the variability is well described and understood, and can therefore be accounted for statistically, and the underlying temperature development can be revealed.

Going above the surface, this picture becomes more blurry. The atmosphere is divided into layers with different properties. The natural variability at the surface may propagate up into the lowermost layer, the troposphere. In the troposphere, the air gets stirred up both vertically as well as horizontally. In the next layer, the stratosphere, the air is stratified, and the air flow is mainly horizontal. The two layers have different chemical compositions, and tend to keep to themselves. Water, e.g., is mainly found in the troposphere. Therefore, when Stratosphere-Troposphere Exchange (STE) does occur the chemical components in the layers change, which influences the temperature in both the Upper Troposphere–Lower Stratosphere (UTLS) as well as at the Earth's surface. Identifying where and when STE takes place may be important for understanding the changes that take place in the atmosphere. Likewise, it is important to describe how the modes of variability influence the atmospheric temperature at different altitude layers.

The modes of variability are commonly described by indices, made from measurements. The ENSO indices are traditionally made from sea surface temperature measurements, and the QBO index by wind measurements in the stratosphere. The atmospheric temperature response follows the atmospheric dynamics, often introducing a time delay. Describing and identifying the temperature response from the different phenomena at different altitude layers in the UTLS with high vertical resolution may therefore help reducing the existing uncertainty in the UTLS.

Satellite observations have been made from space since the late 1970s, covering the Earth. The measurements are usually made in nadir-viewing geometry (looking down at the surface), and have limited vertical resolution. Radiosonde Observation (RAOB), made with weather balloons from the surface and up, have a decent vertical resolution, but they are mainly made over land, for weather predictions, and were not originally intended for monitoring the climate. Both type of measurements need to be calibrated before they can be used for climate applications, e.g. due to instrumental change. Radio Occultation (RO) observations, however, are made in limb-viewing geometry (scans the atmosphere horizontally), have both global coverage, high vertical resolution, and do not need calibration between the different satellite missions. The many satellite missions can therefore be combined into one

single data record. Also the temperature measurements are very precise in the UTLS. All these properties make RO data ideal for monitoring the climate in the UTLS. The RO era is still young, only about 20 years old, which is a relatively short for monitoring the climate. However, it enables very precise diagnostics of UTLS with high vertical resolution, on a global scale, that would not have been possible before.

In the context of reducing uncertainty in how the atmospheric temperature in the UTLS develops in a changing climate, the overall objective of this work is motivated by the following research questions:

1. Can the atmospheric variability be better characterized with high vertical resolution using RO observations?

2. Can RO data contribute to a better knowledge about changes in the vertical temperature structure and climate trends?

3. Which new insights on atmospheric variability and tropopause changes can be gained from RO data?

The work is summarized in four papers. In Paper I (Wilhelmsen et al. 2018), the atmospheric temperature change in the tropical UTLS following the main natural modes of variability in the tropics, the ENSO and the QBO, were described as indices with high vertical resolution using RO data. The indices describe the temperature response from the modes of variability with only a few number of time series. Some of the QBO temperature response described in the QBO indices does likely originate from volcanic aerosols, as the vertical and horizontal aerosol transport depends on the QBO phase. The volcanic influence on the stratospheric temperature, with the QBO statistically removed, was described in Paper II (Stocker et al. 2019). Paper III (Wilhelmsen et al. 2020) showed how the atmospheric structure in the Pacific is influenced by the ENSO, by forming double tropopauses, and possibly enhancing Stratosphere-Troposphere Exchange (STE) in the subtropics. Finally, Paper IV (Meng et al. 2021) showed that the tropopause is rising in the Northern Hemisphere (NH) over the past 40 years.

This synopsis gives an overview of the basic knowledge that is needed to understand the content of the four papers. It is structured in the following chapters. Chapter 2 shows a basic overview of the thermal structure of the UTLS. It also describes the main modes of variability in the tropical UTLS, the ENSO and the QBO. Chapter 3 gives a short description of the data used in the four papers. Chapter 4 gives an overview of the established methods and definitions used in this work. It discusses different tropopause definitions, their optimal implementation for RO data, and results on tropopause variability and trends. In addition it includes results that were not included in the papers, but could be useful for future work. Chapter 5 gives a short summary of the essential results.

2. Atmospheric structure and dynamics

"There was a boy
A very strange enchanted boy
They say he wandered very far, very far
Over land and sea
A little shy and sad of eye
But very wise was he" (Nature boy, eden ahbez)

2.1. The thermal structure of the Upper Troposphere–Lower Stratosphere

The air in the lower part of the atmosphere is composed of several different gases. Although the air gets thinner with height, the main gas components and the ratios between them stay, with some exceptions, the same all the way up to about 100 km. The dynamical and thermal properties, however, are quite different.

In the lowest part of the atmosphere, the *troposphere*, temperature decreases with height. This can e.g. be experienced when walking up a mountain. It is colder at the top than at the foot. At the end of the 18th century a French and a German scientist independently discovered that the temperature does not continue to decrease (Hoinka 1997). At a certain point, at the *tropopause*, the temperature starts increasing. The temperature keeps rising until it reaches the *stratopause*, where it starts to cool again. The layer between the tropopause and the stratopause is called the *stratosphere* (Wallace and Hobbs 2006).

2.1.1. Troposphere

The troposphere is dynamic and turbulent. The part of the solar radiation that reaches all the way down to Earth heats the surface. The heated surface heats the surface air, making it lighter, and therefore rise in the colder, heavier air above it, like bubbles in water. As the air rises, the pressure falls, because the load from the column of air above it gets smaller, and the air expands. With lower pressure and density follows lower temperature, and so, the temperature falls with altitude. The rising surface air gets replaced by air nearby, and the air above gets pushed away, adding to the wind and circulation systems, that mixes the tropospheric air both horizontally and vertically (Wallace and Hobbs 2006; Salby 2012).

2.1.2. Stratosphere

In the stratosphere, however, high energy radiation from the sun splits naturally occurring oxygen (O_2) molecules into single oxygen atoms. The single oxygen atoms react with other O_2 molecules and form ozone (O_3). When high energy solar radiation hits these O_3 molecules, they split again, into single and molecular oxygen, making them available for further O_3 formation. This process both absorbs high energy solar radiation and releases heat which warms the stratospheric air.

Further down in the stratosphere the higher density of the air makes more O_2 molecules available for O_3 formation. At the same time, there is less high energy solar radiation available for splitting the molecules. It has been absorbed while forming the O_3 above. This leads to less heating. At a point, most of the high energy solar radiation has been absorbed by this ozone layer, and the process of creating additional O_3 stops, and with that the heating (Salby 2012).

The air in the stratosphere is stratified. If an air parcel gets lifted upward in the atmosphere, it will experience less load from the air column above it, and therefore expand until it gets the same pressure as the surrounding air. As it expands, it also cools. In the stratosphere, since the air above is warmer than the air below, the lifted, already colder air parcel from below, cools to an even lower temperature than the surrounding air. Same pressure but lower temperature means higher density, which means the air parcel gets heavier than its surroundings. It therefore "wants" to get back to its original position. The analog mechanism happens if the air parcel gets pushed downward. With the same pressure as its new surroundings, but with higher temperature, the density is smaller, and the air parcel gets lifted.

A layer is stable if the lapse rate (negative vertical gradient) is smaller than the dry adiabatic lapse rate, which is about $9.8\,\mathrm{K\,km^{-1}}$. The lower the lapse rate (the higher the gradient) of a layer, the more stable it is. Because the troposphere gets cooler with height, and the stratosphere gets warmer with height, the stratosphere inhibits vertical motion more than the troposphere (Wallace and Hobbs 2006). As a consequence, a displaced air parcel in a stable atmosphere will oscillate. This can e.g. be seen when air is blown over a high mountain, and a wave like pattern forms on the lee side. This type of waves is called gravity waves (e.g. Wallace et al. 1993).

2.1.3. Tropopause

As the temperature decreases with height in the troposphere and increases with height in the stratosphere, the tropopause stands out in the temperature profile as the coldest point in the Upper Troposphere–Lower Stratosphere (UTLS).

The altitude of the tropopause depends on both latitude and season. In the *tropics*, the altitude is found at around 15 km–18 km (Holton et al. 1995; Highwood and Hoskins 1998; Seidel et al. 2001). The shape of the temperature profile does not change much, and the thermal tropopause is clearly defined, also between the different seasons (see the middle column in Figure 2.1). At the *poles* and in

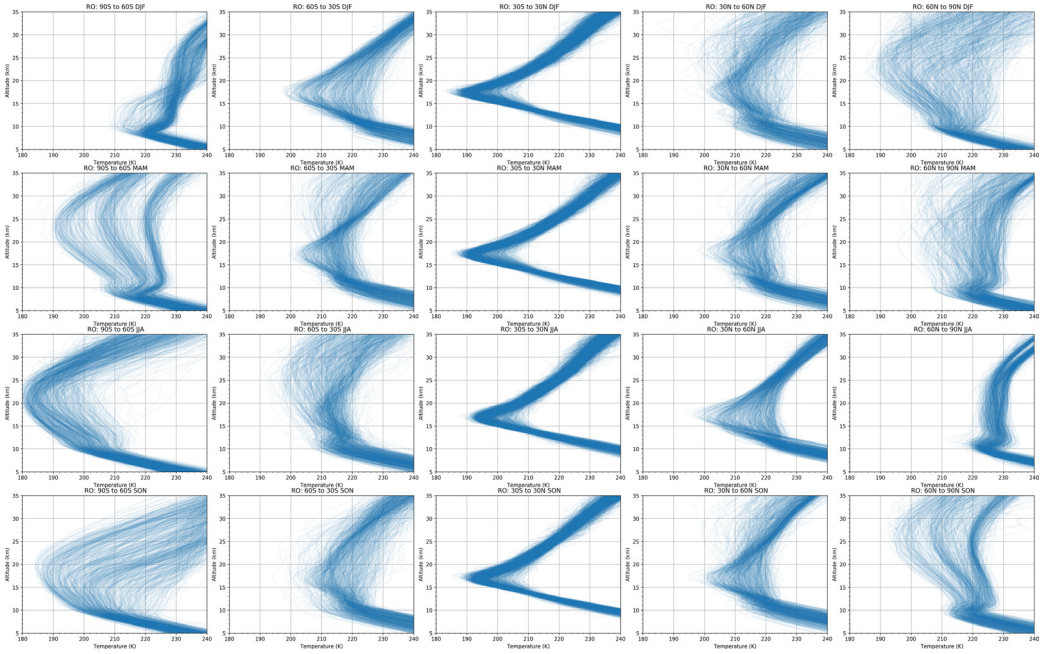


Figure 2.1.: Monthly mean temperature profiles from Radio Occultation (RO) at different latitude intervals for different seasons. From the left the columns show the latitude intervals 90S–60S, 60S–30S, 30S–30N, 30N–60N, and 60N–90N. From the top the rows show the seasons December–January–February (DJF), March–April–May (MAM), June–July–August (JJA), and September–October–November (SON). The axis labels are "Temperature" on the x-axes (180 K–240 K) and "Altitude" on the y-axes (5 km–35 km).

the extratropical regions the tropopause is found several km lower (6 km–8 km), and has a high seasonal dependency. At *mid-latitudes*, the vertical temperature structure is more complicated (see the second and fourth columns in Figure 2.1). In this region, extratropical air masses meet tropical air masses (see section 2.2). The higher altitude tropical tropopause from the tropical air masses may therefore overlap the lower altitude tropopause from the extratropical air masses. As both air masses have their own tropopause, they may form Double Tropopauses (DTs) (Peevey et al. 2014). The tropopause in this region may therefore be ambiguous. The mean mid-latitudinal tropopause may drop by several km, as one moves from the tropical regime to the extratropical regime. Detecting the location of DTs is one of the topics of Paper III (Wilhelmsen et al. 2020).

Tropopause as a layer

Rather than considering the tropical tropopause as a single point on the temperature profile, it is often considered as a region, holding properties of both the troposphere and the stratosphere. Whereas the single points from the temperature profiles compose a surface, the regions compose a layer, called the Tropical Tropopause

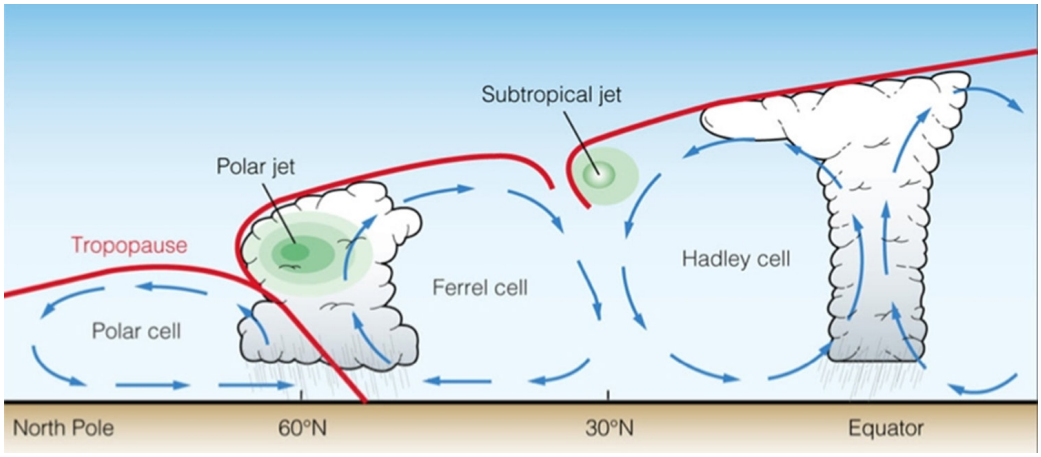


Figure 2.2.: Cross-section of the general global circulation patterns including the STJ. Source: NOAA/NWS. https://commons.wikimedia.org/wiki/File:Jetcrosssection.jpg. Last visited: 2022-06-07.

Layer (TTL)[1]. It is an important layer because it acts as a "gate to the stratosphere", where e.g. moist air from the upper part of the tropical troposphere enters the stratosphere (section 2.2). The chemical components and the processes that take place within the TTL may influence the stratosphere and therefore the global temperature (Fueglistaler et al. 2009; Randel and Jensen 2013).

2.2. Global circulation patterns

2.2.1. Troposphere

The general circulation pattern in the troposphere consists of three cells, the Hadley cell, the Ferrel cell, and the Polar cell (Figure 2.2). Hot and moist surface air rises from solar heating at the Equator. As the rising air reaches the tropopause, the vertical air flow is limited by the barrier at the tropopause, and the air flows out toward the upper air mid-latitudes. This outward flow is amplified by the horizontal temperature gradients between the warm tropics and the colder mid-latitudes. At the edge of the tropics, the air flows downward, and back toward the Equator, and fills the void that was created by the rising air at the equatorial surface. This circular pattern makes up the two Hadley cells, on both hemispheres. In a similar way, the downward flow in the Hadley cell creates the Ferrel cell, and the upward flow in the Ferrel cell creates the Polar cell (Figure 2.2), on both hemispheres. These cells are just schematic illustrations of the net flow. There are constant changes in local weather and wind patterns in all directions in the troposphere.

The Coriolis force bends poleward flow eastward, and equatorward flow westward, on both hemispheres. The surface part of the Hadley cell, therefore, bends westward,

[1]The TTL is sometimes called "Tropical transition layer".

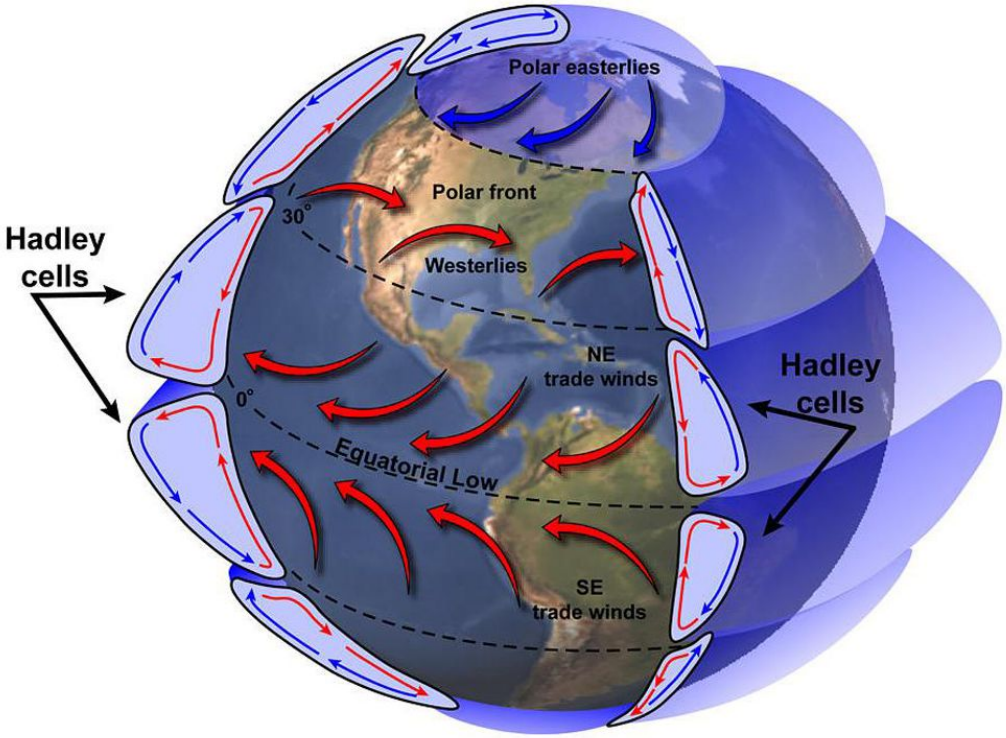


Figure 2.3.: Illustration of the general global circulation. Source: NASA. https://groups.seas.harvard.edu/climate/eli/research/equable/hadley.html. Last visited 2022-07-20.

creating the westward flowing Trade winds (Figure 2.3). The Trade winds play an important role in the dynamics of the El Niño–Southern Oscillation (ENSO) (see subsection 2.3.2 and Paper I (Wilhelmsen et al. 2018) and Paper III (Wilhelmsen et al. 2020)).

Strong horizontal temperature gradients in the *upper* part of the troposphere, at latitudes where the Hadley cell meets the Ferrel cell, accelerate the poleward wind flow. The Coriolis force bends this flow eastward, creating the strong Subtropical Jet Stream (STJ), meandering in a wave like pattern, like a river, around the globe (Figure 2.4). This type of waves are called Rossby waves, or planetary waves. They occur naturally, as the Coriolis force acts on small changes in the STJ. The STJ is located at an altitude just below the tropical tropopause (Figure 2.2), on both hemispheres and is strongest during winter.

Since the tropical tropopause is found at a higher altitude than the mid-latitude tropopause, the STJ marks a region where the mid-latitude stratosphere is found at the same altitude as the tropical troposphere. The vertical barrier at the tropopause is therefore weakened, which enables Stratosphere-Troposphere Exchange (STE), in both directions (Stohl et al. 2003). The STJ occurs in the same region where DTs form. Finding the location of DTs, therefore, may play an important role in

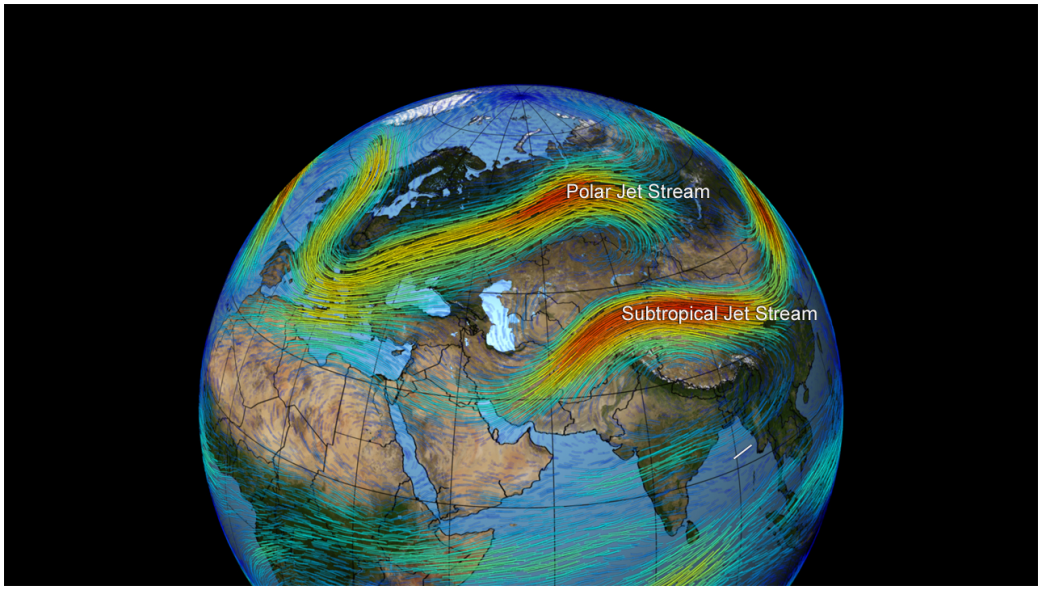


Figure 2.4.: STJ shown on the NH. Source: NASA/GSFC. https://svs.gsfc.nasa.gov/11471. Last visited: 2022-07-21.

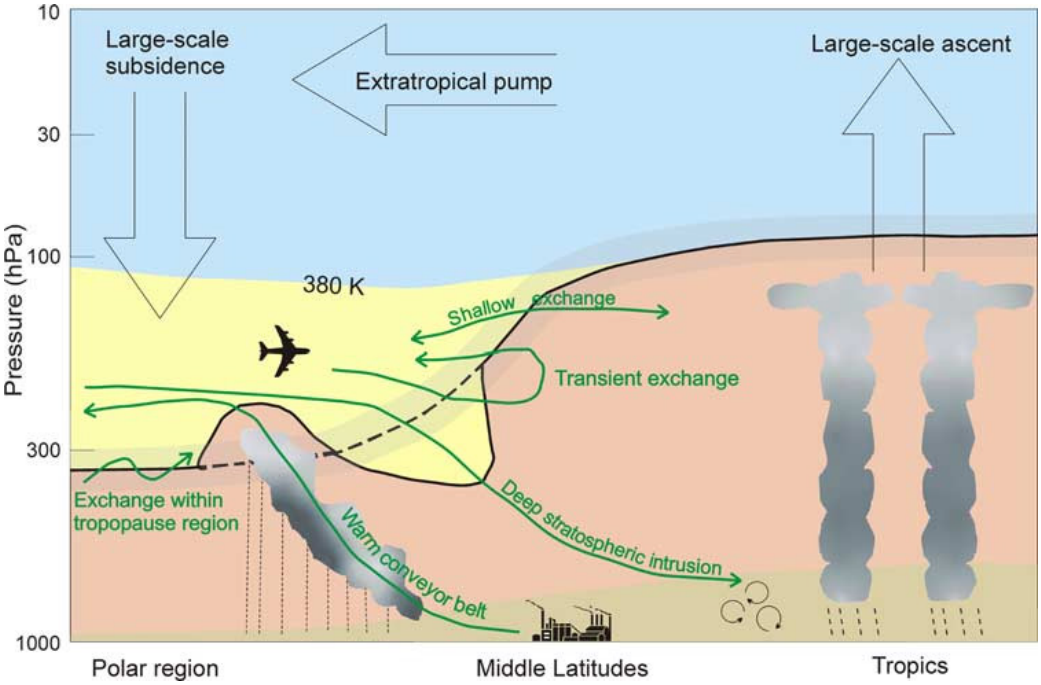


Figure 2.5.: Global aspect of STE. At the mid-latitudes, the extratropical stratosphere is located at the same altitude as the tropical troposphere, which may enable STE. Source: Figure 3 from Stohl et al. (2003).

locating areas where STE takes place (see Paper III (Wilhelmsen et al. 2020)).

The edges of the tropics

Understanding how the tropics behave in a changing climate may be of great interest, especially at the edge of the tropics. The surface temperature outside the tropical region is generally colder than on the inside. The temperature typically changes by 1 K per degree latitude in the transition region (Birner et al. 2014). As the tropical belt has shown to be expanding toward the poles in a changing climate (Seidel et al. 2008; Staten et al. 2018), these regions may experience even larger temperature changes than the average global temperature change, over very short time periods. An expanding tropical belt may therefore have great regional consequences near the edges.

2.2.2. Stratosphere

In the stratosphere the Brewer–Dobson Circulation (BDC) maintains the large scale circulation, from the tropics to the poles (Butchart 2014). The deep convection in the tropics, the rising part of the Hadley Circulation, lifts moist air up to the upper part of the troposphere. From here, the net flow of air ascends into the tropical stratosphere, through the tropopause (Randel and Jensen 2013). The stratospheric air flows poleward above the tropopause in both hemispheres and does not descend back into the troposphere before it reaches mid- and polar latitudes (see Figure 2.5). This is often labeled the "extratropical pump". Gases entering the tropical stratosphere can be traced in the extratropical pump on its path poleward.

When volcanic eruptions are powerful enough, particles such as ash and gases can reach all the way into the stratosphere. The heavy parts fall out quickly, but the lighter parts can stay in the stratosphere for months to years (Robock 2000; Robock 2015). When volcanic sulfur dioxide (SO_2) molecules interact with the stratospheric water (H_2O) they form sulfuric acid (H_2SO_4) (Kremser et al. 2016) which has the potential to cause a warming in the lower stratosphere. Additionally they reflect short wave radiation which causes a cooling below.

The concentration and distribution of particles erupted into the stratosphere from volcanoes are influenced by the strength of the stratospheric circulation. Because the gases and aerosols are radiatively active they influence the stratospheric temperature, therefore, the temperature change induced by volcanic eruptions can be detected. This is what we explore in Paper II (Stocker et al. 2019), where we identify the changes in the temperature associated with volcanic aerosols.

2.3. Atmospheric variability patterns in the tropics

The weather and climate are in constant change. There are intra-seasonal, seasonal, and inter-seasonal changes. In addition to local and rapid changes, the chaotic

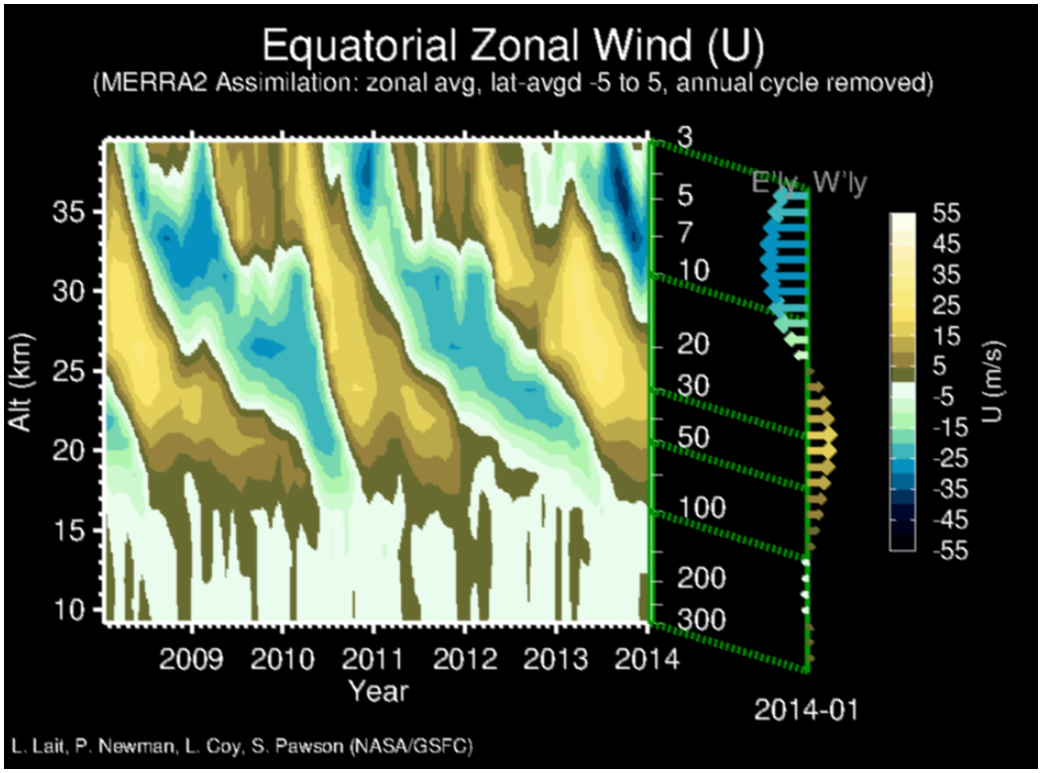


Figure 2.6.: Illustration of the QBO wind patterns. Source: National Aeronautics and Space Administration (NASA). https://acd-ext.gsfc.nasa.gov/Data_services/met/qbo/anim.html. Last visited: 2022-07-20.

atmospheric systems have underlying longer lasting variabilities that oscillate between states.

2.3.1. The Quasi-Biennial Oscillation

The Quasi-Biennial Oscillation (QBO) is the major natural variability above the tropical tropopause, in the lower tropical stratosphere (Wallace et al. 1993; Baldwin et al. 2001). Strong, horizontal zonal winds alternate between westward and eastward flow around the globe. The winds are forced by upward propagating waves originating from the tropical convection that transfer momentum as the waves get absorbed by the zonal flow (see Salby 2012, Chap. 18.5). A wind regime appears to take form around 30 km–35 km, and keeps blowing in the same direction, while "slowly" descending until it, a couple of years later, reaches the tropopause and fades away. As it descends, a new oppositely directed wind regime forms above it. The new wind regime also descends, and fades away at the tropopause, while yet a new oppositely directed wind regime forms above (Figure 2.6). When observed at a fixed altitude, it is experienced as if the winds oscillate between westward and eastwards. The period varies with a 28 months on average (e.g., Baldwin et al.

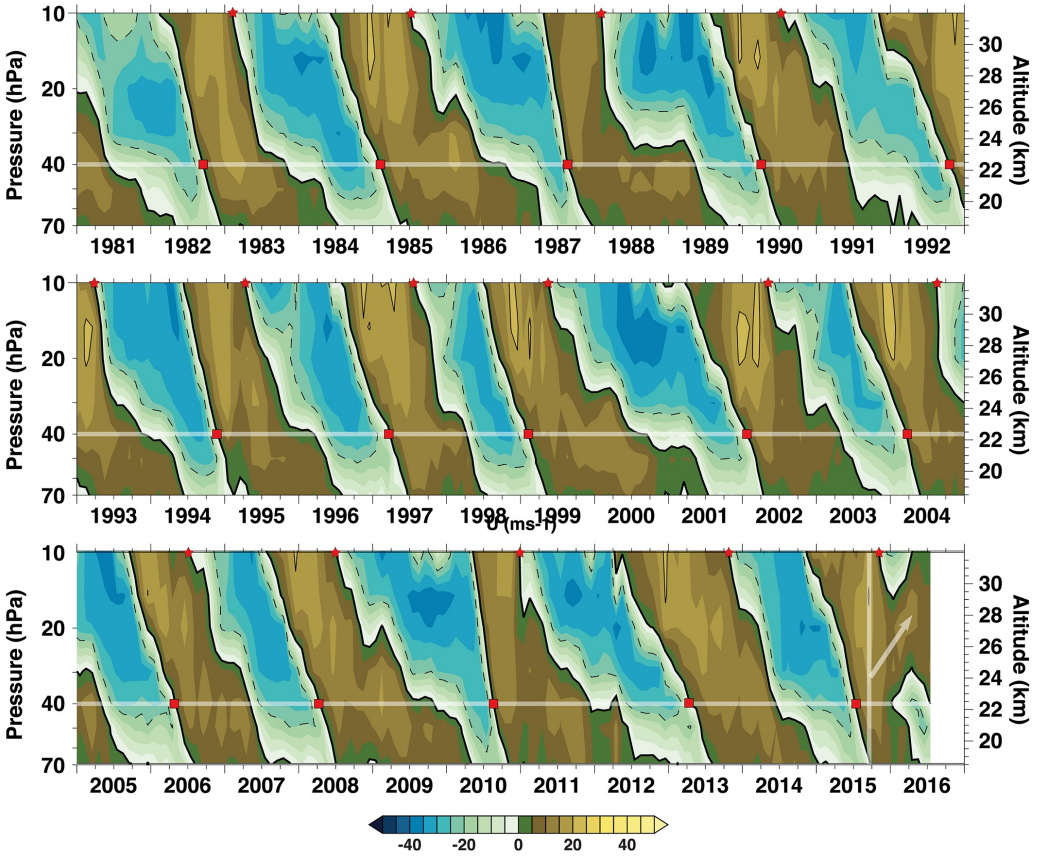


Figure 2.7.: Disruption in the QBO pattern. The wind regimes descend steadily for years until the disruption in 2015–2016, denoted by the upward pointing arrow inside the westerly regime. Note that the color scale enhances the contrast between the westerlies and the easterlies, and the changes are not as sudden as they appear. Source: Figure 1 from Newman et al. (2016).

2001), i.e., with a period of almost two years. This oscillation keeps repeating, and has done so for as long as there has been a record (see Figure 2.7 and Figure 3.2), except for a disruption in 2015–2016 (Osprey et al. 2016; Dunkerton 2017; Newman et al. 2016). The disruption kept the descending QBO regimes out of phase with the previous record, until an additional disruption occurred in 2019–2020, and it now seems to be back in its usual pattern (Anstey et al. 2021). In both disruptions, the wind regime stopped descending half way down, rose a little, and continued into the next period (see Figure 2.7).

The disruption could be seen in Empirical Orthogonal Function (EOF) analysis (subsection 4.1.2) of monthly mean wind fields. When the first time component from the EOF analysis, the PC1, is plotted against the second time component, PC2, the steady, regular, and circular pattern from the previous years takes a shortcut during the period of the disruption (the brown lines in Figure 2.8).

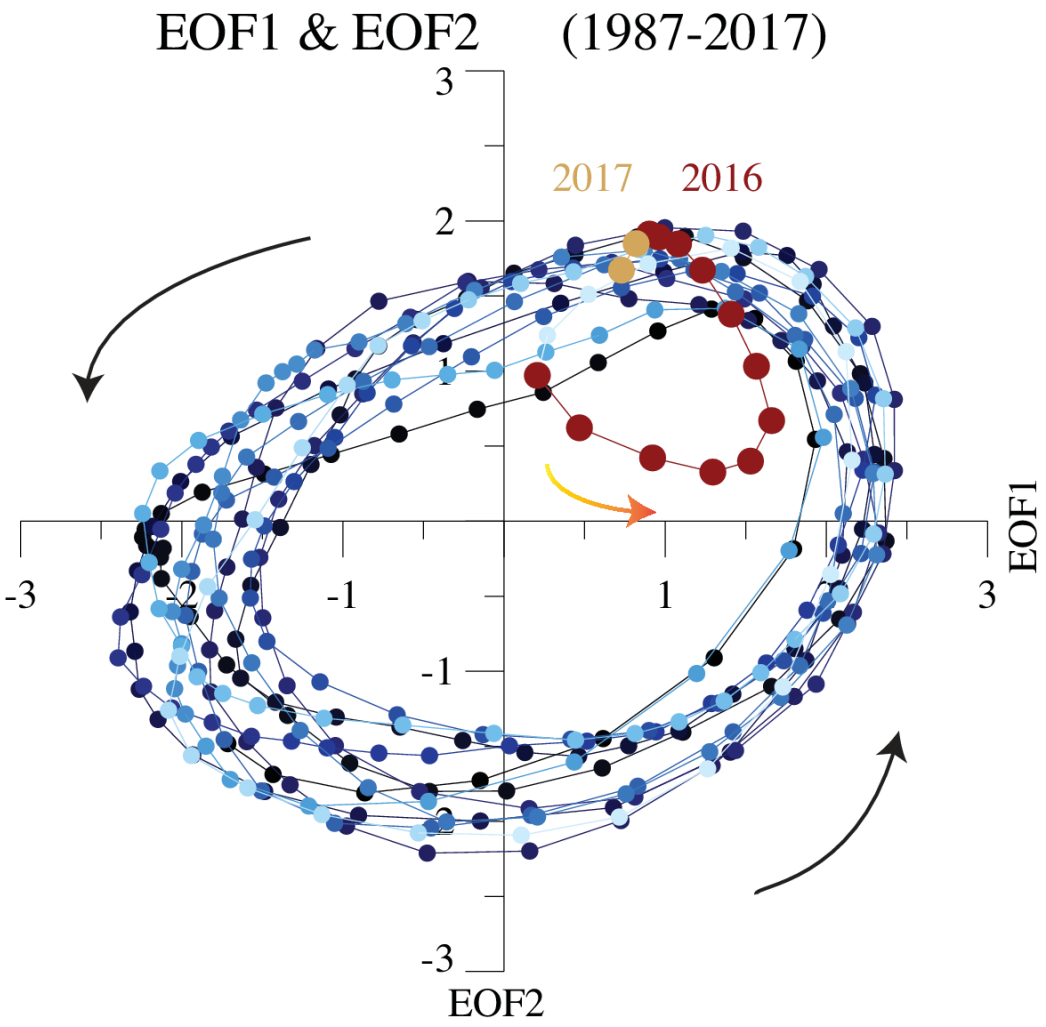


Figure 2.8.: Phase space diagram of the two first time components from the EOF analysis on QBO winds. The labels EOF1 and EOF2 correspond to PC1 and PC2 in this work. Source: Figure 2 from Tweedy et al. (2017).

The horizontal speeds of the QBO winds are of magnitude $\mathrm{m\,s^{-1}}$, whereas the speed of the descending wind regimes is only about 1 km/month. The air mainly mixes horizontally, and the stratosphere keeps its stratified structure, and it shows that a stratified atmosphere does not necessarily imply a calm atmosphere.

With the different phases of the QBO follows temperature change. The atmospheric temperature is proportional to the vertical gradient of the QBO winds (e.g. Baldwin et al. 2001). The temperature pattern can therefore be seen in deseasonalized monthly mean temperature fields. Paper I (Wilhelmsen et al. 2018) takes advantage of these temperature changes to create temperature based QBO indices of high vertical resolution, and Paper II (Stocker et al. 2019) also exploits this to detect the temperature influence of volcanic aerosols.

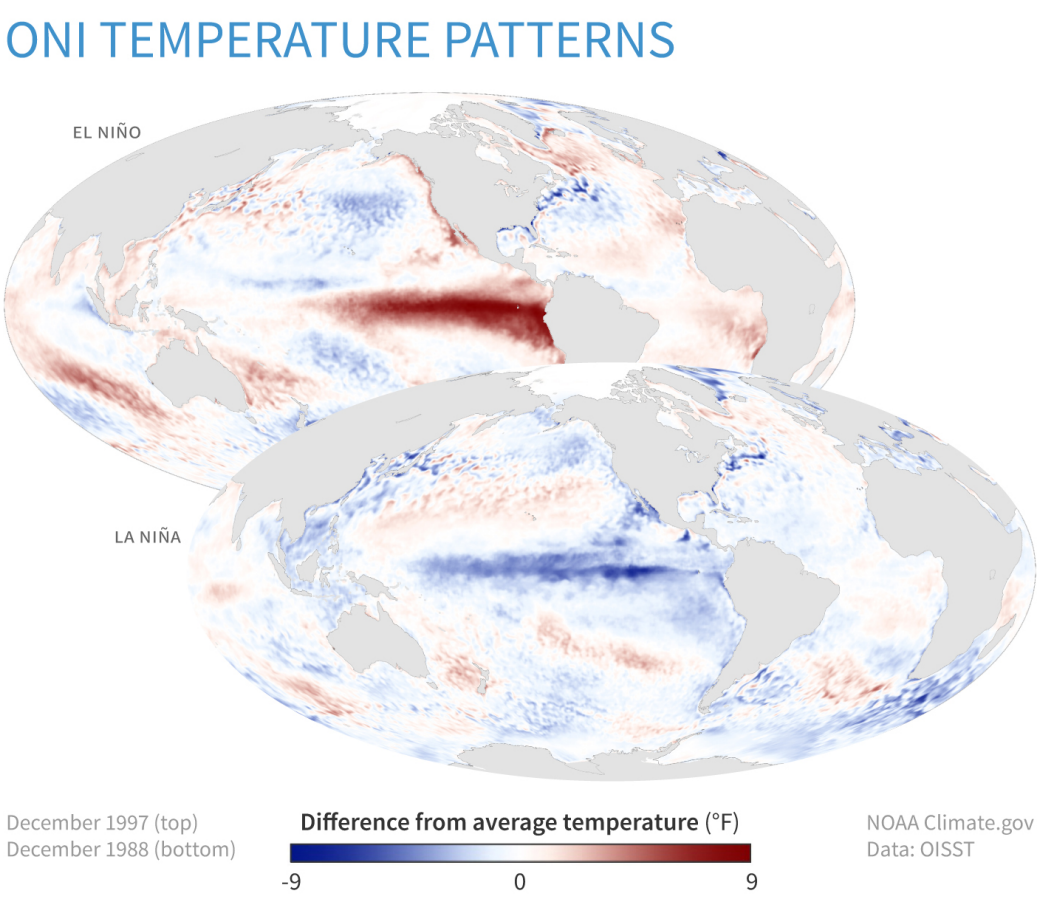


Figure 2.9.: SST anomalies during El Niño (upper) and La Niña (lower). Source: NOAA Climate.gov. https://www.climate.gov/news-features/understanding-climate/climate-variability-oceanic-niño-index. Last visited: 2022-07-20.

2.3.2. The El Niño–Southern Oscillation and the Walker circulation

Below the tropical tropopause, i.e. in the tropical troposphere, the main variability is the ENSO. It is an ocean-atmosphere interacting natural variability that has widespread impact on the world's weather and climate (Figure 2.9).

During *neutral conditions*, the Trade winds (section 2.1), blowing westward at the Equator, push cold water from South America to the Maritime Continent. The water to the east is cold because it is constantly being replaced by cold water from the deep. The westward moving surface water gets heated by the sun and the water in the Maritime continent is therefore warmer than the water to the east. The cold-warm Sea Surface Temperature (SST) difference creates an atmospheric circulation, the Walker Circulation (WC) with warm and moist air rising over the Maritime continent, eastward flow aloft, descending air to the east, and the westward flowing Trade winds at the surface (Figure 2.10).

The *warm phase* of the ENSO, the El Niño (meaning "little boy"), happens when

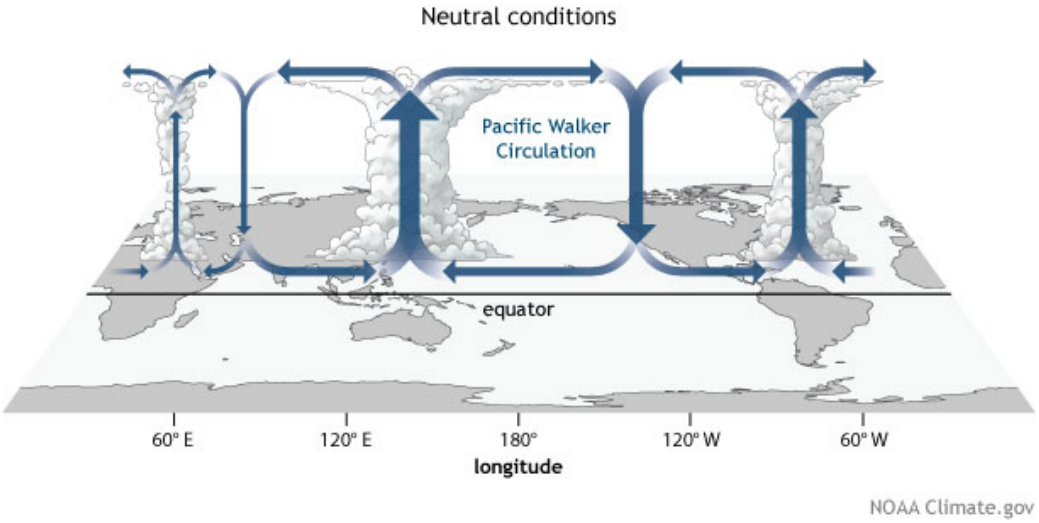


Figure 2.10.: Schematic illustration of the ENSO and the WC during the neutral phase. Source: NOAA Climate.gov, by Fiona Martin. https://www.climate.gov/news-features/blogs/enso/walker-circulation-ensos-atmospheric-buddy. Last visited: 2022-06-07.

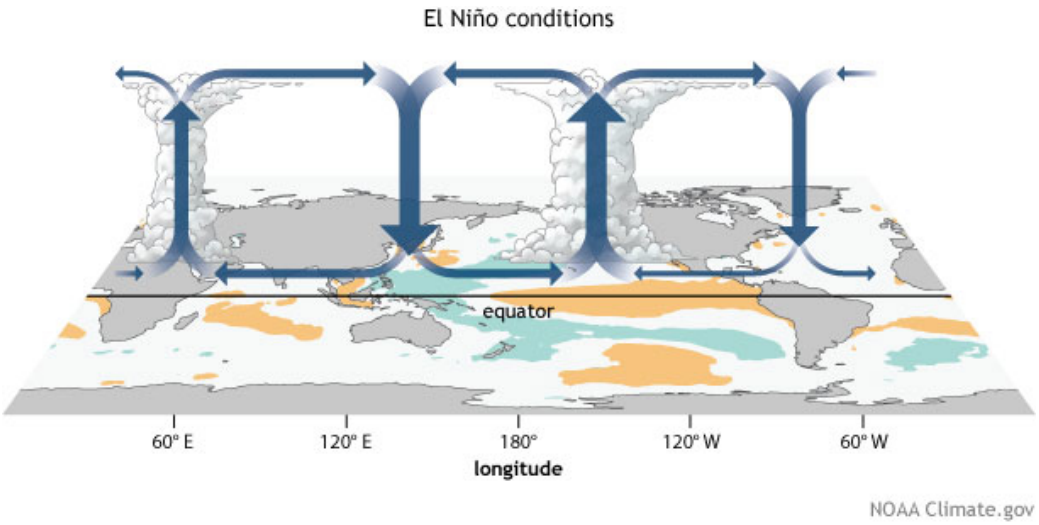


Figure 2.11.: Schematic illustration of the ENSO and the WC during the warm phase, El Niño. Source: NOAA Climate.gov, by Fiona Martin. https://www.climate.gov/news-features/blogs/enso/walker-circulation-ensos-atmospheric-buddy. Last visited: 2022-06-07.

the Trade winds slow down at the surface. Water with high SST at the Maritime continent flows back into the central Pacific, changing the WC. The rising moist air-flow of the WC shifts to the east causing heavy rainfall in the central Pacific. The Maritime continent and South America experiences descending hot and dry air flow (Figure 2.11).

During the *cold phase* of the ENSO, the La Niña (meaning "little girl"), the

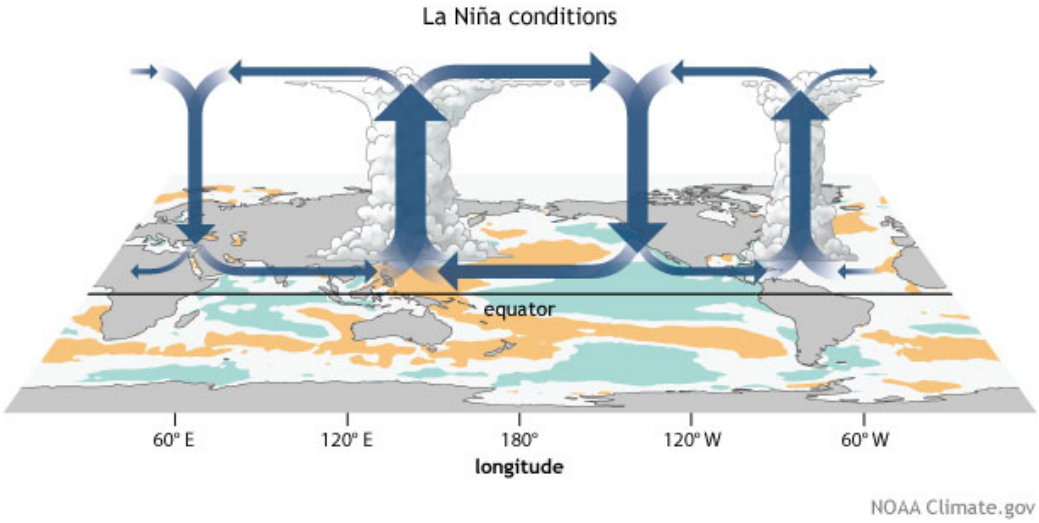


Figure 2.12.: Schematic illustration of the ENSO and the WC during the cold phase, La Niña. Source: NOAA Climate.gov, by Fiona Martin. https://www.climate.gov/news-features/blogs/enso/walker-circulation-ensos-atmospheric-buddy. Last visited: 2022-06-07.

Trade winds blow even stronger than normal, and even more cold water gets pushed from east to west. In the east, more cold water than normal gets pulled up from the deep, and the eastern part of the Pacific gets colder than normal. The enhanced cold-warm difference intensifies the WC, with even greater uplifting of moist air over the Maritime continent, and more descending air to the east (Figure 2.12).

The change in tropospheric temperature has a delay of about 3 months compared to the change in SST (Scherllin-Pirscher et al. 2012). In Paper I (Wilhelmsen et al. 2018) we detect this temperature change using temperature profiles with high vertical resolution. In Paper III (Wilhelmsen et al. 2020), we see that the ENSO influences the location where DTs are found, and therefore potentially also where STE takes place.

3. Data

"It's more fun to compute" (It's more fun to compute, Kraftwerk)

The main data used in this work are atmospheric temperature profiles from Global Navigation Satellite System (GNSS) Radio Occultation (RO) measurements. Additionally, established indices of the El Niño–Southern Oscillation (ENSO) and the Quasi-Biennial Oscillation (QBO) are used to describe and determine the different phases of the known natural variabilities, as well as a commonly used solar index to indicate the change in solar radiation. Stratosphere aerosol data are used to describe the influence of volcanic eruptions on atmospheric temperature. To indicate the location of the Subtropical Jet Stream (STJ), wind data from the European Centre for Medium-Range Weather Forecasts (ECMWF) weather model are used. Radiosonde measurements are used, together with RO, to investigate tropopause changes. Finally, reanalysis data are used for comparison.

3.1. Global Navigation Satellite System Radio Occultation

GNSS RO measurements, or just "RO data", makes use of a limb sounding satellite technique, illustrated schematically in Figure 3.1. The satellite to the left, furthest away from the Earth, is a GNSS satellite (e.g. a GPS satellite). It constantly emits signals to the Earth[1]. Part of the signal passes by the Earth, through the atmosphere, back into space. A GPS receiver on a Low Earth Orbit (LEO) satellite picks up the signal on the other side of the Earth, as illustrated by the ray hitting the satellite closest to Earth in Figure 3.1. As the GPS satellite rises or sets in the horizon, as seen from the LEO satellite, the rays scan the atmosphere. The technique produces profiles of *high vertical resolution*, and the measurements have a global coverage. The number of measurements depends on the number of satellites. LEO satellites with a GNSS receiver the more measurements are made.

If there was no atmosphere, i.e. in vacuum, the rays between the two satellites would be straight lines. But because there is an atmosphere, and because the atmosphere has changing density, the signal is refracted. I.e., the path the GPS signal takes, bends as it goes through the atmosphere, making the path longer than the straight path. The satellite operators know very precisely *where* the satellites are located at all times, and due to the very accurate atomic clocks onboard, they know very precisely *when* the signals were emitted and received. From this, a

[1] E.g. to be used in navigation instruments.



Figure 3.1.: An illustration of a Radio Occultation satellite constallation. The left satellite, furthest away from the Earth, is a Global Positioning System (GPS) satellite. The satellite to the right is a Low Earth Orbit satellite (here a Constellation Observing System for Meteorology, Ionosphere, and Climate (COSMIC) satellite), which has a GPS receiver onboard. Source: UCAR. https://www.cosmic.ucar.edu/what-we-do/gnss-radio-occultation. Last visited: 2022-07-22.

theoretical pathway the ray must have taken from the GPS satellite to the LEO satellite can be derived, and from that, a bending angle, as a measure of how much the ray has bent due to the atmospheric refractivity field. From bending angle the refractivity can be determined. From refractivity, pressure and temperature can be retrieved in a dry atmosphere. In a moist atmosphere, background information (e.g. weather model forecast data from ECMWF) is needed to retrieve pressure, temperature, and humidity. However, in the main region of this work, the tropical Upper Troposphere–Lower Stratosphere (UTLS), the influence of model data is small, and the RO data can be considered as observations (Scherllin-Pirscher et al. 2011). Detailed information on the retrieval of atmospheric parameters from the RO can e.g. be found in Kursinski et al. (1997).

Some of the natural variabilities have periods that span over decades (e.g. the Atlantic Multidecadal Oscillation (AMO) or the Pacific Decadal Oscillation (PDO), not described in this work). In order to get a full picture of a variability mode, the dataset used to describe it must be longer than the periods of the variability itself, preferably several periods longer. The time span of a dataset can therefore limit which phenomena it can detect or describe. If new and more accurate instruments replace previous generation instruments as they improve, e.g. as with Radiosonde Observations (RAOBs) weather balloons, the datasets may have to be calibrated between the instrument upgrades, when the data are used to create a longer time

series. In the same way, data from *single* RO missions are also limited by the relatively short life span of the mission. In the case of RO, the measured property is time, defined of the SI-unit of the second and measured with highly precise and stable clocks (Leroy et al. 2006). Using the same processing to calculate the derived properties from the raw measured data, different RO missions can be combined without inter-calibration (Schreiner et al. 2007; Foelsche et al. 2011; Steiner et al. 2020), and a dataset that combines all the RO missions may span over the whole RO era. The Wegener Center for Climate and Global Change (WEGC) Occultation Processing System version 5.6 (OPSv5.6) dataset does just that (Angerer et al. 2017). It combines all major RO missions since the year 2001. The QBO has an average period slightly longer than two years, and the ENSO around 5 years, and thus, the WEGC OPSv5.6 dataset includes several periods of these variabilities. The WEGC OPSv5.6 dataset was used in all four papers of this work. Only temperature profiles with the highest quality (Quality Control (QC) flag 0), see Angerer et al. (2017), were used.

3.2. Radiosonde observations

Radiosonde Observations (RAOBs) are made from instruments mounted on weather balloons released from the same location, at the same time, every day. The rising balloons move with the winds, collecting information about temperature, humidity, and wind speed in the atmosphere, with high vertical resolution, until it bursts and falls to the ground.

The measurements are meant to be used in weather forecasts, and the instruments are improved over time. The instruments may also differ from station to station. When comparing RAOB measurements, therefore, inter-calibration is needed. The Integrated Global Radiosonde Archive Version 2 (IGRA2) archive[2] is a compilation of RAOBs from 30 different sources, that is updated daily. Data from IGRA2 were used in Paper IV (Meng et al. 2021), with RAOBs from 149 stations between 1980 and 2020, mainly over land on the Northern Hemisphere (NH). The data were downloaded from National Oceanic and Atmospheric Administration (NOAA)[3].

3.3. Reanalysis data

When weather centers calculate the weather forecasts, they work on a tight time schedule. The next forecast must be ready on time. They therefore have to start the calculation even if they have not received all the observed data. To get more robust results, therefore, the forecasts can be calculated again, when all the data has been received. However, the model algorithms used to do the calculations are constantly improved, and the weather forecasts may differ between different model versions. Comparison of the output from the model versions from year to year can

[2] https://doi.org/10.7289/V5X63K0Q
[3] https://www1.ncdc.noaa.gov/pub/data/igra/

therefore be problematic, and not applicable when it comes to climate research. To circumvent the problems, data from a longer time period are recalculated using the same frozen model version for the whole period, with all the relevant observed data sources, assimilated in a statistically optimal way. This is reanalysis data in a nutshell.

Comparing reanalysis data with observational data must be done with care. RO data are often assimilated as input observation data in the reanalysis models, along with a vast amount of other data sources, like Sea Surface Temperature (SST) measurements, RAOBs, and a range of airborne and satellite observations.

There are several reanalysis datasets available (Fujiwara et al. 2017). Most of them provide physical information of the atmosphere, like temperature, pressure, humidity, winds, on a regular horizontal grid at standard pressure levels.

In this work, reanalysis datasets were mainly used for comparison with RO data. In the beginning of the project, we used ECMWF Re-Analysis (ERA) Interim (Dee et al. 2011) by ECMWF. Throughout the course of the thesis, ERA Interim was being replaced by the latest generation ECMWF Re-Analysis Version 5 (ERA5) (Bell et al. 2021; Hersbach et al. 2020), also created by ECMWF. They both have data since 1979, which is before the first RO missions. ERA Interim, however, does not contain data after August 2019.

3.4. Wind data for QBO indices

The QBO index used in this work is made from monthly mean values of daily RAOB wind speed measurements in the stratosphere at the Equator. Wind measurements of the QBO date all the way back to 1953, at different locations near the Equator. Because the QBO is uniform in the same zonal bands, and the differences between the measurements at these locations are small, only measurements from the Singapore station are included for the data after 1987 (Naujokat 1986). Data after 1997 are provided at 15 different pressure levels between 100 and 10 hPa. The data are depicted in Figure 3.2.

When used in an Empirical Orthogonal Function (EOF) analysis (see section 4.1) most of the variability from the QBO can be described by only two time components (Principal Components (PCs)) (Wallace et al. 1993). I.e., the time series at the 15 pressure levels can be reduced to only two time components, and still describe most of the variability. The same principle is used to detect QBO indices of high resolution in Paper I (Wilhelmsen et al. 2018) and Paper II (Stocker et al. 2019).

There are currently at least two sources for QBO indices from wind measurements, one from NOAA and the other from Freie Universität Berlin (FU Berlin)[4]. We used the latter.

[4] https://www.geo.fu-berlin.de/en/met/ag/strat/produkte/qbo/index.html

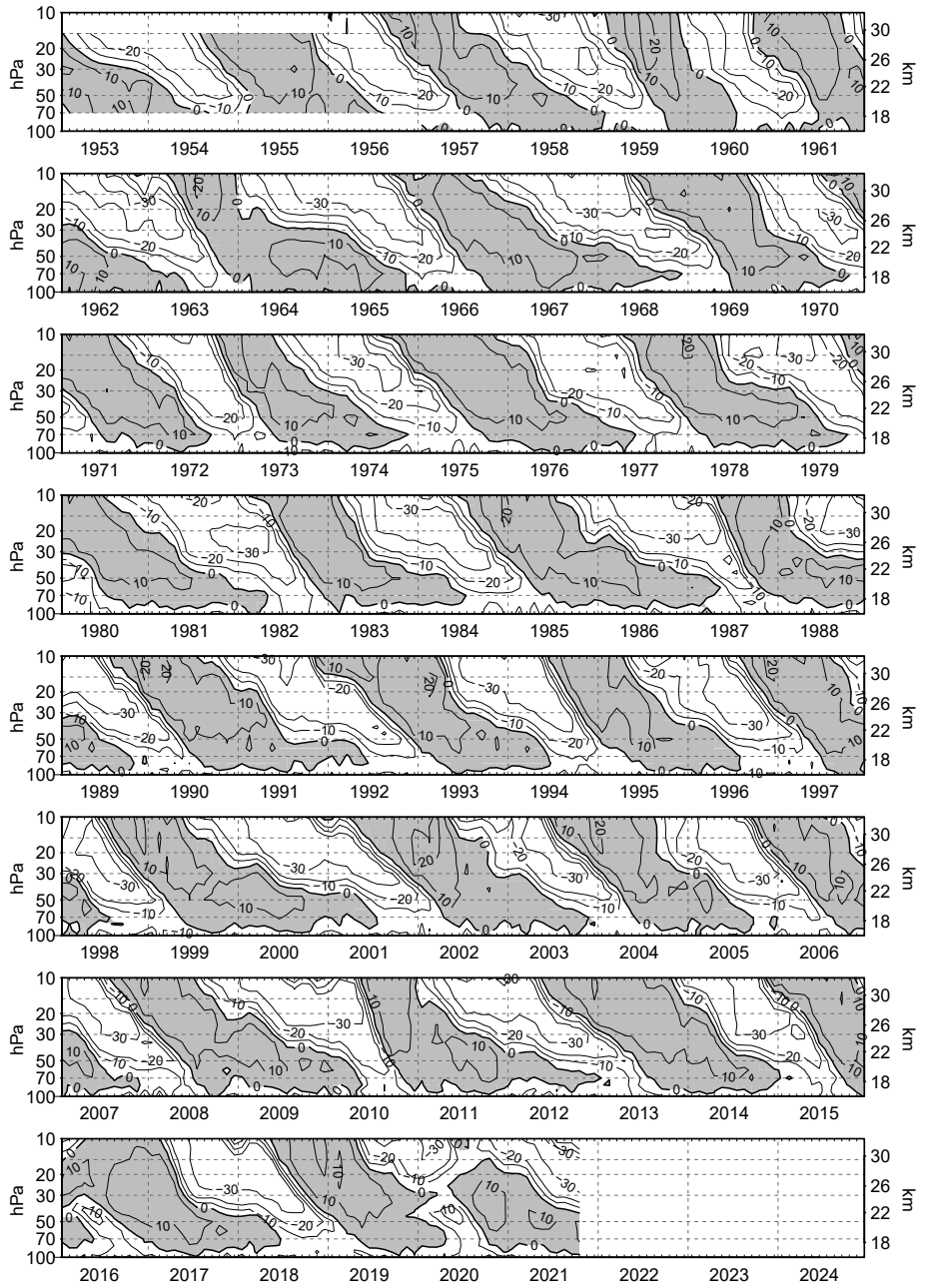


Figure 3.2.: Monthly mean winds, QBO winds, since 1953. The plot is from Naujokat (1986), but updated with the most recent measurements. Areas with eastward blowing winds (positive wind speeds) are colored gray. The wind speeds are given in m/s. Source: FU Berlin. https://www.geo.fu-berlin.de/met/ag/strat/produkte/qbo/index.html. Last visited: 2022-07-20.

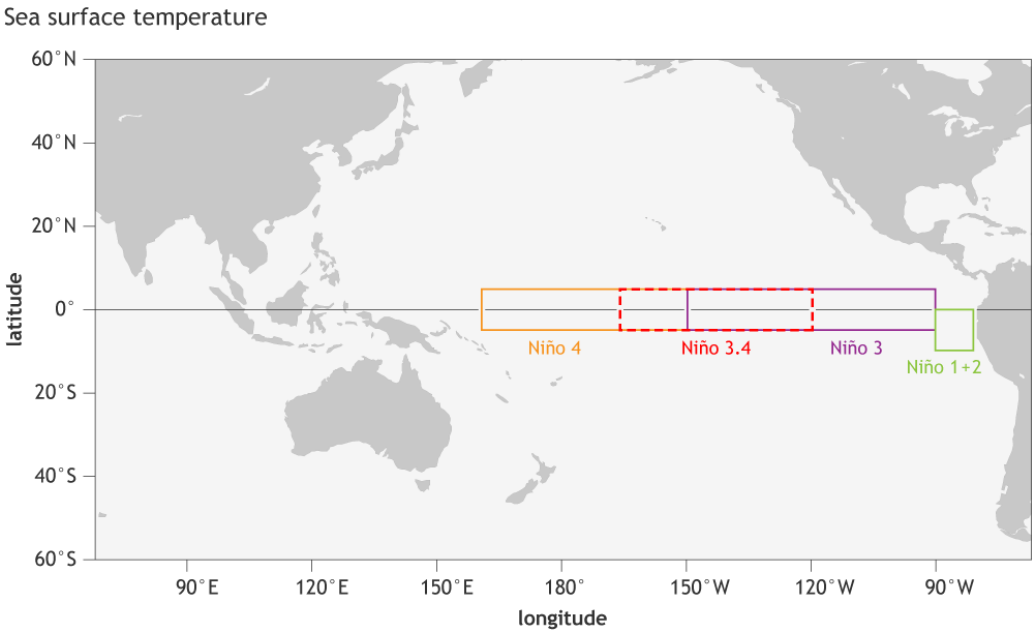


Figure 3.3.: The different ENSO regions in the Pacific. The Niño 3.4 region (red, dashed) is made up from Niño 3 region (purple) and the Niño 4 region (yellow). NOAA Climate.gov, by Fiona Martin. https://www.climate.gov/news-features/understanding-climate/climate-variability-oceanic-niño-index. Last visited: 2022-07-20.

3.5. Sea-surface temperature data for ENSO indices

As described in subsection 2.3.2, the ENSO is a complex interaction between the ocean and the atmosphere, with wide-ranging implications. Several different measurements can therefore be used to represent its different phases. Examples are the Outgoing Longwave Radiation Index, made from anomalies of Outgoing Longwave Radiation satellite measurements, or the Southern Oscillation Index, made from differences in sea level pressure between Tahiti, in the middle of the Pacific Ocean, and Darwin in Australia.

The two ENSO indices used in this work, however, Niño 3.4 Index and the Oceanic Niño Index (ONI), are both made from monthly mean anomalies of SST measurements made within the Niño 3.4 region (5° N to 5° S and 170° W to 120° W) in the Pacific Ocean (see Figure 3.3). Each index consists of a single time series that describes the ENSO. The recent part of the ONI time series can be seen in Figure 3.4. The data are available from the NOAA Climate Prediction Center[5].

The difference between the two is the smoothing. The Niño 3.4 Index uses a 5-month running average, where the ONI uses a 3-month running average. This influences how the La Niña events and the El Niño events are defined in the two indices. Using the Niño 3.4 Index an El Niño event, or a La Niña event, happens

[5] https://www.cpc.ncep.noaa.gov/data/indices/

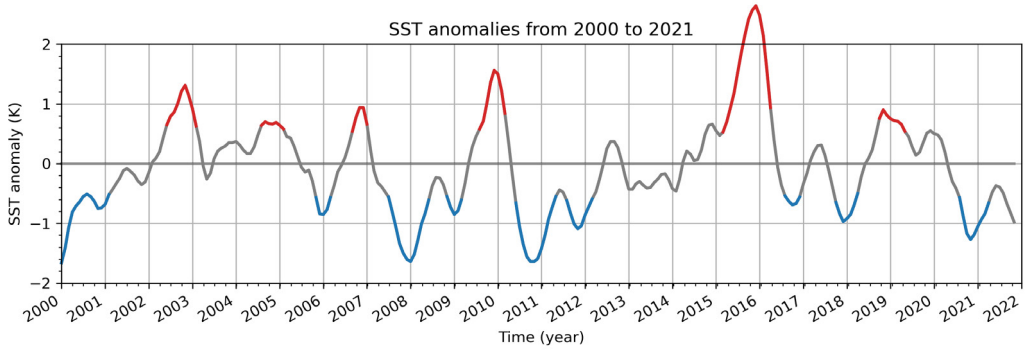


Figure 3.4.: Monthly mean SST anomaly time series between 2000 and 2021 (covering the RO-era) in the Niño 3.4 region, using the ONI. Blue color indicates La Niña events and red color indicates El Niño events.

when the anomalies stay above 0.4 °C, or below −0.4 °C, respectively, for at least *six* months. Using the ONI, the thresholds are ±0.5 °C, and the anomalies must stay outside the thresholds for at least *five* months.

Historically, other regions than the Niño 3.4 region have been used to describe the ENSO, e.g. the Niño 3 region, or the Niño 4 region. The Niño 3.4 region is a combination of the two (see Figure 3.3). We refer to the Niño 3 region in connection with Double Tropopauses (DTs) in Paper III (Wilhelmsen et al. 2020).

3.6. Aerosol data for volcanic impacts

Global Space-based Stratospheric Aerosol Climatology (GloSSAC) is a global aerosol climatology made from several different aerosol observation datasets and instruments. It provides stratospheric aerosol data on a monthly timescale, in 5° latitude zonal bands, on a 500 m vertical grid almost up to 40 km, i.e. the data depend on time, latitude and altitude (Thomason et al. 2018). The mean aerosol concentration from the years 1999, 2000, 2001, 2003, and 2004 is used as background since there was no relevant volcanic eruptions in these years. This background is subtracted from the main data to extract the influence of volcanoes (see Figure 1 in Paper II). The dataset is used in Paper II (Stocker et al. 2019).

3.7. Solar activity index

The solar F10.7 index is commonly used to describe the solar radiation received by the Earth. It is a measurement of solar emission at a wavelength of 10.7 cm (2800 MHz) in solar flux units (sfu), where 1 sfu is $10^{-22}\,\mathrm{W\,m^{-2}\,Hz^{-1}}$, made with parabolic antennas at the Earth's surface. It is a reliable measurement of solar activity regardless of weather conditions. The record goes all the way back to 1947 (Covington 1969; Tapping 2013).

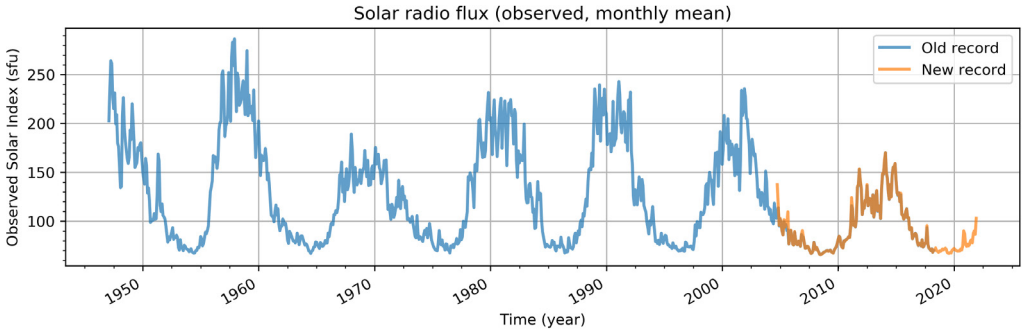


Figure 3.5.: The solar F10.7 index since 1948. Data from NOAA (blue) and Space Weather Canada (orange). The most recent record has been scaled to fit the older record.

The data comes in different variations, e.g. an adjusted flux that accounts for the changing distance between the Earth and the sun, or one that accounts for the solar rotation. We use the actual measured flux density averaged over a month, as it indicates the actual solar radiation received at the Earth and its atmosphere.

Figure 3.5 shows two different datasets, one from NOAA[6] with data between 1947 and 2018, and another from Space Weather Canada[7], with data from 2004 up to now (2022).

[6] https://www.ngdc.noaa.gov/stp/space-weather/solar-data/solar-features/solar-radio/noontime-flux/penticton/penticton_observed/listings/listing_drao_noontime-flux-observed_monthly.txt
[7] https://www.spaceweather.gc.ca/forecast-prevision/solar-solaire/solarflux/sx-5-mavg-en.php

4. Diagnostics of atmospheric variability

The aim of this chapter is to give the reader a basic understanding of the main methods used in the papers included in this work, listed in Part II. The first section is a short review of the methods used to characterize atmospheric variability and for trend computation. The second section focuses on some different methods we used to detect the tropopause and derivatives, their optimal implementation for Radio Occultation (RO) data, and results on tropopause variability and trends. It also inclues results that did not make it into the papers.

4.1. Characterizing atmospheric variability modes in the UTLS

4.1.1. Multivariate linear regression

As mentioned in the introduction (chapter 1), many varying factors influence the temperature in the Upper Troposphere–Lower Stratosphere (UTLS). Some of the variability is however known and can be accounted for. A common way to do this is by using multivariate linear regression. The basic idea is to statistically decompose a measured time series, e.g. a time series of temperature values, into a model made from a linear combination of several components, where each component is a known variability:

$$T(t) = \beta_0 + \beta_1 t + \beta_2 x_2(t) + \beta_3 x_3(t) + \cdots + \beta_p x_p(t) + \varepsilon(t) \tag{4.1}$$

In Equation 4.1, $T(t)$ is the temperature value at each time step, t, in the time series. β_0 represents the magnitude of the level where the data is found (where a linear line would cross the y-axis). β_1 represents the slope of a stable increase or decrease of the data. The x variables, the regressors, describe the known variabilities that have been included in the model, at each time step. Each corresponding β value is a constant scaling factor, describing how much of its corresponding known variability that can be used, in combination with the other known variabilities, to statistically represent the measured data. Finally $\varepsilon(t)$ represents the residual at each time step, whatever explanation, known or unknown.

The original dataset can be reconstructed exactly, using the model in Equation 4.1. This means that when the β values have been determined, the contribution from a known variability can be removed from the dataset, by using the respective parts in Equation 4.1. It also means, that if one of the regressors represents a straight line ($\beta_1 t$), its corresponding β value (β_1) describes the trend in the original dataset (e.g. a temperature trend).

The indices described in chapter 3 are commonly used to describe the known variabilities in the tropics, created from e.g. Sea Surface Temperature (SST) (El Niño–Southern Oscillation (ENSO)) and wind speeds (Quasi-Biennial Oscillation (QBO)). The atmospheric temperature response from the SST indices does not propagate instantly into the troposphere, but with some time delay (e.g., Scherllin-Pirscher et al. 2012). Likewise, the temperature change from the QBO is proportional to the vertical gradient of the horizontal wind speed as the different wind regimes propagate downward (e.g., Baldwin et al. 2001). This introduces a time delay in correspondence to the temperature change in the stratosphere. The speed of the descending pattern is not constant, so the time delay may be different at different altitudes, and may change from month to month. It can therefore be a challenge to find the appropriate time delay. One way to overcome this challenge is to use the Empirical Orthogonal Function (EOF) analysis.

4.1.2. Variability indices from Empirical Orthogonal Function analysis

EOF analysis[1] is an established method to represent multidimensional data with a new set of unit vectors, determined by the variability in the dataset. The new set of unit vectors (here called the "EOFs"), are all orthogonal, have the length 1 ("unit" vector), and are made from linear combinations of the original unit vectors. The new set is organized so, that the direction of the first unit vector has the direction of the largest variability in the original dataset. The second unit vector has the direction of the second largest variability, and is orthogonal to the first unit vector, and so on.

The new time series (here called the "Principal Components (PCs)"), representing the data in the new coordinate system, can, together with the EOFs, reconstruct the whole original dataset in the original coordinates. I.e., applying EOF analysis on a dataset does not result in loss of information from the original dataset.

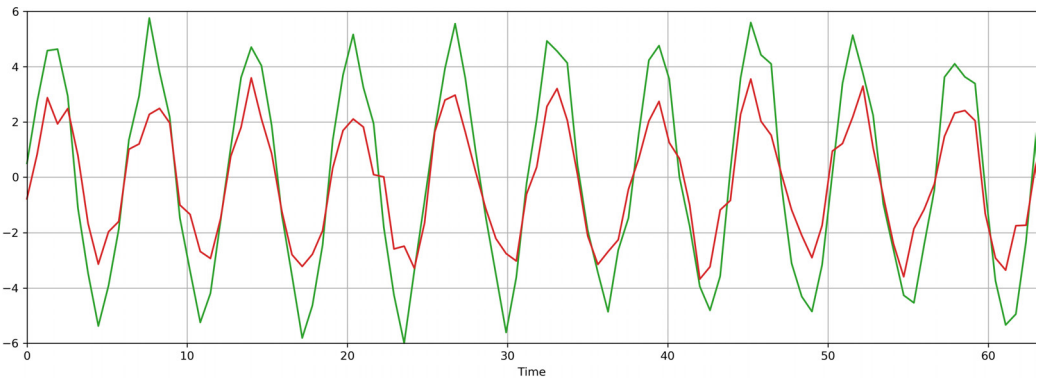


Figure 4.1.: Two time series used as input for the EOF analysis.

[1] EOF analysis is also called Principal Component Analysis (PCA).

This is demonstrated here, with a simple example. Figure 4.1 shows two sinus waves with the same period but with different amplitude, and some added random noise. The same data are plotted in Figure 4.2. The amplitude of each of the data points in the green line in Figure 4.1 are plotted, as x-values, against each of the data points in the red line in Figure 4.1, as y-values. I.e., the data are constructed

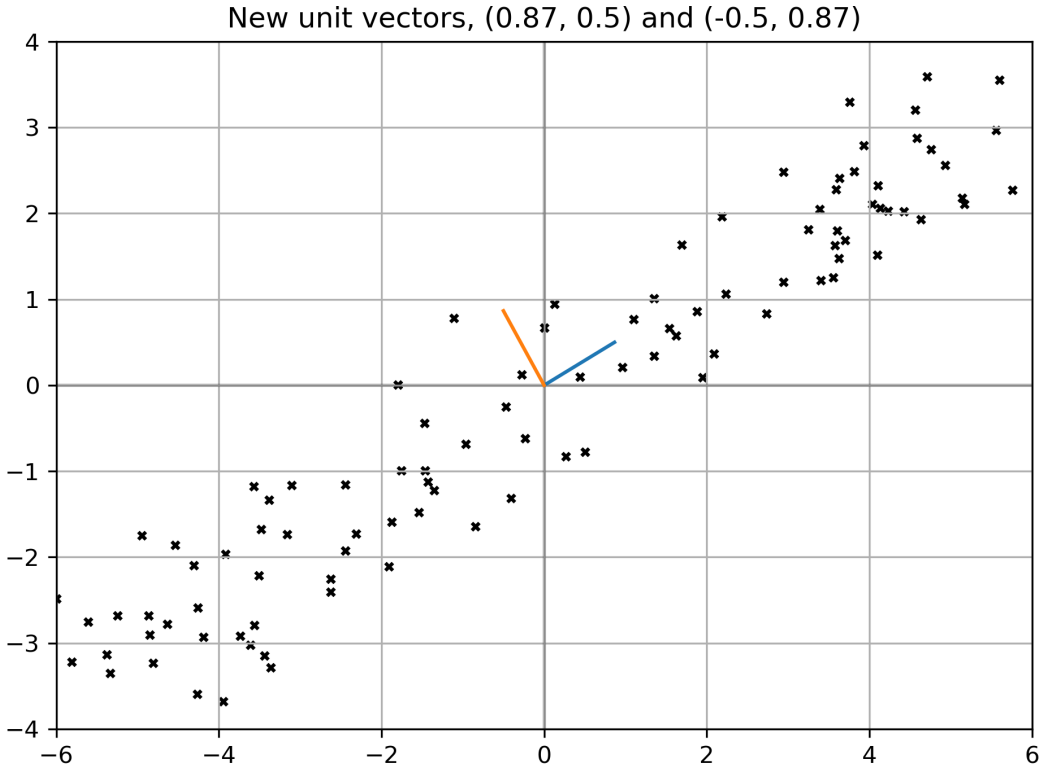


Figure 4.2.: After performing EOF analysis on two sinus curves with random noise (the black points), a new set of unit vectors have been found (blue and orange) to represent the direction of the variability of the data). The first (blue) unit vector represent the direction of the largest variability and the second (orange) the direction of the second largest.

to correlate along the diagonal cluster seen in Figure 4.2.

After performing an EOF analysis on the data, the first EOF shows the direction of the main variability in the dataset. This is represented as the blue straight line in Figure 4.2, starting at the origin, with the length 1. The direction of the second largest variability is represented by the orange straight line of length 1, orthogonal to the blue line. The corresponding time series (PCs), using these new unit vectors, can be seen in Figure 4.3.

When reconstructing the dataset using *only the first* EOF-PC pair in the example (both in blue in Figure 4.2 and Figure 4.3), the data are projected onto the first EOF (the blue unit vector). This can be seen in Figure 4.4. By only using one time series, the main variability from the original dataset is kept, both along the original x-axis and the original y-axis. The variability along the second EOF (orange) is

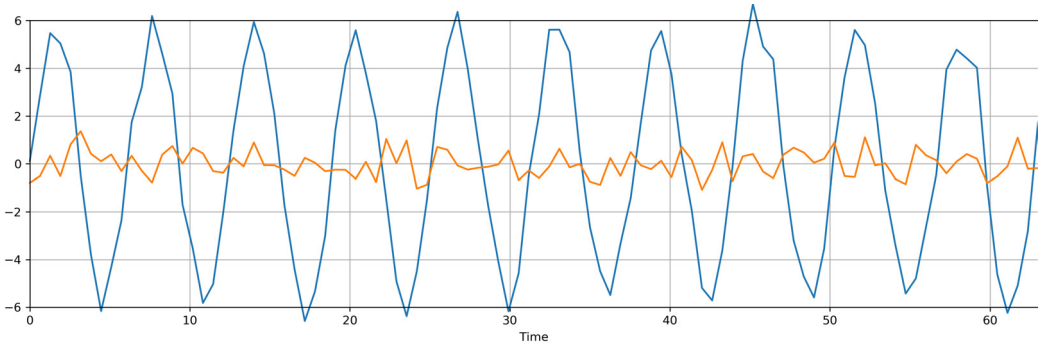


Figure 4.3.: The time series (PCs) that corresponds to the EOFs (blue and orange straight lines) in Figure 4.2.

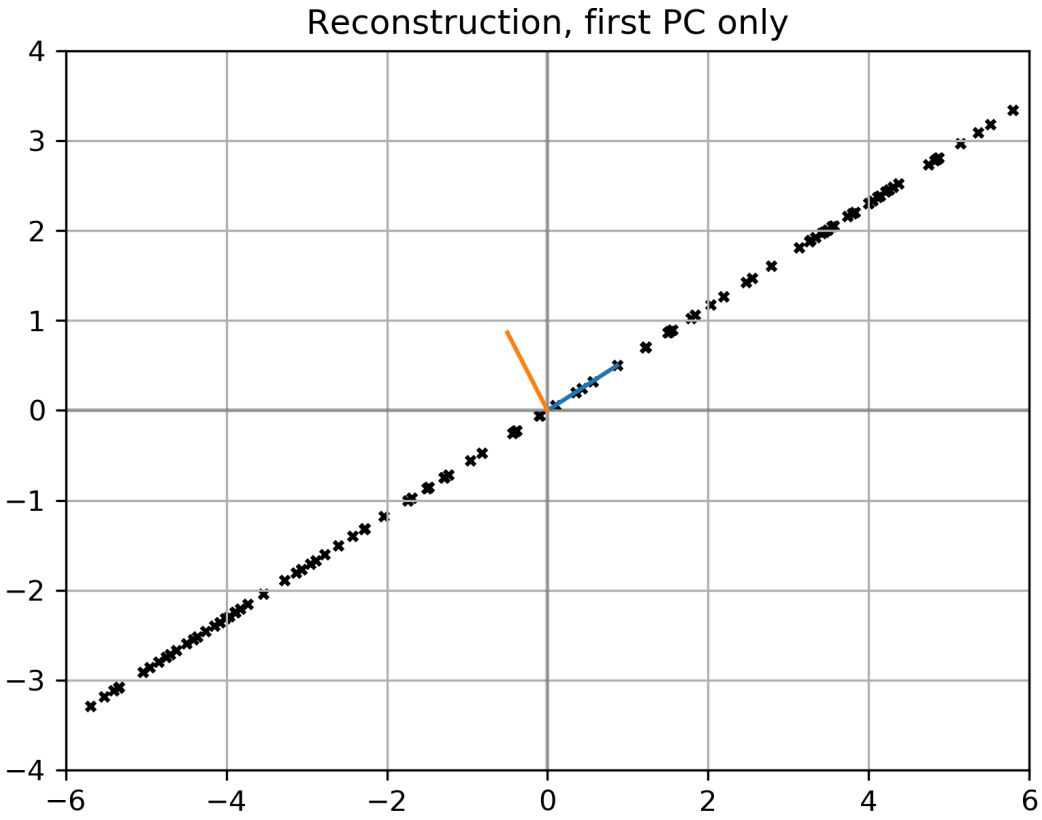


Figure 4.4.: Reconstructed data using the first PC time series only.

filtered away, but the information is kept in the second PC (orange). I.e., if the time series in the original dataset correlate well, a reduced number of time series can represent most of the variability.

This may not be especially useful when the input dataset has only two dimensions, as in the example. However, the method can be expanded to an arbitrary number

of time series, of e.g. temperature measurements. Instead of the x- and y-axis from the example, each grid point (both horizontally and vertically) in a temperature dataset can represent an axis, with a corresponding unit vector.

If we assume, that a variability happens at multiple locations and altitudes at the same time, and the phenomena causing the variability influences the temperature, then the temperature response at these locations should correlate well. As the main known variabilities in the tropical UTLS are the ENSO (see subsection 2.3.2) and the QBO (see subsection 2.3.1), the temperature response from each variability happens over a large area, and should therefore be detectable simultaneously at several locations. By applying an EOF analysis on the dataset, it should be possible to describe these synchronous modes of variability with a reduced number of PCs (and corresponding EOFs).

The PCs represent the time *when* the variabilities take place, and the EOFs represent *where* in the original coordinate system the variabilities take place and *how much* impact each PC has at the different locations. See e.g. Jolliffe (2002) or Hannachi et al. (2007) for further reading on the EOF analysis.

In Paper I (Wilhelmsen et al. 2018), the EOF analysis was performed with two different methods, denoted "M1" and "M2". Before this, the data were prepared to show the variability. First, monthly mean RO temperature measurements were created on a grid with $5° \times 5°$ horizontal resolution and 200 m vertical resolution. The EOF library that was used, from the SciPy ecosystem, requires an input dataset without missing values. Grid points with missing data were therefore filled by interpolation and extrapolation of the nearby values at each horizontal altitude level, for each month. Then, monthly mean temperature anomalies were calculated in each grid point (horizontally and vertically). The monthly mean temperature anomalies are a measure of how the temperature deviates from the climatological mean temperature in each month of the year (see e.g. Figure 1 in Paper I (Wilhelmsen et al. 2018)). Note that this removes the seasonal variations. Only data between 30° S and 30° N latitude and from 2 km to 35 km altitude were used, to cover ENSO and the QBO in the tropics.

In M1, an EOF analysis was performed on the whole vertical and horizontal RO temperature field. In M2, the EOF analysis was also performed on the whole dataset, but separately at each altitude level.

The resulting PCs resemble the well-known patterns of the QBO and the ENSO in the tropics. For both M1 and M2 the EOFs coincide with the typical locations of the ENSO in the troposphere and with the typical locations of the QBO in the stratosphere (see Figure 6 in Paper I (Wilhelmsen et al. 2018), page 79). Whereas M1 provides some information on the vertical structure, M2 captures more of the contributing variability, with only one PC, at each separate altitude level, except for the altitudes around the tropopause.

An advantage of using EOF method to detect the variabilities versus e.g. using an average of the monthly mean temperature anomaly field can be seen in the Figure 2 and Figure 4, both from Paper I (Wilhelmsen et al. 2018). The EOFs show that different areas respond with opposite sign to the variability. An index

based on an average would thus cancel out these differences, whereas the EOF method accounts for it.

The EOF method does, however, not distinguish between different sources for the temperature change, if they operate in the same space. Once the EOFs (the "where") have been established, the PCs (the time series, the "when") describe the variability of the temperature change, independent of the source. Volcanic aerosols, e.g., influence the temperature in the stratosphere. The aerosols are quickly spread with the zonal winds in the QBO, and with the Brewer–Dobson Circulation (BDC). The temperature response from volcanic aerosols, therefore, takes up the same space as the QBO, and is expected to be included in the QBO temperature signal detected by this EOF method. The basic goal of the Paper II (Stocker et al. 2019) was to quantify the temperature response from the volcanic aerosols, by separating it from the QBO signal.

For both M1 and M2„ at most altitude levels, only one or two PCs were enough to explain the main part of the variability, except for the altitude levels around the tropopause. In that region more PCs are needed.

4.2. Characterizing the tropopause, its variability and trends

There are many definitions of the tropopause, from chemical- over dynamical- to thermal-based definitions. Also, the tropopause may be considered as a single point (e.g. the Cold Point Tropopause) or as a region (e.g. the Tropical Tropopause Layer). The following is an overview of the algorithms used in this work, mainly based on temperature profiles.

4.2.1. Cold Point Tropopause

The most obvious definition of the tropopause is the point of minimum temperature, the Cold Point Tropopause (CPTP). The algorithm for that is simply to pick the altitude level with the lowest temperature in a temperature profile.

As temperature data are sampled on a vertical grid, they only represent samples of the actual, true temperature profile. The coldest point in the dataset will therefore always be warmer than (or equal to) the actual minimum temperature in the profile, and therefore create a positive temperature bias.

Fine tuning the cold point tropopause

To reduce the bias, due to vertical sampling, we fine tune the CPTP by assuming that the temperature profile follows a quadratic function around the temperature minimum. I.e., we find the quadratic function that goes through the minimum temperature grid point, the point just below, and the point just above:

$$T = Az^2 + Bz + C, \tag{4.2}$$

where z is altitude and T is temperature, and A, B, and C are constants. The minimum temperature is then found where the gradient of the parabola,

$$\frac{dT}{dz} = 2Az + B, \tag{4.3}$$

equals zero:

$$2Az + B = 0. \tag{4.4}$$

The grid point of minimum temperature, (z_2, T_2), and the point just below, (z_1, T_1), and above, (z_3, T_3), give us three equations that can be used to find the A, B, and C coefficients:

$$\begin{aligned} T_1 &= Az_1^2 + Bz_1 + C \\ T_2 &= Az_2^2 + Bz_2 + C \\ T_3 &= Az_3^2 + Bz_3 + C \end{aligned} \tag{4.5}$$

The coefficients are then found to be:

$$\begin{aligned} A &= \frac{z_3(T_2 - T_1) + z_2(T_1 - T_3) + z_1(T_3 - T_2)}{(z_1 - z_2)(z_1 - z_3)(z_2 - z_3)} \\ B &= \frac{z_3 z_3(T_1 - T_2) + z_2 z_2(T_3 - T_1) + z_1 z_1(T_2 - T_3)}{(z_1 - z_2)(z_1 - z_3)(z_2 - z_3)} \\ C &= \frac{z_2 z_3(z_2 - z_3)T_1 + z_3 z_1(z_3 - z_1)T_2 + z_1 z_2(z_1 - z_2)T_3}{(z_1 - z_2)(z_1 - z_3)(z_2 - z_3)} \end{aligned} \tag{4.6}$$

and the fine tuned CPTP is found in

$$(z_{\mathrm{MIN}}, T_{\mathrm{MIN}}) = \left(\frac{-B}{2A}, C - \frac{B^2}{4A}\right). \tag{4.7}$$

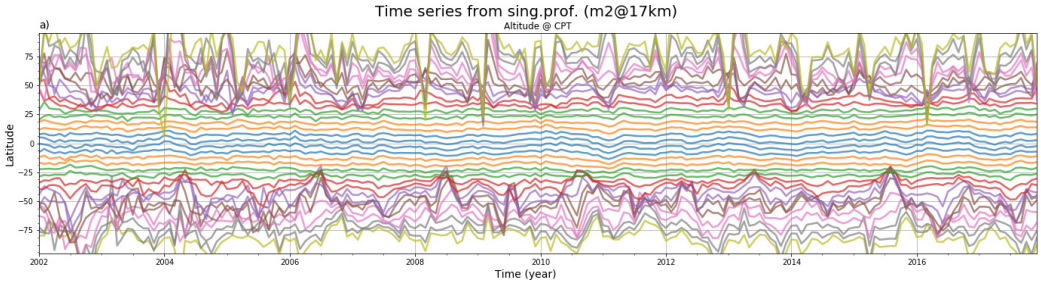


Figure 4.5.: Joy plot of the mean altitude of the CPTP at every 5° zonal band. The CPTP altitudes were created from individual RO temperature profiles, i.e., the CPTP was found on each temperature profile before calculating the average value. The colors denote different latitudes. The labels are "Time (year)" on the x-axis and "Latitude" on the y-axis.

Figure 4.5 shows a joy plot of the monthly mean CPTP altitudes at each 5° zonal band, illustrating how the altitude of the CPTP changes from month to month at different zonal bands. It shows that the CPTP is stable in the tropics, where the temperature profiles show a distinct tropopause (see Figure 2.1). Outside the tropics, however, the mean value makes sudden "jumps" of several km. The reason for this can also be seen in Figure 2.1 (page 11), in how the altitude of the coldest point may change between the seasons. Also, in the subtropics, it is not always clear whether the tropopause in the tropical tropopause regime or the tropopause in the extratropical tropopause regime holds the coldest point. Just small changes in the temperature profile may cause different results in the detected CPTP of several km.

4.2.2. Tropopause proxy at 100 hPa

The tropical tropopause is often found around 100 hPa. The values at 100 hPa are therefore sometimes used as a proxy for the tropopause. This is very convenient, as many weather and climate models come with values at the 100 hPa level, and can therefore be used directly (Highwood and Hoskins 1998). We did not investigate this association systematically in this work, but the 100 hPa level was consistently found very close to the altitude of the Lapse Rate Tropopause whenever added, especially in the tropics.

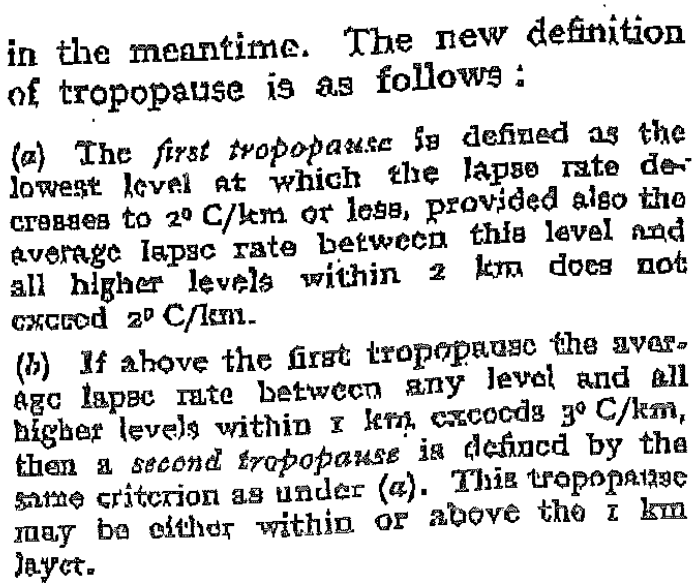
4.2.3. Lapse rate tropopause - implementation and results

Another obvious property of the typical atmospheric temperature profile is the decreasing temperature in the troposphere and the rising temperature in the stratosphere. In 1957 the World Meteorological Organization (WMO) released a report describing a still widely used definition based on the lapse rate, the Lapse Rate Tropopause (LRTP). The lapse rate, Γ, is defined as the negative vertical temperature gradient:

$$\Gamma = -\frac{dT}{dz} \tag{4.8}$$

where T is the temperature and z is the altitude. Figure 4.6 shows a scan from the original WMO report, stating:

> "(a) The *first tropopause* is defined as the lowest level at which the lapse rate decreases to 2 °C/km or less, provided also the average lapse rate between this level and all higher levels within 2 km does not exceed 2 °C/km.
>
> (b) If above the first tropopause the average lapse rate between any level and all higher levels within 1 km exceeds 3 °C/km, then a *second tropopause* is defined by the same criterion as under (a). This tropopause may be either within or above the 1 km layer." (WMO 1957)



in the meantime. The new definition of tropopause is as follows:

(a) The *first tropopause* is defined as the lowest level at which the lapse rate decreases to 2° C/km or less, provided also the average lapse rate between this level and all higher levels within 2 km does not exceed 2° C/km.

(b) If above the first tropopause the average lapse rate between any level and all higher levels within 1 km exceeds 3° C/km, then a *second tropopause* is defined by the same criterion as under (a). This tropopause may be either within or above the 1 km layer.

Figure 4.6.: A scan of the WMO (1957) LRTP definition.

The definition seems clear at first glance. It marks an altitude where the Γ profile *starts* to shift from positive values to negative values, i.e., an altitude where the temperature goes from cooling to heating. Implementing it into code, however, opens for several interpretations. This is likely something that everyone new to the algorithm has encountered. The challenging part is the last half of (a), and special care is required to properly interpret it.[2] To clarify, let's dissect the algorithm step by step:

The *first tropopause* is defined as This is just the introduction. The word "first", however, hints toward more than one tropopause.

the lowest level If the implementation has the possibility to search from either below or above, this part means that the most efficient direction would be from below. This way it may stop the search as soon as a LRTP candidate grid point has been found, and there is no need to search through the rest of the profile.

at which the lapse rate decreases to Meaning that the lapse rate around a LRTP candidate grid point must be decreasing. In most cases, this is not needed, but it may be helpful, depending on the implementation. E.g., when a LRTP candidate grid point is found by searching for two adjacent points that are on each side of the lapse rate threshold, Γ_{LRTP}, (see the next step), this criterion simply adds that the point with the lowest altitude of the two, must have the largest lapse rate value.

[2]Special thanks to Thomas Birner (personal communication), pointing me into the right direction.

2 °C/km We refer to this as the *lapse rate threshold*, Γ_{LRTP}.

or less, This means that the lapse rate in the LRTP candidate grid point, Γ_i, must be less than the lapse rate threshold, Γ_{LRTP}, i.e., $\Gamma_i \leq \Gamma_{\mathrm{LRTP}}$. The LRTP candidate grid point will therefore *always* be found at an altitude *above* the actual altitude where $\Gamma = \Gamma_{\mathrm{LRTP}}$, introducing a positive bias in LRTP altitude and, because the temperature is decreasing with altitude, a negative bias in the LRTP temperature.

provided also the average lapse rate between this level and all higher levels This introduces a second, *smoothed* Γ profile, Γ_{S}. This part is the challenging part, in particular by what is meant by "average". More on this below.

within 2 km This is the size of the smoothing window of the smoothed Γ profile, Γ_{S}. We refer to this as the *thickness interval*.

does not exceed 2 °C/km. We refer to this as the *thickness threshold*, $\Gamma_{\mathrm{THICKNESS}}$. The smoothed Γ profile must stay below this threshold, for a point to be a LRTP candidate grid point. Because $\Gamma_{\mathrm{THICKNESS}} = \Gamma_{\mathrm{LRTP}}$, this can be reduced to just using the Γ_{LRTP} threshold.

In short, the algorithm requires two lapse rate profiles, a *raw* Γ profile, Γ_{R}, and a *smoothed* Γ profile, Γ_{S}, and a LRTP candidate point is found where both profiles are smaller than the Γ_{LRTP} threshold, i.e., when both $\Gamma_{\mathrm{R}} \leq \Gamma_{\mathrm{LRTP}}$ and $\Gamma_{\mathrm{S}} \leq \Gamma_{\mathrm{LRTP}}$. The ambiguity in the interpretation lies in how Γ_{S} is made. There are at least four interpretations:

1. Γ_{S} is made from a standard running average of Γ_{R}, with a running window size of 2 km above each grid point.

2. The "average lapse rate" is interpreted as the lapse rate of the straight line between two grid points. These straight line "lapse rates" are calculated from "this level" to all the "higher levels" for 2 km. I.e., a straight line is drawn from the current grid point in the temperature profile, to each of the grid points within 2 km above it, and none of the lapse rates from these lines may exceed the value of $\Gamma_{\mathrm{THICKNESS}}$ threshold.

   In this interpretation, each grid point in Γ_{S} can be represented by the maximum Γ value of the straight lines within the 2 km above each grid point.

3. The "average lapse rate" is interpreted as the *average* of the lapse rates of the straight lines between each grid point and the grid points within 2 km above it.

   I.e., this is almost like in 2, but instead of representing each grid point in Γ_{S} by the maximum Γ value of the straight lines, it is here represented by the *average* Γ value of the straight lines within the 2 km above.

Another version, that is often seen, is:

4. The lapse rate has been calculated in each grid point from "this level and all higher levels within 2 km", and none of these may exceed the $\Gamma_{\text{THICKNESS}}$ threshold. I.e., *no* average is calculated, and *no* Γ_{S} profile is being used, but none of the Γ values on the Γ_{R} profile may exceed the $\Gamma_{\text{THICKNESS}}$ threshold for 2 km above each candidate point.

Each interpretation may yield different results, depending on the geographical location of the temperature profile and season, especially outside of the tropics where the temperature profiles are more complicated (see Figure 2.1).

However, regardless of the interpretation, the (challenging) smoothing part is useful. The smoothing prevents that small, local bumps in the temperature profile are detected as LRTP candidate grid points while letting the actual LRTP level to be found on the raw, un-smoothed temperature profile. I.e., despite of the smoothing, the algorithm is able to detect small changes in the LRTP altitude, given that the vertical resolution is fine enough.

As mentioned in Highwood and Hoskins (1998), the thresholds may not have physical relevance, and have probably been chosen for operational reasons, originally. Likewise, which interpretation to use, may not be of physical importance. In literature, however, it is often not specified which interpretation has been used. Comparing results from two studies, with different implementations, may therefore be imprecise. It would be helpful if there was a reference paper on the topic.

And such: In this work, we use the *second* interpretation for computing the LRTP.

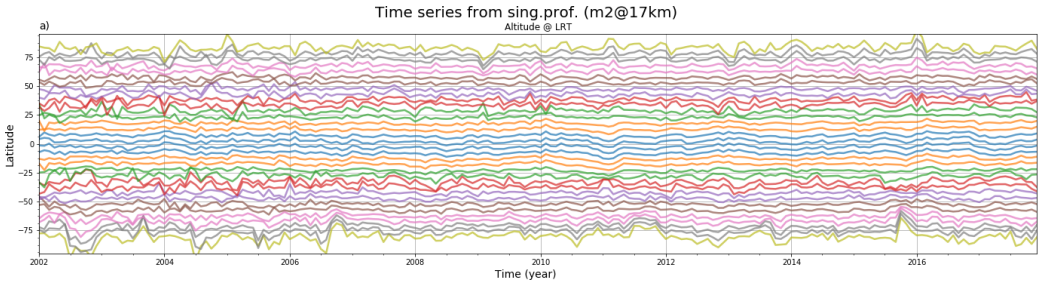


Figure 4.7.: Joy plot of the mean altitude of the LRTP at 5° zonal bands. The LRTPs were first calculated from individual RO temperature measurements, i.e., the LRTPs were found on each individual temperature profile before the zonal mean LRTP was calculated. The colors denote different latitudes. The labels are "Time (year)" on the x-axis and "Latitude" on the y-axis.

Figure 4.7 shows the joy plot of the altitudes at the LRTPs, made from the same temperature profiles as in Figure 4.5 (CPTPs). Compared with Figure 4.5, the large "jumps" outside the tropics are here reduced.

Altitude limits for the LRTP search

High water vapor concentrations in the lower parts of the troposphere can cause temperature gradients which could be interpreted as a tropopause by tropopause algorithms. Therefore, the LRTP algorithm should not start the search for a candidate at a too low altitude. Rieckh et al. (2014) used a table defining lower altitude limits depending on latitude and season. Son et al. (2011) used a latitude dependent lower altitude limit. When plotting global scatter plots LRTPs from individual temperature profiles in latitude-altitude-space, using the Son et al. (2011) lower altitude limit, z_{start}, several LRTPs are excluded from the cluster of tropopauses due to this limit, especially at mid-latitudes. After experimenting with different starting altitudes, evaluated visually, we ended up with a modified version of the one in Son et al. (2011):

$$z_{\text{start}}(\phi) = 6.250 \text{ m} + 1.250 \text{ m} \times \cos 2\phi \tag{4.9}$$

also reported in Paper III (Wilhelmsen et al. 2020).

An additional method that works well in the search for a z_{start} is to use the second part of the WMO (1957) LRTP definition, i.e., apply (b) before (a). In doing so, it is not necessary to rule out the temperature profiles that do not reach all the way down to z_{start}. We did, however, not do this systematically enough to yield any statistics, but could be worth further investigation.

The temperature profiles are rejected if they do not reach all the way down to z_{start}. Additionally, the temperature profile has to exist for 2 km above the candidate point, because the Γ_{S} profile is calculated using all the grid points for 2 km above the candidate point. The temperature profile therefore has to reach all the way up to

$$z_{\text{stop}} = 25.000 \text{ m}. \tag{4.10}$$

Any tropopause found at that altitude is quite certainly not valid. In the tropics, the detected phenomena at these altitudes may very well be the QBO.

Fine tuning the lapse rate tropopause

Like for the CPTP, all candidate points are found on a vertical grid. Because the search starts from below, and both Γ profiles (both raw and smooth) have to fulfill the lapse rate thresholds, the candidate grid point will always be found *above* the "actual" level. This introduces a positive bias in LRTP altitude and a negative bias in the LRTP temperature.

We tried to solve this in the same way as for the CPTP, by fitting the raw lapse rate profile around the candidate point to the quadratic function, simply by finding the altitude where the derivative of the parabola had the gradient equivalent to the lapse rate threshold. I.e., letting Equation 4.4 equal 2 K/km instead of 0. However, the temperature profile, around the LRTP, does *not at all* always correspond to a parabola, which resulted in some very strange solutions, and therefore some LRTP altitudes very far from the gridded temperature profile.

Instead, we found that linear interpolation worked quite well. I.e., the fine tuned LRTP altitude, z_{LRTP}, was first found on a straight line on the *lapse rate curve*,

$$z = A\Gamma + B \tag{4.11}$$

between the candidate grid point, (z_1, Γ_1), with $\Gamma_1 \leq 2$ K/km, and the point *below* the candidate point, (z_2, Γ_2), with $\Gamma_2 > 2$ K/km: The slope, A, of the line is

$$A = \frac{z_1 - z_2}{\Gamma_1 - \Gamma_2} \tag{4.12}$$

and the fine tuned z_{LRTP} was found at

$$\begin{aligned} z_{\mathrm{LRTP}} &= z_1 - A(\Gamma_1 - \Gamma_{\mathrm{LRTP}}) \\ &= z_1 - \frac{z_1 - z_2}{\Gamma_1 - \Gamma_2}(\Gamma_1 - \Gamma_{\mathrm{LRTP}}), \end{aligned} \tag{4.13}$$

where Γ_{LRTP} is the LRTP threshold (2 K/km).

The fine tuned LRTP temperature value, T_{LRTP}, is similarly found using a straight line between the same two points, but on the *temperature* profile. The T_{LRTP} is found where the straight line crosses the altitude value, z_{LRTP}, found from Equation 4.13.

$$T_{\mathrm{LRTP}} = T_1 - \frac{T_1 - T_2}{z_1 - z_2}(z_1 - z_{\mathrm{LRTP}}). \tag{4.14}$$

Lapse rate tropopause trends

Figure 4.8 shows the trends of the monthly mean altitude and temperature values at the first LRTP from RO data, calculated using the WMO LRTP tropopause algorithm, for 5° zonal bands. The trends are calculated using a standard linear fit (orange) as well as a multivariate linear regression (blue). The regressor used is the atmospheric index established in Paper I (Wilhelmsen et al. 2018), using the M2-method at the 17 km altitude level. Only the first PC[3] was used. Results (left panel) show that the altitude of the LRTP is rising on the Northern Hemisphere (NH). This is also the topic of Paper IV (Meng et al. 2021), which shows a continuous rise of the tropopause on the NH over the period 1980–2020, based on Radiosonde Observations (RAOBs) and confirmed with RO data from 2002–2020.

Regarding tropopause temperature, Figure 4.8 (right panel) shows that there is no rise in temperature at the LRTP on the NH, but it shows, however, that the LRTP temperature in the tropics is rising. Moreover, Figure 4.9 shows the LRTP temperature trends during two seasons, December–January–February (DJF) (upper panel) and June–July–August (JJA) (lower panel). The results suggest that the rise in LRTP temperature in the tropics mainly happens during boreal winter.

For the tropics, the time series of the mean altitude and temperature at the LRTP, is presented in Figure 4.10, averaging over all the temperature profiles in

[3]The time component that describes the largest variability.

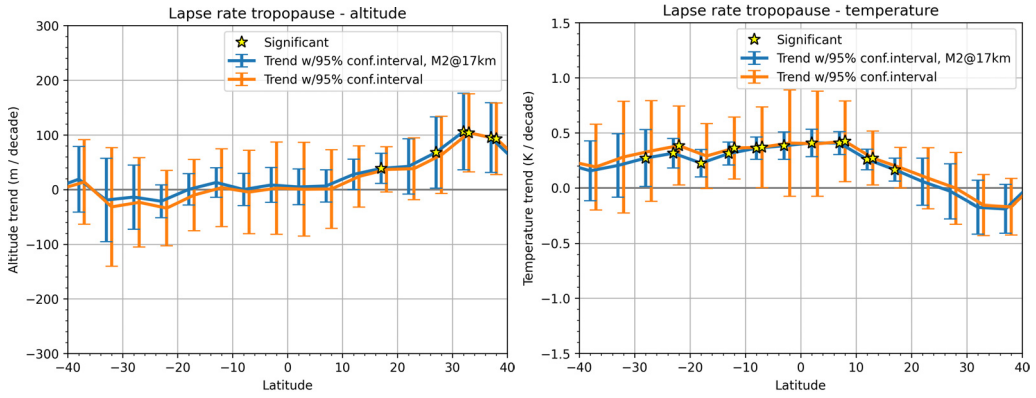


Figure 4.8.: Trends of the LRTP for 5° zonal bands, using RO data from September 2001 to the end of 2020. Trends of the LRTP altitude (left panel) and trends of the LRTP temperature (right panel). Trends and confidence intervals are calculated using a standard linear fit (orange) and using multivariate linear regression (blue) with the M2-indices at 17 km as regressor. The yellow stars indicate that the trends are significant.

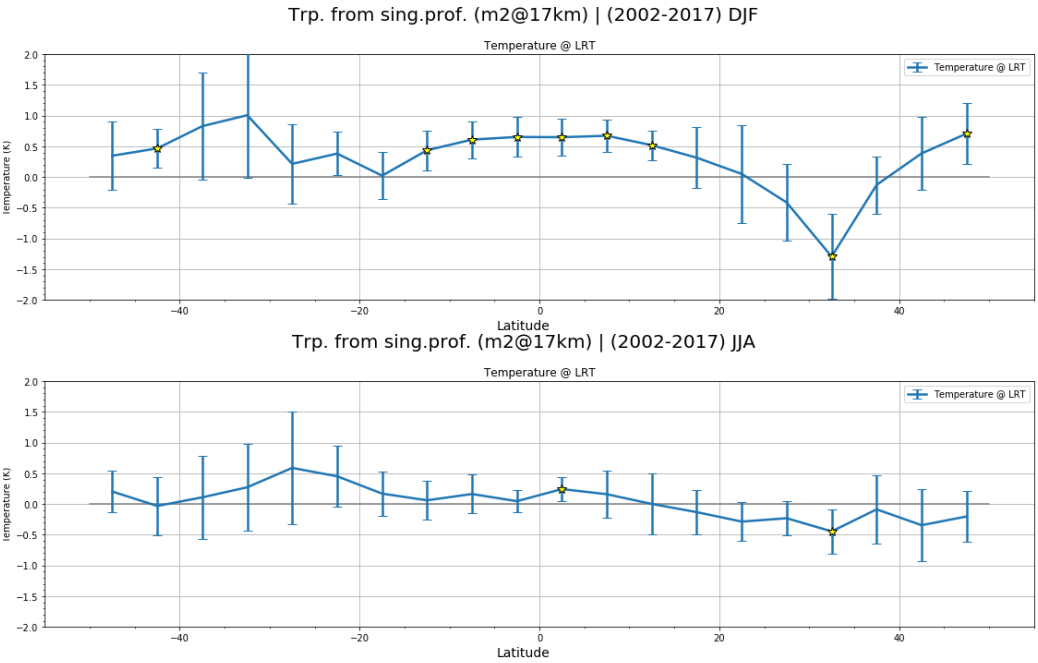


Figure 4.9.: Trends of the LRTP temperature for 5° zonal bands, using RO data from 2002–2017, for DJF (upper panel) and JJA (lower panel). Trends, colors and stars as in Figure 4.8. The labels are "Latitude" on the x-axes, and (should be) "Temperature trend (K/decade)" on the y-axis for both panels.

the tropical zonal band (15° S to 15° N) from the same data as used in Figure 4.8. It shows, like in Figure 4.8, that the tropical LRTP temperature is increasing, while the tropical LRTP altitude stays the same.

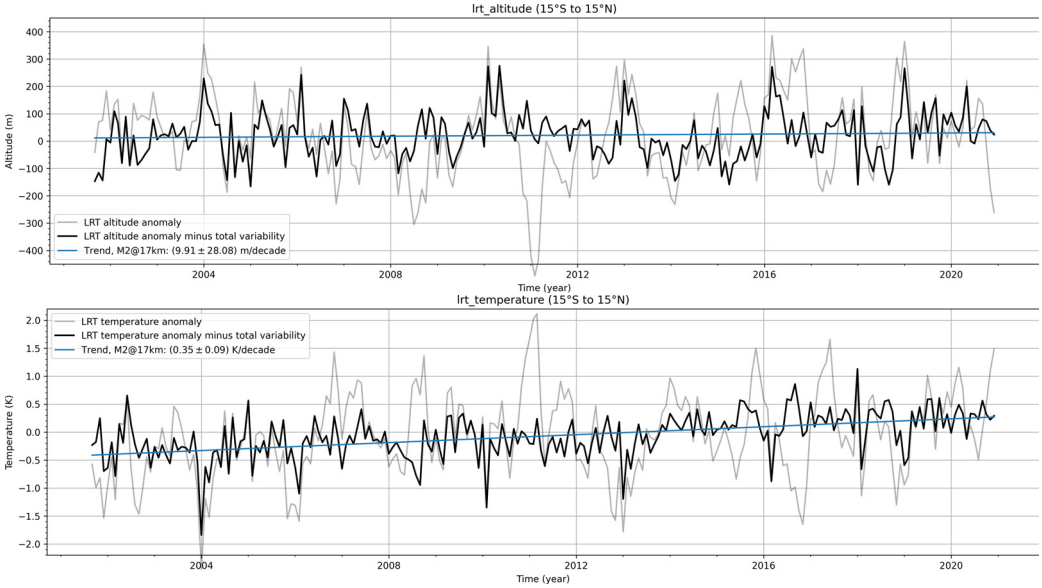


Figure 4.10.: Trend of the altitude (upper panel) and temperature (lower panel) at the LRTP in the tropics (15° S–15° N), using RO data from September 2001 to the end of 2020. The labels are "Time (year)" on both x-axes and "Altitude (m)" (upper panel) and "Temperature (K)" (lower panel) on the y-axes.

Mean LRTPs from individual temperature profiles versus LRTPs from mean temperature profiles

The LRTP altitudes shown in Figure 4.7 are first calculated from each individual RO temperature profile and then averaged over monthly means and 5° zonal bands. If we instead calculate the monthly zonal mean temperature profiles *first*, and use these to find the LRTPs, the altitude of the LRTPs makes sudden "jumps" from months to months, or from latitude to latitude, similar to the CPTPs in Figure 4.5. This is shown in Figure 4.11.

Figure 4.12 illustrates the reason for this. Each panel shows three monthly *mean* temperature profiles representing the same three zonal bands on the NH, for February 2010 (upper panel) and February 2011 (lower panel). The mean temperature profiles do not change much from year to year, and it would be expected that the LRTP would be found close to the same altitudes each year. The altitude representing the LRTP in the orange profiles, however, "jumps" several km between 2010 and 2011, while the LRTPs found on the blue and the green profiles, stay close to the same altitude in both years.

This happens because the LRTP algorithm works as a step function. As soon as both the raw Γ_R profile and the smoothed Γ_S profile cross the hard Γ_{LRTP} threshold, there is a candidate point. If the two Γ profiles only *almost* cross the Γ_{LRTP} threshold in a grid point, or if only one of them does, it is not considered to be a LRTP candidate point, and the LRTP algorithm continues the search. The

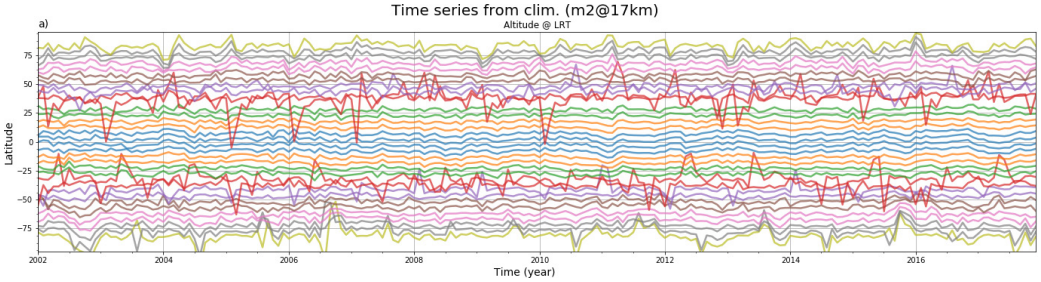


Figure 4.11.: Joy plot of the altitude of the LRTP at 5° zonal bands. The LRTPs were calculated from climatology (zonal mean) temperatures profiles. I.e., for each month, the average zonal mean temperature profile was calculated, and then the LRTPs were found based on these. The colors denote different latitudes. The labels are "Time (year)" on the x-axis and "Latitude" on the y-axis.

LRTP algorithm may therefore find the LRTP candidate points several km apart in very similar temperature profiles. Likewise, the different interpretations of the LRTP algorithm (subsection 4.2.3) may result in LRTP candidate points several km apart, e.g. if the Γ_S profile crosses the Γ_{LRTP} threshold in one interpretation and not in the other.

When the LRTP is computed based on a mean temperature profile, the resulting LRTP depends on that one temperature profile. When the mean LRTP value is instead calculated from *several individual* temperature profiles and then averaged, the step function "jumping" effect may still happen in some of the individual temperature profiles, but it becomes less important, because the mean value is based on several LRTP values and not only one. The question is also whether the "jumping" LRTP values should be assigned to different tropopause regimes, instead of being mixed together. This is discussed further in subsection 4.3.3.

When calculating the LRTP trends, therefore, the results may come out differently if the values are based on *individual* temperature profiles and then averaged or on a *mean* temperature profiles. Figure 4.13 shows the LRTP trends in each zonal band calculated based on individual temperature profiles (upper panel) and based on zonal mean temperature profiles (lower panel).

In the tropics, the individual temperature profiles do not change much. The zonal mean temperature profiles are quite similar to the individual profiles (see Figure 2.1), and the trends are found accordingly. Therefore, it does not matter much whether the tropical LRTP is computed based on individual temperature profiles or based on zonal mean temperature profiles. This is illustrated in Figure 4.14. It shows the time series used to calculate the trend at the LRTP in the tropical band between 20° S and 20° N, both from individual temperature profiles and zonal mean temperature profiles. However, in the extra-tropics, it is more robust to compute the mean LRTP based on individual temperature profiles, and then averaged to a mean LRTP.

The learning is that the LRTP algorithm contains a step function and should be

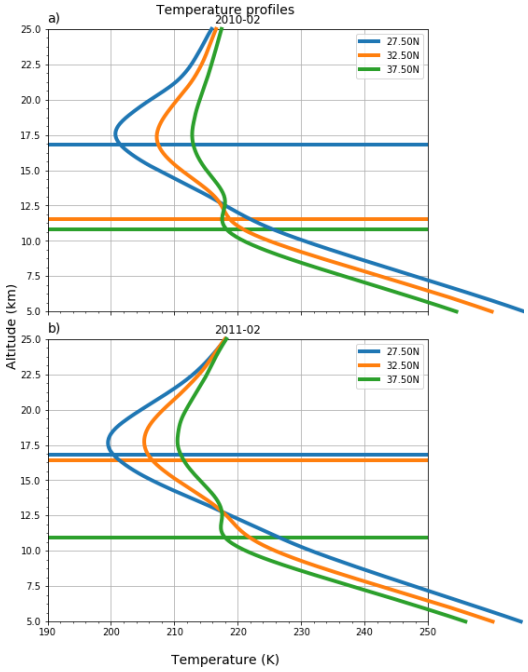


Figure 4.12.: Monthly averaged temperature profiles from RO measurements. Each mean profile is created from all the RO measurements within a 5° zonal band (labels show the center latitudes) from February 2010 (upper panel) and February 2011 (lower panel). These mean profiles have been used to calculate the LRTP. The altitudes of the LRTPs are shown as horizontal lines in the same colors as their corresponding mean temperature profiles. Because the LRTP algorithm acts as a step function, the LRTP can be found several km apart for very similarly looking temperature profiles. The LRTPs in the example are found using the 1st interpretation, and would not be considered a tropopause using the 2nd interpretation. However, the problem is the same for all the interpretations, or with different smoothing, because the algorithm acts as a step function. When there are several tropopauses, the same problem occurs for the CPTP. It may therefore be misleading to use an single temperature profile to represent the altitude of the LRTP. The step function effect also happens when the temperature profiles are smoothed.

used with care on monthly mean temperature profiles, especially in the subtropics where there are overlapping tropopause regimes.

The same problem happens for the CPTP in the subtropics. When finding the CPTP using the monthly mean temperature profile the resulting coldest point may "jump" between the tropical tropopause regime and the extratropical regime. Thus, if the CPTP values are based only on a mean temperature profile, this may be inaccurate.

4.2.4. Double tropopauses - implementation and results

When a LRTP has already been found, the second part of the WMO (1957) LRTP definition ((b) in Figure 4.6, subsection 4.2.3) describes how to search for additional

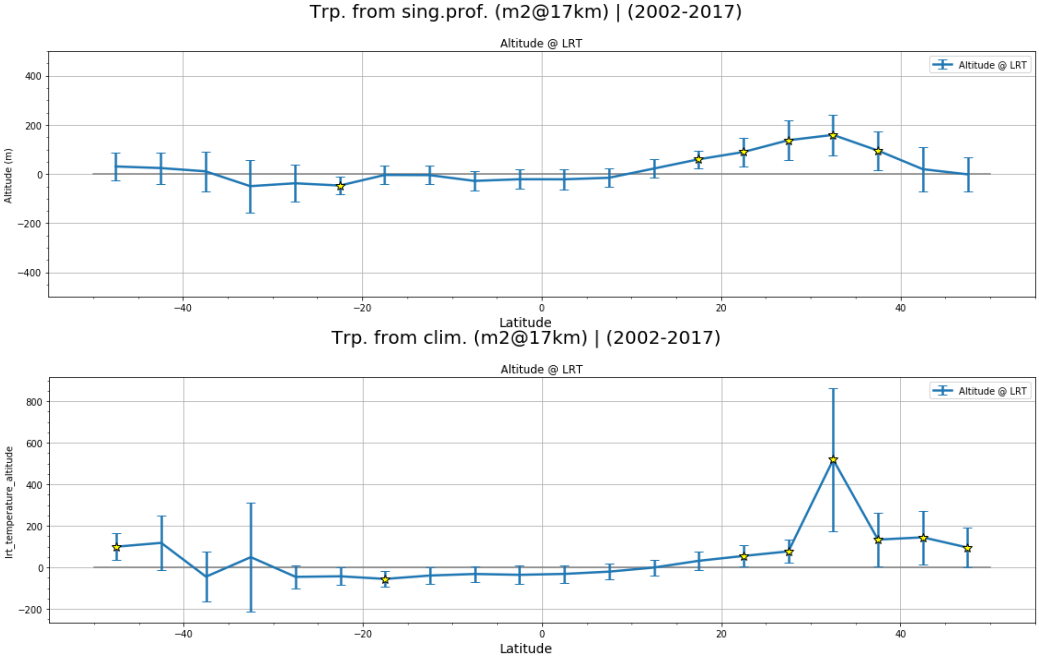


Figure 4.13.: Trends of the temperature at the LRTP at 5° zonal bands using RO data from 2002–2017, with LRTPs from individual profiles (upper panel) and LRTPs from zonal monthly mean temperature profiles (lower panel). The labels are "Latitude" on both x-axes and "Altitude trend (m/decade)" on both y-axes. Please mind the different scaling of the y-axes.

tropopauses. The algorithm requires yet another smoothed Γ profile, built from an "average lapse rate" of the grid points above each grid point, like in the first part ((a) in Figure 4.6). We use the same interpretation as in the first part[4], but the thickness interval of the running window is set to 1 km (instead of the 2 km in the first part (a)). Starting at the altitude of the first LRTP, the first point where the new smoothed Γ profile is larger than $3\,°\mathrm{C\,km^{-1}}$ is used as a new starting altitude, z_{start}. In other words, if the smoothed temperature profile starts to cool again after the first LRTP has been found, and the cooling is large enough, and maintained long enough, we can search for additional LRTPs in the same way as we search for the first LRTP.

Figure 4.15 depicts the second LRTPs (orange pixels). Second LRTPs are mainly found above the extratropical tropopause regime, at the same height as the tropical tropopause regime.

Double Tropopauses (DTs) were the main focus of Paper III (Wilhelmsen et al. 2020). It showed a connection between the ENSO and the occurrence of DTs in the Pacific ocean. A higher number of DTs is detected during cold La Niña events while warmer El Niño events result in a lower number of DTs. This relates to a

[4]The second interpretation.

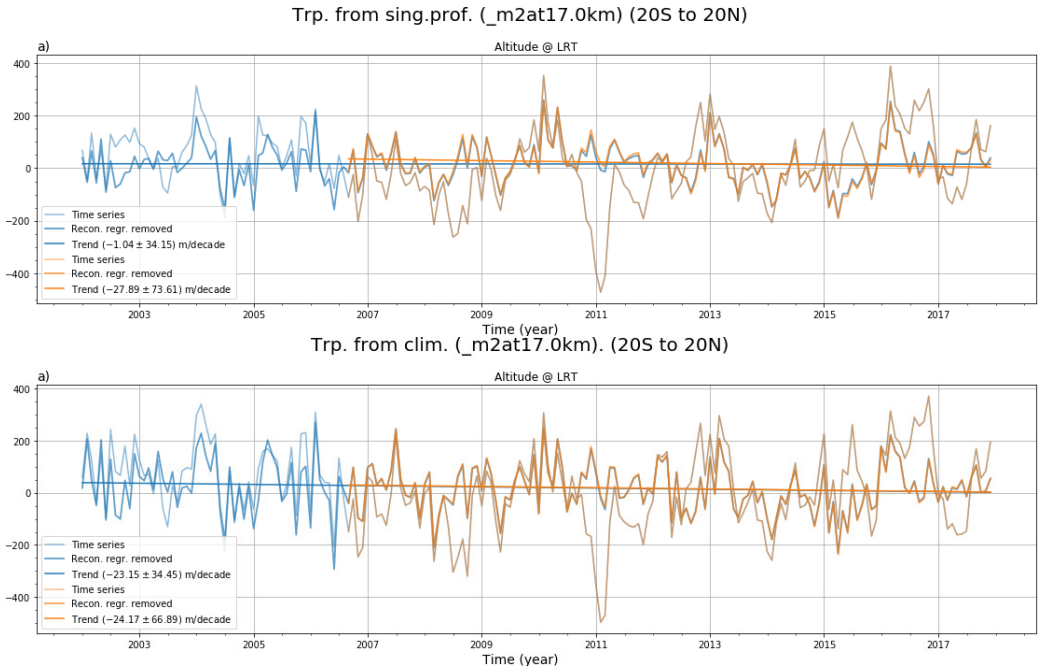


Figure 4.14.: Tropical (20° S–20° N) LRTP altitude trends, using RO data from 2002–2017, calculated from individual temperature profiles (upper panel) and from zonal monthly mean temperature profiles (lower panel). The labels are "Time (year)" on both x-axes and "Altitude trend (m/decade)" on both y-axes.

much lower first LRTP height during La Niña corresponding to a narrowing of the tropical belt in the tropical East Pacific ocean region.

Interestingly, we also found a correlation between time series of DTs rates with time series of monthly mean temperature anomalies in the stratosphere. They were found both on the Southern Hemisphere (SH) and on the NH. The correlations were especially prominent around 25 km (see Figure 4.16 and Figure 4.17). Because DTs are associated with enhanced Stratosphere-Troposphere Exchange (STE) and stratospheric temperature anomaly with the QBO, the correlation could indicate a connection between the QBO and enhanced subtropical STE. It could also be related to the Holton-Tan effect (Anstey and Shepherd 2014), which describes a connection between the stratospheric winter polar vortex and the QBO. We did not investigate this further.

In the light of the results of Paper III (Wilhelmsen et al. 2020) and Paper IV (Meng et al. 2021) it could be interesting to investigate the cause of the rising trend of the LRTP height in the NH further (Figure 4.8), whether the altitude of the LRTP is rising because DTs are found more frequently from the tropical tropopause regime, e.g. because the tropical belt is expanding (see subsection 4.3.3).

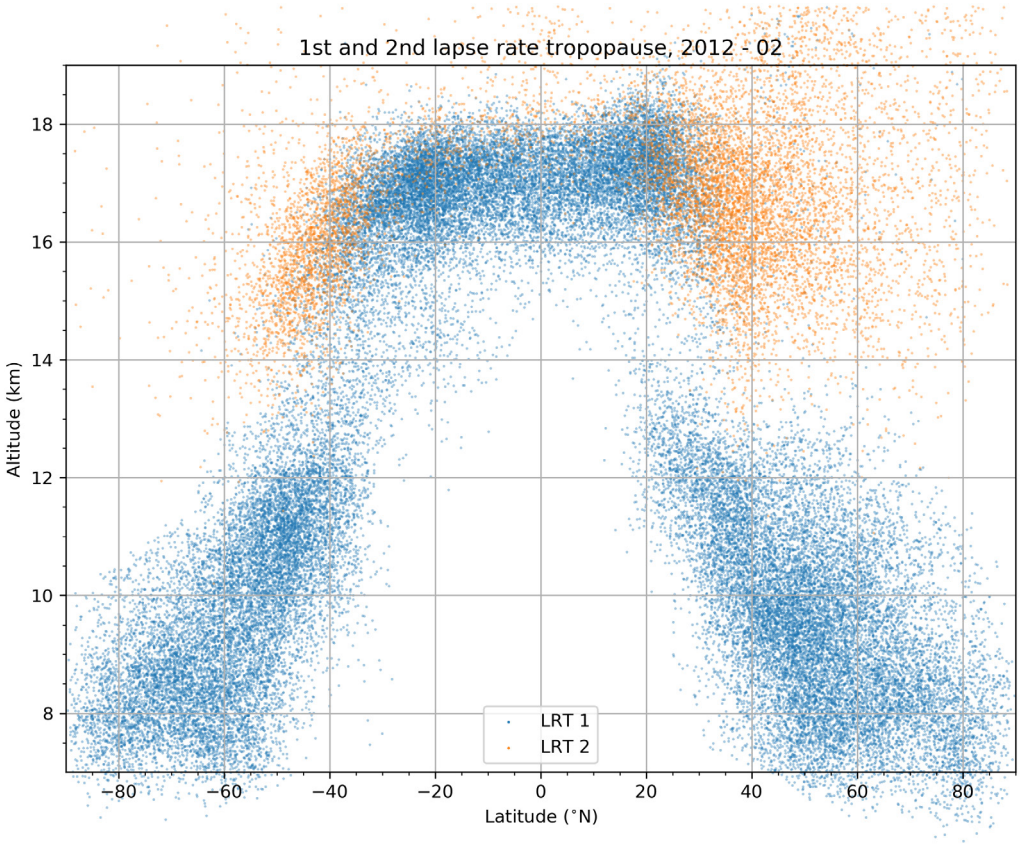


Figure 4.15.: A cross section of all the 1st (blue) and the 2nd (orange) LRTPs using individual RO temperature profiles in February 2012 by latitude and altitude.

4.2.5. Zero lapse rate tropopause

As seen in Figure 4.5, the altitude of the CPTP may "jump" between the seasons and different latitudes, especially in the subtropics, where the tropical and extratropical regimes overlap. To circumvent this, I used the WMO LRTP algorithm (subsection 4.2.3) to find the CPTP[5]. This corresponds to setting both of the two Γ thresholds (the Γ_{LRTP} threshold and the $\Gamma_{\text{THICKNESS}}$ threshold) to $0\,\text{K}\,\text{km}^{-1}$, instead of the $2\,\text{K}\,\text{km}^{-1}$ from the specification (subsection 4.2.3), and leaving all the other parameters unchanged. The algorithm then finds the first *local* temperature minimum of a certain thickness in the temperature profile, named Zero Lapse Rate Tropopause (ZLRTP), instead of the coldest point in the whole profile. Because this algorithm finds a minimum value, we use the same fine tuning as for the CPTP around a quadratic function (section 4.2.1).

In the tropics, where there are no overlapping tropopauses, this algorithm finds the ZLRTP to be at the same altitude as the CPTP. This is supported by

[5]Thanks to Thomas Birner for this useful tip.

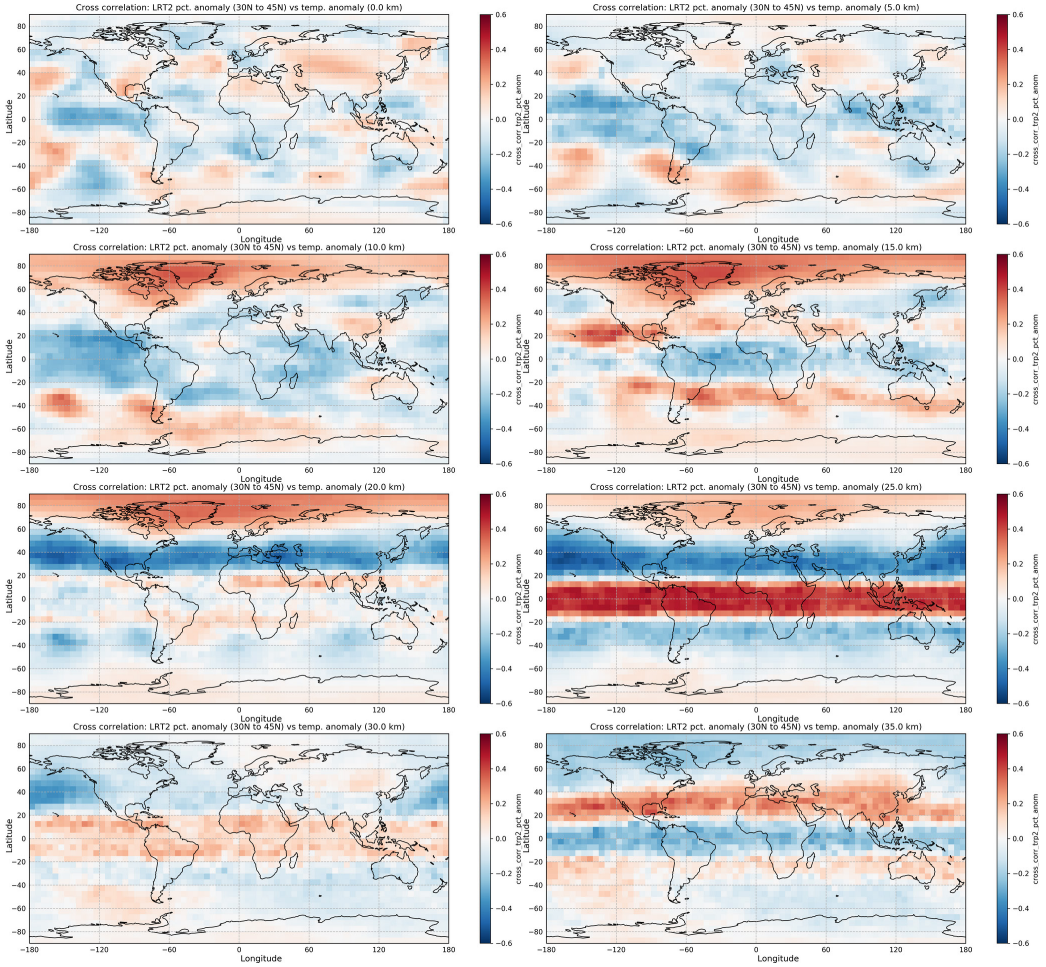


Figure 4.16.: Cross correlation between the monthly mean DT rates on the NH (30° N to 45° N) and monthly mean temperature anomalies at each $5° \times 5°$ grid point for different altitudes levels. From left to right, starting from the top, the panels correspond to 0 km, 5 km, 10 km, 15 km, 20 km, 25 km, 30 km, and 35 km. The labels are "Longitude" on all x-axes and "Latitude" on all y-axes. The color scale shows the correlation coefficient between −0.6 and 0.6.

Figure 4.18 which shows the tropical trend of both the altitude of the CPTP and the altitude of the ZLRTP.

The 5° monthly mean zonal trends of the altitude at the CPTP and the altitude at the ZLRTP can be seen in Figure 4.19. Like in Figure 4.18, the trends are very similar in the tropics, but start to differ at subtropical latitudes, where the overlapping tropopauses can be found. The ZLRTP algorithm, in other words, seems to be able to detect the CPTP further poleward, and yield results similar to those using the LRTP algorithm with $2\,°\mathrm{C\,km^{-1}}$ for the thresholds. This can e.g. also be seen when comparing the joy plot for the ZLRTP, Figure 4.20, with

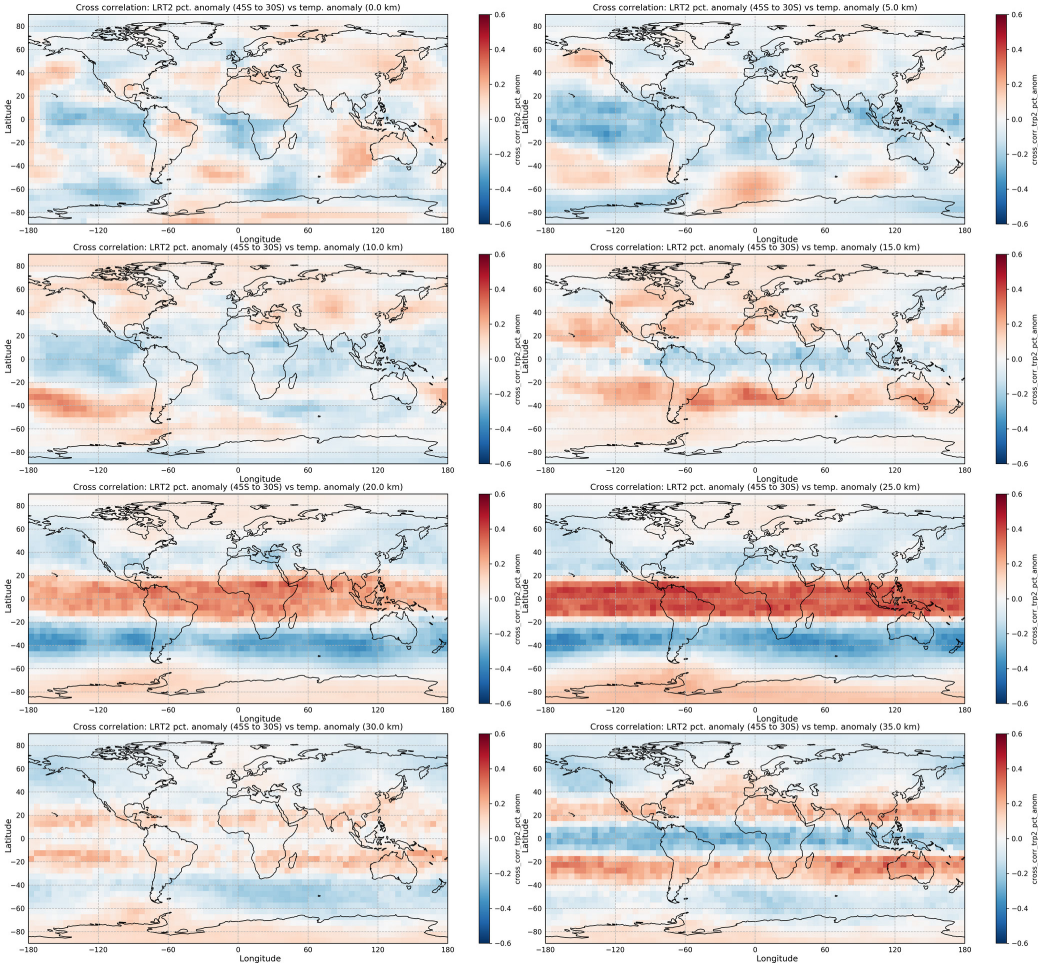


Figure 4.17.: Cross correlation between the monthly mean DT rates on the SH (45° S–30° S) and monthly mean temperature anomalies at each 5° × 5° grid point for different altitudes levels. From left to right, starting from the top, the panels correspond to 0 km, 5 km, 10 km, 15 km, 20 km, 25 km, 30 km, and 35 km. The labels are "Longitude" on all x-axes and "Latitude" on all y-axes. The color scale shows the correlation coefficient between -0.6 and 0.6.

the corresponding joy plot for the CPTP, Figure 4.5. Both plots are made with tropopauses from individual temperature profiles, and then averaged.

4.3. Characterizing the tropopause region

We also investigate different definitions for the tropopause region. Specifically we explored the tropical belt width in a novel way by applying cluster analysis. Since the method is experimental the results have not yet been published. However, the results are documented here for completeness and potential use in future work.

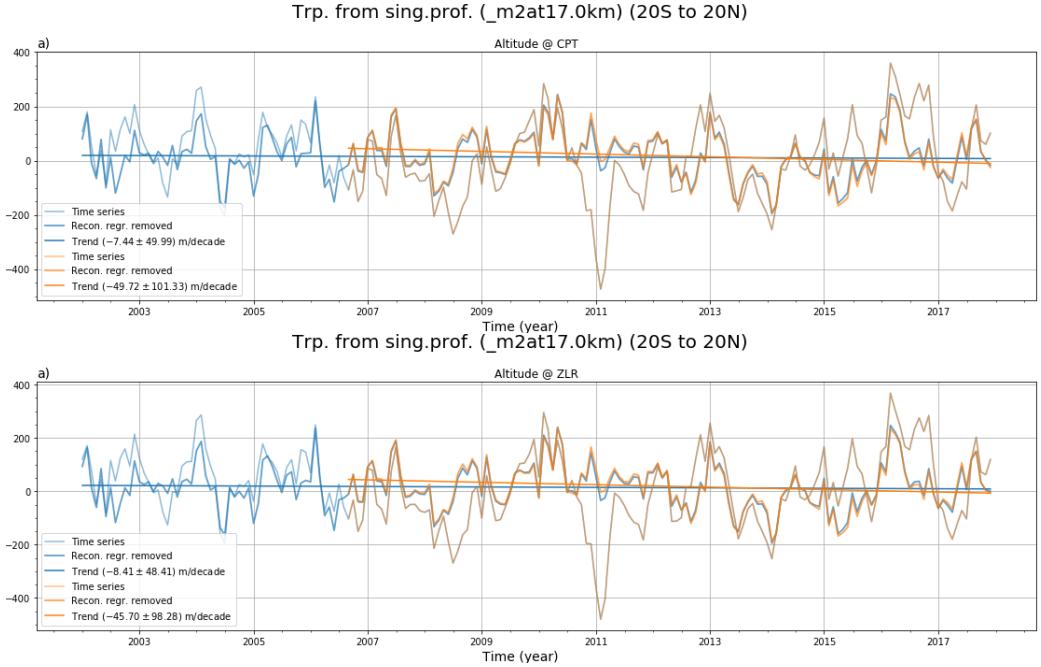


Figure 4.18.: Time series and trends of the CPTP altitude (upper panel) and of the ZLRTP altitude (lower panel) are very similar in the tropics. The labels are "Time (year)" on the x-axes and "Altitude (m)" on the y-axes.

4.3.1. Tropopause Inversion Layer

In the lowermost part of the stratosphere, just above the CPTP, the atmosphere is especially stable, in a layer called the Tropopause Inversion Layer (TIL). It reveals itself in tropopause coordinates by relating the altitude of the temperature profile (z) to the altitude of the CPTP (z_{CPTP}), $z - z_{CPTP}$, so that all CPTPs are found at level zero (Birner et al. 2002; Birner et al. 2006). This peak in stability is as such not a "tropopause definition", but a measure that is part of the tropopause as a phenomena.

The atmospheric stability can be measured with static stability, N:

$$\begin{aligned} N^2 &= g\frac{dln\theta}{dz} \\ &= \frac{g}{\theta}\frac{d\theta}{dz} \end{aligned} \tag{4.15}$$

where g is the gravitational acceleration, θ is the potential temperature, and z is the height (Salby 2012). To find the altitude of the N^2 peak, we use the same algorithm as finding the LRTP and the ZLRTP[6], but on the N^2 profile instead of the Γ profile. The search is started at the altitude of the first ZLRTP. As mentioned in subsection 4.2.5, the ZLRTP is the same as the CPTP in the tropics, whereas

[6]With a raw gradient profile and a smooth gradient profile (subsection 4.2.3)

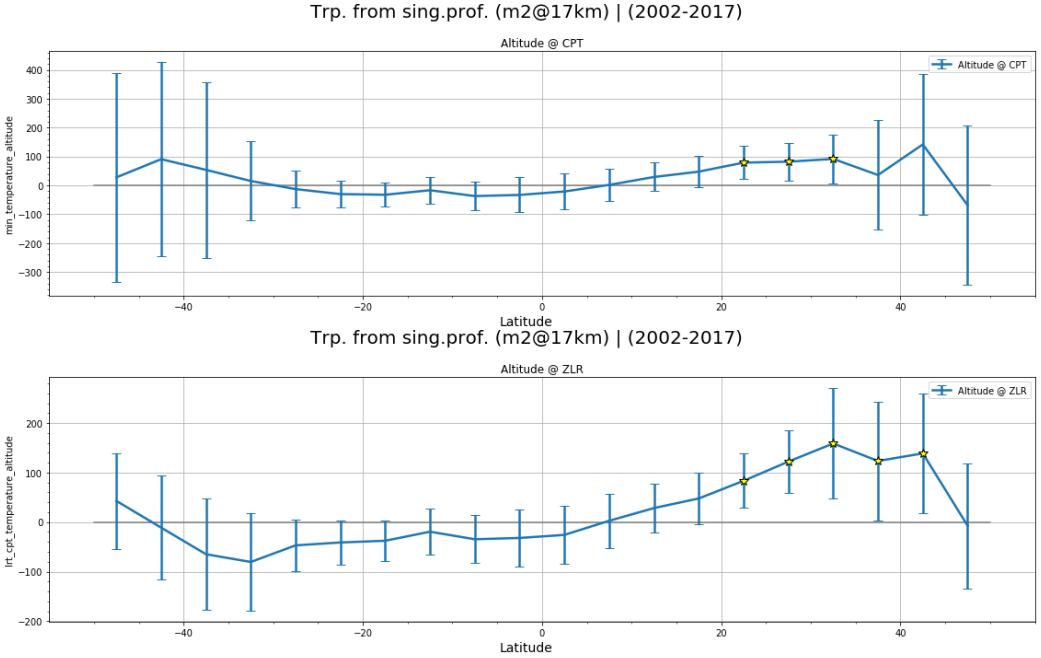


Figure 4.19.: Trends of the CPTP altitude (upper panel) and the ZLRTP altitude (lower panel) at 5° zonal bands using RO data from 2002–2017, using multivariate linear regression with the high resolved atmospheric index at 17 km as regressor. The labels are "Latitude" on both x-axes and "Altitude trend (m/decade)" on both y-axes. Please mind the different scaling of the y-axes.

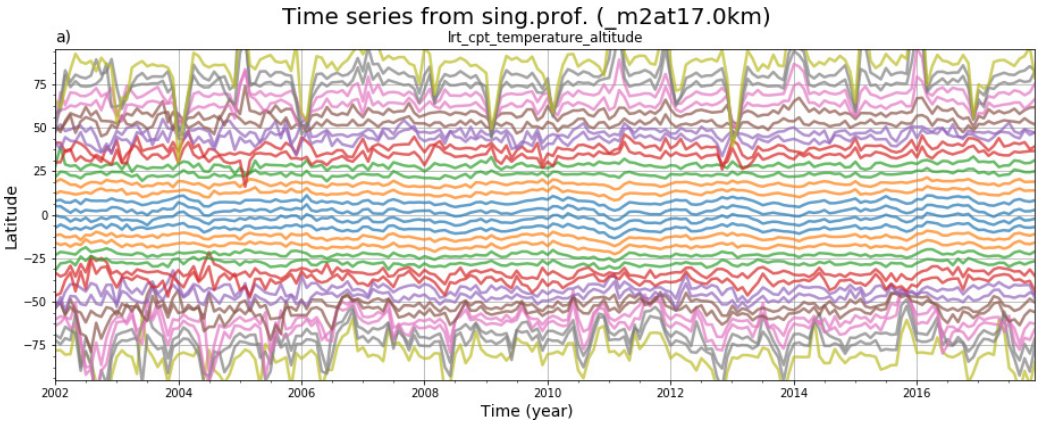


Figure 4.20.: Joy plot of the mean altitude of the ZLRTP at 5° zonal bands. The ZLRTPs were first calculated from individual RO temperature profiles and then averaged. The colors denote different latitudes. The labels are "Time (year)" on the x-axis and "Latitude" on the y-axis.

it corresponds to the *first* tropopause in the extra-tropics, which may either be found in the tropical tropopause regime or in the extratropical tropopause regime.

4.3.2. Tropical Tropopause Layer

The general definition of the Tropical Tropopause Layer (TTL) is "the zone where the properties of both troposphere and stratosphere can be observed." (Fueglistaler et al. 2009). Several definitions have been suggested for the TTL. In this work, we used the following four definitions:

1. Altitude at CPTP (or Altitude at ZLRTP) minus altitude at $\frac{d\theta}{dz}|_{\mathrm{MIN}}$
2. Altitude at 150 hPa minus altitude at 70 hPa
3. Altitude at $N^2|_{\mathrm{MAX}}$ above ZLRTP minus altitude at $N^2|_{\mathrm{MIN}}$ below the ZLRTP
4. Vertical variance of the tropical LRTP domain, using the Gaussian mixture model (GMM).

Gettelman and Forster (2002) used the CPTP as upper level, and the level of minimum vertical change in potential temperature, θ, as lower level, i.e., $\frac{d\theta}{dz}|_{\mathrm{MIN}}$. The CPTP represents the coldest point in the UTLS (see subsection 4.2.1), and $\frac{d\theta}{dz}|_{\mathrm{MIN}}$ represents the level of maximum convective outflow in the troposphere.

As described in subsection 4.2.1, the CPTP has some limitations outside of the tropics. We therefore tried to extend this TTL measure by using the ZLRTP as CPTP, which enabled us to calculate the thickness further out of the tropics. Considering the general understanding of the TTL (see above) and what I learned about overlapping tropopauses and DTs (see subsection 4.2.4) in this work, this may not make sense, as it is not clear what a TTL measure would mean in the DT regions. Therefore, keep in mind that the physical meaning of the measure changes toward the extra-tropics.

Figure 4.21 shows two temperature profiles and their corresponding potential temperature gradient profiles, $\frac{d\theta}{dz}$. The $\frac{d\theta}{dz}$ does not always show a clear minimum in the troposphere. The tropospheric part of the $\frac{d\theta}{dz}$ profiles is often quite constant (vertically), and there are only small differences between the values of the local minima. The minimum altitude of the $\frac{d\theta}{dz}$ profile, therefore, seems to be somehow random. We did not investigate this further, but we tried to make an overview of the TTL based on this definition. Figure 4.22 shows the TTL thickness values calculated from all individual RO profiles in each month in 2013. Some of the thickness values in Figure 4.22 are clearly invalid. Some outliers have a magnitude of 20 km, and negative thickness values are of course impossible. These would need to be sorted out, before used for e.g. trend investigations. A likely reason for the outliers is that the values were calculated separately, resulting in $\frac{d\theta}{dz}|_{\mathrm{MIN}}$ values above the ZLRTP, which e.g. can be seen in the lowermost profile in Figure 4.21. Another reason is that some of the minimum values were simply found too low. The altitude of $\frac{d\theta}{dz}|_{\mathrm{MIN}}$ should therefore be restricted to below the ZLRTP, and also a minimum value should be considered. If we disregard the outliers in Figure 4.22, the data seem to gather around a 5 km thickness in the tropics.

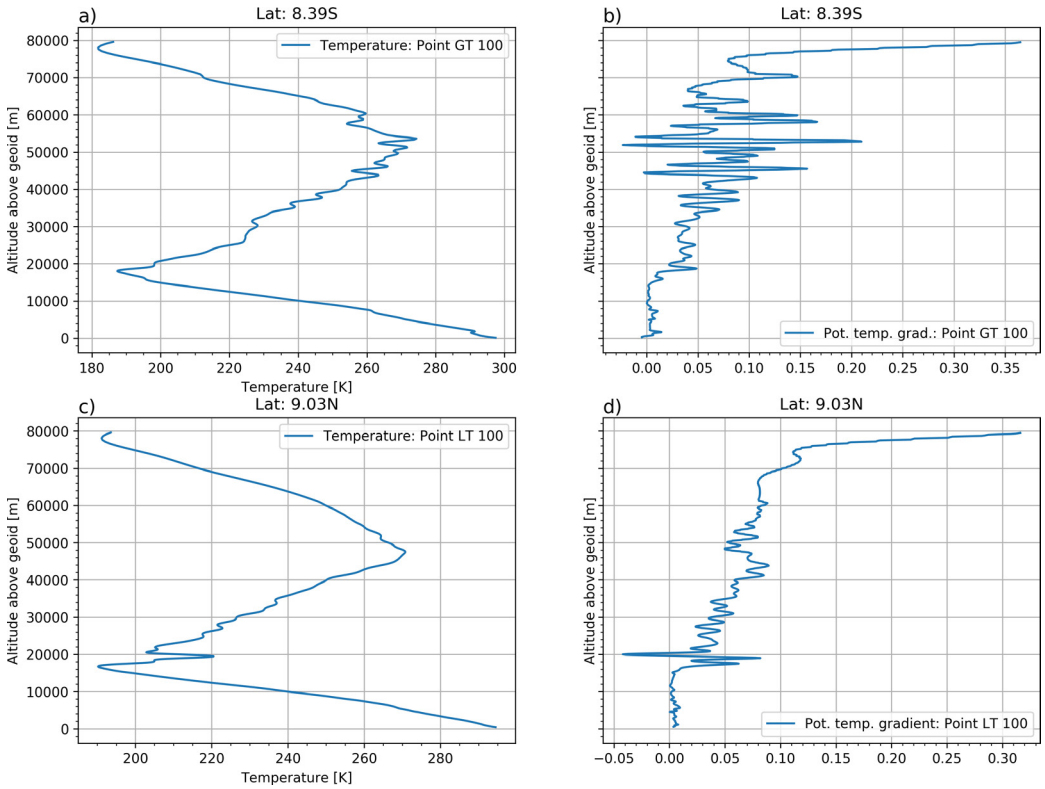


Figure 4.21.: Two temperature profiles (left column) and the corresponding $\frac{d\theta}{dz}$ profiles (right column).

Fueglistaler et al. (2009) considered both the CPTP and the $\frac{d\theta}{dz}|_{\mathrm{MIN}}$ level to be too low. The CPTP and the LRTP should be *part of* the TTL, and the maximum convective outflow is considered a typical feature of the troposphere. They therefore suggested the 150 hPa level as lower limit and the 70 hPa level as upper limit. As the LRTP is generally found around the 100 hPa level in the tropics (subsection 4.2.2), the 70 hPa is in the stratosphere[7], and 150 hPa is in the troposphere.

The Wegener Center for Climate and Global Change (WEGC) Occultation Processing System version 5.6 (OPSv5.6) dataset is provided on a fixed 100 m vertical grid. To get the RO data at the 150 hPa and 70 hPa pressure levels, we picked the pressure levels below and above on the vertical altitude grid, and found the right pressure level by log-linear-interpolation. An overview of the thickness of the TTL for each month in 2013, as calculated from the altitude at these two pressure levels can be seen in Figure 4.23. The values look more reasonable in Figure 4.22, with tropical thicknesses of about 4.4 km to 4.5 km.

The trends of the TTL thickness, using the 150 hPa to 70 hPa definition at 5° zonal bands can be seen in the upper panel of Figure 4.24. There seems to be an

[7]One of the QBO wind measurements is provided on the 70 hPa level (section 3.4).

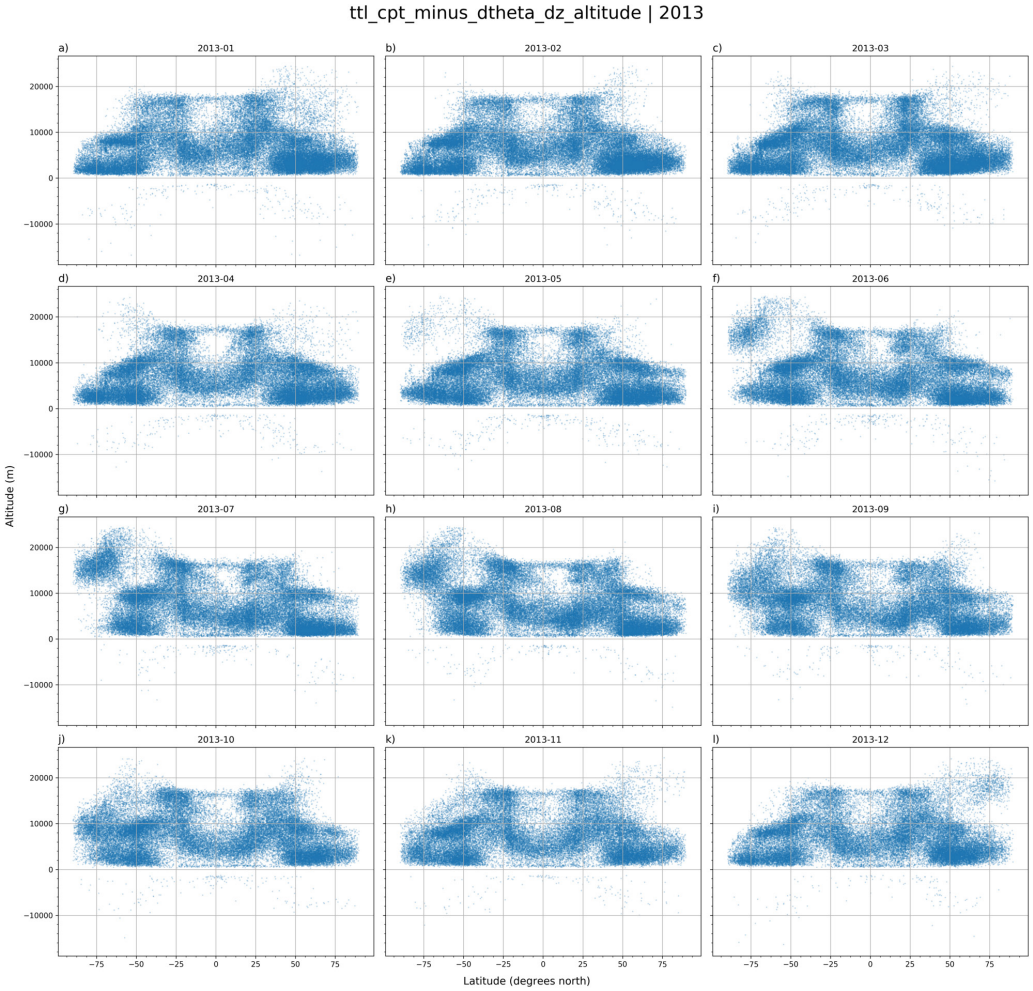


Figure 4.22.: TTL thickness from the altitude at the ZLRTP minus the altitude at the $\frac{d\theta}{dz}$ minimum peak, using RO data. The labels are "Latitude" on the x-axes and "Altitude (m)" on the y-axes. Each panel represents a month of 2013, starting with January 2013 in the top left panel.

increase in the TTL thickness in the tropics over the years. Both pressure levels are rising in altitude, and the main rise seems to come from the stratospheric part (70 hPa). In the NH regions where the LRTPs altitude is rising (see Figure 4.8), the opposite effect can be seen, i.e., shrinking of the TTL. At the same latitudes (in the NH), the difference in temperature between the two pressure surfaces shows a significant negative trend (not shown). Note that these trends are computed only for a short time series.

A different study (Sunilkumar et al. 2017) used the first local peak in static stability N^2 above and below the CPTP as upper and lower limit, respectively. Like for the definition that uses the CPTP as upper limit, we here used the ZLRTP

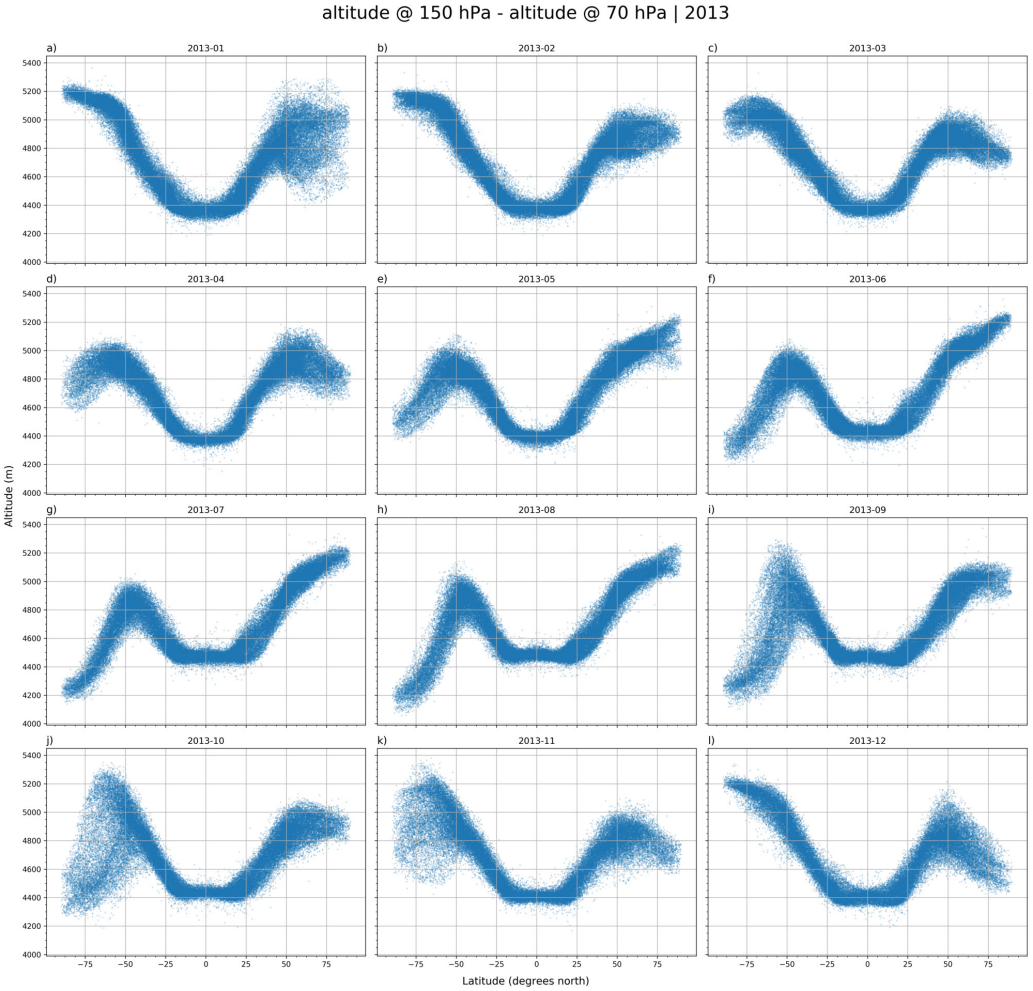


Figure 4.23.: TTL thickness from the altitude at 70 hPa subtracted from the altitude at 150 hPa for individual temperature profiles in 2013. The labels are "Latitude" on the x-axes and "Altitude (m)" on the y-axes. Each panel represents a month of 2013, starting with January 2013 in the top left panel.

instead, with its considerations. Figure 4.25 shows an overview of the TTL when calculated from the peaks in N^2 above and below the ZLRTP. The altitudes of the lower peaks were found in the same way as the upper peaks. We just rotated the N^2 profiles 180° around the ZLRTP, and used the same algorithm, starting from the ZLRTP level.

The thickness values, using the peaks in N^2 (Figure 4.25) seem to be consistent from month to month, even though the spread is quite large, between 1 km and 10 km. There seems to be a clear minimum thickness at all latitudes of about 1 km. This is also the case for Figure 4.22.

Finally, we investigate the thickness of the TTL based on the vertical variance of

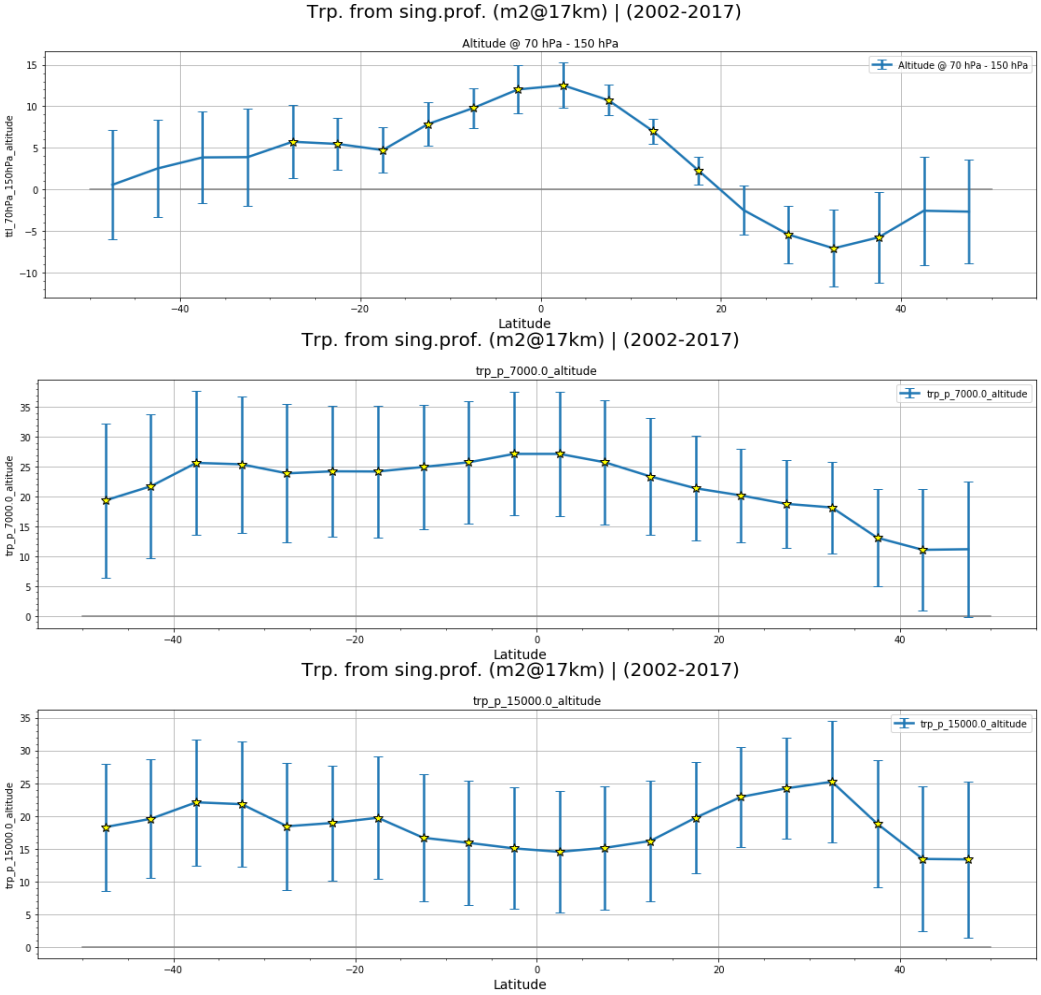


Figure 4.24.: The trends of the TTL as the difference between the altitude at 70 hPa and the altitude at 150 hPa (upper panel), shown for different latitudes. The trends of the altitude at 70 hPa (middle panel). The trends of the altitude at 150 hPa (lower panel), using RO data from 2002–2017. The labels are "Latitude" on the x-axes between 50° S and 50° N, and "Altitude trend (m/decade)" on the y-axes. Please mind the different scaling of the y-axes.

the tropical LRTP domain. We analyzed the cluster that was made from the LRTP altitudes. We did this by using the altitude component of the covariance matrix that comes out of the Gaussian mixture model (GMM) clusters analysis. The GMM is also used to define the tropical edge in subsection 4.3.3, and is described in detail there. The method seemed to work well, but I did not compile these results, because I focused on the tropical belt instead. It may be worth investigating this method further.

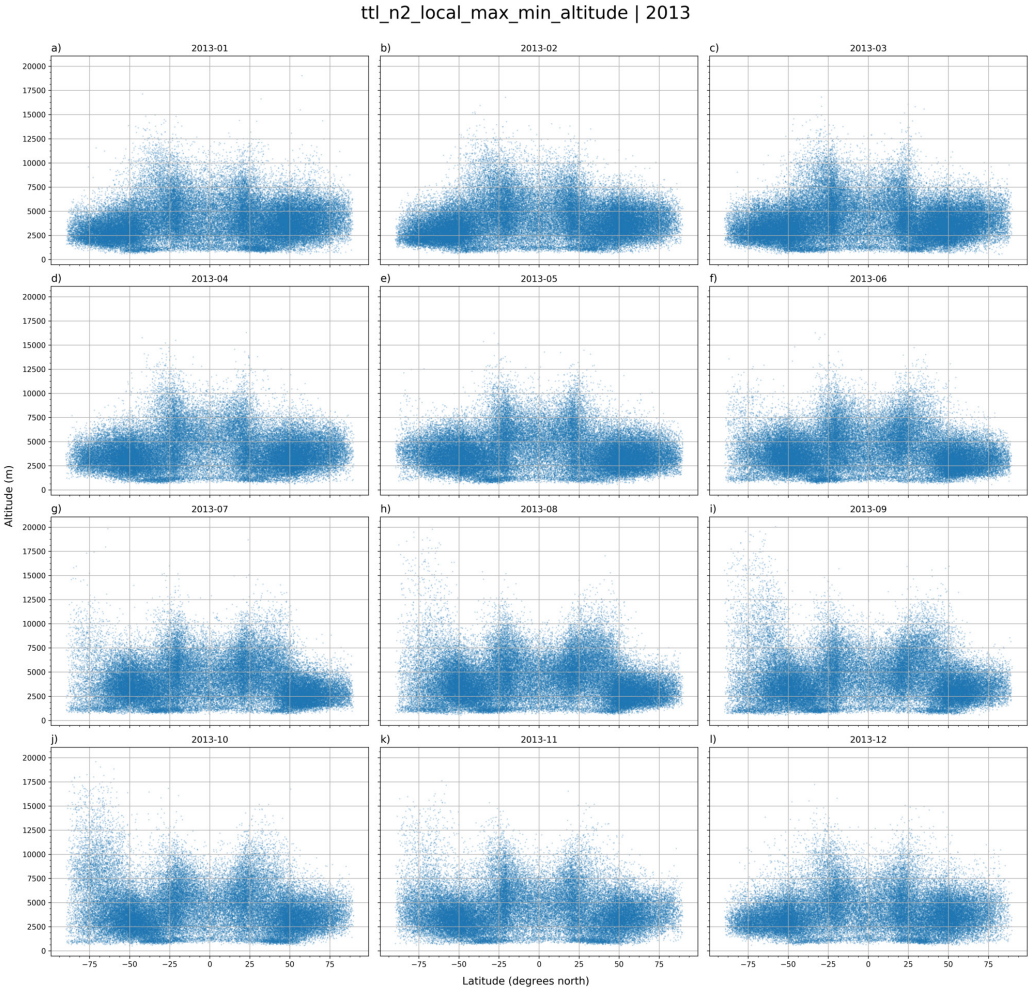


Figure 4.25.: TTL thickness from the altitude at the N^2 peak above the ZLRTP minus the altitude at the N^2 minimum peak below the ZLRTP from each RO temperature profile in each month of 2013. Labels are "Latitude" on the x-axes and "Altitude (m)" on the y-axes.

4.3.3. Tropical belt width - cluster analysis

How to best define the tropical belt is still under discussion (e.g., Davis and Birner 2017; Staten et al. 2018; Staten et al. 2020). We came up with the idea to use the cluster that makes up the tropical tropopause regime, including both the 1st LRTPs and the 2nd LRTPs, to describe the width of the tropical belt.

When observing the altitude of the LRTPs by latitude, the separation of the tropical tropopause regime and the two extratropical tropopause regimes stands out clearly to the human eye. Figure 4.15 shows that the 2nd LRTPs (orange) mainly are located at the same altitude as the 1st LRTPs (blue) in the tropics. This suggests that we should *not* consider the 1st and the 2nd LRTPs as different,

but rather make the differentiation between the tropical tropopause regime and the extratropical tropopause regimes, as also indicated in the previous sections.

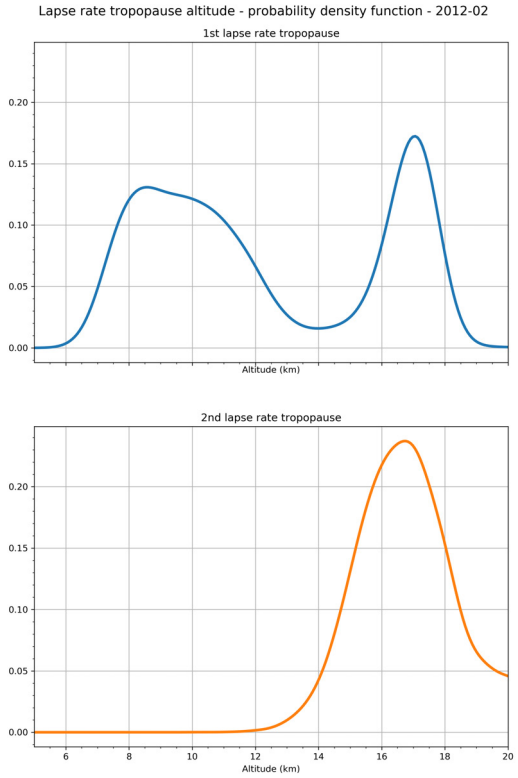


Figure 4.26.: The Probability Density Function of the altitude (km, x-axis) of the 1st (top) and the 2nd (bottom) LRTP during February 2012. Using the same data as in Figure 4.15.

To support this, Figure 4.26 shows a Probability Density Function (PDF) of the altitudes at the LRTPs using the same data that was used in Figure 4.15. The sharp separation of the upper and lower tropopause regimes becomes very noticeable in the upper panel, which is made from the 1st LRTPs only. Comparing the lower panel with the upper panel, the figure confirms that the majority of the 2nd LRTPs are found around the same altitude as the highest peak of the 1st LRTPs, i.e., the tropical tropopause regime. This is also the case for the other months (not shown).

The 1st and the 2nd LRTPs were therefore combined into a single dataset. The different cluster detection algorithms available from the Scikit Learn[8] Python library were then tested to separate the clusters. From all the algorithms the Gaussian mixture model (GMM) algorithm was found to be the most suitable to detect these tropopause clusters. The GMM identifies the clusters by adjusting the parameters of a number of multivariate normal distributions (Gaussians) to best

[8] https://scikit-learn.org, part of the SciPy ecosystem.

match the data. The output of the GMM method is a collection of parameters that describes the Gaussian used to identify each cluster, i.e., a mean value and a covariance matrix for each cluster (see Figure 4.27). I tried to use these GMM

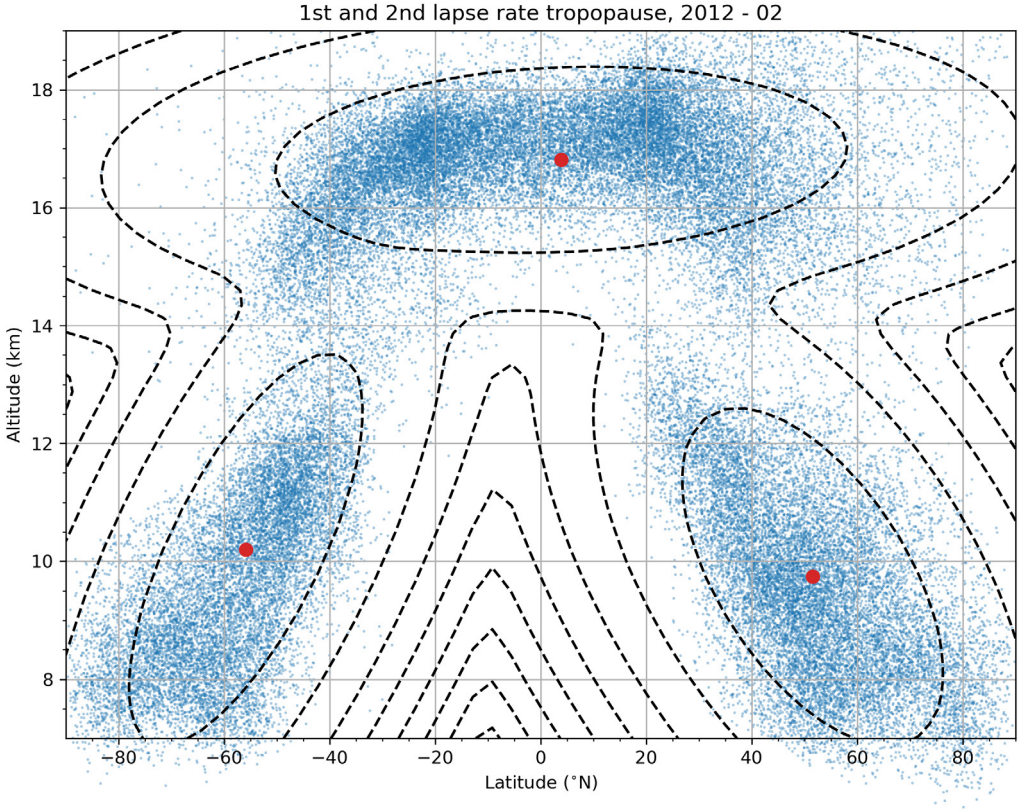


Figure 4.27.: A cross section of all the 1st and the 2nd LRTPs detected in February 2012 including the mean values for each cluster (red dots) when using the GMM cluster algorithm. Contours of the multivariate Gaussians are shown in dashed lines at arbitrary levels. The data are the same as in Figure 4.15 and Figure 4.26.

parameters directly as a measure of tropical belt width. The distribution of the tropical cluster is mostly horizontal. Thus, I made the assumption that the horizontal variance part of the covariance matrix represents the latitudinal variance of the full cluster. The square root of the horizontal component therefore represents the latitudinal component of the standard deviation of the cluster. Two standard deviations in both the NH and the SH were added to the mean value from the parameters to represent the latitude of the edge of the tropics. The resulting time series can be seen in Figure 4.28.

As a reference, two other measures were used to indicate the latitude of the edge of the tropics (Davis and Rosenlof 2012) in Figure 4.28. They both take advantage of the meridional change in LRTP, where the altitude of the LRTP drops moving from the tropical tropopause regime to the extratropical tropopause regimes.

The first metric, the "Maximum gradient latitude" (Figure 4.28) was calculated as the latitude where the gradient of the meridional LRTP altitude is at its maximum:

$$\text{Max grad. lat.} = \frac{dz_{\text{LRTP}}}{d\theta}|_{\text{MAX}}. \tag{4.16}$$

The second metric, the Tropical Edge Latitude (TEL) was calculated as the mean area-weighted latitude of the tropopause gradient:

$$\text{TEL} = \frac{\sum_{15}^{60} \theta \times \frac{dz_{\text{LRTP}}}{d\theta} \cos\theta}{\sum_{15}^{60} \frac{dz_{\text{LRTP}}}{d\theta} \cos\theta}, \tag{4.17}$$

where θ denotes latitude, ranging from 15° to 60° at 1° steps and $\frac{dz_{\text{LRTP}}}{d\theta}$ denotes the meridional gradient of the LRTP altitude.

They were both calculated on the NH and the SH. Figure 4.28 compares time series on the tropical edge, based on the three methods, showing that the time series of the GMM parameter method (green lines) follows the shape of the other two methods fairly well. However, the width differs.

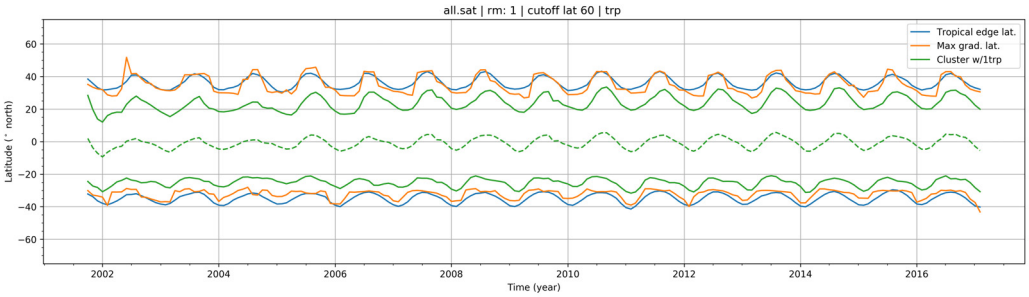


Figure 4.28.: Time series of the width of the tropical belt from three methods, TEL (blue solid lines), maximum gradient latitude (orange solid lines), and GMM cluster analysis (green solid lines). The dashed green line shows the center latitude of the tropics from the GMM parameters. The labels are "Time (year)" on the x-axis and "Latitude" on the y-axis.

When using RO data, however, there are some drawbacks of using the GMM parameters for describing the tropical belt. The first issue is, that there is not much data in the beginning of the RO era. The data do, however, represent an underlying distribution, but if the coverage is too sparse the detected distribution may be misleading. The second issue is that the RO data are not uniformly distributed globally. There are more data at the mid-latitudes (see Figure 4.29). It is an advantage that the RO observations are not station specific, like e.g. RAOBs data (section 3.2), and that RO measurements are well distributed. The uneven density of RO measurements has several peaks (see upper-right panel in Figure 4.30), and the distribution is quite wide, which widens the shape of the Gaussian. This could, in other words, indicate that a normal distribution is not the correct assumption for the underlying distribution, and that the spatial density of the measurements

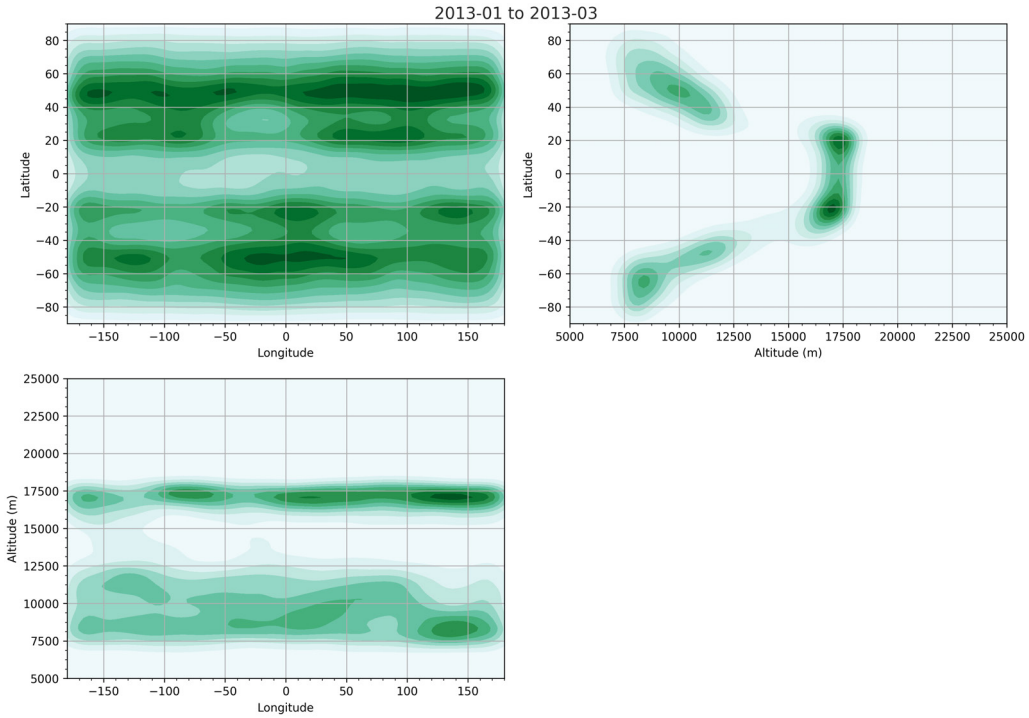


Figure 4.29.: PDFs of spatial distribution of the 1st LRTPs based on RO measurements from the 3 first months of 2013, using the altitude of the *1st LRTPs only*. The upper left panel shows the global distribution of the LRTPs from RO measurements. The distributions also reflect where on the globe the RO measurements are found more often. The upper right panel shows the zonal distribution of the altitude of the 1st LRTPs. The lower panel shows the meridional distribution of the altitude of the 1st LRTPs. The PDF values are unitless, and the values (strength of the colors) are not comparable between the panels, nor are they comparable with Figure 4.30. The plots show where the 1st LRTPs are found using RO data.

might influence the results. Therefore, the GMM parameters may not be valid for detecting the tropical edge.

The GMM algorithm can still be used to identify the tropical tropopause regime and the two extratropical tropopause regimes. A different way to do the identification is to exploit the dip between the two peaks in the upper panel of Figure 4.26. Every LRTP, both 1st and 2nd, found at an altitude higher than that value would be assigned to the tropical tropopause regime, and every LRTP below to the extratropical tropopause regimes. The two extratropical tropopause regimes could then easily be separated to the NH and the SH at the Equator.

Once the regimes have been separated, the uneven spatial density of the RO data is still a challenge to the statistics. The more measurements there are at the edges, the wider the underlying distribution. This can be handled by up-sampling, i.e. artificially adding sample points, or by down-sampling, i.e. removing sample points.

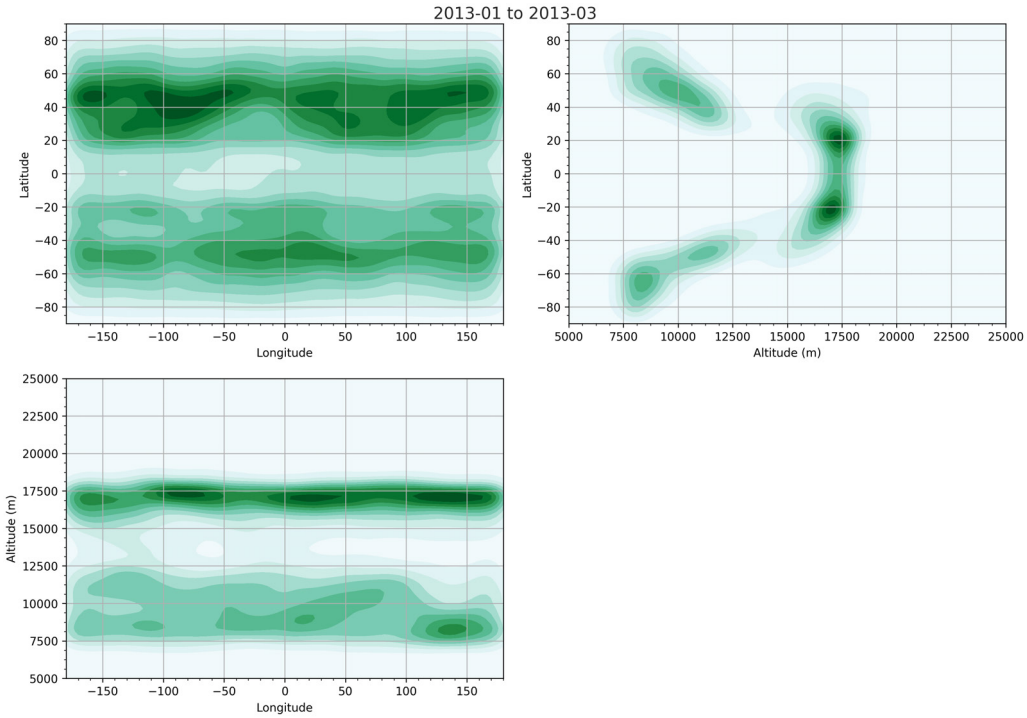


Figure 4.30.: PDFs of spatial distribution of both altitude of *both* the *1st* and *2nd LRTPs* based on RO measurements from the 3 first months of 2013. The upper left panel shows the global distribution of these LRTPs from RO measurements. It shows the enhanced number of DTs on the NH during winter compared to the SH. The upper right panel shows the zonal distribution of the altitude of both the 1st and 2nd LRTPs. The lower panel shows the meridional distribution of the altitude of both the 1st and 2nd LRTPs. The PDF values are unitless, and the values (strength of the colors) are not comparable between the panels, nor are they comparable with Figure 4.29. The plots show where the 1st and the 2nd LRTPs are found using RO data.

I could not come up with a workable way to up-sample the data. One up-sampling attempt was to randomly pick locations and create new temperature profiles based on actual, measured temperature profiles in the proximity. Figure 4.31 shows examples of temperature profiles at randomly selected locations, as an average of the k closest temperature profiles. The averaged up-sampled temperature profile always ends up smoother than the measured temperature profiles it was based on. The smoother profile is therefore subject to the challenges of the step function in the LRTP algorithm discussed in section 4.2.3. All the individual temperature profiles may find its LRTPs in the extratropical domain, while the averaged, smoother profile finds its LRTP in the tropical domain. Also, the altitude of the LRTP may "jump" several km depending on the number of measurements (k in Figure 4.31) the average temperature profile is based on. Adjusting k is not resolving the issue. The smoothing is obvious even for small values of k ($k = 2$). Finally, the lowest

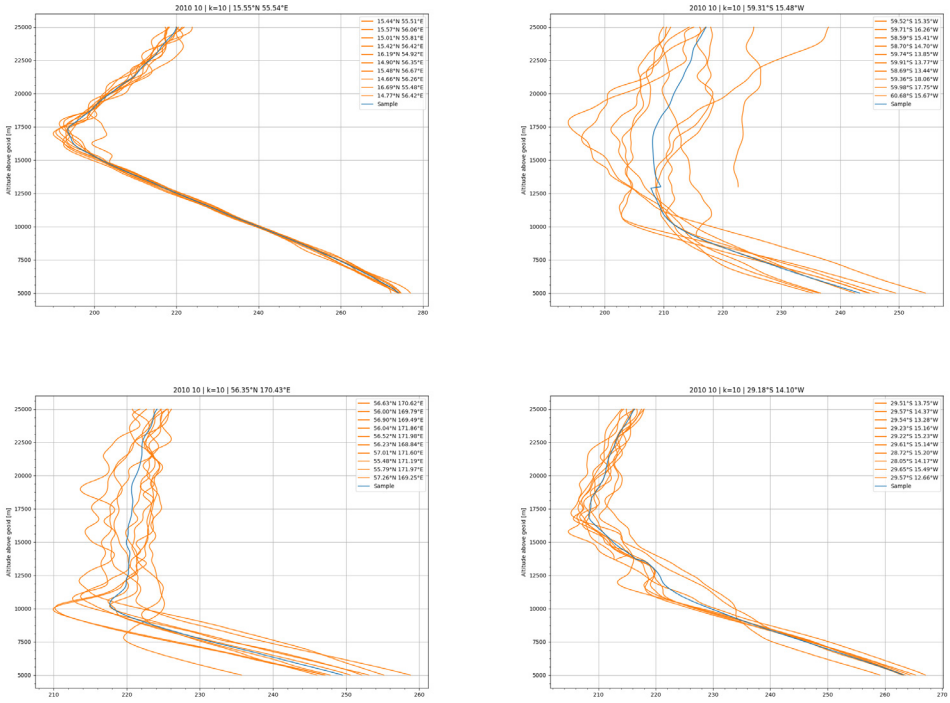


Figure 4.31.: Mean temperature (blue) based on the closest 10 profiles (k=10) at randomly selected locations for October 2010 (orange). Labels are "Temperature (K)" on the x-axes and "Altitude (m)" on the y-axes.

altitudes of the neighboring temperature profiles are different. This may create a discontinuity in the resulting mean temperature profile which could introduce an artificial LRTP in the resulting temperature profile.

Up-sampling by duplicating nearby already calculated LRTPs[9] to randomly selected locations does also not work, mainly because it is not clear how far poleward the new points should be introduced. Adding points too far poleward artificially widens the tropical belt.

Down-sampling, on the other hand, could work. I.e., to simply remove some of the RO measurements, and keep the temperature profiles as they are (no smoothing). Which temperature profiles to remove could e.g. be based on the spatial density of measurements. For illustration, Figure 4.32 shows a number of randomly created points. A weight is assigned to each point based on the distance to k of the nearest points, inspired by the *k-nearest* method. The darker the color, the more samples are found in the proximity of each point. This could be applied to the location of RO measurements, and the weights could be used to randomly select

[9] Or raw temperature profiles.

RO measurements to remove. The higher the weight, the higher the probability of removal.

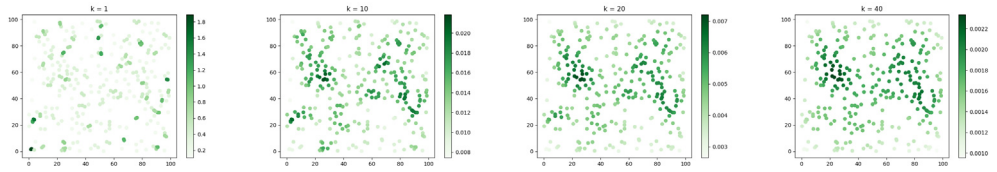


Figure 4.32.: Example of weights given to points, depending on the number of points nearby, with k describing how many points are being accounted for in the weight. No axis labels.

As a final issue, Figure 4.15 illustrates that some LRTPs are found quite far north at an altitude that is obviously not part of a tropopause. They therefore introduce a poleward directed bias in the cluster statistics. I failed to remove these outliers in several home made methods. An attempt can be seen in Figure 4.33, where the outermost percentile of measurements were removed for each 100 m altitude layer. Another attempt was to use a latitude-dependent upper limit, inspired by

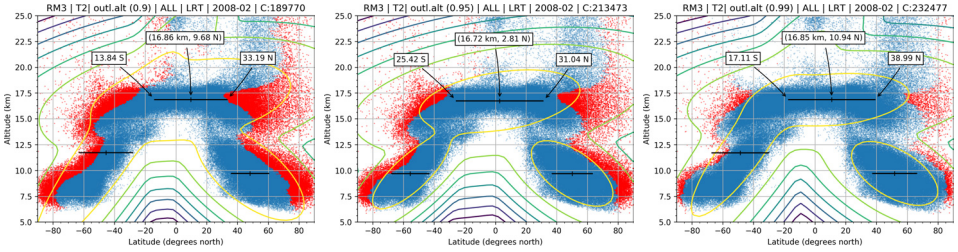


Figure 4.33.: The same LRTP scatter plot in all panels, illustrating the anomalies being removed with the ±0.1- (left), ±0.05- (middle), ±0.01-percentiles (right) for each 100 m altitude steps. The outermost horizontal percentiles of the LRTPs (red) are the ones being removed. Labels are "Latitude" on the x-axes and "Altitude (km)" on the y-axes.

the lower limit described in section 4.2.3. That did not work because the clusters move meridionally with the seasons, and the cutoff appeared arbitrary. Instead, I believe it would be better to use a technique called "Isolation Forest". It randomly divides the dataset in two, and counts the number of data points in each part ("branch"). It then does the same for each of the two new parts, and then again on the new parts, recursively, building a tree structure. The division is repeated until all the data points are isolated (alone in a square). This process is then repeated multiple times, and the trees become a forest. The points that quickly get isolated in most of the trees are considered outliers. A library for this can be found in the Scikit Learn library.

To summarize, these the steps in the proposed method for detecting the width of the tropical belt:

1. Separate the tropical LRTP regime from the extratropical LRTP regimes, e.g. using a PDF in latitude-/altitude-space, or longitude-/altitude-space.
2. Down-sample the data e.g. using density based weighting in latitude-/longitude-space.
3. Remove the anomalies, e.g. using the Isolation Forest method.
4. Apply simple statistics to describe the width in the tropical belt.

It should be noted, that analog to the tropical belt, a similar method could be used for the altitude component to represent the TTL.

5. Summary and conclusions

Human-induced climate change in atmospheric temperature is well studied near the Earth's surface, however, the picture higher up in the atmosphere is still unclear and more detailed insights are needed. Specifically, the Upper Troposphere–Lower Stratosphere (UTLS) region shows large variability, which masks the climate change signal and requires better characterization of the main variability modes.

In this thesis, I therefore addressed the diagnostics of atmospheric variability. Using highly accurate observations from Global Navigation Satellite System (GNSS) Radio Occultation (RO) as key dataset, I answered the following research questions:

1. Can the atmospheric variability be better characterized with high vertical resolution using RO observations?

2. Can RO data contribute to a better knowledge about changes in the vertical temperature structure and climate trends?

3. Which new insights on atmospheric variability and tropopause changes can be gained from RO data?

This thesis, including the synopsis in Part I and four published papers in Part II, provides improved diagnostics of atmospheric variability in the troposphere and stratosphere by establishing novel atmospheric variability indices, examining the impact of volcanic eruptions on the stratosphere, addressing tropopause characterization, and analyzing double tropopause frequencies and tropopause changes.

Paper I (Wilhelmsen et al. 2018) demonstrated that atmospheric variability indices for the most significant modes of natural climate variability in the tropical troposphere and stratosphere can be derived from GNSS RO temperature observations. They offer a high vertical resolution and were constructed based on a standard Empirical Orthogonal Function (EOF) analysis using monthly mean temperature profiles from RO.

The resulting indices, from the first of two methods, already show the characteristics of the El Niño–Southern Oscillation (ENSO) and the Quasi-Biennial Oscillation (QBO) but do not fully describe the vertical structure of the input field. Therefore, in a second method, the EOF analysis was performed on each altitude level separately to obtain the main horizontal variability at each altitude level, taking advantage of the high vertical resolution of the RO data. These resulting vertically-resolved indices capture the atmospheric variability modes in full detail.

Paper II (Stocker et al. 2019) analyzed the impact of minor volcanic eruptions during the RO period and provided detailed insight of induced changes in the

vertical temperature structure. Using new vertically high-resolved aerosol data together with RO temperature measurements, even signatures from small volcanic eruptions could be detected. Although the temperature signals were found to be small compared to other main variability modes such as the QBO, their contribution to the temperature trend can be up to 20%. Thus, volcanic signals may influence the results of short-term trend analysis, depending on when they occur in the time series. As a conclusion, detailed knowledge about the vertical structure of volcanic temperature impacts is crucial for comprehensive trend analysis, as their influence varies for different altitudes and latitudes.

Another major aspect of my work was the investigation of changes in the tropopause region as it is an important transition zone between the troposphere and stratosphere. Therefore, a variety of different tropopause parameters was investigated. Methodologies for implementing different tropopause algorithms and the interpretation of the results are documented in this work. Additionally, experimental methods such as cluster analysis for detection of the tropical belt width have also been explored.

The main focus, however, was on the lapse rate tropopause definition and on implementing a robust detection of tropopause altitudes. Based on RO data, a time series of lapse rate tropopause parameters was created and analyzed for the occurrence of Double Tropopauses (DTs).

Paper III (Wilhelmsen et al. 2020) establishes a connection between these DT occurrences and the ENSO phases by analyzing the global and seasonal DT characteristics. We found that colder La Niña events lead to a higher number of DTs while warmer El Niño events result in lower DT rates. The difference in DT occurrences is caused by the changing regimes between the ENSO phases. During the cold La Niña phase a lower first lapse rate tropopause is observed, resulting in a higher frequency of DTs. This corresponds to an apparent narrowing of the tropical belt in the Eastern Pacific, potentially enabling exchange of air between the troposphere and the stratosphere at lower latitudes than normal.

Having established better knowledge about variability in the tropopause region, the last paper focuses on long-term changes of the tropopause altitude.

In Paper IV (Meng et al. 2021), we used observations from radiosondes to reveal a continuous rise of the tropopause of about 50 m decade over 1980–2020 in the Northern Hemisphere. This is confirmed by GNSS RO data for the period 2002–2020. The increase is found almost equally due to tropospheric warming and stratospheric cooling over 1980–2000 while the continuous rise after 2000 results primarily from enhanced tropospheric warming when stratospheric cooling ceased. The increase in tropopause altitude provides further observational evidence of human-induced climate change.

Exploiting the potential of RO, the results contribute to an overall better understanding of atmospheric variability, reduce uncertainties and improve the separation of natural variability from long-term trends, pinpointing human-induced changes.

Part II.

Published papers

Atmos. Meas. Tech., 11, 1333–1346, 2018
https://doi.org/10.5194/amt-11-1333-2018
© Author(s) 2018. This work is distributed under
the Creative Commons Attribution 4.0 License.

Atmospheric Measurement Techniques
Open Access
EGU

Atmospheric QBO and ENSO indices with high vertical resolution from GNSS radio occultation temperature measurements

Hallgeir Wilhelmsen[1,2,3], **Florian Ladstädter**[1,3], **Barbara Scherllin-Pirscher**[4], **and Andrea K. Steiner**[1,2,3]

[1]Wegener Center for Climate and Global Change (WEGC), University of Graz, Graz, Austria
[2]FWF-DK Climate Change, University of Graz, Graz, Austria
[3]Institute for Geophysics, Astrophysics, and Meteorology/Institute of Physics, University of Graz, Graz, Austria
[4]Zentralanstalt für Meteorologie und Geodynamik (ZAMG), Vienna, Austria

Correspondence: Hallgeir Wilhelmsen (hallgeir.wilhelmsen@uni-graz.at)

Received: 5 July 2017 – Discussion started: 13 July 2017
Revised: 30 November 2017 – Accepted: 21 January 2018 – Published: 6 March 2018

Abstract. We provide atmospheric temperature variability indices for the tropical troposphere and stratosphere based on global navigation satellite system (GNSS) radio occultation (RO) temperature measurements. By exploiting the high vertical resolution and the uniform distribution of the GNSS RO temperature soundings we introduce two approaches, both based on an empirical orthogonal function (EOF) analysis. The first method utilizes the whole vertical and horizontal RO temperature field from 30° S to 30° N and from 2 to 35 km altitude. The resulting indices, the leading principal components, resemble the well-known patterns of the Quasi-Biennial Oscillation (QBO) and the El Niño–Southern Oscillation (ENSO) in the tropics. They provide some information on the vertical structure; however, they are not vertically resolved. The second method applies the EOF analysis on each altitude level separately and the resulting indices contain information on the horizontal variability at each densely available altitude level. They capture more variability than the indices from the first method and present a mixture of all variability modes contributing at the respective altitude level, including the QBO and ENSO. Compared to commonly used variability indices from QBO winds or ENSO sea surface temperature, these new indices cover the vertical details of the atmospheric variability. Using them as proxies for temperature variability is also of advantage because there is no further need to account for response time lags. Atmospheric variability indices as novel products from RO are expected to be of great benefit for studies on atmospheric dynamics and variability, for climate trend analysis, as well as for climate model evaluation.

1 Introduction

Two modes of interannual variability dominate the natural temperature variability in the tropical region: the Quasi-Biennial Oscillation (QBO) and El Niño–Southern Oscillation (ENSO).

In the stratosphere, equatorial zonal wind regimes of easterlies (winds blowing from east) and westerlies propagate downwards at about 1 km month^{-1}. As soon as the westerlies fade out, the easterlies take over, and vice versa. The winds at 10 hPa are out of phase with the winds at 70 hPa. The period of the regimes varies considerably, with an average period of a little more than two years (approximately 28 months), which gives the phenomenon its name, QBO.

There are several characteristics describing the QBO. The two wind regimes do not change much along the longitudinal axis (Naujokat, 1986), but exhibit a distinct latitudinal structure. Strongest QBO-related winds are latitudinally symmetric, centered over the Equator (Dunkerton and Delisi, 1985), and decrease considerably off the Equator with a meridional half width of less than 15°. The winds are strongest in the middle to lower tropical stratosphere, although the QBO is detectable from the tropopause up to 50 km (Wallace et al., 1993). The atmospheric temperature anomalies are proportional to the vertical gradient of the zonal winds (Randel et al., 1999; Baldwin et al., 2001), which makes it possible to investigate the QBO through temperature anomalies. For a review on QBO features, see Baldwin et al. (2001).

Recently there was a disruption in the stable QBO cycle, where the westerlies took a shortcut upwards, and prevented the easterlies from propagating downwards to the tropo-

sphere, as it usually does (Newman et al., 2016; Osprey et al., 2016; Dunkerton, 2017); this also resulted in an anomalous behavior response of trace gases (Tweedy et al., 2017). The causes of this unprecedented disruption in the QBO observational record are still under investigation. Possible explanations include dynamical forcing from waves (Osprey et al., 2016; Coy et al., 2017) or coupling with the 2015/2016 warm ENSO event (Newman et al., 2016; Dunkerton, 2016).

In the troposphere, the dominant interannual variability mode is the ENSO. Its irregular variability originates from a Pacific Ocean–atmosphere interaction and manifests itself as a warm phase (El Niño) and a cold phase (La Niña). Its effects can be detected globally, from the surface to the lower stratosphere (Free and Seidel, 2009; Randel et al., 2009). Commonly the characteristics are described with an ENSO sea surface temperature (SST) index, which can be derived from anomalies in SST in the Niño 3.4 region (5° N to 5° S and 170 to 120° W) of the tropical Pacific. El Niño or La Niña periods are defined to occur if a certain mean SST anomaly threshold is exceeded over several months, e.g., if 5-month running means of SST anomalies in the Niño 3.4 region exceed $+0.4$ or -0.4 °C, respectively, for a minimum of 6 months as defined by Trenberth (1997).

During an El Niño event, there is also warming in the tropical troposphere, with a maximum around 8 km and a cooling in the lowermost stratosphere above the tropopause (Reid, 1994; Randel et al., 2009). There is also an eddy signal, i.e., deviations from the zonal mean (Fernández et al., 2004), with a maximum around 11 km (Scherllin-Pirscher et al., 2012).

The interaction between ENSO and QBO has been investigated in many studies (Taguchi, 2010; Schirber, 2015; Christiansen et al., 2016; Geller et al., 2016; Hansen et al., 2016). For further information on the relationship between ENSO, QBO, and teleconnections, see, e.g., the introduction in Dunkerton (2017) and references within.

Several indices have been introduced to describe the variability of QBO and ENSO in order to better characterize the events, to determine their strength, and to describe their evolution. Trenberth and Stepaniak (2001) suggested the need for a second index, in addition to the Niño 3.4 SST index, to describe the different characteristics of the ENSO-originated variability. Wolter and Timlin (2011) established an extended multivariate ENSO index that is more complete and flexible compared to single-variable ENSO indices.

The QBO is often characterized by wind measurements. Naujokat (1986) established the well-known set of time series from winds at different pressure levels above Singapore. Most frequently used QBO indices are wind anomalies at 30 and 50 hPa pressure levels. Wallace et al. (1993) introduced the representation of the equatorial stratospheric QBO in derived parameters using the leading empirical orthogonal functions of the vertical wind structure.

In this work, we describe a method for creating atmospheric variability indices with high vertical resolution, using global navigation satellite system (GNSS) radio occultation (RO) satellite data.

GNSS RO is a limb sounding technique, where the GNSS signals traverse the Earth's atmosphere and are picked up by receivers at low-Earth orbit (LEO) satellites as they rise or set behind the Earth's horizon relative to the GNSS satellite. On their way to the LEO satellites, the signals are refracted by the atmosphere as they propagate through it. The resulting excess phase path is measured at the LEO satellite. With the help of inversion methods and prior knowledge about the atmosphere, the refraction can be inverted into several atmospheric parameters, one of which is temperature (Melbourne et al., 1994; Kursinski et al., 1997).

The GNSS RO measurements provide vertical atmospheric temperature profiles with a high vertical resolution that are well distributed globally. There have been several RO missions throughout the years, providing data continuously since 2001, and it has been shown that there is no need for calibration between the missions (Schreiner et al., 2007; Foelsche et al., 2011). The greatest-quality GNSS RO measurements are those for the upper troposphere and lower stratosphere region, at about 8 to 35 km in the tropics (Scherllin-Pirscher et al., 2011).

Randel et al. (2003) and Schmidt et al. (2004) showed clear evidence that GNSS RO temperature anomalies can be used for detecting the QBO. This was achieved with only a few years of data in the early phase of the GNSS RO period.

Scherllin-Pirscher et al. (2012) were able to demonstrate that the structure of the ENSO can be detected with GNSS RO temperature anomalies using only 4 years of data. They confirmed the spatial structure of the ENSO during the El Niño events, and showed that the zonal atmospheric response lags SST anomalies by 3 months.

Several other studies have investigated the atmospheric QBO and ENSO signal using GNSS RO data in analyses of climate trends (e.g., Lackner et al., 2011; Steiner et al., 2011) and climate variability (e.g., Randel and Wu, 2015). Teng et al. (2013) and Sun et al. (2014) investigated signatures and characteristics of the ENSO, while Gao et al. (2017) used RO measurements to create an index that describes the strength of the atmospheric response from ENSO and QBO.

We extend this previous work, and use the whole available GNSS RO time series from 2001 to 2017 to create atmospheric variability proxies. We describe the GNSS RO data set in Sect. 2 and explain the applied methods in Sect. 3. Results are presented and discussed in Sect. 4. A summary and conclusions are given in Sect. 5.

2 Data

We use data from the Wegener Center (WEGC) OPSv5.6 RO multi-satellite record (Schwärz et al., 2016; Angerer et al., 2017) to produce monthly mean gridded temperature fields with a horizontal resolution of $5° \times 5°$ in longitude and lat-

itude and 200 m vertical resolution. The time period ranges from September 2001 to February 2017.

The WEGC OPSv5.6 data record is a data set with global coverage, but in order to obtain mainly the QBO and ENSO signals, we restrict it to 2 to 35 km altitude and 30° S to 30° N. At each time step and each altitude level, grid points with missing data are filled horizontally using bilinear interpolation. Our input data set used in this study therefore has $N_\phi = 12$ grid points in latitude (ϕ), $N_\theta = 72$ grid points in longitude (θ), $N_z = 166$ grid points in altitude (z), and $N_t = 186$ grid points in time (t).

We create monthly mean temperature anomalies to deseasonalize the data. This is done by calculating the average temperature for each month for the reference time period January 2002 to December 2015. These monthly averages are then subtracted from the original temperature data at the corresponding months. To reduce the month-to-month variations, the monthly mean anomalies are then smoothed with a 1-2-1 running mean filter over time. Finally, time series at each grid point are detrended to avoid any trend in indices of atmospheric variability.

Figure 1 shows zonal mean RO temperature anomalies from 20° S to 20° N for illustration purposes. We clearly see the downward-propagating QBO pattern in the lower stratosphere, known from previous work, where negative temperature anomalies correspond to westerlies and positive temperature anomalies correspond to easterlies. The highest variability is attributed to the transition from westerlies to easterlies (Scherllin-Pirscher et al., 2017). In the troposphere, we see the variability from the ENSO phenomenon. Several El Niño events are revealed during the GNSS RO time period: during winter 2002–2003, 2004–2005, 2006–2007, and 2009–2010, and during a major event in 2014–2016 that lasted longer than normal (Blunden and Arndt, 2016). The La Niña events 2007–2008, 2010–2011, and 2011–2012 can also be seen.

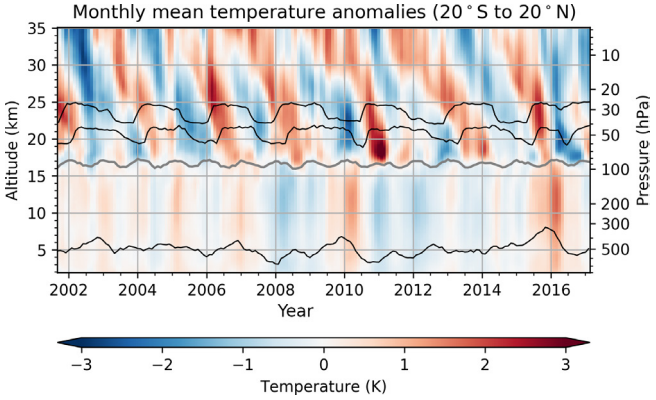


Figure 1. Zonal monthly mean temperature anomalies from GNSS RO from 20° S to 20° N and 2 to 35 km. The gray line near 17 km indicates the tropopause height for the monthly mean temperature profiles, calculated according to the WMO definition of the lapse rate tropopause (WMO, 1957). For illustration, the thinner black lines indicate the conventional QBO30 and QBO50 wind indices (depicted at 30 and 50 hPa, respectively, with arbitrary scale), and the Niño 3.4 SST index (depicted at an arbitrary altitude level with arbitrary scale). The corresponding mean RO pressure levels are indicated on the right y axis. Besides visualizing the features of the QBO in the RO record, they can also be made audible through sonification. Interested readers can hear QBO sounds at https://sysson.iem.at/sounds.html.

3 Methods

We create the atmospheric variability indices using two different methods, in the following denoted M1 and M2. They are described in more detail in Sect. 3.1 and 3.2, respectively.

In both methods the main variability patterns in the input data set are obtained using an empirical orthogonal function (EOF) analysis. The EOF analysis can extract major modes from spatial and temporal variations. The EOF analysis decomposes the data set into a reduced set of space components and time components (denoted as indices). The first few components will describe most of the variability in descending order of importance (Jolliffe, 2002; Hannachi et al., 2007).

Many names have been used to describe the output from the EOF analysis (see discussion in Wilks, 2006; Hannachi et al., 2007). In the following, we use the terminology from Hannachi et al. (2007), where "EOF" denotes the spatial component, while "PC" denotes the time component. When needed, we use the whole word "principal component" to describe the collection of EOFs, PCs, and eigenvalues.

3.1 EOF analysis on the whole temperature field (M1)

In the first method, denoted M1, a space–time matrix is constructed from the monthly mean temperature anomalies described in Sect. 2. The space dimensions are all reshaped into a single axis, (ϕ, θ, z), to reduce the number of dimensions. The resulting matrix is therefore two-dimensional, in space (s) and time (t) only, $\mathbf{X}(s_{(\phi,\theta,z)}, t)$, represented by Eq. (1), where each row, $\boldsymbol{x}_{s_p}(t)$, corresponds to a time series at a specific location (in ϕ, θ, z).

$$\mathbf{X} = \begin{pmatrix} x_{(s_1,t_1)} & x_{(s_1,t_2)} & \cdots & x_{(s_1,t_q)} & \cdots & x_{(s_1,t_Q)} \\ x_{(s_2,t_1)} & x_{(s_2,t_2)} & \cdots & x_{(s_2,t_q)} & \cdots & x_{(s_2,t_Q)} \\ \vdots & \vdots & \ddots & \vdots & \ddots & \vdots \\ x_{(s_p,t_1)} & x_{(s_p,t_2)} & \cdots & x_{(s_p,t_q)} & \cdots & x_{(s_p,t_Q)} \\ \vdots & \vdots & \ddots & \vdots & \ddots & \vdots \\ x_{(s_P,t_1)} & x_{(s_P,t_2)} & \cdots & x_{(s_P,t_q)} & \cdots & x_{(s_P,t_Q)} \end{pmatrix} \quad (1)$$

Each spatial location is denoted with index s_p, where $p = 1 \ldots P$. Each point in time is denoted t_q, where $q = 1 \ldots Q$. For M1, using the input data set described in Sect. 2, the spatial direction has the length, $P = N_\phi \cdot N_\theta \cdot N_z = 143\,424$. The time dimension has the length $Q = 186$.

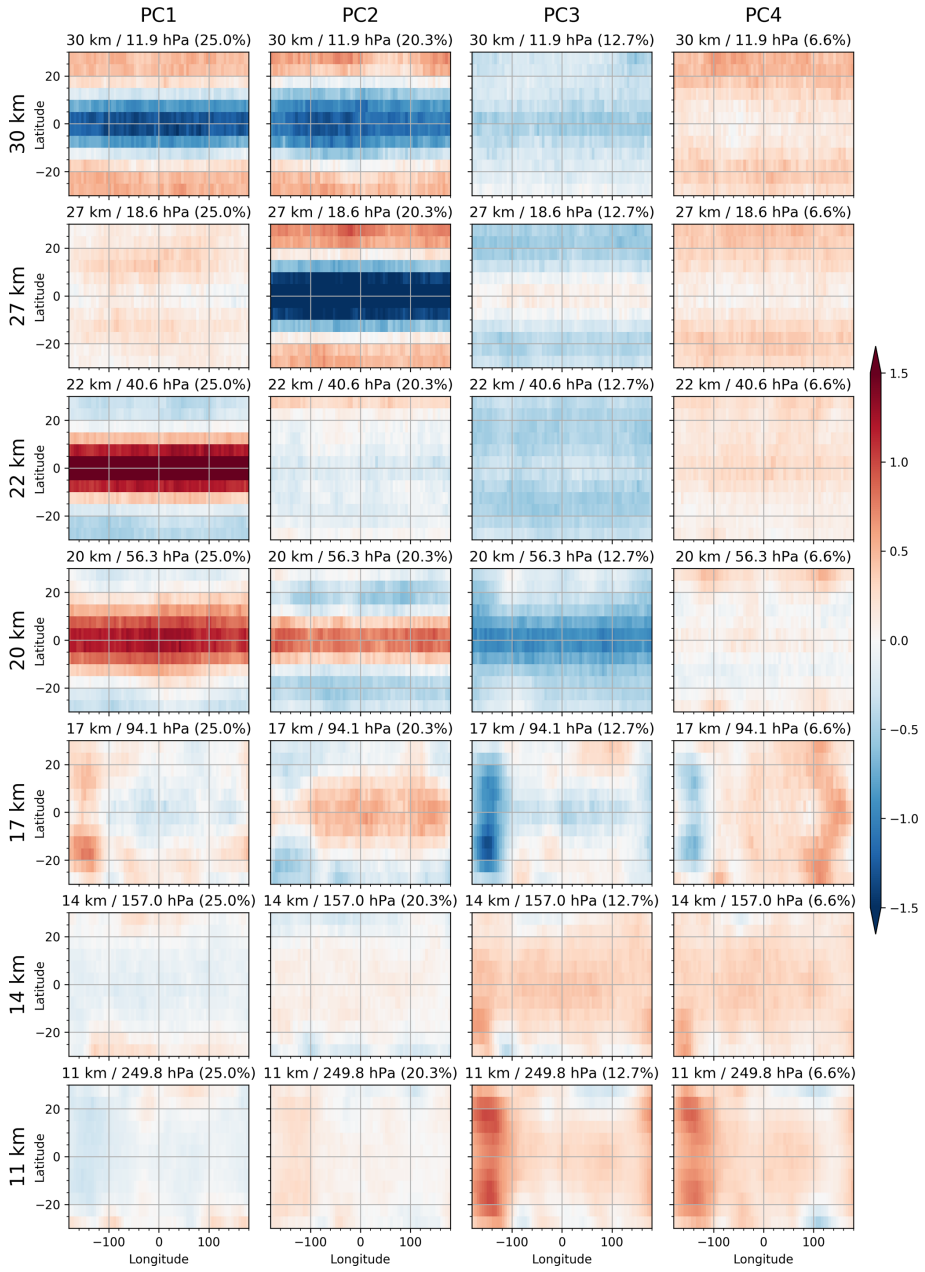


Figure 2. The first four EOFs computed from M1, EOF1 to EOF4 (left to right), are shown for selected altitudes at 30, 27, 22, 20, 17, 14, and 11 km (top to bottom). The explained variance ratio is given in parentheses in the titles.

The EOF analysis is then based on the decomposition of the covariance matrix (Jolliffe, 2002).

The output of the EOF analysis is a set of EOFs (eigenvectors, in this context called $\mathrm{EOF_{out}}$), PCs ($\mathrm{PC_{out}}$), and their corresponding eigenvalues (λ). The eigenvalues are used to scale the corresponding output EOFs and PCs, according to both Eqs. (2) and (3):

$$\mathrm{EOF}_i = \mathrm{EOF}_{\mathrm{out},i}\sqrt{\boldsymbol{\lambda}_i}, \tag{2}$$

$$\mathrm{PC}_i = \frac{\mathrm{PC}_{\mathrm{out},i}}{\sqrt{\boldsymbol{\lambda}_i}}. \tag{3}$$

The first few PCs from Eq. (3) can now be used as proxies for the temporal variability. We call these *indices* in the following. Calculating cross correlations between these indices and conventional indices can hint at their physical interpretation.

3.2 EOF analysis at each altitude level (M2)

To take advantage of the high vertical resolution from RO we also calculate atmospheric variability indices at all altitude

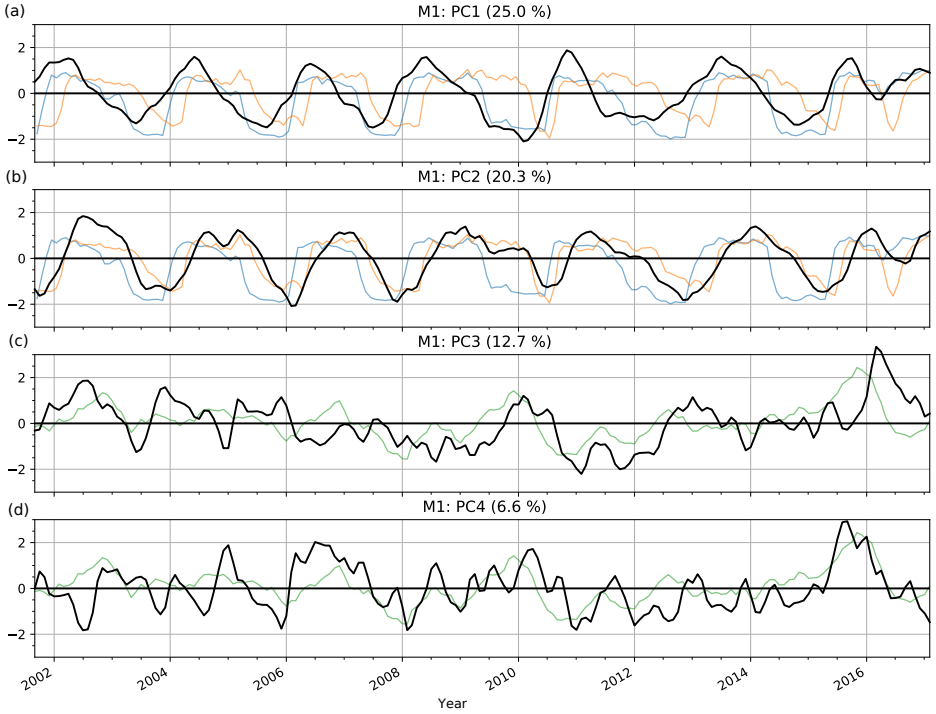


Figure 3. The first four PCs computed from M1, PC1 to PC4 (top to bottom, in black). The explained variance ratio is given in parentheses in the titles. For illustration, the conventional QBO wind indices at 30 hPa (blue) and 50 hPa (orange, **a, b**), and the Niño 3.4 SST index (green, **c, d**), are indicated on arbitrary scales.

levels. In this second method, denoted M2, we do the EOF analysis for each altitude level separately, instead of using the whole field. No altitude-dependent variability is therefore included in the analysis.

To keep the altitude dimension separated from the other dimensions, a space–time matrix is constructed for each altitude level. Therefore, only the latitude and longitude dimensions are reshaped into one axis, leaving us with the space (ϕ, θ) and time (t) dimensions, leading to matrix $\mathbf{X}_z(s_{(\phi,\theta)}, t)$, which is represented by Eq. (1) at each altitude level, z.

The spatial direction has the length $P = N_\phi \cdot N_\theta = 864$ and the time dimension has the length $Q = 186$. The subsequent steps in the EOF analysis are the same as for M1.

4 Results

The values within each independent EOF show *where* the principal component contributes to the variability, and how much each point is influenced by its corresponding PC. In the same way, each independent PC shows *when* the corresponding variability changes.

In this section, we compare the EOFs and PCs constructed from M1 and M2 with characteristics of known atmospheric variability patterns.

4.1 M1 results

The first four resulting EOFs from M1 are presented in Fig. 2. Each EOF has been reshaped to the same space dimensions as the input data set, (ϕ, θ, z). Each column shows an EOF at selected altitude levels.

The spatial structure of the variability from the first and the second EOFs (EOF1 and EOF2, respectively) show characteristics of the QBO. From the stratosphere to the tropopause at around 17 km, the two EOFs do not show distinct longitudinal variability. The patterns are strongest over the Equator with a symmetrical latitudinal dependency, and the tropical band varies with opposite sign to the extratropical latitude band. These features can also be observed with the QBO winds (Naujokat, 1986; Wallace et al., 1993; Baldwin et al., 2001).

EOF1 and EOF2 both exhibit only a weak signal at and below the tropopause, where the pattern also looks different than above.

This longitudinal variability pattern around the tropopause is also visible in the third and the fourth EOFs (EOF3 and EOF4, respectively). The longitudinal pattern disappears at around 14 km where zonal variability dominates. However, it reappears with opposite sign further below at 11 km. This vertical behavior resembles quite well the results of Scherllin-Pirscher et al. (2012), who found a strong eddy

ENSO signal with a node at approximately 14 km. This eddy ENSO signal is superimposed with a zonal-mean ENSO signal, which has its node at 17 km.

EOF3 and EOF4 also contribute to the variability above the tropopause. Although the pattern is weak, it is interesting that the signals resemble the patterns of EOF1 and EOF2 above the tropopause.

Figure 3 shows the PC time series (indices) corresponding to the EOFs. The first two PCs, PC1 and PC2, have a regular, sine-wave-like pattern, where one follows the other, with a period of about 2 years. PC3 and PC4 change more rapidly and less regularly.

The output patterns from M1 are not sensitive to the vertical resolution of the input field. We pruned the data to only include every 1 km before performing M1. The EOF pattern looked very much the same as described above, except the PCs showed a coarser pattern, and the explained variances were a little smaller (not shown).

4.2 M2 results

Figure 4 shows the set of the two first EOFs from M2 at the same selected altitude levels as in Fig. 2. Remember that while the EOFs of M1 are functions of latitude, longitude, and altitude, there are separate EOFs for each altitude level resulting from M2. All of these separate EOFs are functions of latitude and longitude only.

The recomposed time series of the two first PCs from M2 are presented in Fig. 5. As for the EOFs, each PC represents an altitude level.

The first set of PCs (Fig. 5a) reveals a separation into a part above the tropopause and into a part below the tropopause. Above the tropopause, the first PCs show the typical downward-propagating QBO pattern. Below the tropopause, the PCs are associated with ENSO events.

The separation at the tropopause can also be seen in Fig. 4. Above the tropopause, the EOF1s from M2 resemble the patterns of either EOF1 or EOF2 of M1 shown in Fig. 2. Above the tropopause the EOF2s also show the same horizontal QBO pattern, though weaker. Below the tropopause, the horizontal patterns of EOF1s and EOF2s resemble EOF3 and EOF4 of M1, which we identified as ENSO-related variability.

The separation is not as clear in the second set of PCs (Fig. 5b). It shows part of the residual variability that is not described by the first set of PCs. These also show downward-propagating patterns, but different from the first set of PCs, and less regular in the stratosphere.

Keep in mind that both the EOFs and the PCs have been scaled by their corresponding eigenvalues (see Sect. 3.1), at each altitude level separately. The corresponding eigenvalues are proportional to the explained variance ratios (see Fig. 6). The magnitude of each time series therefore does not necessarily describe its importance, nor are the contributions from each EOF or PC directly comparable. The actual contribu-

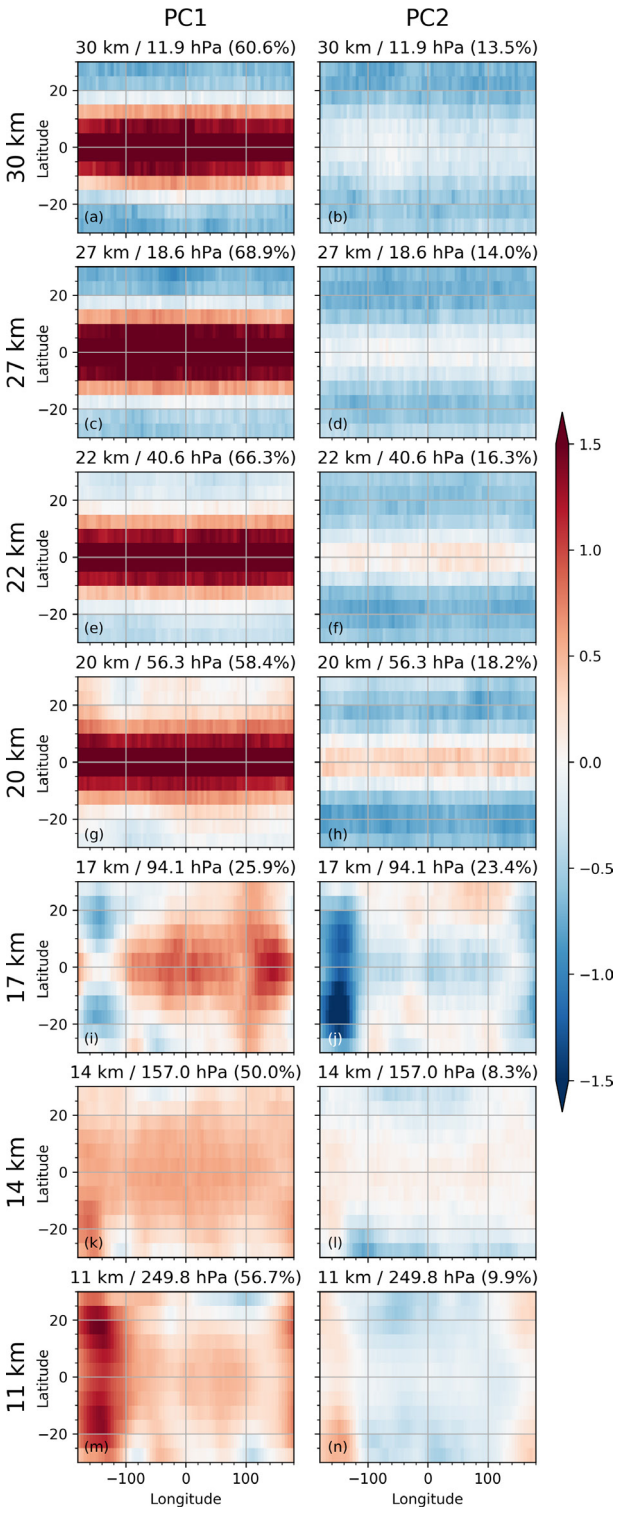


Figure 4. The first EOFs (left) and second EOFs (right) computed from M2, shown for selected altitude levels from the stratosphere (top) to the troposphere (bottom). The same altitude levels as for Fig. 2 are shown. The explained variance ratio is shown in parentheses in the titles.

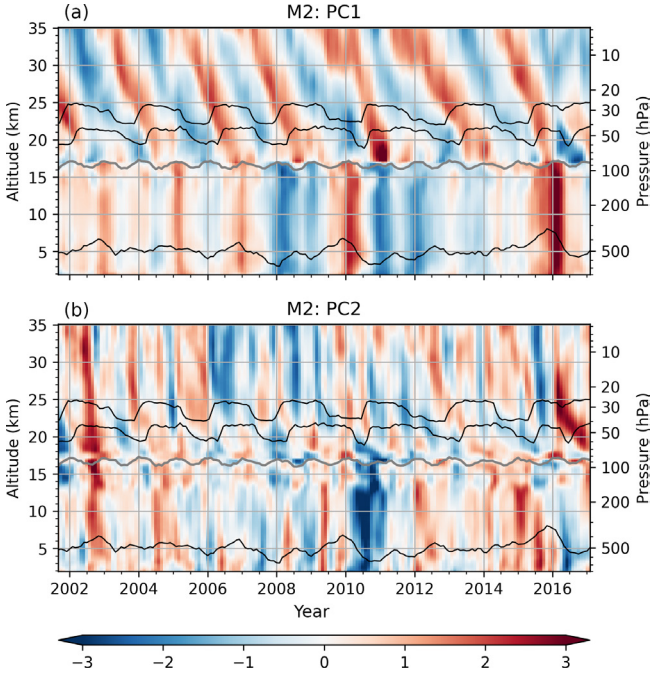


Figure 5. PC1s **(a)** and PC2s **(b)** from M2 for each altitude level. The gray line indicates the height of the tropopause. For illustration, the thinner black lines indicate the conventional QBO30 and QBO50 wind indices (depicted at 30 and 50 hPa, respectively, with arbitrary scale), and the Niño 3.4 SST index (depicted at an arbitrary altitude level with arbitrary scale).

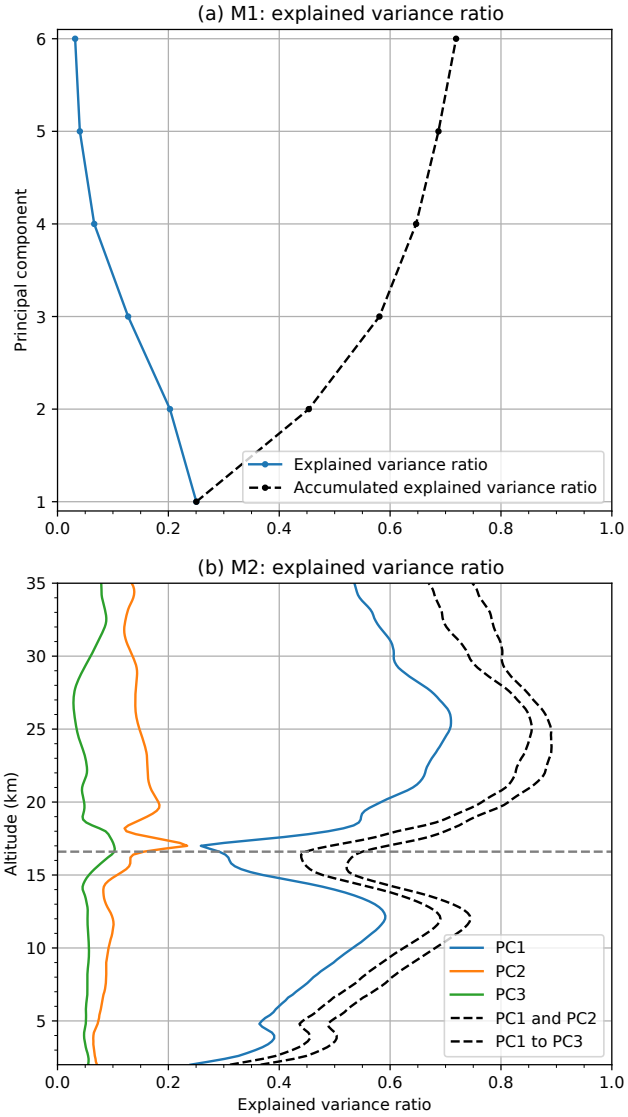


Figure 6. Explained variance ratio for M1 **(a)** shown as classical scree plot. Explained variance ratio for M2 **(b)** shown as a function of altitude for PC1s to PC3s. The dashed lines show the cumulative sums of the explained variance ratios. The horizontal dashed gray line indicates the mean tropopause height.

tions can be seen in the reconstruction. See Sect. 4.3 and 4.6 for further details.

Also keep in mind that dominating atmospheric variability at different altitude levels can be caused by different physical mechanisms. The physical context of the first principal components may therefore also change with altitude because the calculations are performed separately at each altitude level for M2. Finally, if independent variability modes explain a similar amount of variance, their corresponding PC time series can switch between two PCs (e.g., between PC1 and PC2) at neighboring altitude levels.

4.3 Explained variance

Figure 6 shows how much each principal component contributes to the total variability. For M1, the first four principal components sum up to 65 % of the total variability (Fig. 6a). Remaining natural variability, associated with, e.g., volcanic eruptions or sudden stratospheric warming events (Randel and Wu, 2015), as well as some remaining sampling issues from GPS RO, account for 35 % of the variance.

For M2 (Fig. 6b) the explained variance ratios are shown for the first three principal components at each altitude. Most of the variability is explained by the first principal component, except near the tropopause region, where the first and the second principal components almost touch. In the stratosphere and the troposphere the EOF analysis captures the dominant variability of the QBO and the ENSO, respectively. The tropopause region is less uniform. It is a transition layer between the troposphere and the stratosphere, and more complex in nature (Gettelman and Forster, 2002), possibly explaining the lower explained variance ratio.

4.4 Correlations to conventional indices

In order to show that our deduced indices capture the QBO and ENSO we compute the correlations between the derived PCs and conventional SST and QBO indices.

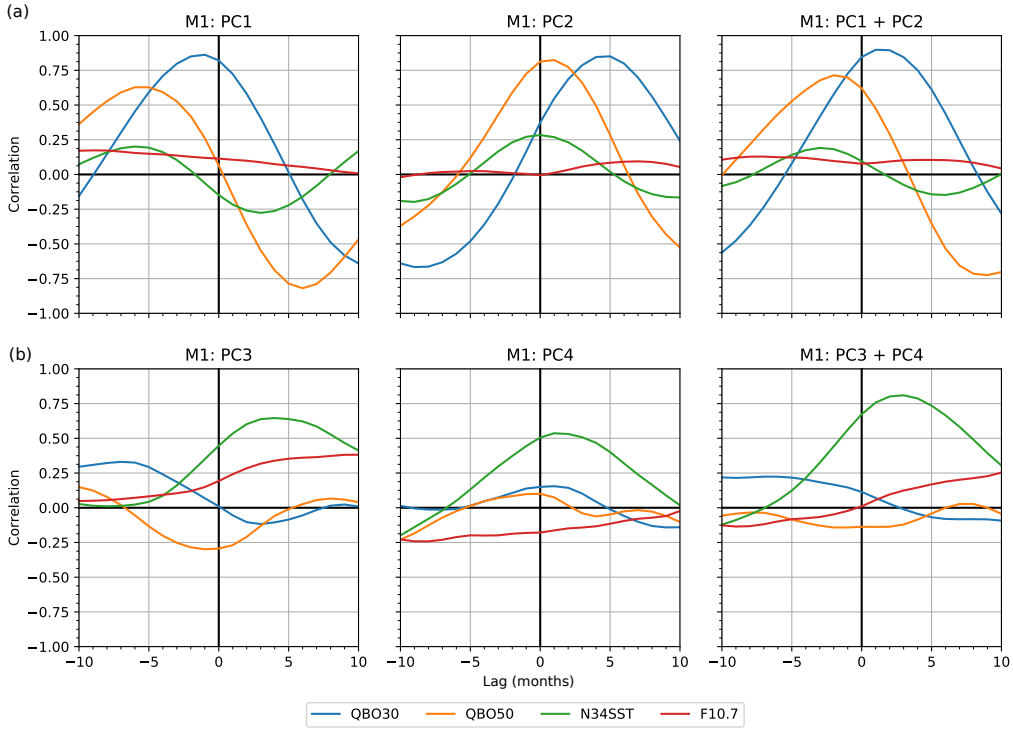


Figure 7. Correlations between derived indices (PCs) from M1 with conventional variability indices, QBO30, QBO50, Niño 3.4 SST (N34SST), and F10.7 solar flux (F10.7), shown for ±10-month time lag. Upper panels show PC1, PC2, and PC1 added element-wise to PC2. Lower panels show PC3, PC4, and PC3 added element-wise to PC4.

Figure 7 shows the correlations between the PCs from M1 with the conventional QBO wind indices at 30 hPa (QBO30) and 50 hPa (QBO50), and the Niño 3.4 SST index. The correlations to the solar F10.7 cm flux index are also shown. We do not smooth nor detrend these indices.

We find that both QBO30 and QBO50 correlate well with PC1 alone (top left), and with PC2 alone (top middle), and with PC1 superimposed on (added element-wise to) PC2 (top right). They correlate less well with PC3 alone (bottom left), with PC4 (bottom middle), and with PC3 superimposed with PC4. The time lags are results of the PCs representing the variability at altitudes specified by the EOF patterns. They therefore introduce a time lag when correlating to wind fields at only two pressure levels.

PC3 and PC4 (bottom left and middle) correlate best with the Niño 3.4 SST index. When PC3 is superimposed with PC4 (bottom right), the total correlation to the Niño 3.4 SST index is improved with a time lag of 3 months, known from, e.g., Scherllin-Pirscher et al. (2012).

Figure 8 shows how the PC1s and PC2s derived from M2 correlate with the QBO30 index, QBO50 index, Niño 3.4 SST index, and solar F10.7 cm flux index at each altitude level.

The recomposed set of PC1s correlates well with the QBO30 and QBO50 above the tropopause, and Niño 3.4 SST index below the tropopause, depending on altitude and time lag. There is also some correlation between the set of PC2s to the same indices, although weaker, and without a clear pattern. Both the PC1s and the PC2s have only weak correlation to the solar F10.7 cm flux index.

4.5 Phase space diagram

In order to show the relationship between the PCs we present phase space diagrams in Fig. 9, following Fig. 5 in Wallace et al. (1993). Figure 9a shows the relationship between the two first PCs from QBO winds as a trajectory in phase space (PC1 versus PC2). For comparison purposes M1 has been performed using QBO winds at seven pressure levels from 70 to 10 hPa after Wallace et al. (1993). We use the same time period as available in the WEGC OPSv5.6 data set from September 2001 to February 2017. Before plotting we apply a 5-month running mean on the PCs. The resulting phase plot confirms the long history of circularity and nearly constant amplitude of the QBO. The QBO disruption that was observed during 2016 can be clearly seen from the winds (Dunkerton, 2016), and it seems to have found its way back to normal by the end of 2016 (Tweedy et al., 2017).

Figure 9b shows the same as the left plot, but is constructed from RO temperature anomalies, using PC1 and PC2 from M1 (cf. Fig. 3a, b). It has a similar structure and features as the phase plot from the winds. The QBO disruption is also

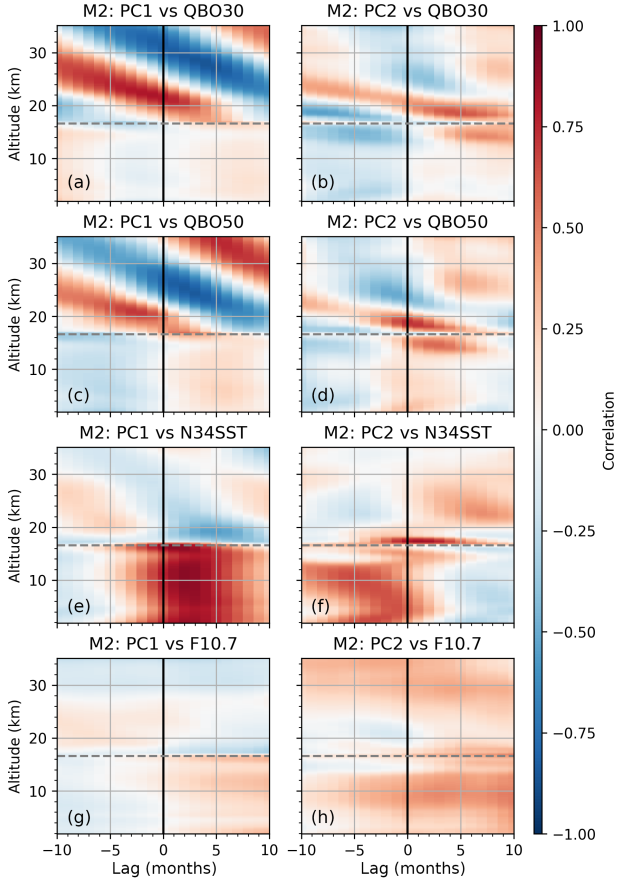


Figure 8. Correlations between the first PCs (left) and the second PCs (right) derived from M2 with known variability indices QBO30, QBO50, Niño 3.4 SST (N34SST), F10.7 solar flux (F10.7; top to bottom), shown for each altitude level. The horizontal dashed line indicates the mean tropopause height.

revealed here, but it has not ended yet in temperature space. This further supports our findings that the main variability obtained by EOF1 and EOF2 from M1 is the QBO.

In Fig. 9c, a phase plot of two PC1s from M2, at two selected altitude levels in the QBO region, is shown. It does not show exactly the same circularity as seen in the two other plots, which could be a result of not covering the same altitude range as in the two other plots. Nevertheless the recent disruption of the QBO can also be seen here.

4.6 Reconstruction of temperature fields

The actual contribution from each principal component to the resulting temperature anomaly field can be seen when reconstructing the principal components. We do this by multiplying the EOF with its corresponding PC (Wilks, 2006). Any scaling by the eigenvalues, or sign flipping, is then canceled out.

Figure 10a shows the reconstructed field using a combination of the first and the second principal components from M1 (see Fig. 3a, b). In contrast to Fig. 5, where the PC1s and the PC2s are plotted in EOF space, we map the PC1s and the PC2s back into anomaly space. We see that most of the contribution to the resulting temperature anomaly field is in the QBO region, which is also expected from the pattern of the EOFs. We clearly see the downward-propagating pattern of the QBO, and only a weak signal in the troposphere. It should be noted that the downward-propagating pattern cannot be created by one principal component alone.

Figure 10c shows the reconstruction using a combination of the third and the fourth principal component from M1 (see Fig. 3c, d). In the troposphere region we see a positive contribution to the temperature field during the El Niño events. The signal right above the tropopause might also be associated with El Niño (e.g., Scherllin-Pirscher et al., 2012), but further up the features seem to be related to the QBO.

Figure 10e shows the reconstruction using all four principal components from M1. This time series well resembles the input temperature anomalies shown in Fig. 1.

For M2, temperature anomaly time series have been reconstructed separately at each altitude level from the resulting principal components. Figure 10b shows the reconstruction using the first principal component of each altitude level (see Fig. 3). The result reveals that much of the features in Fig. 1 are already obtained.

Similarly, Fig. 10d shows the reconstructions from the second principal component for each altitude layer from M2. It describes some features of the variability in the QBO region that are not caught by the first principal component. The stratospheric variability pattern seen in the first principal component (Fig. 10b) seems to find its continuation in the second principal component (Fig. 10d) just above the tropopause.

This suggests that the first principal components are attributable to different variabilities with altitude, and that the attribution can swap between the principal components. It is therefore important to include both indices to catch the variability, especially around the tropopause.

Figure 10f shows a combination of the first and second principal components, and as for M1, it also resembles the input temperature field (cf. Fig. 1) very well.

The resulting difference between the input field (Fig. 1) minus the respective reconstructed fields (Fig. 10, bottom) from M1 and M2 are presented in Fig. 11. This therefore describes the residue of the two methods. For M1 there is still some residue temperature variability left, especially in the tropopause region, but also in the other regions. For M2, however, there is only some minor residue left, especially in the tropopause region. M2 shows a much smaller residue than M1 which indicates that the altitude-resolved indices better capture the atmospheric variability.

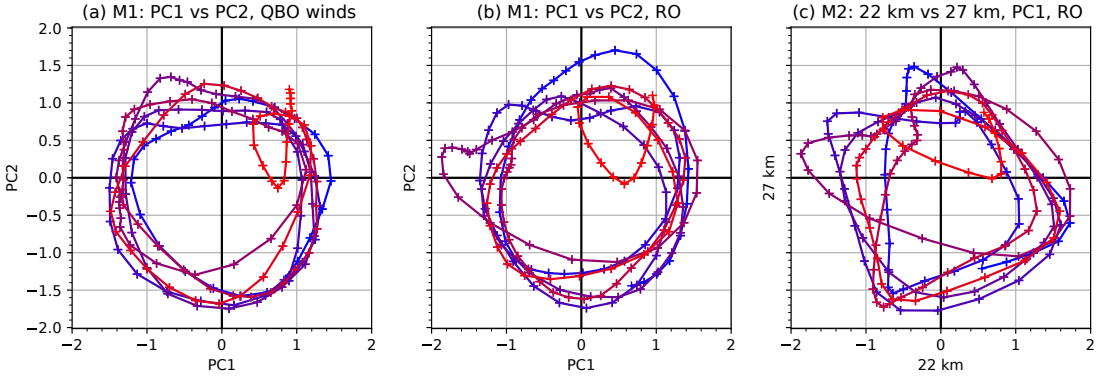


Figure 9. Phase space diagrams are shown for the RO time period September 2001 to February 2017. Blue color denotes the beginning of the period and turns into red towards the end of the period. PC1 vs. PC2 from M1 based on QBO winds **(a)**. PC1 vs. PC2 from M1 based on RO temperature **(b)**, and PC1 at 22 km vs. PC1 at 27 km from M2 based on RO temperature **(c)**. For comparison, the PC1 at 27 km **(c)** is multiplied by −1 to match the orientation of the other panels.

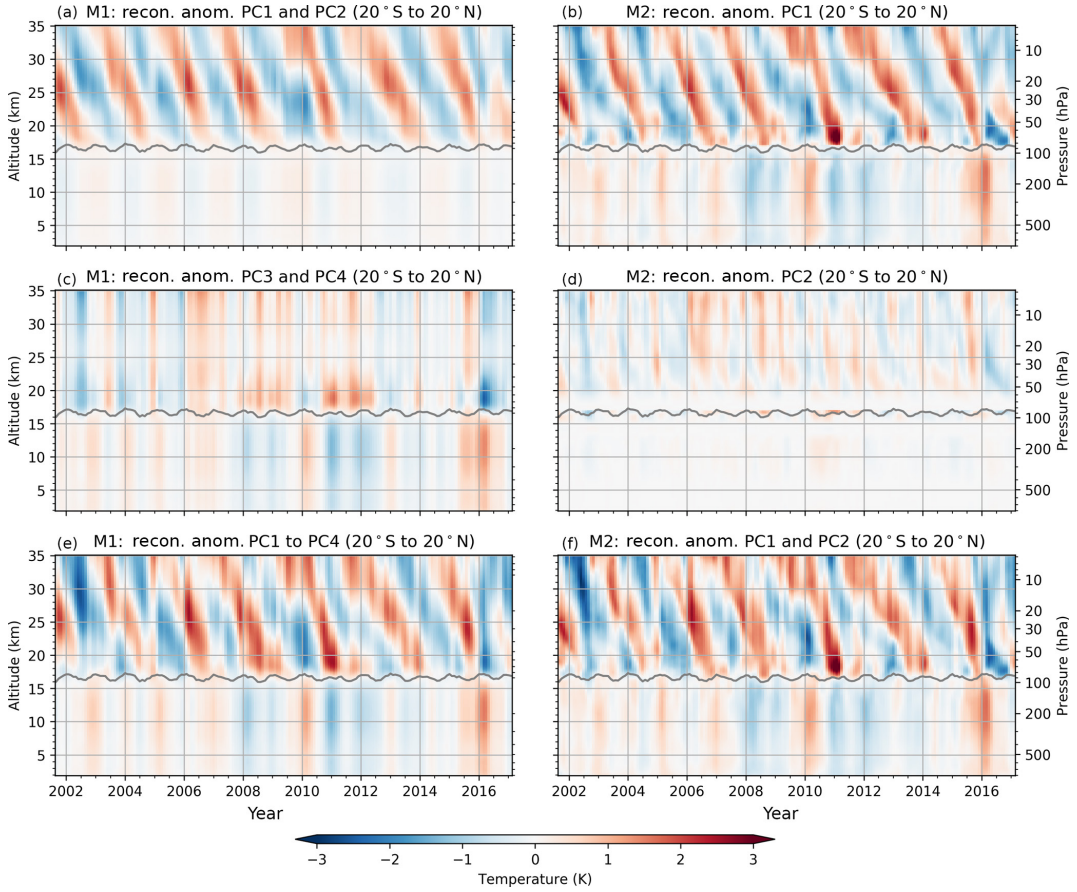


Figure 10. Reconstructed temperature fields from the first principal components which explain maximum variability. For M1 (left panels), reconstructed field using PC1 and PC2 **(a)**, PC3 and PC4 **(c)**, and using PC1 to PC4 **(e)**. For M2 (right panels), reconstructed field using the altitude-resolved PC1s **(b)**, using the altitude-resolved PC2s **(d)**, and using PC1s plus PC2s **(f)**. The gray line near 17 km indicates the tropopause height.

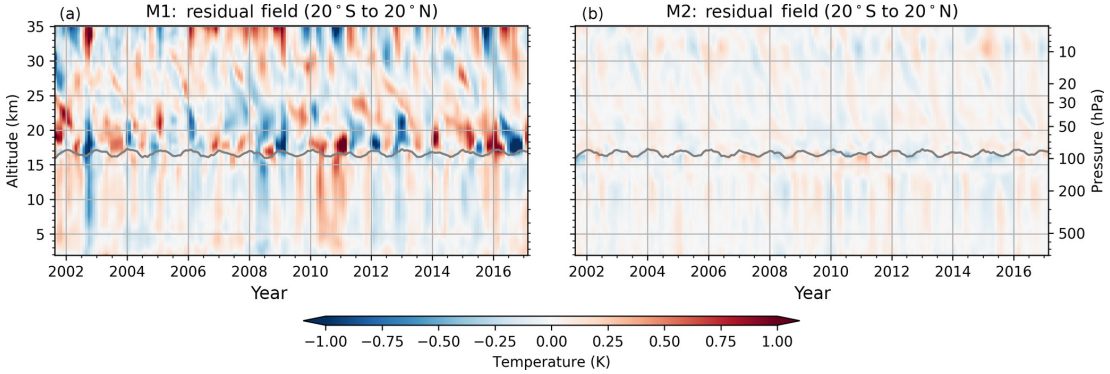


Figure 11. The residual temperature field for M1 **(a)** and M2 **(b)** showing the difference of the input minus the reconstructed fields, using PC1 to PC4 for M1 and PC1s to PC2s for M2. The gray line near 17 km indicates the tropopause height.

5 Summary and conclusions

Atmospheric variability in the tropical region is often described by indices of the two main modes of variability, the QBO and the ENSO. These indices, commonly derived from stratospheric winds and SST anomalies, do not cover the vertical details. Since they are not derived from atmospheric temperatures, we need to account for a potentially unknown time lag when using them as proxies for atmospheric temperature variability at a specific altitude level.

In this work we introduce new atmospheric variability proxies constructed directly from GNSS RO temperature measurements of high vertical resolution, using standard EOF analysis. We prepared the GNSS RO temperature field for the EOF analysis in two ways.

In the first method, the input field for the EOF analysis includes the whole vertical and horizontal information from 2 to 35 km and from 30° S to 30° N. The resulting principal components show the well-known characteristics of QBO and ENSO, seen in previous work, and the first four PC time series describe the major part of the variability as a whole. However, they still contain an unknown time lag from the actual variability at different altitude levels, and do not show a strong dependency on the vertical resolution of the input field.

In the second method, we take advantage of the high vertical resolution of GNSS RO and perform an EOF analysis at each altitude level separately to obtain the main horizontal variability at each altitude level. These variability indices, which hold the high vertical resolution from RO, also show the well-known characteristics of the QBO and ENSO, and as they are obtained directly where the variability occurs, they (by their nature) contain no time lag from the actual variability. However, the resulting PCs cannot be attributed to only one or the other mode of variability, but instead present a mixture of all variability modes found at the respective altitude level.

We find that the altitude-resolved indices of the second method capture more of the atmospheric variability than the indices derived from the first method.

Testing the correlation with known classical sea surface temperature indices and wind indices confirmed that the indices derived from RO temperature represent atmospheric variability indices. Further confidence in the results is given as we find the characteristic relationship over time between PC time series from RO temperature consistent with those in winds.

We thus demonstrated that information on the most significant modes of natural climate variability in the tropical troposphere and stratosphere can be derived from GNSS RO temperature observations. Taking advantage of these results, we derive novel products from RO with high added value. Atmospheric variability indices with high vertical resolution can deliver improved information on the natural variability patterns such as QBO and ENSO. Good representation and better knowledge of atmospheric and climate variability is of importance for studies of atmospheric physics and dynamics, the analysis of climate variability and trends, and for the evaluation of climate models.

Data availability. The WEGC OPSv5.6 RO data set is available on request from the authors and will be made publicly available soon. The QBO wind indices were downloaded from http://www.geo.fu-berlin.de/en/met/ag/strat/produkte/qbo (Freie Universität Berlin, 2018). The Niño 3.4 SST index was downloaded from http://www.cpc.ncep.noaa.gov/data/indices/sstoi.indices (NOAA, 2018a). The solar F10.7 cm flux indices were downloaded from ftp://ftp.ngdc.noaa.gov/STP/space-weather/solar-data/solar-features/solar-radio/noontime-flux/penticton/penticton_observed/listings/listing_drao_noontime-flux-observed_monthly.txt (NOAA, 2018b).

Appendix A: Sign flipping

The depicted PCs carry an arbitrary sign that comes from the nature of the EOF analysis method. As we, for M2, perform an EOF analysis independently at each altitude level, the sign of the EOFs and PCs can make sudden changes between the altitude layers. It does not affect the reconstruction, as the sign is simply canceled out in a reconstruction, but it results in a hashed image when visualized as in Fig. 5. To avoid this, we take the following steps.

First, the top altitude layer is chosen as the first basis for the PC direction, $\mathrm{PC_b}$ (b denotes "basis"). Then, the following steps are performed, for each altitude layer, in descending order:

1. If $\mathrm{PC_b}$ correlates negatively to the PC at the altitude level i (PC_i), the signs of both EOF_i and the PC_i are flipped (multiplied by -1).
2. The $\mathrm{PC_b}$ is updated with the resulting PC_i, according to

$$\mathrm{PC_b} \leftarrow (1-\alpha)\cdot \mathrm{PC_b} + \alpha \cdot \mathrm{PC}_i, \tag{A1}$$

   and used as basis for the next altitude layer.

The factor α can take values between 0 and 1. Using $\alpha = 0.3$ seemed to work well for us. $\mathrm{PC_b}$ is updated no matter if sign flipping takes place or not. It is therefore only used for holding information about the previous PCs, with fading influence with distance to the previous altitude layer.

This is done for all principal components in the resulting data set. It creates much smoother results, without sudden sign changes.

Author contributions. HW performed the computational implementation and the analysis, created the figures, and wrote the first draft of the paper. All authors contributed to the study design. FL provided advice on the analysis design and made major contributions to the text. BSP provided advice on the method and interpretation of the results, and contributed to the text. AKS provided guidance and advice on all aspects of the study, and contributed to the text.

Competing interests. The authors declare that they have no conflict of interest.

Special issue statement. This article is part of the special issue "Observing Atmosphere and Climate with Occultation Techniques – Results from the OPAC-IROWG 2016 Workshop". It is a result of the International Workshop on Occultations for Probing Atmosphere and Climate, Leibnitz, Austria, 8–14 September 2016.

Acknowledgements. We are grateful to UCAR/CDAAC (Boulder, CO, USA) for provision of RO phase and orbit data and to ECMWF (Reading, UK) for providing access to analysis and forecast data. The WEGC processing team members (Marc Schwärz, Barbara Angerer) are thanked for providing the OPSv5.6 RO data. We acknowledge FU Berlin (Berlin, DE) for providing QBO wind indices, CPC for ENSO indices, and NOAA for the solar flux indices. We thank Harald Rieder (WEGC, AT), Thomas Mendlik (WEGC, AT), and Alejandro de la Torre (Universidad Austral, AR) for their help and fruitful discussion. This work was funded by the Austrian Science Fund (FWF) under research grants P27724-NBL (VERTICLIM) and W1256-G15 (Doctoral Programme Climate Change – Uncertainties, Thresholds and Coping Strategies).

Edited by: Anthony Mannucci
Reviewed by: five anonymous referees

References

Angerer, B., Ladstädter, F., Scherllin-Pirscher, B., Schwärz, M., Steiner, A. K., Foelsche, U., and Kirchengast, G.: Quality aspects of the Wegener Center multi-satellite GPS radio occultation record OPSv5.6, Atmos. Meas. Tech., 10, 4845–4863, https://doi.org/10.5194/amt-10-4845-2017, 2017.

Baldwin, M. P., Gray, L. J., Dunkerton, T. J., Hamilton, K., Haynes, P. H., Randel, W. J., Holton, J. R., Alexander, M. J., Hirota, I., Horinouchi, T., Jones, D. B. A., Kinnersley, J. S., Marquardt, C., Sato, K., and Takahashi, M.: The Quasi-Biennial Oscillation, Rev. Geophys., 39, 179–229, 2001.

Blunden, J. and Arndt, D. S.: State of the Climate in 2015, B. Am. Meteorol. Soc., 97, Si–S275, https://doi.org/10.1175/2016BAMSStateoftheClimate.1, 2016.

Christiansen, B., Yang, S., and Madsen, M. S.: Do strong warm ENSO events control the phase of the stratospheric QBO?, Geophys. Res. Lett., 43, 10489–10495, https://doi.org/10.1002/2016GL070751, 2016.

Coy, L., Newman, P. A., Pawson, S., and Lait, L. R.: Dynamics of the Disrupted 2015/16 Quasi-Biennial Oscillation, J. Climate, 30, 5661–5674, https://doi.org/10.1175/JCLI-D-16-0663.1, 2017.

Dunkerton, T. J.: The quasi-biennial oscillation of 2015–2016: Hiccup or death spiral?, Geophys. Res. Lett., 43, 10547–10552, https://doi.org/10.1002/2016GL070921, 2016.

Dunkerton, T. J.: Nearly identical cycles of the quasi-biennial oscillation in the equatorial lower stratosphere, J. Geophys. Res.-Atmos, 122, 8467–8493, https://doi.org/10.1002/2017JD026542, 2017.

Dunkerton, T. J. and Delisi, D. P.: Climatology of the Equatorial Lower Stratosphere, J. Atmos. Sci., 42, 376–396, https://doi.org/10.1175/1520-0469(1985)042<0376:COTELS>2.0.CO;2, 1985.

Fernández, N. C., García, R. R., Herrera, R. G., Puyol, D. G., Presa, L. G., Martín, E. H., and Rodríguez, P. R.: Analysis of the ENSO signal in tropospheric and stratospheric temperatures observed by MSU, 1979–2000, J. Climate, 17, 3934–3946, 2004.

Foelsche, U., Scherllin-Pirscher, B., Ladstädter, F., Steiner, A. K., and Kirchengast, G.: Refractivity and temperature climate records from multiple radio occultation satellites consistent within 0.05 %, Atmos. Meas. Tech., 4, 2007–2018, https://doi.org/10.5194/amt-4-2007-2011, 2011.

Free, M. and Seidel, D. J.: Observed El Niño–Southern Oscillation temperature signal in the stratosphere, J. Geophys. Res., 114, D23108, https://doi.org/10.1029/2009JD012420, 2009.

Freie Universität Berlin: The Quasi-Biennial-Oscillation (QBO) Data Serie, available at: http://www.geo.fu-berlin.de/en/met/ag/strat/produkte/qbo, last access: 22 February 2018.

Gao, P., Xu, X., and Zhang, X.: On the relationship between the QBO/ENSO and atmospheric temperature using COSMIC radio occultation data, J. Atmos. Sol.-Terr. Phy., 156, 103–110, https://doi.org/10.1016/j.jastp.2017.03.008, 2017.

Geller, M. A., Zhou, T., and Yuan, W.: The QBO, gravity waves forced by tropical convection, and ENSO, J. Geophys. Res.-Atmos, 121, 8886–8895, https://doi.org/10.1002/2015JD024125, 2016.

Gettelman, A. and Forster, P.: A climatology of the tropical tropopause layer, J. Meteor. Soc. Jpn., 80, 911–924, 2002.

Hannachi, A., Jolliffe, I. T., and Stephenson, D. B.: Empirical orthogonal functions and related techniques in atmospheric science: A review, Int. J. Climatol., 27, 1119–1152, https://doi.org/10.1002/joc.1499, 2007.

Hansen, F., Matthes, K., and Wahl, S.: Tropospheric QBO–ENSO interactions and differences between the Atlantic and Pacific, J. Climate, 29, 1353–1368, https://doi.org/10.1175/JCLI-D-15-0164.1, 2016.

Jolliffe, I. T.: Principal Component Analysis, Springer Series in Statistics, Springer, https://doi.org/10.1007/b98835, 2002.

Kursinski, E. R., Hajj, G. A., Schofield, J. T., Linfield, R. P., and Hardy, K. R.: Observing Earth's atmosphere with radio occultation measurements using the Global Positioning System, J. Geophys. Res., 102, 23429–23465, https://doi.org/10.1029/97JD01569, 1997.

Lackner, B. C., Steiner, A. K., Kirchengast, G., and Hegerl, G. C.: Atmospheric Climate Change Detection by Radio Occultation Data Using a Fingerprinting Method, J. Climate, 24, 5275–5291, https://doi.org/10.1175/2011JCLI3966.1, 2011.

Melbourne, W. G., Davis, E. S., Duncan, C. B., Hajj, G. A., Hardy, K. R., Kursinski, E. R., Meehan, T. K., Young, L. E., and Yunck, T. P.: The application of spaceborne GPS to atmospheric limb sounding and global change monitoring, Tech. rep., Jet Propulsion Laboratory, NASA, Pasadena, California, USA, 1994.

National Oceanic and Atmospheric Administration (NOAA): Monthly OISST.v2, available at: http://www.cpc.ncep.noaa.gov/data/indices/sstoi.indices, last access: 22 February 2018a.

National Oceanic and Atmospheric Administration (NOAA): Solar Flux (10.7cm), available at: ftp://ftp.ngdc.noaa.gov/STP/space-weather/solar-data/solar-features/solar-radio/noontime-flux/penticton/penticton_observed/listings/listing_drao_noontime-flux-observed_monthly.txt, last access: 22 February 2018b.

Naujokat, B.: An Update of the Observed Quasi-Biennial Oscillation of the Stratospheric Winds over the Tropics, J. Atmos. Sci., 43, 1873–1877, https://doi.org/10.1175/1520-0469(1986)043<1873:AUOTOQ>2.0.CO;2, 1986.

Newman, P. A., Coy, L., Pawson, S., and Lait, L. R.: The anomalous change in the QBO in 2015–2016, Geophys. Res. Lett., 43, 8791–8797, https://doi.org/10.1002/2016GL070373, 2016.

Osprey, S. M., Butchart, N., Knight, J. R., Scaife, A. A., Hamilton, K., Anstey, J. A., Schenzinger, V., and Zhang, C.: An unexpected disruption of the atmospheric quasi-biennial oscillation, Science, 353, 1424–1427, https://doi.org/10.1126/science.aah4156, 2016.

Randel, W. J. and Wu, F.: Variability of Zonal Mean Tropical Temperatures Derived from a Decade of GPS Radio Occultation Data, J. Atmos. Sci., 72, 1261–1275, https://doi.org/10.1175/JAS-D-14-0216.1, 2015.

Randel, W. J., Wu, F., Swinbank, R., Nash, J., and O'Neill, A.: Global QBO circulation derived from UKMO stratospheric analyses, J. Atmos. Sci., 56, 457–474, 1999.

Randel, W. J., Wu, F., and Rivera Ríos, W.: Thermal variability of the tropical tropopause region derived from GPS/MET observations, J. Geophys. Res., 108, 4024, https://doi.org/10.1029/2002JD002595, 2003.

Randel, W. J., Garcia, R. R., Calvo, N., and Marsh, D.: ENSO influence on zonal mean temperature and ozone in the tropical lower stratosphere, J. Geophys. Res., 36, L15822, https://doi.org/10.1029/2009GL039343, 2009.

Reid, G. C.: Seasonal and interannual temperature variations in the tropical stratosphere, J. Geophys. Res., 99, 18923–18932, 1994.

Scherllin-Pirscher, B., Steiner, A. K., Kirchengast, G., Kuo, Y.-H., and Foelsche, U.: Empirical analysis and modeling of errors of atmospheric profiles from GPS radio occultation, Atmos. Meas. Tech., 4, 1875–1890, https://doi.org/10.5194/amt-4-1875-2011, 2011.

Scherllin-Pirscher, B., Deser, C., Ho, S.-P., Chou, C., Randel, W., and Kuo, Y.-H.: The vertical and spatial structure of ENSO in the upper troposphere and lower stratosphere from GPS radio occultation measurements, Geophys. Res. Lett., 39, L20801, https://doi.org/10.1029/2012GL053071, 2012.

Scherllin-Pirscher, B., Randel, W. J., and Kim, J.: Tropical temperature variability and Kelvin-wave activity in the UTLS from GPS RO measurements, Atmos. Chem. Phys., 17, 793–806, https://doi.org/10.5194/acp-17-793-2017, 2017.

Schirber, S.: Influence of ENSO on the QBO: Results from an ensemble of idealized simulations, J. Geophys. Res.-Atmos, 120, 1109–1122, https://doi.org/10.1002/2014JD022460, 2015.

Schmidt, T., Wickert, J., Beyerle, G., and Reigber, C.: Tropical tropopause parameters derived from GPS radio occultation measurements with CHAMP, J. Geophys. Res., 109, D13105, https://doi.org/10.1029/2004JD004566, 2004.

Schreiner, W., Rocken, C., Sokolovskiy, S., Syndergaard, S., and Hunt, D.: Estimates of the precision of GPS radio occultations from the COSMIC/FORMOSAT-3 mission, Geophys. Res. Lett., 34, L04808, https://doi.org/10.1029/2006GL027557, 2007.

Schwärz, M., Kirchengast, G., Scherllin-Pirscher, B., Schwarz, J., Ladstädter, F., and Angerer, B.: Multi-Mission Validation by Satellite Radio Occultation – Extension Project, Final report for ESA/ESRIN No. 01/2016, WEGC, University of Graz, Graz, Austria, 2016.

Steiner, A. K., Lackner, B. C., Ladstädter, F., Scherllin-Pirscher, B., Foelsche, U., and Kirchengast, G.: GPS radio occultation for climate monitoring and change detection, Radio Sci., 46, RS0D24, https://doi.org/10.1029/2010RS004614, 2011.

Sun, Y.-Y., Liu, J.-Y., Tsai, H.-F., Lin, C.-H., and Kuo, Y.-H.: The Equatorial El Niño-Southern Oscillation Signatures Observed by FORMOSAT-3/COSMIC from July 2006 to January 2012, Terr. Atmos. Ocean. Sci., 25, 545–558, https://doi.org/10.3319/TAO.2014.02.13.01(A), 2014.

Taguchi, M.: Observed connection of the stratospheric quasi-biennial oscillation with El Niño-Southern Oscillation in radiosonde data, J. Geophys. Res., 115, D18120, https://doi.org/10.1029/2010JD014325, 2010.

Teng, W.-H., Huang, C.-Y., Ho, S.-P., Kuo, Y.-H., and Zhou, X.-J.: Characteristics of global precipitable water in ENSO events revealed by COSMIC measurements, J. Geophys. Res., 118, 8411–8425, https://doi.org/10.1002/jgrd.50371, 2013.

Trenberth, K. E.: The Definition of El Niño, B. Am. Meteorol. Soc., 78, 2771–2777, https://doi.org/10.1175/1520-0477(1997)078<2771:TDOENO>2.0.CO;2, 1997.

Trenberth, K. E. and Stepaniak, D. P.: Indices of El Niño Evolution, J. Climate, 14, 1697–1701, https://doi.org/10.1175/1520-0442(2001)014<1697:LIOENO>2.0.CO;2, 2001.

Tweedy, O. V., Kramarova, N. A., Strahan, S. E., Newman, P. A., Coy, L., Randel, W. J., Park, M., Waugh, D. W., and Frith, S. M.: Response of trace gases to the disrupted 2015–2016 quasi-biennial oscillation, Atmos. Chem. Phys., 17, 6813–6823, https://doi.org/10.5194/acp-17-6813-2017, 2017.

Wallace, J. M., Panetta, R. L., and Estberg, J.: Representation of the equatorial stratospheric Quasi-Biennial Oscillation in EOF phase space, J. Atmos. Sci., 50, 1751–1762, 1993.

Wilks, D. S.: Statistical methods in the atmospheric sciences, Elsevier, 2 edn., Burlington, MA, USA, San Diego, California, USA, London, UK, 2006.

WMO: Meteorology – A three dimensional science: Second session of the commission for aerology, WMO Bull. 4, World Meteorological Organization (WMO), Geneva, Switzerland, 1957.

Wolter, K. and Timlin, M. S.: El Niño/Southern Oscillation behaviour since 1871 as diagnosed in an extended multivariate ENSO index (MEI.ext), Int. J. Climatol., 31, 1074–1087, https://doi.org/10.1002/joc.2336, 2011.

Geophysical Research Letters

RESEARCH LETTER
10.1029/2019GL084396

Quantifying Stratospheric Temperature Signals and Climate Imprints From Post-2000 Volcanic Eruptions

Matthias Stocker[1], Florian Ladstädter[1,2], Hallgeir Wilhelmsen[1,3], and Andrea K. Steiner[1,2]

[1]Wegener Center for Climate and Global Change (WEGC), University of Graz, Graz, Austria, [2]Institute for Geophysics, Astrophysics, and Meteorology/Institute of Physics, University of Graz, Graz, Austria, [3]FWF-DK Climate Change, University of Graz, Graz, Austria

Key Points:
- The imprints of minor volcanic eruptions on stratospheric temperature are precisely quantified
- Vertically high resolved aerosol and temperature observations facilitate the accurate detection of volcanic signals in space and time
- Minor volcanic eruptions clearly affect the short-term temperature trend in the lower stratosphere

Correspondence to:
A. K. Steiner,
andi.steiner@uni-graz.at

Citation:
Stocker, M., Ladstädter, F., Wilhelmsen, H., & Steiner, A. K. (2019). Quantifying stratospheric temperature signals and climate imprints from post-2000 volcanic eruptions. *Geophysical Research Letters*, *46*, 12,486–12,494. https://doi.org/10.1029/2019GL084396

Received 2 JUL 2019
Accepted 20 SEP 2019
Accepted article online 29 OCT 2019
Published online 3 NOV 2019

Abstract Small volcanic eruptions and their effects have recently come into research focus. While large eruptions are known to strongly affect stratospheric temperature, the impacts of smaller eruptions are hard to quantify because their signals are masked by natural variability. Here, we quantify the temperature signals from small volcanic eruptions between 2002 and 2016 using new vertically resolved aerosol data and precise temperature observations from radio occultation. We find characteristic space-time signals that can be associated with specific eruptions. In the lower stratosphere, robust warming signals are observed, while in the midstratosphere also cooling signals of some eruptions appear. We find that the volcanic contribution to the temperature trend is up to 20%, depending on latitude and altitude. We conclude that detailed knowledge of the vertical structure of volcanic temperature impacts is crucial for comprehensive trend analysis in order to separate natural from anthropogenic temperature changes.

1. Introduction

Volcanic eruptions can substantially influence the climate system (Kremser et al., 2016; Robock, 2000, 2015; Timmreck, 2012) through the emission of trace gases, volcanic ash, and aerosol forming substances, such as sulfur dioxide (SO_2). In the troposphere, the volcanic ash causes local weather changes (Robock, 2015). In the stratosphere, sulfate aerosols formed by volcanic SO_2 emissions absorb and backscatter solar and terrestrial radiation and also enhance chemical reactions, for example, ozone depletion. This affects surface temperature as well as stratospheric temperature and dynamics (Aquila et al., 2013; Robock, 2000, 2015). Those sulfate aerosols are among the main components of the stratospheric aerosol layer (Kremser et al., 2016). Besides aerosol chemistry and physics, their distribution in the stratosphere is governed by large-scale processes such as the Brewer Dobson Circulation and the Quasi-biennial Oscillation (QBO; Baldwin et al., 2001; Kremser et al., 2016; Timmreck, 2012; Trepte & Hitchman, 1992).

The last major volcanic eruptions were those of El Chichón in 1982 and Pinatubo in 1991. They emitted tremendous amounts of SO_2, and their consequences have been addressed in several studies (e.g., Aquila et al., 2013; Free & Lanzante, 2009; Randel et al., 2009). They were found to strongly affect tropospheric as well as stratospheric temperature and chemistry. Following the Pinatubo eruption, a global tropospheric cooling of up to 0.6 K (Parker et al., 1996) and a stratospheric warming of 2 K (Robock, 2000) were detected. In the lowermost stratosphere, model studies showed an even stronger warming due to the Pinatubo aerosols compared to the observed one (Free & Lanzante, 2009). Moreover, Aquila et al. (2013) modeled a drop of approximately 8% in tropical stratospheric ozone concentration directly after the eruption.

Recently, a series of smaller volcanic eruptions that started in 2002 has been of research interest. Those eruptions most likely led to a steady increase in stratospheric aerosol optical depth (AOD) during the last decade (Mehta et al., 2015; Vernier et al., 2011). Also, a contribution of those eruptions to the 21st century warming hiatus has been discussed (Santer et al., 2015).

Not all of the small eruptions reach the stratosphere, depending on the latitude of the eruption, the explosivity, the emitted SO_2 mass (Robock, 2000), and also the emission height. Only aerosols reaching the stratosphere have a sufficient lifespan (up to 3 years) to affect climate (Robock, 2015).

©2019. The Authors.
This is an open access article under the terms of the Creative Commons Attribution License, which permits use, distribution and reproduction in any medium, provided the original work is properly cited.

Table 1
Eruptions Between 2002 and 2017 With a Minimum VEI of 4

Name	Start date	VEI	SO_2 mass (kt)	SO_2 altitude (max.; km)	Latitude	Country
Ruang (Ru)	09-25-2002	4	80	22	2.3°N	Indonesia
Reventador	11-03-2002	4	84	17	0.077°S	Ecuador
Manam (Ma)	10-24-2004	4	152[a]	24[a]	4.08°S	Papua New Guinea
Rabaul (Tavurvur; Ta)	08-11-2006	4	300	18	4.271°S	Papua New Guinea
Chaitén	05-02-2008	4	14	17	42.833°S	Chile
Okmok	07-12-2008	4	150	15	53.43°N	United States (Alaska)
Kasatochi (Ka)	08-07-2008	4	2,000	15	52.177°N	United States (Alaska)
Sarychev Peak (Sp)	06-11-2009	4	1,200	17	48.092°N	Russia
Eyjafjallajökull	03-20-2010	4	466	9	63.633°N	Iceland
Merapi (Me)	10-26-2010	4	300	17	7.54°S	Indonesia
Grímsvötn	05-21-2011	4	300	12	64.416°N	Iceland
Puyehue-Cordón Caulle	06-04-2011	5	200	14	40.59°S	Chile
Nabro (Na)	06-13-2011	4	3,650	18	13.37°N	Eritrea
Tolbachik	11-27-2012	4	200	10	55.832°N	Russia
Sinabung	09-15-2013	4	20	7	3.17°N	Indonesia
Kelut (Ke)	02-13-2014	4	200	19	7.93°S	Indonesia
Calbuco (Ca)	04-22-2015	4	400	20	41.33°S	Chile
Wolf	05-25-2015	4	200	7	0.02°N	Ecuador

Note. Eruptions reaching the stratosphere are in bold. Data are from the Global Volcanism Program (2013).
[a]Main emission event during the eruption.

The Volcanic Explosivity Index (VEI), which describes the magnitude of the eruption, is a first indication of whether the eruption can cause stratospheric temperature changes. For post-2000 volcanoes, eruptions that reached the stratosphere typically had a minimum VEI of 4 (Table 1). Yet, not all of the >VEI 4 eruptions reached the stratosphere. The Puyehue in 2011, for example, had a VEI of 5, but most of the emitted aerosols were not transported to altitudes above 14 km. Data for these indicators used here are taken from the Global Volcanism Program (2013) database, "Volcanoes of the World."

The impact of specific smaller eruptions on atmospheric temperature has been addressed by Wang et al. (2009), who investigated the Mount Chaitén eruption in 2008, and Okazaki and Heki (2012), who studied the Eyjafjallajökull eruption in 2010 and the Puyehue eruption in 2011. They found significant negative tropospheric temperature signals induced by those eruptions using novel radio occultation (RO) satellite data. Biondi et al. (2017) also employed RO data to observe the volcanic clouds of the Puyehue and the Nabro eruptions in 2011. For Puyehue they found tropospheric cooling signals, while for Nabro considerable stratospheric warming was detected. Mehta et al. (2015) examined eruptions between 2001 and 2010 using RO and found small but significant warming in the upper troposphere-lower stratosphere region for the Soufrière Hills and Tavurvur eruptions, which occurred in quick succession.

However, the accurate quantification of temperature signals of such small eruptions is challenging. The emitted SO_2 mass of these eruptions (Table 1) is up to three orders of magnitude smaller than that of, for example, Pinatubo (20 Mt), illustrating the difficulty. Previous studies relied on AOD data as a proxy for the identification of volcanically induced temperature signals. Yet the AOD does not account for a vertically resolved distribution of the volcanic aerosols, which are lofted within the "tropical pipe" (Flury et al., 2013; Kremser et al., 2016; Vernier et al., 2011).

In this study, we quantify the stratospheric volcanic temperature signals in space and time for post-2000 volcanoes. We use the potential of a newly available, vertically resolved aerosol data set in combination with precise temperature observations from RO. We focus on the tropical stratospheric region and accurately characterize natural atmospheric variability to investigate the imprint of volcanic signals on short-term temperature trends.

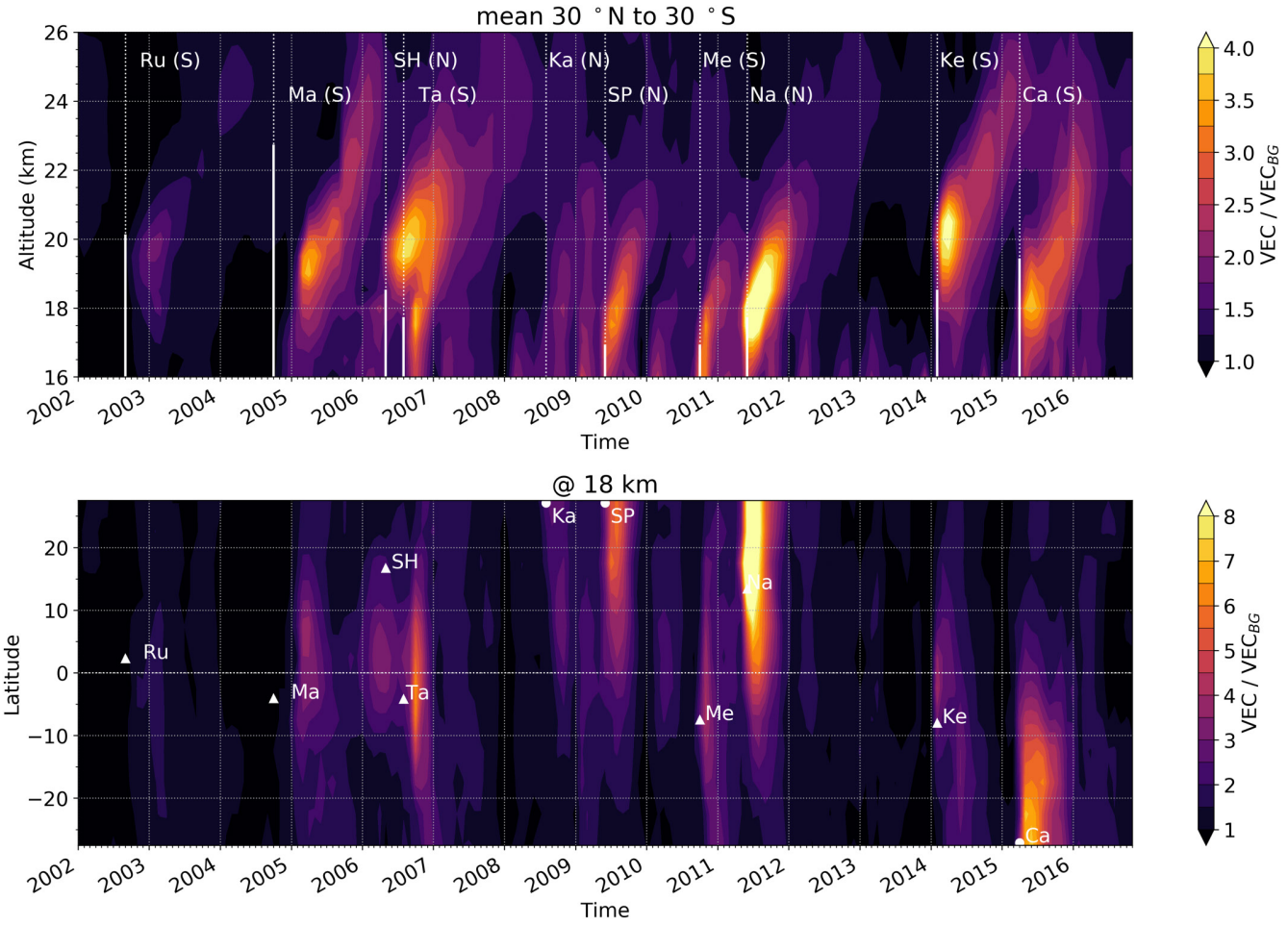


Figure 1. Altitude time pattern of the aerosol concentration divided by the background concentration (mean 30°N to 30°S; top) as well as the latitude time pattern of the aerosol concentration divided by the background concentration at 18 km (bottom). Vertical lines in the altitude time pattern mark the date of the eruptions as well as the maximum SO_2 altitude reported in the Global Volcanism Program (2013) database (solid lines). N and S in brackets indicate north and south of the equator. Triangles in the latitude time pattern mark the time of the eruption as well as the latitude of the eruption. Eruptions that occurred at latitudes not part of the plot range are marked with a semicircle. Note that, for example, for the Manam (Ma), the start date of the eruption does not coincide with the date of the main emission event.

2. Data and Method

2.1. Aerosol and Temperature Data

We use stratospheric aerosol data from the Global Space-based Stratospheric Aerosol Climatology (GloSSAC; Thomason, 2017; Thomason et al., 2018). GloSSAC is based on various aerosol measurement missions (e.g., SAGE, OSIRIS and CALIPSO; Thomason et al., 2018) and became available in 2017. We employ the vertically resolved Volume Extinction Coefficient measured at 525 nm with a latitudinal resolution of 5° zonal bands and a vertical resolution of 500 m. We inspect altitudes above 16 km as below this level, tropical data are not complete. Since the focus is on the tropical upper troposphere-lower stratosphere region, the upper limit is set to 26 km and we use data between 30°S to 30°N. From the original aerosol concentration data, we subtract the provided background aerosol concentration to create deseasonalized aerosol anomalies. The background aerosol concentration represents the state of the stratosphere without volcanic influence and is the monthly average concentration of the years 1999 to 2004, excluding 2002 since in this year the eruption of the Ruang occurred (Thomason, 2017; Thomason et al., 2018). The aerosol concentration divided by the background concentration is illustrated in Figure 1 and clearly shows a volcanic pattern of aerosols which are lofted into the middle stratosphere over time.

We take advantage of the vertically high resolved data from RO to analyze the spatiotemporal imprint of volcanoes on temperature. RO is a limb sounding technique exploiting signals from Global Navigation Satellite

Systems and provides long-term stability, global coverage, high accuracy, and vertical resolution in the upper troposphere and lower stratosphere (Steiner et al., 2011). We use temperature data from the Wegener Center OPSv5.6 RO multisatellite record (Angerer et al., 2017) on 5° latitudinal bands with a vertical gridding of 500 m to match the aerosol data. Temperature anomalies are created by subtracting the mean seasonal cycle for the investigated time series.

The GloSSAC data set is currently available from 1979 until the end of 2016. The RO temperature record is available from end of 2001 onward. Therefore, our investigated time period is from 2002 to 2016.

2.2. Regression Analysis

We estimate the volcanic signals in stratospheric temperature using multiple linear regression analysis. To account for autocorrelation in the monthly temperature data, we utilize a Generalized Least Squares with Autocorrelated AR(p) Errors model.

For the small eruptions in the study period, temperature signals are hard to detect because they are masked by natural variability. For large eruptions, volcanic signals can be estimated from the regression residuals when natural variability modes such as El Niño–Southern Oscillation (ENSO) or QBO are taken into account. Conventional variability indices, such as the Niño 3.4 SST or QBO winds at specific pressure levels, have been used in previous studies (Randel et al., 2009). This approach is less effective for smaller eruptions, because the residual variability is comparable to the volcanic signal amplitude (Mehta et al., 2015).

To separate the small post-2000 volcanic signals from other variability, we therefore take advantage of the temperature variability indices introduced by Wilhelmsen et al. (2018), which leave very small temperature residuals by construction. Compared to conventional indices these indices are of high vertical resolution and are created directly from the temperature anomalies derived from the RO measurements, using an empirical orthogonal function (EOF) analysis (Hannachi et al., 2007) on each separate altitude level in the data set. The leading principal components (PCs) are used as variability indices for the corresponding altitude level.

These variability indices do not only include QBO or ENSO, but all other main modes of variability such as aerosol-induced temperature changes, which leads to a nonzero correlation between the aerosol index and the variability indices. Additionally, the aerosol distribution itself is correlated to the QBO phase (Trepte & Hitchman, 1992). This means that a regression analysis, using only the regular aerosol anomalies as explanatory variable, would result in volcanic temperature signals that also include QBO related temperature variability. Therefore, when both the aerosol and the temperature variability indices are used in the multiple linear regression analysis, this results in collinearity between the regressors (see Santer et al., 2001).

To avoid collinearity, we remove in a first step the QBO signal from the aerosol index, and in a second step the resulting QBO-free aerosol signal from the variability indices.

In the first step, we subtract the QBO signal from the aerosol anomalies using linear regression. Hereby, we utilize QBO indices derived from the Singapore wind fields via EOF analysis. The reconstructed aerosol concentration for the leading two PCs derived from the wind field indicates a relatively weak QBO signal in the lower stratospheric aerosol concentration, which becomes stronger toward the middle stratosphere. Around 24 km, the impact of the QBO phases on the aerosol anomalies is reversed, changing from positive to negative, and vice versa. This agrees with the QBO-induced aerosol mixing ratio anomalies found by Hommel et al. (2015), who investigated the influence of the QBO on stratospheric aerosol distribution using an aerosol-coupled climate model.

After subtracting the QBO reconstructed aerosol concentration from the aerosol anomalies, primarily the volcanic pattern remains in the aerosol regressor, as verified by correlation analysis.

In the second step, we create the temperature variability indices from the residual temperature anomalies that remain after excluding the aerosol variability. This is done by subtracting a first estimate of the volcano-related temperature variability from the original temperature anomalies. The first estimate is computed using the Generalized Least Squares with Autocorrelated AR(p) Errors model on the temperature anomalies with the volcanic aerosols distribution, as the only explanatory variable. Since we removed the QBO signals from the aerosols distribution the first estimate of the volcanic temperature signals does not include QBO variability. Then we apply an EOF analysis on the residual temperature anomalies as explained above, and use the resulting variability indices in the following steps.

The final regression model then includes the QBO-free aerosol anomalies as well as the aerosol-free variability indices derived from the temperature anomalies after subtracting the estimated volcanic temperature signal. It can be written as

$$X^{\mathrm{Mod}}_{\phi,h,t} = \beta^{\mathrm{const}}_{\phi,h} + \beta^{\mathrm{linear}}_{\phi,h} t + \beta^{\mathrm{aer}}_{\phi,h} A^{\mathrm{anom}}_{\phi,h,t} + \beta^{\mathrm{PC1}}_{\phi,h} \mathrm{PC1}_{h,t} + \beta^{\mathrm{PC2}}_{\phi,h} \mathrm{PC2}_{h,t} + \beta^{\mathrm{PC3}}_{\phi,h} \mathrm{PC3}_{h,t} + \epsilon \quad (1)$$

where $X^{\mathrm{Mod}}_{\phi,h,t}$ represents the temperature anomalies as function of latitude (ϕ), altitude (h), and time (t), $A^{\mathrm{anom}}_{\phi,h,t}$ the QBO-free aerosol anomalies, $\mathrm{PC1}_{h,t}$, $\mathrm{PC2}_{h,t}$, and $\mathrm{PC3}_{h,t}$ the aerosol-free variability indices, and ϵ the residual.

3. Results and Discussion

Signals from several central tropical eruptions such as those of Manam, Soufrière Hills and Tavurvur, Merapi, Nabro, and Kelut are clearly visible in the aerosol data (Figure 1). Yet, also perturbations from higher-latitude eruptions such as those of Sarychev Peak and Calbuco can be identified. After the eruptions, the aerosols rise with roughly 4 km/year (cf. Vernier et al., 2011) in the lower to middle tropical stratosphere due to the vertical transport within the tropical pipe. However, a considerable amount of aerosols reaches higher altitudes only after particular eruptions such as that of Tavurvur and Soufrière Hills, respectively and also of Kelut and Calbuco. From Nabro, which emitted several times more aerosols than the other eruptions, seemingly only a small amount reached altitudes above 20 km.

This difference in the efficiency of the vertical transport of the aerosols not only depends on the injection height but also on the phase of the QBO during the time of the eruption, since the strength of the horizontal and vertical transport processes within the tropical pipe are connected to the phase of the QBO (Flury et al., 2013; Kremser et al., 2016). Flury et al. (2013) note that in the westerly shear zone of the QBO the transport out of the tropical pipe toward higher latitudes is enhanced while the vertical transport within the pipe is reduced. This means that during the QBO westerly shear volcanic aerosols are less likely transported to higher altitudes but are rather transported to the midlatitudes. Conversely, during the QBO easterly shear higher altitudes are more likely to be reached.

3.1. Volcanic Temperature Signals

In the reconstructed temperature for the volcanic aerosols (Figure 2), warming signals following the different eruptions are visible in the lowermost stratosphere up to around 20 km. Especially the Tavurvur (2006), Merapi (2010), Nabro (2011), and Calbuco (2015) eruptions show strong temperature impacts of about 0.5 K in the tropical mean. Weaker, but also visible signals of about 0.2 K can be associated with the Manam (2005), the Sarychev Peak (2009), and the Kelut (2014) eruptions. The warming at this altitude is most likely a result of absorption of solar and terrestrial long wave radiation by the volcanic sulfate aerosols (Robock, 2015, 2000; Mehta et al., 2015). The magnitude of the temperature increase following the Tavurvur and Soufrière Hills eruptions is consistent with the warming signal found by Mehta et al. (2015), who estimated the warming signal as the difference of averaged temperature residuals before and after the eruptions. Nabro emitted far more aerosols to this altitude, the subsequent warming, however, is only slightly stronger than for the Soufrière Hills and Tavurvur eruptions. This results from the Nabro aerosols being spread predominantly to the Northern hemisphere by the Asian monsoon (Bourassa et al., 2012). Thus, the main aerosol concentration is located at latitudes north of 10°N (Figure 1, bottom). For the Calbuco eruption, in contrast, a large amount of aerosols was transported toward the equator.

The altitude time cross section (Figure 2, top) further displays cooling signals of up to 0.3 K between 20 and 24 km. Since the signals follow the pattern of the volcanic aerosols as seen in Figure 1, we assume that they originate from the specific eruptions, which affected the aerosol concentration at altitudes between 20 and 24 km. Eruptions that have an impact on temperature at this height are those of Manam (2005) and Tavurvur and Soufrière Hills (2006; cf. Mehta et al., 2015), as well as Kelut (2014) and Calbuco (2015). Other eruptions such as Nabro (2011), which also caused a substantial temperature increase in the lower stratosphere (Biondi et al., 2017), appear to have nearly no cooling effect at higher altitudes. This correlates with the findings in Figure 1 (top), which indicates that the Merapi or the Nabro eruption did not substantially influence the aerosol concentration at altitudes above 20 km.

However, the cooling between 22 and 24 km is an interesting feature that cannot simply be explained by the radiative properties of the sulfate aerosols. A possible explanation for the cooling is given by Robock (2015)

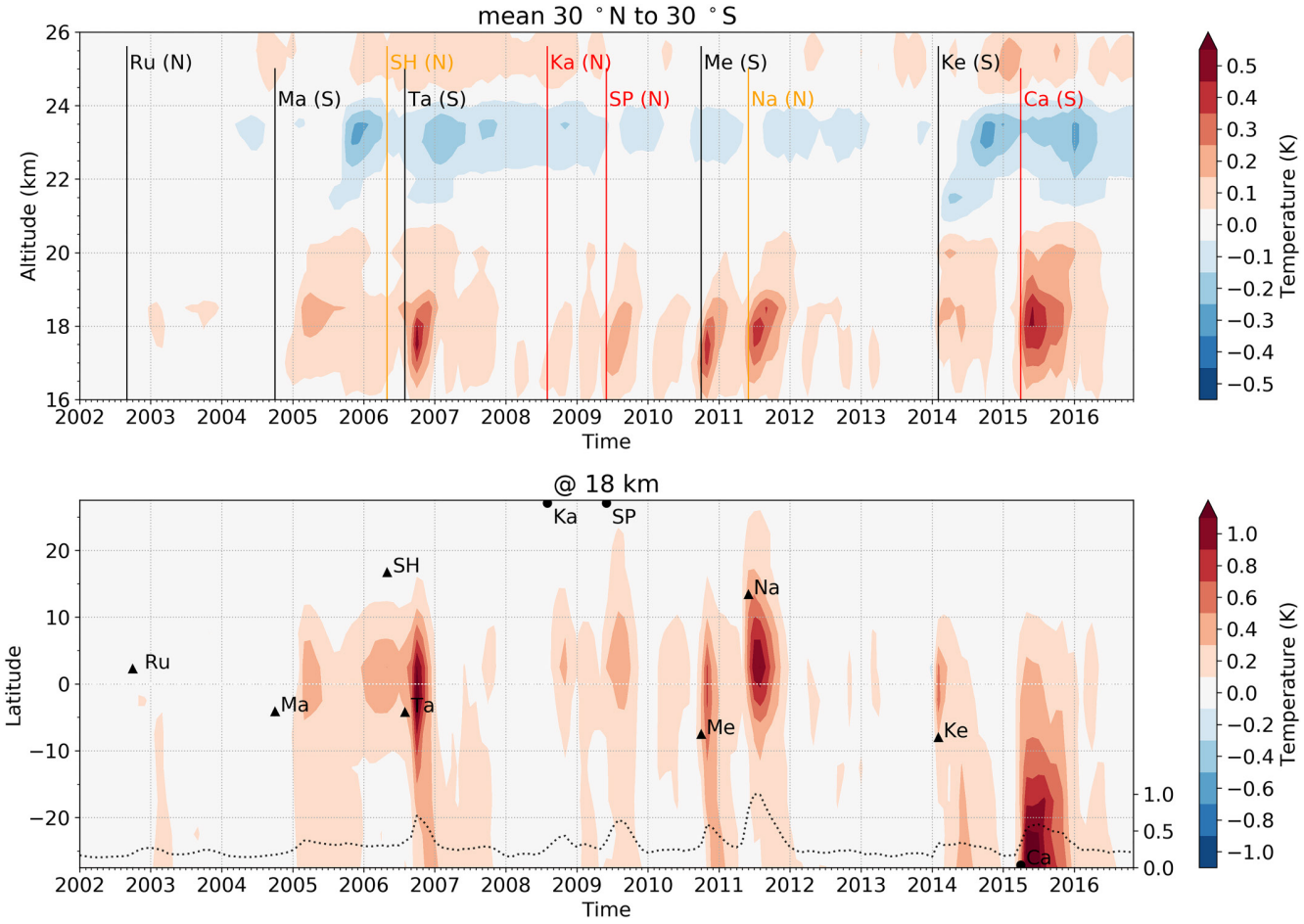


Figure 2. Altitude time cross section of the volcanic aerosol reconstructed temperature (mean 30°N to 30°S; top) as well as the latitude time cross section at 18 km (bottom). Vertical lines in the altitude time pattern mark the date of the eruptions. N and S in brackets indicate north and south of the equator. Line colors indicate the latitude of the eruption (red >30, orange >10, and black <10). Triangles in the latitude time pattern mark the date as well as the latitude of the eruption. Eruptions that occurred at latitudes not part of the plot range are marked with a semicircle. The dashed line represents the normalized VEC for the 18-km altitude level (mean 30°N to 30°S).

and Aquila et al. (2013). As described by Robock (2015), aerosols, in addition to their effects on the radiative flux, can also affect stratospheric dynamics and chemistry (especially ozone depletion). Robock (2015) also notes that in the tropics volcanic clouds enhance the tropical upwelling and hence bring low ozone concentration layers to higher altitudes, possibly causing cooling. Simulations by Aquila et al. (2013) showed a decrease in ozone shortly after the Pinatubo eruption, strongest at about 24 km, which was mainly due to increased tropical upwelling. For large eruptions, the warming effect due to the huge amount of aerosols is dominant (Free & Lanzante, 2009; Randel et al., 2009; Robock, 2015). However, for the small eruptions considered in this study, the dynamical ozone reduction could be more relevant and could explain the observed cooling signals.

A strong indication that the cooling signals are caused by changes in the ozone concentration is that they disappear when we include ozone variability (not shown). The warming signals in the lowermost stratosphere, however, remain robust. As the cooling is assumed to be an aerosol-induced effect, we do not further account for ozone.

Other possible explanations for cooling signals in the tropical stratosphere are ENSO-related changes in the ozone concentration due to increased tropical upwelling (Diallo et al., 2018; Domeisen et al., 2019; Randel et al., 2009). Diallo et al. (2018) found a strong reduction of tropical ozone related to the 2015/2016 ENSO event. We investigated the influence of ENSO on the volcano-induced temperature variability and found that it is negligible (consistent with Santer et al., 2015). Additionally, the midstratospheric cooling signals in

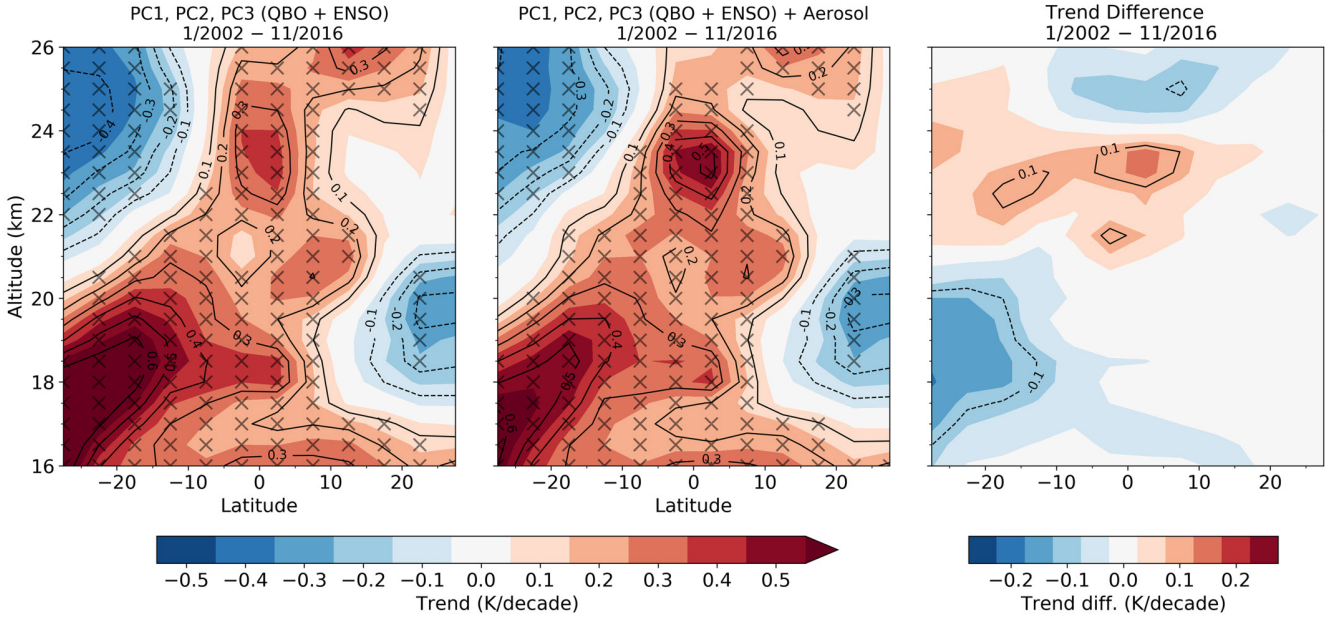


Figure 3. Altitude-latitude cross section of the linear trend for the time series from 2002 to 2016 considering only natural variability indices (left), and natural variability indices together with the volcanic aerosols (center); trend difference (right). Trend values that are significant at the 95% confidence level are indicated with an X mark. QBO = Quasi-biennial Oscillation; ENSO = El Niño–Southern Oscillation; PC = principal component.

2010 and 2014 do not coincide with ENSO events. Therefore, we assume that the cooling signals resulting from our approach are not related to an ENSO pattern in the stratospheric circulation.

The small positive temperature signals around 26 km presumably result from volcanic modulations of the aerosol concentration in the stratospheric aerosol layer, which has its strongest mixing ratio at this altitude (Hommel et al., 2015; Vernier et al., 2011).

Figure 2 (bottom) shows the latitudinal distribution of the warming signals maxima at 18 km, which reveals additional features. Except for the Calbuco, the warming signals appear to be limited to approximately 15°N to 15°S in latitude and are largest close to the equator. This even applies to eruptions that took place at high latitudes and of which only a small fraction of aerosols reached the tropical region, where their effect is more pronounced (Ferraro et al., 2011; Mehta et al., 2015).

In contrast to other higher-latitude eruptions, for the Calbuco eruption in the Southern Hemisphere, a strong warming is observed. As shown in Figure 1 (bottom), a large amount of the Calbuco aerosols was transported toward low latitudes. However, the latitude time cross section in Figure 2 (bottom) also shows that the Calbuco warming for this altitude level is largest outside the central tropics. This may be explained by the fact that at the time of the Calbuco eruption there was an extraordinary strong ENSO event (Stockdale et al., 2017). ENSO events cause a comparatively warm troposphere and also lead to reduced temperature in the lower stratosphere, not only in the tropics but also at midlatitudes (Free & Seidel, 2009). Such conditions increase the warming potential of the volcanic aerosols (Ferraro et al., 2011) and hence may explain why the Calbuco signal is strongest at midlatitudes.

3.2. Linear Trend Analysis

For analyzing the volcanic impacts on short-term climatological trends, we perform the regression with and without including aerosols. We find that including the aerosol index causes substantial changes in the resulting linear trend (Figure 3). The differences are more pronounced in the Southern Hemisphere between 30°S and 10°S where the trend is reduced by more than 0.1 K (approximately 20%). This is related to the Calbuco eruption, which occurred at the end of the investigated time series. A slightly increased trend is detected in the equatorial region between 22 and 24 km, presumably due to the cooling signals from the ozone reduction. In the central tropical lower stratosphere, where most of the eruptions show the strongest warming signals, the trend differences are small. This is because the eruptions with strong signals are distributed roughly uniformly in time over the investigated time period.

4. Conclusions

This is the first study addressing the precise quantification of the impact of recent minor volcanic eruptions on temperature variability and trends using a combination of vertically high resolved temperature and aerosol data, both from satellite measurements. This facilitates the accurate detection of signals of post-2000 volcanic eruptions in space and time and their imprint on stratospheric temperature.

We found robust warming signals in the lower stratosphere up to 20 km from the inspected explosive volcanoes. The strongest imprint was found for Tavurvur, Merapi, Nabro, and Calbuco. The latitudinal distribution of the volcanic imprints was clearly resolved and strongest in the central tropics, with the exception of Calbuco. The results for specific eruptions agree with findings of previous studies that used standard AOD to represent volcanic variability.

In the middle stratosphere we found small cooling signals for the investigated volcanic eruptions. A suggested explanation is an indirect aerosol effect on ozone due to an enhanced upwelling of ozone-poor air after the eruption. The results indicate that small eruptions may also be relevant when investigating stratospheric ozone in the tropics.

Compared to major variability modes such as the QBO, the overall variability due to post-2000 volcanic eruptions was found to be small; however, they are of importance for short-term trend analysis. For the investigated time series we found that the impact on linear trends can be up to 20%, depending on altitude and latitude. While the temperature trend is reduced in the lower stratosphere, an enhanced positive trend is observed in the middle stratosphere.

The results show that detailed knowledge of the vertical structure of volcanic temperature changes is crucial for comprehensive trend analysis, as their influence varies for different altitudes and latitudes. Exploiting the potential of the newly available, highly resolved data sets is beneficial for gaining better knowledge on the impacts of volcanic eruptions. This further helps to separate natural climate variability from anthropogenic influences in climate trend detection, and to improve climate models.

Acknowledgments
The authors express their gratitude to UCAR/CDAAC (Boulder, CO, USA) for providing access to RO phase and orbit data as well as to ECMWF (Reading, UK) for giving access to analysis and forecast data. We also thank the WEGC EOPAC team for providing the OPSv5.6 RO data, which are available online (https://doi.org/10.25364/WEGC/OPS5.6:2019.1). The GloSSAC data set was obtained from the NASA Langley Research Center Atmospheric Sciences Data Center. We acknowledge Global Volcanism Program, Smithsonian Institution (https://volcano.si.edu/) for providing data on the volcanic eruptions and FU Berlin (Berlin, DE) for providing Singapore wind data (https://www.geo.fu-berlin.de/met/ag/strat/produkte/qbo/). The authors want to particularly thank Harald Rieder (WEGC, AT), Jean-Paul Vernier (LARC, USA), and William Randel (NCAR, USA) for fruitful discussions and sharing their expertise. We thank two anonymous reviewers for their helpful comments. This work was funded by the Austrian Science Fund (FWF) under Research Grant P27724-NBL (VERTICLIM) and W1256-G15 (Doctoral Programme Climate Change-Uncertainties, Thresholds and Coping Strategies) as well as by the FFG-ALR project ATROMSAF1(ASAP-13 859771).

References

Angerer, B., Ladstädter, F., Scherllin-Pirscher, B., Schwärz, M., Steiner, A. K., Foelsche, U., & Kirchengast, G. (2017). Quality aspects of the WEGC multi-satellite GPS radio occultation record OPSv5.6. *Atmospheric Measurement Techniques*, *10*, 4845–4863. https://doi.org/10.5194/amt-10-4845-2017

Aquila, V., Oman, L. D., Stolarski, R., Douglass, A. R., & Newman, P. A. (2013). The response of ozone and nitrogen dioxide to the eruption of Mt. Pinatubo at southern and northern midlatitudes. *Journal of the Atmospheric Sciences*, *70*(3), 894–900. https://doi.org/10.1175/jas-d-12-0143.1

Baldwin, M. P., Gray, L. J., Dunkerton, T. J., Hamilton, K., Haynes, P. H., Randel, W. J., et al. (2001). The quasi-biennial oscillation. *Reviews of Geophysics*, *39*(2), 179–229. https://doi.org/10.1029/1999RG000073

Biondi, R., Steiner, A. K., Kirchengast, G., Brenot, H., & Rieckh, T. (2017). Supporting the detection and monitoring of volcanic clouds: A promising new application of global navigation satellite system radio occultation. *Advances in Space Research*, *60*(12), 2707–2722. https://doi.org/10.1016/j.asr.2017.06.039

Bourassa, A. E., Robock, A., Randel, W. J., Deshler, T., Rieger, L. A., Lloyd, N. D., et al. (2012). Large volcanic aerosol load in the stratosphere linked to Asian monsoon transport. *Science*, *337*, 78–81. https://doi.org/10.1126/science.1219371

Diallo, M., Riese, M., Birner, T., Konopka, P., Müller, R., Hegglin, M. I., et al. (2018). Response of stratospheric water vapor and ozone to the unusual timing of El Niño and the QBO disruption in 2015–2016. *Atmospheric Chemistry and Physics*, *18*(17), 13,055–13,073. https://doi.org/10.5194/acp-18-13055-2018

Domeisen, D. I., Garfinkel, C. I., & Butler, A. H. (2019). The teleconnection of El Niño Southern Oscillation to the stratosphere. *Reviews of Geophysics*, *57*, 5–47. https://doi.org/10.1029/2018rg000596

Ferraro, A. J., Highwood, E. J., & Charlton-Perez, A. J. (2011). Stratospheric heating by potential geoengineering aerosols. *Geophysical Research Letters*, *38*, L24706. https://doi.org/10.1029/2011GL049761

Flury, T., Wu, D. L., & Read, W. G. (2013). Variability in the speed of the Brewer–Dobson circulation as observed by Aura/MLS. *Atmospheric Chemistry and Physics*, *13*(9), 4563–4575. https://doi.org/10.5194/acp-13-4563-2013

Free, M., & Lanzante, J. (2009). Effect of volcanic eruptions on the vertical temperature profile in radiosonde data and climate models. *Journal of Climate*, *22*(11), 2925–2939. https://doi.org/10.1175/2008jcli2562.1

Free, M., & Seidel, D. J. (2009). Observed El Niño–Southern Oscillation temperature signal in the stratosphere. *Journal of Geophysical Research*, *114*, D23108. https://doi.org/10.1029/2009JD012420

Global Volcanism Program (2013). Volcanoes of the world, v. 4.3.4.https://doi.org/10.5479/si.gvp.votw4-2013 (Smithsonian Institution, Downloaded 08 Nov 2018).

Hannachi, A., Jolliffe, I. T., & Stephenson, D. B. (2007). Empirical orthogonal functions and related techniques in atmospheric science: A review. *International Journal of Climatology*, *27*(9), 1119–1152. https://doi.org/10.1002/joc.1499

Hommel, R., Timmreck, C., Giorgetta, M. A., & Graf, H. F. (2015). Quasi-biennial oscillation of the tropical stratospheric aerosol layer. *Atmospheric Chemistry and Physics*, *15*(10), 5557–5584. https://doi.org/10.5194/acp-15-5557-2015s.

Kremser, S., Thomason, L. W., von Hobe, M., Hermann, M., Deshler, T., Timmreck, C., et al. (2016). Stratospheric aerosol—Observations, processes, and impact on climate. *Reviews of Geophysics*, *54*, 278–335. https://doi.org/10.1002/2015RG000511

Mehta, S. K., Fujiwara, M., Tsuda, T., & Vernier, J. P. (2015). Effect of recent minor volcanic eruptions on temperatures in the upper troposphere and lower stratosphere. *Journal of Atmospheric and Solar-Terrestrial Physics*, *129*, 99–110. https://doi.org/10.1016/j.jastp.2015.04.009

Okazaki, I., & Heki, K. (2012). Atmospheric temperature changes by volcanic eruptions: GPS radio occultation observations in the 2010 Icelandic and 2011 Chilean cases. *Journal of Volcanology and Geothermal Research*, *245–246*, 123–127. https://doi.org/10.1016/j.jvolgeores.2012.08.018

Parker, D. E., Wilson, H., Jones, P. D., Christy, J. R., & Folland, C. K. (1996). The impact of Mount Pinatubo on world-wide temperatures. *International Journal of Climatology*, *16*(5), 487–497. https://doi.org/10.1002/(SICI)1097-0088(199605)16:5<487::AID-JOC39>3.0.CO;2-J

Randel, W. J., Garcia, R. R., Calvo, N., & Marsh, D. (2009). ENSO influence on zonal mean temperature and ozone in the tropical lower stratosphere. *Journal of Geophysical Research*, *36*, L15822. https://doi.org/10.1029/2009GL039343

Robock, A. (2000). Volcanic eruptions and climate. *Reviews of Geophysics*, *38*(2), 191–219. https://doi.org/10.1029/1998rg000054

Robock, A. (2015). *Climatic impacts of volcanic eruptions Edited by* H. Sigurdsson (pp. 935–942). https://doi.org/10.1016/B978-0-12-385938-9.00053-5

Santer, B. D., Solomon, S., Bonfils, C., Zelinka, M. D., Painter, J. F., Beltran, F., et al. (2015). Observed multivariable signals of late 20th and early 21st century volcanic activity. *Geophysical Research Letters*, *42*, 500–509. https://doi.org/10.1002/2014GL062366

Santer, B. D., Wigley, T. M. L., Doutriaux, C., Boyle, J. S., Hansen, J. E., Jones, P. D., et al. (2001). Accounting for the effects of volcanoes and ENSO in comparisons of modeled and observed temperature trends. *Journal of Geophysical Research*, *106*, 28,033–28,059. https://doi.org/10.1029/2000JD000189

Steiner, A. K., Lackner, B. C., Ladstädter, F., Scherllin-Pirscher, B., Foelsche, U., & Kirchengast, G. (2011). GPS radio occultation for climate monitoring and change detection. *Radio Science*, *46*, RS0D24. https://doi.org/10.1029/2010RS004614

Stockdale, T., Balmasedaand, M., & Ferranti, L. (2017). The 2015/2016 El Niño and beyond. ECMWF Newsletter. https://www.ecmwf.int/node/18187 https://doi.org/10.21957/m3c157

Thomason, L. W. (2017). GloSSAC Level 3 netCDF file—Version 1 [Data set]. https://doi.org/10.5067/glossac-l3-v1.0 (NASA Langley Atmospheric Science Data Center DAAC).

Thomason, L. W., Ernest, N., Millán, L., Rieger, L., Bourassa, A., Vernier, J. P., & Peter, T. (2018). A global space-based stratospheric aerosol climatology: 1979–2016. *Earth System Science Data*, *10*(1), 469–492. https://doi.org/10.5194/essd-10-469-2018

Timmreck, C. (2012). Modeling the climatic effects of large explosive volcanic eruptions. *WIREs Climate Change*, *3*, 545–564. https://doi.org/10.1002/wcc.192

Trepte, C. R., & Hitchman, M. H. (1992). Tropical stratospheric circulation deduced from satellite aerosol data. *Nature*, *355*(6361), 626–628. https://doi.org/10.1038/355626a0

Vernier, J. P., Thomason, L. W., Pommereau, J. P., Bourassa, A., Pelon, J., Garnier, A., et al. (2011). Major influence of tropical volcanic eruptions on the stratospheric aerosol layer during the last decade. *Geophysical Research Letters*, *38*, L12807. https://doi.org/10.1029/2011GL047563

Wang, K.-Y., Lin, S.-C., & Lee, L.-C. (2009). Immediate impact of the Mt Chaiten eruption on atmosphere from FORMOSAT-3/COSMIC constellation. *Geophysical Research Letters*, *36*, L03808. https://doi.org/10.1029/2008GL036802

Wilhelmsen, H., Ladstädter, F., Scherllin-Pirscher, B., & Steiner, A. K. (2018). Atmospheric QBO and ENSO indices with high vertical resolution from GNSS radio occultation temperature measurements. *Atmospheric Measurement Techniques*, *11*(3), 1333–1346. https://doi.org/10.5194/amt-11-1333-2018

Geophysical Research Letters

RESEARCH LETTER
10.1029/2020GL089027

Double Tropopauses and the Tropical Belt Connected to ENSO

Hallgeir Wilhelmsen[1,2,3], **Florian Ladstädter**[1,3], **Torsten Schmidt**[4], and **Andrea K. Steiner**[1,2,3]

[1]Wegener Center for Climate and Global Change (WEGC), University of Graz, Graz, Austria, [2]FWF-DK Climate Change, University of Graz, Graz, Austria, [3]Institute for Geophysics, Astrophysics, and Meteorology/Institute of Physics (IGAM/IP), Graz, Austria, [4]GeoForschungsZentrum Potsdam (GFZ), Potsdam, Germany

Abstract A detailed analysis of double tropopause (DT) occurrences requires vertically well resolved, accurate, and globally distributed information on the troposphere-stratosphere transition zone. Here, we use radio occultation observations from 2001 to 2018 with such properties. We establish a connection between El Niño-Southern Oscillation (ENSO) phases and the distribution of DTs by analyzing the global and seasonal DT characteristics. The seasonal distribution of DTs reveals several hotspot locations, such as near the subtropical jet stream and over high mountain ranges, where DTs occur particularly often. In this study, we detect a higher number of DTs during the cold La Niña state while warmer El Niño events result in lower DT rates, affecting the structure of the tropopause region. Close to the Niño 3 region, this relates to a much lower first lapse rate tropopause altitude during La Niña and corresponds to an apparent narrowing of the tropical belt there.

Plain Language Summary Double tropopauses (DTs) are associated with several phenomena in the transition zone between the troposphere and the stratosphere. DTs may occur when midlatitudinal and tropical air masses meet and warmer air overlaps colder air. A detailed analysis of DT occurrences requires accurate and globally distributed temperature information with high vertical resolution. In this study, we use radio occultation temperature observations from 2001 to 2018 with such properties. This enables us to establish a connection between the El Niño-Southern Oscillation (ENSO) phases and the distribution of DTs and to analyze the global and seasonal DT characteristics.
The seasonal distribution of DTs reveals locations where DTs occur particularly often. During the colder La Niña state of the ENSO, a higher number of DTs is detected, while the warmer El Niño events result in lower DT rates. Close to the tropics in the Pacific Ocean, this relates to a much lower tropopause height during La Niña, which corresponds to an apparent narrowing of the tropical belt.

Key Points:
- Double tropopause characteristics and the connection to ENSO are analyzed using vertically high resolved GPS RO observations
- More double tropopauses are detected during the cold La Niña phase and less during El Niño
- During La Niña, a much lower first lapse rate tropopause corresponds to a narrowing of the tropical belt around the Niño 3 region

Correspondence to:
H. Wilhelmsen,
hallgeir.wilhelmsen@uni-graz.at

Citation:
Wilhelmsen, H., Ladstädter, F., Schmidt, T., & Steiner, A. K. (2020). Double tropopauses and the tropical belt connected to ENSO. *Geophysical Research Letters*, *47*, e2020GL089027. https://doi.org/10.1029/2020GL089027

Received 25 MAY 2020
Accepted 13 JUN 2020
Accepted article online 18 JUN 2020

©2020. The Authors.
This is an open access article under the terms of the Creative Commons Attribution License, which permits use, distribution and reproduction in any medium, provided the original work is properly cited.

1. Introduction

The tropopause, the transition zone between the troposphere and the stratosphere, is of substantial importance to the exchange between these two atmospheric regimes (Holton et al., 1995). Depending on season and latitude, the tropopause is typically found at around 16 km in the tropics and at around 9 km at high latitudes (e.g., Schmidt et al., 2005; Seidel & Randel, 2006). At midlatitudes, the higher tropical tropopause domain may overlap the lower high-latitude tropopause domain and form double tropopauses (DTs), either because the high-latitude tropopause domain extends equatorward (Peevey et al., 2014; Wang & Polvani, 2011) or because the tropical tropopause domain extends poleward (Homeyer et al., 2010; Castanheira et al., 2012; Liu & Barnes, 2018; Pan et al., 2009; Randel et al., 2007). The more complex structure and variability of the upper troposphere and lower stratosphere (UTLS) region at midlatitudes, related to this overlap and the existence of DTs there, is key to understand the stratosphere-troposphere exchange (e.g., Boothe & Homeyer, 2017).

DT events are found especially frequently at midlatitudes in both hemispheres, in storm track regions, on the poleward side of the subtropical jet stream (STJ), more frequently during winter (Bischoff et al., 2007; Schmidt et al., 2006; Seidel & Randel, 2006), and over land (Schmidt et al., 2006). The STJ is of special interest, not only because it marks a region where midlatitudinal and tropical air meet, but the STJs are linked to Rossby wave breaking events, which again are associated to DTs and stratosphere-troposphere exchange

(e.g., Castanheira & Gimeno, 2011; Peevey et al., 2012). The exchange is enhanced when DTs are present (Liu & Barnes, 2018).

DTs have also been found in association with mountain gravity waves (Schmidt et al., 2006), cyclogenesis (Añel et al., 2008) and the upward vertical motion in warm conveyor belts in strong cyclonic circulation systems (Peevey et al., 2014; Wang & Polvani, 2011). DTs are linked to the strength of the upward branch of the Brewer-Dobson circulation (Castanheira et al., 2012) and are detected in cloud-top inversion layers (Biondi et al., 2012).

Previous studies (e.g., Reid & Gage, 1985; Rieckh et al., 2014) have shown a strong correlation between the altitude of the first lapse rate tropopause (LRT) and the El Niño-Southern Oscillation (ENSO). Castanheira et al. (2012) showed a clear signal of both the quasi-biennial oscillation (QBO) and the ENSO in DT frequencies from reanalyzed data (ERA-Interim).

However, a systematic analysis of globally distributed DTs from observations and their link to ENSO phases has not yet been conducted. Previous studies on multiple tropopauses have mainly used radiosonde or reanalysis data. Due to the sparse sampling of radiosondes, a global view on the characteristics of DTs is hardly possible. Data with lower vertical resolution or smoother temperature profiles tend to smear out DT features and underestimate DT frequencies (Biondi et al., 2012; Manney et al., 2017; Vergados et al., 2014; Xian et al., 2019). Since the early 2000s, however, globally distributed measurements from radio occultation (RO) are available. This limb sounding technique provides temperature profiles with high accuracy and vertical resolution in the UTLS for applications in atmospheric research and climate (Anthes, 2011; Steiner et al., 2011). Some studies have used a subset of available RO data to study DTs (e.g. Lakkis & Canziani, 2009; Randel et al., 2007; Schmidt et al., 2006; Xu et al., 2014).

In this study, we take advantage of the precise DT detection with RO to present the global and seasonal characteristics of DTs from observations. For the first time, we analyze the relation between DTs and ENSO events and its implication on the tropopause structure based on the recent full multiyear RO record, which now covers 11 ENSO events. This larger sample substantially improves our ability to investigate these relations.

2. Data

Due to their high vertical resolution and global distribution, RO satellite measurements are well suited for investigating the thermal tropopause. RO measurements from different missions can be combined and used in continuation of each other (Foelsche et al., 2011; Schreiner et al., 2007). We used the Wegener Center OPSv5.6 data set (Angerer et al., 2017), a compilation of most RO satellite missions to date, enabling us to study DTs over a longer time period than previous studies. In this study, we use temperature profiles from September 2001 to December 2018, interpolated to an evenly spaced, fixed vertical grid with $h = 100$ m between the grid points.

El Niño and La Niña events are identified using the Oceanic Niño Index (ONI), which is a ± 1 running mean of monthly mean sea surface temperature anomalies in the Niño 3.4 region (5°S to 5°N and 170°W to 120°W). An event is called "El Niño" or "La Niña" when five succeeding months of the ONI are all above 0.5 K or all below −0.5 K, respectively.

In addition, we indicate the location of the STJ using the maximum mean horizontal wind speed between 200 and 300 hPa within 5° latitude × 5° longitude grid cells from European Centre for Medium-Range Weather Forecasts (ECMWF) 6-hourly analysis wind fields.

3. Methods

The standard definition of the World Meteorological Organization (WMO, 1957) was used to calculate the thermal LRTs: "(a) The first tropopause is defined as the lowest level at which the lapse rate decreases to 2°C/km or less, provided also the average lapse rate between this level and all higher levels within 2 km does not exceed 2°C/km. (b) If above the first tropopause the average lapse rate between any level and all higher levels within 1 km exceeds 3°C/km, then a second tropopause is defined by the same criterion as under (a). This tropopause may be either within or above the 1 km layer." This algorithm was applied to each RO

temperature profile on an evenly spaced 100-m grid. The search started from below, using a latitude, φ, dependent lower altitude limit, z_{start} (in meters), following

$$z_{\text{start}}(\varphi) = 6,250\ \text{m} + 1,250\ \text{m} \times \cos\varphi. \quad (1)$$

This limit was adapted from Son et al. (2011) and adjusted downwards to include more LRTs at midlatitudes. The search was terminated at 25 km.

A candidate LRT altitude was first found on the evenly spaced 100-m vertical grid, according to the thresholds in the WMO (1957) definition. Due to the implementation, this point was always found at an altitude above the threshold. To avoid a positive bias, the altitude was fine tuned, by linear interpolation, down to the altitude where the lapse rate equals $\Gamma = 2°\text{C km}^{-1}$. This altitude was selected to represent the LRT.

The number of first LRTs, N_1, and the number of second LRTs, N_2, from all the available temperature profiles were counted and the corresponding DT percentages calculated using

$$\text{DT percentage} = \frac{N_2}{N_1} \times 100\%. \quad (2)$$

We calculated these percentages within $5° \times 5°$ grid cells and within each 5° zonal band or each 5° meridional band. Finally, monthly mean DT anomalies were created relative to the mean seasonal cycle from 2007 to 2018.

4. Results

4.1. Global DT Occurrences

The main characteristics of the global DT distribution can be deduced from Figure 1. The figure reaffirms previous studies (e.g., Peevey et al., 2012, 2014; Randel et al., 2007; Schmidt et al., 2006; Wang & Polvani, 2011; Xu et al., 2014) and shows that the features are consistently revealed in the multiyear RO record. The seasonal features have been described in greater detail in Peevey et al. (2012). DTs are mainly found at midlatitudes along the STJ and are more frequent during winter and over land. The strong belt of DTs in the STJ regions gets weaker during summer, on both hemispheres, due to the weaker eddy activity as the summer STJ slows down. The STJs are primarily radiatively driven and move equatorward during winter (e.g., Maher et al., 2020; Manney et al., 2014), which is also the case for the location of the DT belt during December-January-February (DJF) (Figure 1a) and June-July-August (JJA) (Figure 1c).

The enhanced DT percentages in the tropical regions for all seasons may be explained by cloud tops (Biondi et al., 2012) or gravity waves in the stratosphere (e.g., Hoffmann et al., 2013 and references therein), both caused by deep convection in the tropics. Additionally, some of the DTs detected in the tropics are related to changing QBO phases (e.g., Kedzierski et al., 2016). We also detect these QBO-related DTs because we use a rather high upper altitude limit of 25 km when finding the LRTs, which is several kilometers above the mean LRT altitude, well into the QBO region in the stratosphere.

Furthermore, Figure 1 reveals locations where DTs are found particularly often. In the Northern Hemisphere (NH), such hotspots are located east of the Rocky Mountains, over the Himalayas, and over Japan. In the Southern Hemisphere (SH), they are found over and east of the southern Andes and over southeast Australia. All these DT hotspots are found on the STJ band, on the lee side of high mountains. They get weaker during summer, supporting the source to be mountain gravity waves related to the STJ (Schmidt et al., 2006). The enhancement east of Japan more or less disappears during JJA but is globally the strongest hotspot during DJF. The hotspot leeward of the Southern Andes is, as an exception, prominent for all seasons and is globally the strongest hotspot during JJA. The area is known for its high number of occurrences of gravity waves (Ern et al., 2018; Hoffmann et al., 2013; Sato et al., 2012).

To the *west* of the Andes, there is a DT *tail*, pointing toward the tropics, that only shows up during DJF (Figure 1a). As the main STJ flow is eastward, the tail is on the windward side of the Andes and therefore requires an alternative explanation. There may also be a similar, somewhat weaker, feature during JJA (Figure 1c) in the northeastern Pacific, west of the Rocky Mountains, also pointing toward the tropics.

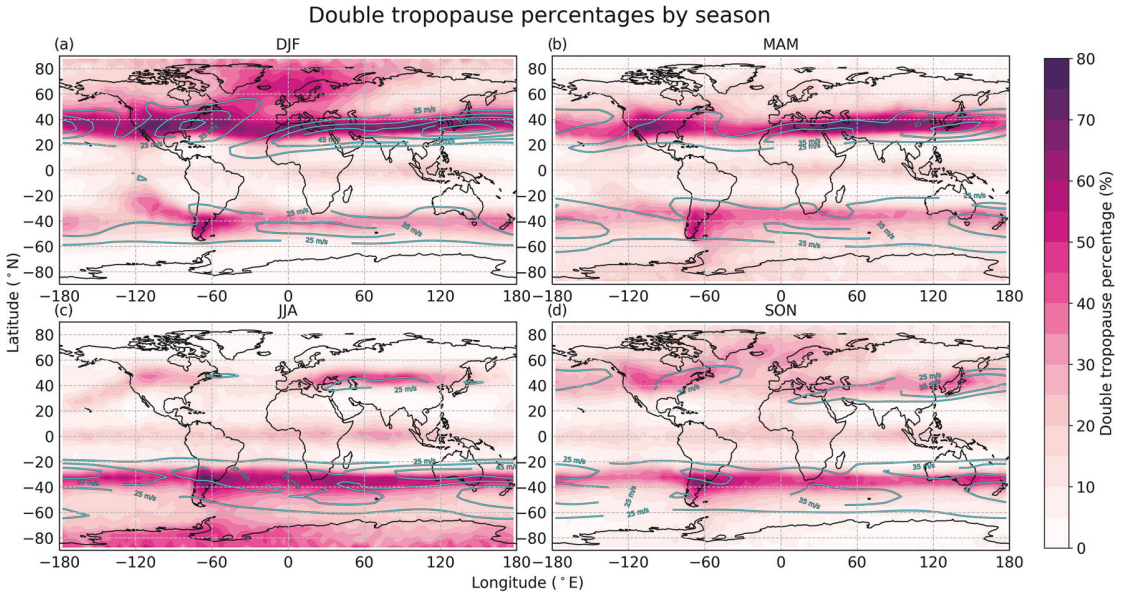


Figure 1. Global spatial distribution of DTs from the years 2001 to 2018 by season: (a) December-January-February (DJF), (b) March-April-May (MAM), (c) June-July-August (JJA), and (d) September-October-November (SON). Cyan contour lines: Mean winds (of the maximum between 300 and 200 hPa) stronger than 25 ms^{-1} are indicated, with 10 ms^{-1} between the contours.

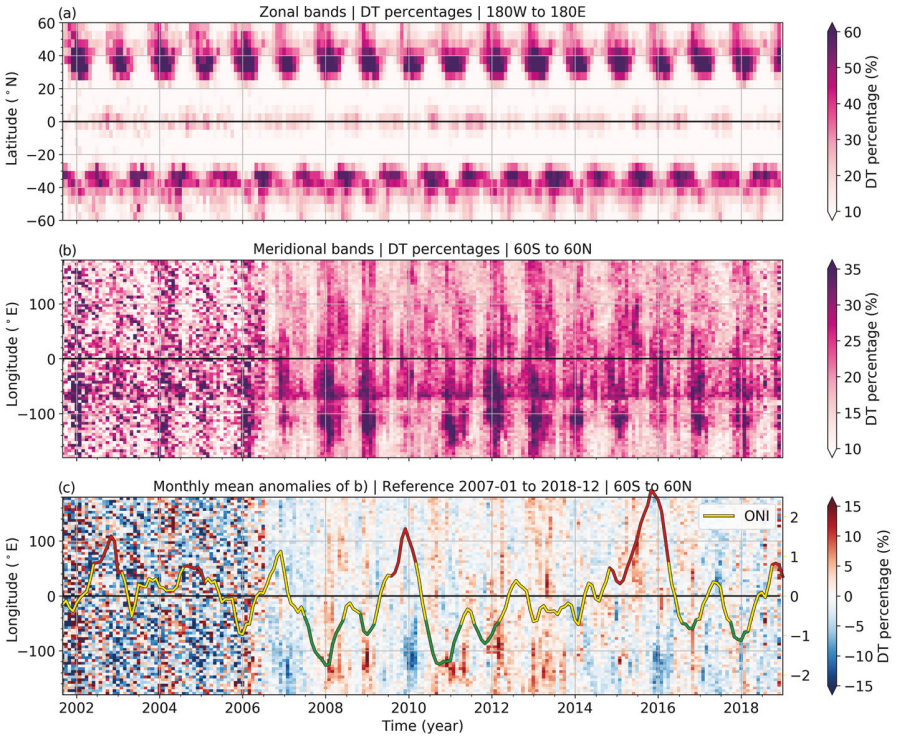


Figure 2. Monthly time series of DT percentages split into (a) 5° zonal bands, (b) 5° meridional bands, and (c) monthly mean anomalies of the meridional bands in panel (b). Only the DTs found between 60°S and 60°N were included in panels (b) and (c). Line in panel (c): The Oceanic Niño Index (ONI), with La Niña events in green and El Niño events in red. The right *y* axis in panel (c) corresponds to the ONI, in Kelvin.

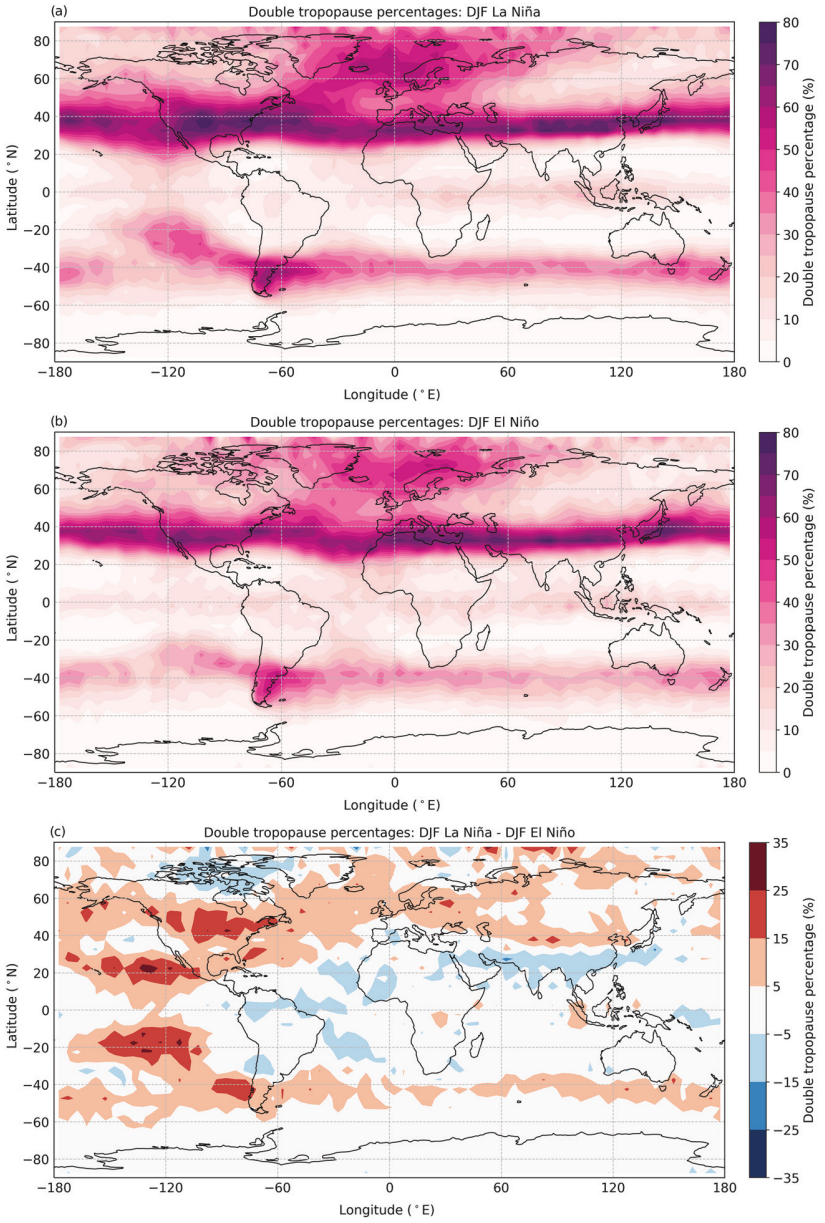


Figure 3. Global spatial distribution of DTs during (a) DJF La Niña, (b) DJF El Niño, and (c) difference between DJF La Niña and DJF El Niño (i.e., a minus b).

4.2. Annual Patterns of DTs

The seasonal DT development is exposed in Figure 2 in zonal (Figure 2a) and meridional (Figure 2b) bands. The noisy structure before 2006 is caused by the lower number of RO measurements in the early RO phase (see, e.g., Steiner et al., 2011), especially apparent in the meridional view in Figure 2b. The seasonality and clear zonal DT distribution mainly in the subtropics of both hemispheres become evident in Figure 2a. In both hemispheres, an annual pattern of peaks in DT numbers moves equatorward during winter, stopping at around ±30° latitude and withdrawing poleward in summer. The DT rates in the NH are more pronounced, last longer, and cover a greater area than in the SH, due to the different land-sea distribution and thus different Rossby wave patterns (e.g., Schmidt et al., 2006; Xian et al., 2019).

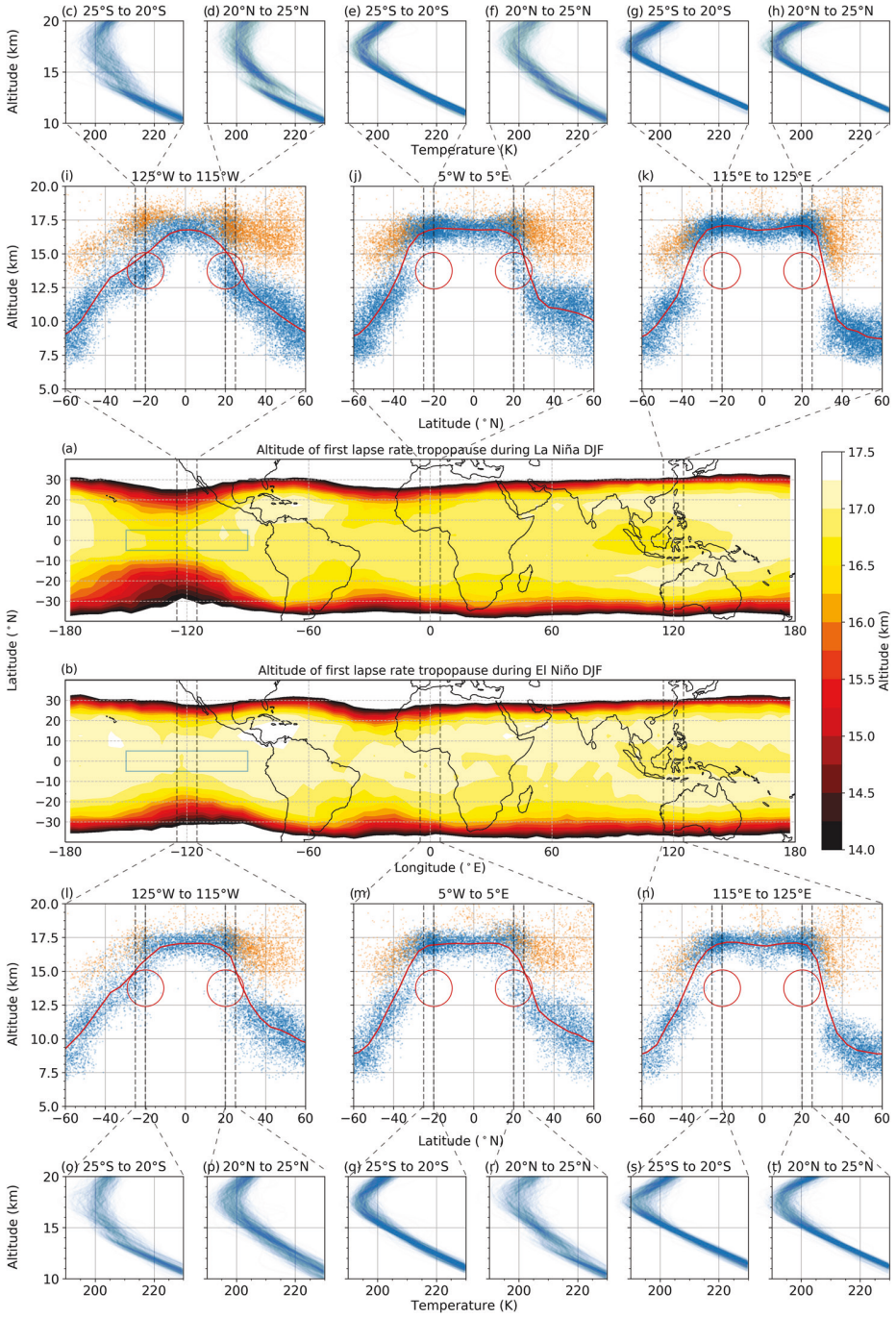


Figure 4. Middle panels (a and b): The mean altitude of the first LRT for DJF only, during (a) La Niña and (b) El Niño. The blue rectangles mark the location of the Niño 3 region. Second topmost (i, j, k) and second bottommost panels (l, m, n): The location of all the first (blue) and the second (orange) LRTs found within the meridional bands marked by dashed lines in the middle panels. Red lines: The mean altitudes of the first LRT within these dashed lines. The red circles have the same location in each panel, for comparison. Topmost (c to h) and bottommost (o to t) panels: The temperature profiles from 25°S to 20°S and 20°N to 25°N (i.e., the profiles within the dashed lines in panels i to k and l to n).

The prominent straight line in Figure 2b, around 75°W, is attributed to the hotspot leeward of the southern Andes that shows up in every season in Figure 1. In contrast, the dip just west of 75°W reveals a meridional band with rarely any DTs, just to the west of the Andes, from the beginning to the end of the time series.

The irregularly recurring patterns further west in Figure 2b, between 150°W and 90°W, resemble ENSO time patterns. The peaks mainly show up between 30°S and 10°S and again between 10°N and 30°N, which is just north and south of the Niño 3 region (5°N to 5°S, 150°W to 90°W). Both the locations and the pattern suggest a link to the ENSO. In the following, we unravel more details and possible explanations.

4.3. ENSO and DT Structure

The relation between ENSO and DT occurrences becomes evident in Figure 2c. First, it reveals that the warmer El Niño events result in lower DT rates. The indication of an ENSO connection is especially prominent for the El Niño events in 2009/2010 and 2015/2016. The ONI peak in 2006/2007 is not called an El Niño event because the values did not last long enough above the 0.5 K threshold, but nevertheless, the rate of DTs is also reduced. Second, the colder La Niña events lead to more DTs, especially between 150°W and 90°W.

For further investigation of the DT and ENSO relation, we limit the considered DTs to the DJF seasons only and examine El Niño and La Niña periods separately. This minimizes the seasonal influence on the difference between the two ENSO states. ENSO events occur more frequently during DJF, with 16 La Niña and 16 El Niño months detected in the considered time period. Figure 3 shows the global spatial distribution of DTs split into DJF La Niña events (Figure 3a) and DJF El Niño events (Figure 3b). It appears that the DT tail to the west of the Andes (cf. Figure 1a) mainly originates from the DJF La Niña time periods, as it is much weaker during DJF El Niño and the other time periods (not shown). Figure 3c shows the difference between the DT percentages during DJF La Niña and DJF El Niño, that is, the difference between Figures 3a and 3b. It uncovers that the tail is not only a SH feature but also shows up on the NH, disguised (in Figure 3a) by the high frequency of DTs in the latitudinal band around the NH STJ during DJF.

The increased DT occurrences in the eastern Pacific region during La Niña compared to El Niño periods are caused by distinct atmospheric circulation regimes. During La Niña, the upwelling part of the Walker circulation is located over the Maritime continent, while during El Niño the main upwelling moves to the central Pacific (see, e.g., Gettelman et al., 2001; Lau & Yang, 2015). An analysis of atmospheric parameters related to cyclonic activity (divergence and vorticity; not shown here) confirmed that during La Niña (El Niño), cyclonic (anticyclonic) activity is dominant in the tropopause region above the eastern Pacific. According to Randel et al. (2007), upper tropospheric level cyclonic vorticity is related to an enhancement of DT occurrence and lower LRT heights compared to anticyclonic vorticity at the same altitude level. This is in good agreement with the observed differences in Figure 3c.

Figure 3 additionally suggests that during DJF La Niña, more DTs should be expected at locations where they are usually found than during DJF El Niño. The regions just west of the Andes hotspot and east of the Rocky Mountains hotspot especially stand out. The enhancement east of Japan, on the other hand, seems to be unaffected by ENSO events. There is a southward shift around the Himalayan hotspot during DJF El Niño, also seen between the seasons (Figure 1), related to jet stream shifts (Maher et al., 2020).

4.4. Narrowing the Tropical Belt During La Niña

We investigate the impact of ENSO conditions on the tropopause structure in Figure 4. Figures 4a and 4b show the mean of all the *first* LRT altitudes during DJF La Niña and DJF El Niño, respectively. For most longitudes, the mean first LRTs in the tropics are found at a slightly lower altitude during DJF La Niña (Figure 4a) than during DJF El Niño (Figure 4b). This is in agreement with Randel et al. (2007) (see above). Poleward of the Niño 3 region, they are exceptionally low, corresponding to a remarkable narrowing of the tropical belt around those longitudes. Figure 4i shows the altitude of all the first (blue) and second (orange) LRTs within a 10° meridional band at the Niño 3 region (leftmost dashed meridional band in Figure 4a), at their corresponding latitudes during La Niña. Additional tropopauses appear below the tropical tropopause domain (approximately 20°S to 20°N) from what seems to be an equatorward expansion of the high-latitude tropopause domain. The tropical LRT domain is still present, as a mix of first and second LRTs, but the mean first LRT appears much lower than usual in the specified region for DJF La Niña. The corresponding temperature profile cluster plots in Figures 4c–4h (DJF La Niña) and Figures 4o–4t (DJF El Niño) support these observations. This becomes especially clear in Figure 4d, where the temperature profiles start off with a steady lapse rate until they are sliced in two "branches" at the first LRT and break into typical, although less sharply defined, tropical temperature profiles (cf. Figure 4g). For comparison, the regular tropopause characteristics are depicted for two additional meridional bands in Figure 4.

Similar to the DT frequency as described in the previous section, the altitude of the first LRT is also influenced by the circulation patterns. As cyclonic vorticity leads to lower first LRT altitudes (Randel et al., 2007), the shifting cyclonic circulation patterns during La Niña, induced by the change in the Walker circulation, are therefore considered to be connected to the observed tropical belt narrowing.

5. Conclusions

To summarize, high vertical resolution and global coverage make RO satellite measurements well suited for studying DTs. The measurements are especially accurate in the altitude range of the tropopause. We exploited these characteristics to investigate for the first time the relation of ENSO and the occurrence of DTs in global multiyear RO observations.

We demonstrated that findings from previous studies are consistently revealed and presented a seasonally and regionally resolved picture of various DT hotspots. DTs are mainly triggered along the STJ in winter, especially prominent over the Rocky Mountains, the Himalayas, and the Andes.

Temporal, resolved DT patterns introduced a connection between ENSO and DT occurrences. It revealed an increase in DTs to the west of the Andes, poleward of the Niño 3 region (5°N to 5°S, 150°W to 90°W). We found that the strength and location of this increase is evidently connected to the ENSO. Colder La Niña events lead to a higher number of DTs while warmer El Niño events result in lower DT rates. This difference in DT occurrences is considered to be caused by the changing atmospheric circulation regimes of the Walker circulation between the ENSO phases.

During La Niña, the higher number of DTs detected at the Niño 3 region seems to be an equatorward expansion of the high-latitude tropopause domain. This leads to a mix of first and second LRTs at the edge of the tropical belt and a mean first LRT altitude that is much lower than usual. This corresponds to an apparent narrowing of the tropical belt there.

Knowledge of the detailed structure of the UTLS region is of great relevance for the analysis of the stratosphere-troposphere exchange. Identifying regions of increased DT occurrences points to a possible enhanced exchange. This has implications for the composition of the atmosphere, influencing, for example, the radiative balance and the dynamics of the atmosphere (see, e.g., Stohl et al., 2003 and references therein). The enhanced DT frequencies and lower first LRTs suggest that these processes are of increased relevance in the tropical Eastern Pacific during La Niña.

Recent studies have discussed the widening of the tropical belt (e.g., Staten et al., 2018 and references therein). This widening is difficult to determine due to large internal variability. The dependence of the tropical belt width on ENSO presented in this study might be of relevance to future studies on this topic.

Compared to neutral ENSO phases, ENSO events substantially alter the UTLS structure at midlatitudes and the tropics. For a detailed analysis, vertically high resolved information with global coverage is needed. Our results show that RO observations are able to provide such analysis and contribute to gaining improved knowledge of the transition between troposphere and stratosphere and the variability of the tropical belt.

Acknowledgments
The authors express thanks to the WEGC EOPAC team for providing the OPSv5.6 RO data set (https://doi.org/10.25364/WEGC/OPS5.6:2019.1), to NOAA for the Oceanic Niño Index (https://www.cpc.ncep.noaa.gov/data/indices/oni.ascii.txt), to ECMWF for wind fields (https://www.ecmwf.int/en/forecasts/datasets), and to Thomas Birner for pointing to a more robust interpretation of the LRT definition than initially used. This work was funded by the Austrian Science Fund (FWF) under Research Grants P27724-NBL (VERTICLIM) and W1256-G15 (Doctoral Programme Climate Change-Uncertainties, Thresholds and Coping Strategies). Finally, a special thanks to the open source community, particularly those funded by NumFOCUS.

References

Añel, J., Antuña, J. C., de la Torre, L., Castanheira, J. M., & Gimeno, L. (2008). Climatological features of global multiple tropopause events. *Journal of Geophysical Research*, *113*, D00B08. https://doi.org/10.1029/2007JD009697

Angerer, B., Ladstädter, F., Scherllin-Pirscher, B., Schwärz, M., Steiner, A. K., Foelsche, U., & Kirchengast, G. (2017). Quality aspects of the WEGC multi-satellite GPS radio occultation record OPSv5.6. *Atmospheric Measurement Techniques*, *10*, 4845–4863. https://doi.org/10.5194/amt-10-4845-2017

Anthes, R. A. (2011). Exploring Earth's atmosphere with radio occultation: contributions to weather, climate, and space weather. *Atmospheric Measurement Techniques*, *4*, 1077–1103. https://doi.org/10.5194/amt-4-1077-2011

Biondi, R., Randel, W. J., Ho, S. P., Neubert, T., & Syndergaard, S. (2012). Thermal structure of intense convective clouds derived from GPS radio occultations. *Atmospheric Chemistry and Physics*, *12*(12), 5309–5318. https://doi.org/10.5194/acp-12-5309-2012

Bischoff, S. A., Canziani, P. O., & Yuchechen, A. E. (2007). The tropopause at southern extratropical latitudes: Argentine operational rawinsonde climatology. *International Journal of Climatology*, *27*(2), 189–209. https://doi.org/10.1002/joc.1385

Boothe, A. C., & Homeyer, C. R. (2017). Global large-scale stratosphere-troposphere exchange in modern reanalyses. *Atmospheric Chemistry and Physics*, *17*(9), 5537–5559. https://doi.org/10.5194/acp-17-5537-2017

Castanheira, J. M., & Gimeno, L. (2011). Association of double tropopause events with baroclinic waves. *Journal of Geophysical Research*, *116*, D19113. https://doi.org/10.1029/2011JD016163

Castanheira, J. M., Peevey, T. R., Marques, C. A. F., & Olsen, M. A. (2012). Relationships between Brewer-Dobson circulation, double tropopauses, ozone and stratospheric water vapour. *Atmospheric Chemistry and Physics*, *12*, 10,195–10,208. https://doi.org/10.5194/acp-12-10195-2012

Ern, M., Trinh, Q. T., Preusse, P., Gille, J. C., Mlynczak, M. G., Russell III, J. M., & Riese, M. (2018). GRACILE: A comprehensive climatology of atmospheric gravity wave parameters based on satellite limb soundings. *Earth System Science Data*, *10*(2), 857–892. https://doi.org/10.5194/essd-10-857-2018

Foelsche, U., Scherllin-Pirscher, B., Ladstädter, F., Steiner, A. K., & Kirchengast, G. (2011). Refractivity and temperature climate records from multiple radio occultation satellites consistent within 0.05 %. *Atmospheric Measurement Techniques*, *4*, 2007–2018. https://doi.org/10.5194/amt-4-2007-2011

Gettelman, A., Randel, W. J., Massie, S., Wu, F., Read, W. G., & Russell III, J. M. (2001). El Niño as a natural experiment for studying the tropical tropopause region. *Journal of Climate*, *14*, 3375–3392.

Hoffmann, L., Xue, X., & Alexander, M. J. (2013). A global view of stratospheric gravity wave hotspots located with Atmospheric Infrared Sounder observations. *Journal of Geophysical Research: Atmosphere*, *118*, 416–434. https://doi.org/10.1029/2012JD018658

Holton, J. R., Haynes, P. H., McIntyre, M. E., Douglass, A. R., Rood, R. B., & Pfister, L. (1995). Stratosphere-troposphere exchange. *Reviews of Geophysics*, *33*(14), 403–439. https://doi.org/10.1029/95RG02097

Homeyer, C. R., Bowman, K. P., & Pan, L. L. (2010). Extratropical tropopause transition layer characteristics from high-resolution sounding data. *Journal of Geophysical Research*, *115*, D13108. https://doi.org/10.1029/2009JD013664

Kedzierski, R. P., Matthes, K., & Bumke, K. (2016). The tropical tropopause inversion layer: Variability and modulation by equatorial waves. *Atmospheric Chemistry and Physics*, *16*(18), 11,617–11,633. https://doi.org/10.5194/acp-16-11617-2016

Lakkis, S., & Canziani, P. (2009). A comparative analysis of the temperature behavior and multiple tropopause events derived from GPS, radiosonde and reanalysis datasets over Argentina, as an example of Southern mid latitudes. *Revista de Climatología*, *9*, 1–14.

Lau, K. M., & Yang, S. (2015). Tropical meteorology & climate | Walker circulation, (2nd ed.). In G. R. North, J. Pyle, & F. Zhang (Eds.), *Encyclopedia of atmospheric sciences* (pp. 177–181). Oxford: Academic Press. https://doi.org/10.1016/B978-0-12-382225-3.00450-3

Liu, C., & Barnes, E. (2018). Synoptic formation of double tropopauses. *Journal of Geophysical Research: Atmosphere*, *123*, 693–707. https://doi.org/10.1002/2017JD027941

Maher, P., Kelleher, M. E., Sansom, P. G., & Methven, J. (2020). Is the subtropical jet shifting poleward? *Climate Dynamics*, *54*(3), 1741–1759. https://doi.org/10.1007/s00382-019-05084-6

Manney, G. L., Hegglin, M. I., Daffer, W. H., Schwartz, M. J., Santee, M. L., & Pawson, S. (2014). Climatology of upper tropospheric-lower stratospheric (UTLS) jets and tropopauses in MERRA. *Journal of Climate*, *27*, 3248–3271. https://doi.org/10.1175/JCLI-D-13-00243.1

Manney, G. L., Hegglin, M. I., Lawrence, Z. D., Wargan, K., Millán, L. F., Schwartz, M. J., & Daffer, W. H. (2017). Reanalysis comparisons of upper tropospheric–lower stratospheric jets and multiple tropopauses. *Atmospheric Chemistry and Physics*, *17*(18), 11,541–11,566. https://doi.org/10.5194/acp-17-11541-2017

Pan, L., L., Randel, W. J., Gille, J. C., Hall, W. D., Nardi, B., et al. (2009). Tropospheric intrusions associated with the secondary tropopause. *Journal of Geophysical Research*, *114*, D10302. https://doi.org/10.1029/2008JD011374

Peevey, T. R., Gille, J. C., Homeyer, C. R., & Manney, G. L. (2014). The double tropopause and its dynamical relationship to the tropopause inversion layer in storm track regions. *Journal of Geophysical Research: Atmosphere*, *119*, 10,194–10,212. https://doi.org/10.1002/2014JD021808

Peevey, T. R., Gille, J. C., Randall, C. E., & Kunz, A. (2012). Investigation of double tropopause spatial and temporal global variability utilizing High Resolution Dynamics Limb Sounder temperature observations. *Journal of Geophysical Research*, *117*, D01105. https://doi.org/10.1029/2011JD016443

Randel, W. J., Seidel, D. J., & Pan, L. L. (2007). Observational characteristics of double tropopauses. *Journal of Geophysical Research*, *112*, D07309. https://doi.org/10.1029/2006JD007904

Reid, G. C., & Gage, K. S. (1985). Interannual variations in the height of the tropical tropopause. *Journal of Geophysical Research*, *90*(D3), 5629–5635. https://doi.org/10.1029/JD090iD03p05629

Rieckh, T., Scherllin-Pirscher, B., Ladstädter, F., & Foelsche, U. (2014). Characteristics of tropopause parameters as observed with GPS radio occultation. *Atmospheric Measurement Techniques*, *7*, 3947–3958. https://doi.org/10.5194/amt-7-3947-2014

Sato, K., Tateno, S., Watanabe, S., & Kawatani, Y. (2012). Gravity wave characteristics in the Southern Hemisphere revealed by a high-resolution middle-atmosphere general circulation model. *Journal of the Atmospheric Sciences*, *69*(4), 1378–1396. https://doi.org/10.1175/JAS-D-11-0101.1

Schmidt, T., Beyerle, G., Heise, S., Wickert, J., & Rothacher, M. (2006). A climatology of multiple tropopauses derived from GPS radio occultations with CHAMP and SAC-C. *Geophysical Research Letters*, *33*, L04808. https://doi.org/10.1029/2005GL024600

Schmidt, T., Heise, S., Wickert, J., Beyerle, G., & Reigber, C. (2005). GPS radio occultation with CHAMP and SAC-C: Global monitoring of thermal tropopause parameters. *Atmospheric Chemistry and Physics*, *5*(6), 1473–1488. https://doi.org/10.5194/acp-5-1473-2005

Schreiner, W., Rocken, C., Sokolovskiy, S., Syndergaard, S., & Hunt, D. (2007). Estimates of the precision of GPS radio occultations from the COSMIC/FORMOSAT-3 mission. *Geophysical Research Letters*, *34*, L04808,. https://doi.org/10.1029/2006GL027557

Seidel, D. J., & Randel, W. J. (2006). Variability and trends in the global tropopause estimated from radiosonde data. *Journal of Geophysical Research*, *111*, D21101. https://doi.org/10.1029/2006JD007363

Son, S. W., Tandon, N. F., & Polvani, L. M. (2011). The fine-scale structure of the global tropopause derived from COSMIC GPS radio occultation measurements. *Journal of Geophysical Research*, *116*, D20113. https://doi.org/10.1029/2011JD016030

Staten, P. W., Lu, J., Grise, K. M., Davis, S. M., & Birner, T. (2018). Re-examining tropical expansion. *Nature Climate Change*, *8*(43), 768–775. https://doi.org/10.1038/s41558-018-0246-2

Steiner, A. K., Lackner, B. C., Ladstädter, F., Scherllin-Pirscher, B., Foelsche, U., & Kirchengast, G. (2011). GPS radio occultation for climate monitoring and change detection. *Radio Science*, *46*, RS0D24. https://doi.org/10.1029/2010RS004614

Stohl, A., Bonasoni, P., Cristofanelli, P., Collins, W., Feichter, J., Frank, A., & Zerefos, C. (2003). Stratosphere-troposphere exchange: A review, and what we have learned from STACCATO. *Journal of Geophysical Research*, *108*(D12), 8516. https://doi.org/10.1029/2002JD002490

Vergados, P., Luo, Z. J., Emanuel, K., & Mannucci, A. J. (2014). Observational tests of hurricane intensity estimations using GPS radio occultations. *Journal of Geophysical Research: Atmosphere*, *119*, 1936–1948. https://doi.org/10.1002/2013JD020934

WMO (1957). *Meteorology—A three dimensional science: Second session of the commission for aerology*. Geneva: World Meteorological Organization (WMO). (WMO Bull. No. 4).

Wang, S., & Polvani, L. M. (2011). Double tropopause formation in idealized baroclinic life cycles: The key role of an initial tropopause inversion layer. *Journal of Geophysical Research*, *116*, D05108. https://doi.org/10.1029/2010JD015118

Xian, T., & Homeyer, C. R. (2019). Global tropopause altitudes in radiosondes and reanalyses. *Atmospheric Chemistry and Physics*, *19*(8), 5661–5678. https://doi.org/10.5194/acp-19-5661-2019

Xu, X., Gao, P., & Zhang, X. (2014). Global multiple tropopause features derived from COSMIC radio occultation data during 2007 to 2012. *Journal of Geophysical Research: Atmosphere*, *119*, 8515–8534. https://doi.org/10.1002/2014JD021620

CLIMATOLOGY

Continuous rise of the tropopause in the Northern Hemisphere over 1980–2020

Lingyun Meng[1,2], Jane Liu[3,4]*, David W. Tarasick[5], William J. Randel[6]*, Andrea K. Steiner[7,8,9], Hallgeir Wilhelmsen[7,8,9], Lei Wang[10,11,12], Leopold Haimberger[13]

Copyright © 2021 The Authors, some rights reserved; exclusive licensee American Association for the Advancement of Science. No claim to original U.S. Government Works. Distributed under a Creative Commons Attribution NonCommercial License 4.0 (CC BY-NC).

Tropopause height (*H*) is a sensitive diagnostic for anthropogenic climate change. Previous studies showed increases in *H* over 1980–2000 but were inconsistent in projecting *H* trends after 2000. While *H* generally responds to temperature changes in the troposphere and stratosphere, the relative importance of these two contributions is uncertain. Here, we use radiosonde balloon observations in the Northern Hemisphere (NH) over 20°N to 80°N to reveal a continuous rise of *H* over 1980–2020. Over 2001–2020, *H* increases at 50 to 60 m/decade, which is comparable to the trend over 1980–2000. The GPS radio occultation measurements from satellites and homogenized radiosonde records are in good agreement with those results. The continuous rise of the tropopause in the NH after 2000 results primarily from tropospheric warming. A large trend in *H* remains after major natural forcings for *H* are removed, providing further observational evidence for anthropogenic climate change.

INTRODUCTION

The tropopause identifies the top of the troposphere and marks a separation with the stratosphere in terms of both thermal structure and chemical composition (*1*–*3*). In addition to its relevance to meteorological and chemical structures in the atmosphere, the height of the tropopause has been suggested as a sensitive indicator of anthropogenic climate change (*4*). Increases in tropopause height from the 1980s to the 1990s/2000s have been reported based on radiosonde observations (*5*, *6*), reanalysis data (*7*, *8*), and climate model simulations (*9*). Reanalyses and model simulations have suggested that the rise in the tropopause over these periods was mainly induced by tropospheric warming due to increasing greenhouse gases (GHGs) and stratospheric cooling due to stratospheric ozone depletion and increasing GHGs. However, the relative importance of tropospheric warming and stratospheric cooling remains uncertain (*4*). From radiosonde observations up to the early 2000s, a link between tropopause height increase and lower stratospheric cooling was established (*5*). However, a link between the change in tropopause height and that in tropospheric temperature was not apparent in either the extratropics or the tropics (*5*). Since the mid-1990s, cooling of the lower stratosphere has subsided owing to the successful implementation of the Montreal Protocol and its amendments (*10*–*14*). On the other hand, in the troposphere, a temporary warming slowdown appears in the early 2000s after the large El Niño of 1997–1998. This slowdown is termed the "global warming hiatus" and is widely discussed (*15*–*19*). It was found that during this period, the cooling effect from internal variability and natural forcings overwhelmed the GHG warming effect (*15*–*18*). However, as the IPO (Interdecadal Pacific Oscillation) shifted from a negative to positive phase in 2014, a combined effect of the IPO- and GHG-related forcings has since accelerated global warming (*15*, *19*–*21*). Such an evolution in tropospheric temperature since 2000 can also drive changes in tropopause height. Previously, considering changes in stratospheric cooling and tropospheric warming, some models projected a continuous increase in global tropopause height after 2000 at a rate comparable to that before 2000 (*7*, *22*), while other models projected that the rate of tropopause rise would become weaker after 2000, with a slowdown mostly in the Southern Hemisphere (SH) (*9*). Son *et al.* (*9*) compared the projection from the stratosphere-resolving chemistry climate models (CCMs) with that from the Intergovernmental Panel on Climate Change Fourth Assessment Report (AR4) models. The projections are different by hemisphere. For the Northern Hemisphere (NH), the CCMs projected that the rate of tropopause rise would slowly decrease after 2000, while the AR4 models projected a slightly larger increasing trend after 2000 than that before 2000. For the SH, both CCMs and AR4 models agreed that the tropopause would continue to rise after 2000 at a weaker rate than that before 2000, although in different magnitudes between the CCMs and AR4 models and among the CCMs. This reduction in the SH tropopause trend after 2000 was mainly attributed to stratospheric ozone recovery. In a recent numerical study (*23*), two sensitivity experiments were conducted by fixing the amount of ozone depleting substances (ODS) and GHG emissions at their 1960 levels. The results show that, on the global scale, tropopause height would continue to rise at a faster rate over 2000–2080 than before if the amount of ODS is fixed. If GHG emissions are instead fixed, the tropopause height would decrease after 2000. If all forcings are considered, the rate of tropopause rise before and after 2000 would be comparable.

In 2016, the Integrated Global Radiosonde Archive (IGRA) was updated to version 2 (IGRA2), which includes more stations and reduces more biases than the previous version. In recent decades, satellite GPS radio occultation (RO) measurements and the homogenized gridded radiosonde data have also become available. Therefore,

[1]School of Atmospheric Sciences, Nanjing University, Nanjing, China. [2]International Institute for Earth System Science, Nanjing University, Nanjing, China. [3]Department of Geography and Planning, University of Toronto, Toronto, Canada. [4]Key Laboratory for Humid Subtropical Eco-geographical Processes of the Ministry of Education, College of Geographical Sciences, Fujian Normal University, Fuzhou, China. [5]Air Quality Research Division, Environment and Climate Change Canada, Downsview, ON M3H 5T4, Canada. [6]National Center for Atmospheric Research, Boulder, CO, USA. [7]Wegener Center for Climate and Global Change, University of Graz, Graz, Austria. [8]Institute for Geophysics, Astrophysics, and Meteorology/Institute of Physics, University of Graz, Graz, Austria. [9]FWF-DK Climate Change, University of Graz, Graz, Austria. [10]Department of Atmospheric and Oceanic Sciences & Institute of Atmospheric Sciences, Fudan University, Shanghai, China. [11]Shanghai Qi Zhi Institute, Shanghai, China. [12]Big Data Institute for Carbon Emission and Environmental Pollution, Fudan University, Shanghai, China. [13]Department of Meteorology and Geophysics, University of Vienna, Wien, Austria.
*Corresponding author. Email: janejj.liu@utoronto.ca (J.L.); randel@ucar.edu (W.J.R.)

Downloaded from https://www.science.org at Universitaet Graz on December 06, 2021

in view of the issues discussed above, this study is motivated (i) to determine the long-term (1980–2020) changes in tropopause height associated with anthropogenic activities using the updated IGRA2 and other datasets, (ii) to provide a robust assessment on the sensitivity of tropopause height to the temperature variations in the troposphere and stratosphere, and (iii) to assess the relative importance of tropospheric warming and stratospheric cooling to the change in tropopause height before and after 2000 under a combined influence of GHG emissions and stratospheric ozone changes. Specifically, we investigate the variation in tropopause height (referred as *H*; see Materials and Methods for its definition) in the NH, primarily over 20°N to 80°N, where most radiosonde stations are located (fig. S1). We compare the *H* variations in two periods before and after 2000 based on the dense radiosonde balloon observations, largely over land, from the IGRA2 data [(*24*); see Materials and Methods on how to select stations and see fig. S1 and table S1 for information of all selected stations]. We further use the GPS RO measurements over 2001–2020 (*25*) and the gridded homogenized radiosonde observations from the Radiosonde Observation Correction Using Reanalyses (RAOBCORE) data and Radiosonde Innovation Composite Homogenization (RICH) data (*26*, *27*) over 1980–2020 to compare with the IGRA2 data. We evaluate the behavior of the tropopause height changes in the NH with time and by latitude. To isolate the impact of anthropogenic activities on the tropopause, the variations related to major natural forcings, including volcanic eruptions, ENSO (El Niño–Southern Oscillation), and QBO (quasi–biennial oscillation), are statistically removed from the original time series of the IGRA2, GPS RO, RAOBCORE, and RICH data to generate natural variability–removed time series (see Materials and Methods and fig. S2 for details; all the discussion in this paper is based on the natural variability–removed time series unless stated otherwise). We evaluate the relative importance of temperature changes in the troposphere and stratosphere to the tropopause height changes through detailed comparisons with the radiosonde temperature profiles using robust statistical methods (see Materials and Methods) and thus demonstrate that the continuous rise of the tropopause in the NH after 2000 is mainly due to ongoing warming of the troposphere.

RESULTS

Long-term variability in tropopause height in the NH over 20°N to 80°N from 1980 to 2020

Over the entire study period from 1980 to 2020, a continuous rise of *H* in the NH over 20°N to 80°N is evident in the natural variability–removed IGRA2 radiosonde time series (Fig. 1A). Positive trends in *H* prevail in IGRA2 over most subperiods longer than 10 years (fig. S3A). Similarly, the corresponding *H* in gridded RAOBCORE or RICH data also increases monotonously with a faster rate (70 to 80 m/decade) than that in IGRA2 (50 to 60 m/decade) (Table 1A). These differences may be due to that *H* for RAOBCORE and RICH is determined based on a monthly mean temperature profile, while for IGRA2, *H* is determined based on single profiles, and the resulting *H* values are then averaged for monthly means. In addition, the vertical resolution of the RAOBCORE and RICH data is somewhat coarser than that of IGRA2 (see Materials and Methods). The correlation coefficient between the monthly anomalies of *H* in IGRA2 and RAOBCORE (or RICH) data is 0.87 (or 0.89) over 1980–2020. In the original IGRA2 data in which the signals of natural variability are not filtered out, the mean *H* increases from 12.2 km in 1980 to 12.4 km in 2020 in absolute altitude. The increasing trend in *H* over 1980–2020 is estimated to be 49.7 ± 3.6 m/decade in the original IGRA2 data and 44.0 ± 2.5 m/decade in the natural variability–removed IGRA2 data.

For the first subperiod of 1980–2000, *H* rises with a rate of 50.3 ± 7.2 m/decade in the natural variability–removed IGRA2 radiosonde data (Fig. 1A for time series and fig. S4A for spatial variation). Similar positive trends over this period were reported for the

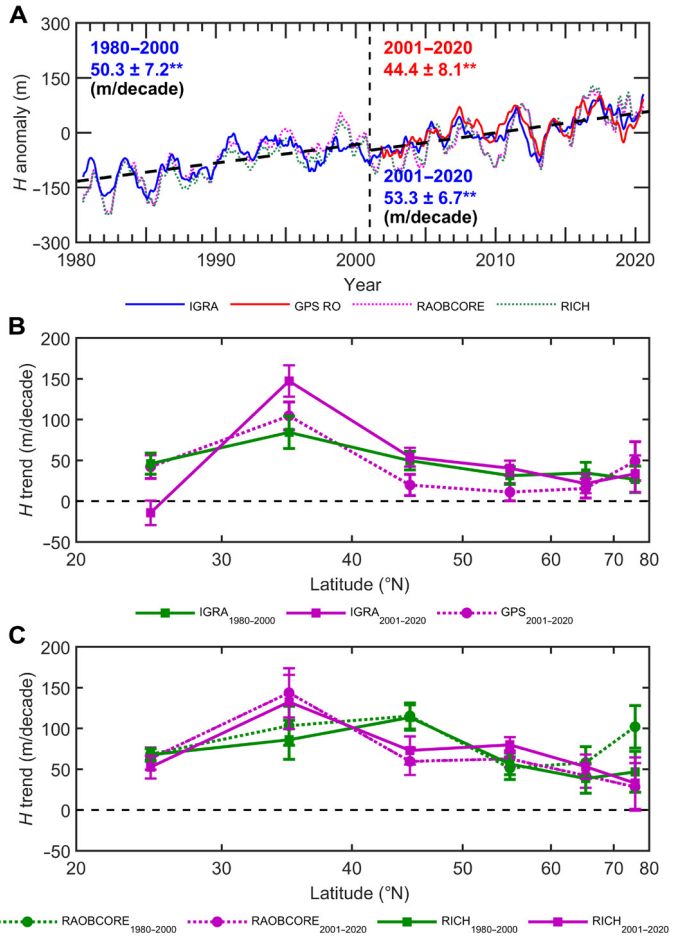


Fig. 1. Variations in zonal mean tropopause height over the NH and derived trends from the IGRA2, RAOBCORE, and RICH data over the time period 1980–2020 and GPS RO satellite data over 2001–2020. (**A**) Time series of deseasonalized monthly anomalies of tropopause height (*H*) from IGRA2 (solid blue line), RAOBCORE (dashed purple line), RICH (dashed green line), and GPS RO (solid red line) averaged over 20°N to 80°N. The vertical dashed black line indicates the end of 2000, dividing the study period into two subperiods (1980–2000 and 2001–2020). The dashed thick black lines denote the linear trends in IGRA2 over the corresponding periods. The values of the trends and their 95% confidence intervals in the two subperiods are denoted in blue for IGRA2 and in red for GPS RO, all statistically significant at the 95% confidence level (indicated by double asterisks). (**B**) Trends in zonal-mean *H* from IGRA2 are compared between the two subperiods (1980–2000 in solid green line and 2001–2020 in solid purple line) and also from GPS RO over 2001–2020 (dashed purple line). The *x* axis is shown on the cosine latitude scale. The error bars indicate the 95% confidence intervals for the trends. In the time series, the effects of volcanic eruptions, ENSO, and QBO have been statistically removed. (**C**) The same as (B) but for trends in zonal-mean *H* from RAOBCORE (dashed line) and RICH (solid line) over the two subperiods (1980–2000 in green and 2001–2020 in purple).

Downloaded from https://www.science.org at Universitaet Graz on December 06, 2021

globe (*5*) and other regions (*6*, *28*). For the second subperiod of 2001–2020, a comparable increase of *H*, 53.3 ± 6.7 m/decade is observed in IGRA2 (Fig. 1A and fig. S4B). In the same period, the trend in *H* in satellite GPS RO data is 44.4 ± 8.1 m/decade, and the monthly anomalies of *H* in GPS RO are closely correlated with those in IGRA2 [the correlation coefficient (*r*) is 0.84; similar to *H* in IGRA2, *H* in GPS RO is also calculated based on single profiles]. The *H* trends by latitude over 2001–2020 are similar to those over 1980–2000 in IGRA2 (Fig. 1B). In both IGRA2 and GPS RO, a rise of *H* over 2001–2020 prevails in all latitudinal bands with larger trends around 30°N to 40°N reaching about 100 m/decade. The maximum *H* trend around 30°N to 40°N possibly includes effects from a tropical expansion and poleward shift of the subtropical jet over the past four decades (*29*–*31*), which is associated with enhanced tropospheric warming and lower stratospheric cooling in the mid-latitudes (*14*, *29*). In RAOBCORE and RICH (Fig. 1C), the latitudinal variation in the *H* trend is more similar to that in IGRA2 over 2001–2020 than over 1980–2000. The relative differences in the *H* trends between the original and natural variability–removed time series in all datasets are less than 30% for both subperiods (Table 1), demonstrating that anthropogenic forcings are the primary drivers for the changes in *H*.

Table 1. Trends in tropopause height (*H*), tropospheric temperature (T_{TRO}), and stratospheric temperature (T_{STR}). The trends in *H* and their 95% confidence intervals are listed for the NH (20°N to 80°N) over 1980–2000 and 2001–2020, based on the radiosonde IGRA2, RAOBCORE, and RICH data. In addition, trends in *H* over 2001–2020 based on the GPS RO data are shown. The trends are derived from the natural variability–removed time series (A) in which the effects of volcanic eruptions, ENSO, and QBO have been statistically removed (Figs. 1 and 4) and from the original time series (B). All trends are statistically significant at the 95% confidence level.

A. Trends in the natural variability–removed time series

Trend	Data source	1980–2000	2001–2020
H (m/decade)	IGRA2	50.3 ± 7.2	53.3 ± 6.7
	GPS RO	–	44.4 ± 8.1
	RAOBCORE	83.7 ± 7.2	76.9 ± 9.4
	RICH	74.0 ± 7.0	79.8 ± 9.9
T_{TRO} (K/decade)	IGRA2	0.17 ± 0.03	0.31 ± 0.02
	RAOBCORE	0.20 ± 0.03	0.29 ± 0.02
	RICH	0.20 ± 0.03	0.33 ± 0.02
T_{STR} (K/decade)	IGRA2	−0.58 ± 0.05	−0.14 ± 0.04
	RAOBCORE	−0.41 ± 0.05	−0.14 ± 0.04
	RICH	−0.44 ± 0.05	−0.10 ± 0.04

B. Trends in the original time series

Trend	Data source	1980–2000	2001–2020
H (m/decade)	IGRA2	57.8 ± 9.8	58.8 ± 10.4
	GPS RO	–	56.8 ± 12.1
	RAOBCORE	102.2 ± 12.4	75.0 ± 10.9
	RICH	92.2 ± 12.8	78.4 ± 11.6
T_{TRO} (K/decade)	IGRA2	0.18 ± 0.04	0.34 ± 0.04
	RAOBCORE	0.22 ± 0.04	0.32 ± 0.04
	RICH	0.23 ± 0.04	0.36 ± 0.03
T_{STR} (K/decade)	IGRA2	−0.72 ± 0.08	−0.09 ± 0.06
	RAOBCORE	−0.52 ± 0.07	−0.13 ± 0.06
	RICH	−0.56 ± 0.07	−0.09 ± 0.06

Responses of tropopause height to temperature variations in the troposphere and stratosphere

Variability in tropopause height is closely related to the thermal structure below and above (*5*, *8*, *32*). On the monthly scale (Fig. 2A), monthly anomalies of tropopause height are positively correlated with tropospheric temperature anomalies and negatively correlated with stratospheric temperature anomalies. Vertically, the maximum correlation coefficient between *H* and temperature (r_{max}) is 0.74 around 400 hPa and the minimum correlation coefficient (r_{min}) is −0.64 around 100 hPa, consistent with previous studies (*5*, *32*). The correlation between *H* and vertical temperature profiles on the monthly scale is similar to that on the synoptic scale presented in literature (*5*), which is linked to the balanced dynamical structure in cyclones and anticyclones (*33*). The similar vertical variations in the correlations on monthly and synoptic scales suggest that the accumulated effect of synoptic variability, in the troposphere and lower stratosphere, can influence monthly temperature variability and, in turn, modulate monthly anomalies in *H*. Quantitatively, at the altitude of r_{max}, the regression coefficient between *H* and tropospheric temperature averaged over the NH is ~220 m/K over 1980–2020, while at the altitude of r_{min}, the averaged regression coefficient between *H* and stratospheric temperature is about −170 m/K (Fig. 2B). The responses of *H* to variations in tropospheric temperature (T_{TRO}; see Materials and Methods for its calculation) and stratospheric temperature (T_{STR}; see Materials and Methods for its calculation) are further investigated on the multidecadal scale by analyzing relationships between derived trends in *H* and those in T_{TRO} and T_{STR} across the different stations and for different periods (see Materials and Methods). For the decadal-scale variations, we find that the trends in *H* and those in T_{TRO} are positively correlated

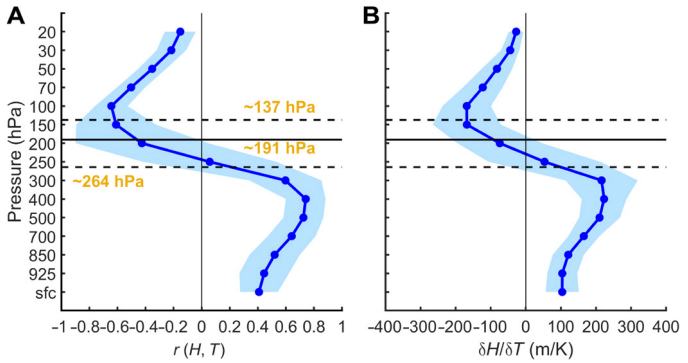


Fig. 2. Vertical profile of the correlation between *H* and temperature at a given altitude. (**A**) Mean correlation coefficients (*r*) between deseasonalized monthly anomalies of *H* and temperature at different altitudes in the troposphere and stratosphere over 1980–2020. The shaded area represents ±SD. Each value of *r* shown is a mean over 149 stations in the NH. The mean *H* (solid horizontal line) and its ±SD (dashed horizontal line) are also indicated. For presentation, altitudes are converted to pressures. (**B**) The same as (A) but for the vertical profile of the regression coefficients (m/K) between *H* and temperature at a given altitude. The time series of monthly anomalies used here include the signals of volcanic eruptions, ENSO, and QBO.

Downloaded from https://www.science.org at Universitaet Graz on December 06, 2021

across the different stations and significant at the 95% level, ranging over 0.2 to 0.8 (Fig. 3A) with a mean correlation of 0.49. In contrast, the trends in H and those in T_{STR} are all negatively correlated, ranging from −0.6 to zero with a mean of −0.32 and most (96%) being statistically significant (Fig. 3C). To account for temporal autocorrelation, the significance of the mean r between trends in H and those in T_{TRO} and T_{STR} is tested using a bootstrap method [(*34*); see Materials and Methods]. The results indicate that both the mean r values are significant at the 95% confidence level, with confidence intervals of ±0.25 for T_{TRO} and ±0.19 for T_{STR}. Such a significant relationship between the trends in H and T_{TRO} (Fig. 3A) was not observed in the IGRA version 1 radiosonde data over 1980–2004 (*5*). With IGRA2, we also reveal a closer association between the trends of H and of T_{TRO} than that between the trends of H and of T_{STR} in the NH over 1980–2020, as well as over 1980–2004 [the same period as in (*5*)]. These new results may be partially due to better calibration, more station records, and longer station records in IGRA2, especially in the NH. Another reason may be related to the difference in the study domains between this study and the previous study of (*5*), as the latter considered H over the entire globe, and variability in the thermal structures above and below the tropopause differs significantly with latitude (*14*, *21*). The correlation between the trends of H and of T_{STR} in Fig. 3C is weaker than previously reported from observations for the globe (*5*) and model simulations for the NH (*9*). In addition to the differences in radiosonde data versions and study domains between this and the previous studies discussed above, the weaker correlation in the trends of H and of T_{STR} from this study may also be related to the observed inflection point in stratospheric cooling near the years of 1995–2000 (the specific inflection point might vary with region) (*10*, *12*, *13*, *35*), while tropospheric temperature keeps rising (*14*, *21*). The link between H and T_{STR} is generally weaker if the analysis period encompasses the inflection point of stratospheric temperature.

Quantitatively, by applying a multiple linear regression model and using T_{TRO} and T_{STR} trends as two predictors for the H trend (see Materials and Methods), the mean response of decadal trends in H is estimated to be 172 m/K to T_{TRO} (Fig. 3B) and −73 m/K to T_{STR} (Fig. 3D) in the NH over 1980–2020, demonstrating a larger response in H to the variation in T_{TRO} than to that in T_{STR}. Although this is the case over 1980–2020 and the two subperiods (table S2), there are differences in the regression coefficient between trends of H and T_{TRO} (or T_{STR}) among different periods, indicating that the quantitative response of H to the change in T_{TRO} or T_{STR} is influenced by the evolution of long-term trends in T_{TRO} and T_{STR}.

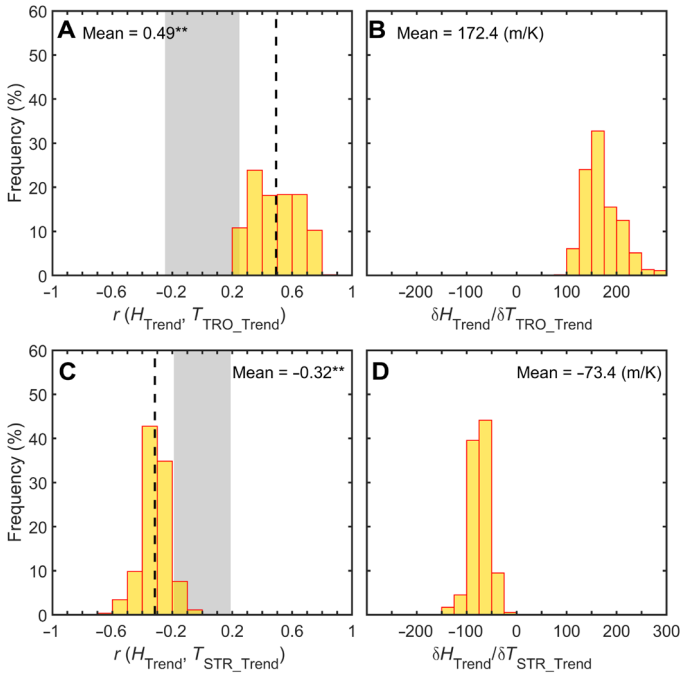


Fig. 3. Histograms of correlation and regression slope between trends of *H* and T_{TRO} and between trends of *H* and T_{STR}. Histograms of the correlation coefficients (r) between derived trends of H and T_{TRO} (**A**) and T_{STR} (**C**) in the NH over 1980–2020. Each r is a correlation coefficient between the trends in the two corresponding variables (e.g., the trend of H versus the trend of T_{TRO}) across the 149 stations over a specified period. All possible periods between 1980 and 2020 longer than 10 years are considered; thus, periods are between 10 and 41 years, and this results in 528 sample values of r. The mean r, shown in text and by the vertical dashed line, is significant at the 95% confidence level, indicated by double asterisks. The gray shaded areas indicate the "null hypothesis" regions for the confidence level, which is determined with consideration of autocorrelation. The corresponding regression coefficients between the trends of H and T_{TRO} (**B**) and T_{STR} (**D**) are also shown, which are determined from a multiple linear regression model that takes the trends of T_{TRO} and T_{STR} as two predictors for the trend of H.

The relative importance of tropospheric warming and stratospheric cooling to *H* rising

Analyzing the long-term trends of T_{TRO} and T_{STR} is useful for assessing their roles in modulating the trend in H. Over 1980–2000, the IGRA2 radiosonde data show that the mean T_{TRO} rises at 0.17 ± 0.03 K/decade (Fig. 4A), while T_{STR} decreases at −0.58 ± 0.05 K/decade (Fig. 4B). After 2000, warming of T_{TRO} is amplified with a rate of 0.31 ± 0.02 K/decade, while cooling of T_{STR} slows down with a rate of −0.14 ± 0.04 K/decade (Fig. 4). As discussed, tropospheric warming is associated with increasing GHGs, while stratospheric cooling is associated with both stratospheric ozone depletion and increasing GHGs. After the late 1990s, partial recovery of stratospheric ozone has been observed from satellite and ozonesonde data in both NH and SH (*36*–*38*). The ozone assessment by the World Meteorological Organization (WMO) (*39*) stated that "outside the polar regions, upper stratospheric ozone has increased by 1–3% per decade since 2000." Total column ozone from satellite observations has stabilized since the late 1990s (*40*). The enhanced rate of tropospheric warming and reduced rate of stratospheric cooling after 2000 are further illustrated in fig. S3 (B and C) (long-term evolution) and in fig. S5 (spatial variations). The slowdown in tropospheric warming over the period 2002–2013 was strongly influenced by weak low-latitude temperature trends (*17*), pointing to a driver at low latitudes such as Pacific variability (*15*, *18*). After weaker warming in the early 2000s, temperature increased during the development of El Niño conditions in 2014–2016 (*20*). The present acceleration of tropospheric warming after 2014 results from further continuous increase in GHG emissions and internal climate variability, with the onset of a positive phase of the IPO in 2014 (*19*), which represents ENSO-like variations on an interdecadal scale (*41*). Overall, the warming rate of T_{TRO} has increased since 2001 compared with the earlier decades (*14*), which is associated with increases in sea surface temperatures (*21*). Comparing the T_{TRO} trends between the original and natural variability–removed time series over 2001–2014, we found that the trend is 0.09 ±

Downloaded from https://www.science.org at Universitaet Graz on December 06, 2021

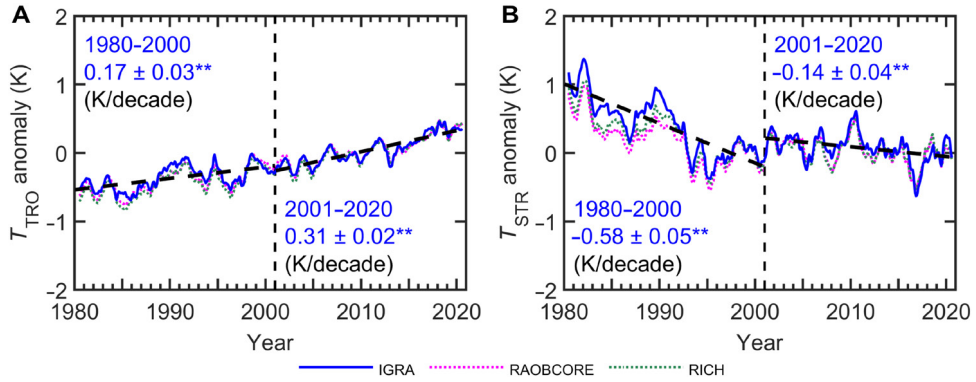


Fig. 4. Time series of tropospheric temperature (T_{TRO}) and lower stratospheric temperature (T_{STR}) in the NH over the time period 1980–2020. As in Fig. 1A, the solid blue, dashed purple, and dashed green lines show the time series of (T_{TRO}) (**A**) and (T_{STR}) (**B**) from the radiosonde IGRA2, RAOBCORE, and RICH data, respectively, smoothed with an 11-month running mean, while the dashed thick black lines denote the linear trends in IGRA2 over the indicated periods. The linear trends in IGRA2, denoted in the text, are all statistically significant at the 95% confidence level (indicated by double asterisks). The linear trends in RAOBCORE and RICH are listed in Table 1A. In the time series, the effects of volcanic eruptions, ENSO, and QBO have been statistically removed.

0.04 K/decade for the former and 0.21 ± 0.04 K/decade for the latter, indicating the importance of ENSO to suppressing tropospheric warming over 2001–2014. We further compare T_{TRO} and T_{STR} in IGRA2 with those in RAOBCORE and RICH. In terms of magnitude, interannual variation, and trend (Fig. 4 and Table 1), T_{TRO} and T_{STR} in RAOBCORE and RICH are highly consistent with those in IGRA2 with minor differences. For example, over 1980–2000, the magnitude of T_{STR} cooling trend is lower in RAOBCORE and RICH than in IGRA2 (Fig. 4B and Table 1).

Over 1980–2000, both tropospheric warming and stratospheric cooling cause H to rise. In comparison, over 2001–2020, the trend in tropospheric warming increases, while the trend in stratospheric cooling subsided (Fig. 4). As the trends in H for the two subperiods are comparable, we infer that after 2000, the effect of stratospheric cooling on rising H is reduced, which is compensated by the enhanced effect of tropospheric warming on rising H. Therefore, tropospheric warming plays a larger role in elevating H over 2001–2020 than over 1980–2000. To further evaluate the contributions of these two factors to H rise, we combine the response rate of H to the variations in T_{TRO} and T_{STR} (table S2) and the trends of T_{TRO} and T_{STR} (Table 1A) and thus estimate that the changes in T_{TRO} and T_{STR} over 2001–2020 contributed to H rise at rates of 54 ± 3 and 14 ± 4 m/decade, respectively. In terms of fractional contribution, the variations in T_{TRO} and T_{STR} contribute 79 and 21% to H rise, if we ignore other minor contributing factors discussed by Santer *et al.* (*4*). In comparison, over 1980–2000, using the relevant numbers in Table 1A and table S2, the corresponding contributions of T_{TRO} and T_{STR} are estimated to be 32 ± 6 and 31 ± 3 m/decade, equivalent to fractional contributions of 51 and 49%, respectively. Therefore, the contributions of T_{TRO} and T_{STR} to H rise are comparable before the inflection point around 1995–2000, while H rise after 2000 is primarily due to tropospheric warming.

DISCUSSION

Both the trend analysis (Figs. 1 and 4) and correlation analysis on monthly and multidecadal scales (Figs. 2 and 3) indicate that under a combined influence of the continuous increase in GHG emissions and partial recovery of stratospheric ozone, the H rise in the NH since 2000 is mainly attributable to the warming of the troposphere. The role that tropospheric warming plays in elevating H in the NH dominates over 2001–2020 in both the original and natural variability–removed time series of the radiosonde data. Overall, H in the NH is more sensitive to the temperature variability in the troposphere than in the stratosphere (Fig. 3). These conclusions appear robust as the trends in H and those in T_{TRO} (or T_{STR}) are correlated at highly significant levels based on large samples over multiple decades. This study uses recently updated radiosonde observations, combined with GPS RO satellite observations and homogenized radiosonde data, to reveal a clear long-term trend in H in the NH over 20°N to 80°N. After major natural variability is removed, a continuous rise trend in H remains. This provides an important piece of observational evidence for anthropogenic climate change.

MATERIALS AND METHODS

Data and trend calculations

IGRA is the largest and most comprehensive global radiosonde dataset (*24*, *42*). We used IGRA2 (*24*) with data from the 149 stations listed in table S1. The selection criteria for these stations are based on the length and completeness of their sounding records over 1980–2020 (the details are provided later). Stations with sufficient observations are mostly located from 20°N to 80°N over land (fig. S1). Tropopause height (H) was determined based on the WMO lapse-rate tropopause definition (*43*). We adopted the method of Zängl and Hoinka (*44*) to determine H from the geopotential height and temperature profiles in each of the radiosonde records. Individual soundings, which have different vertical resolutions, were linearly interpolated to a 200-m vertical grid before tropopause identification. For each sounding at a given station, the calculated H is valid only if (i) H is between 5 and 18 km, (ii) the sounding extends at least 2 km above H, and (iii) H is within a range of ±2 SDs of the 1980–2020 mean H at that station.

Considering that the tropopause has some diurnal variation, and radiosonde data are usually available for the standard hours (0000 and 1200 UT), we calculated the daily mean H if the data are available at both 0000 and 1200 UT. If the observational time is not at

Downloaded from https://www.science.org at Universitaet Graz on December 06, 2021

the standard hours, we treated the soundings between 2100 and 0300 UT as soundings at 0000 UT and between 0900 and 1500 UT as soundings at 1200 UTC. The monthly mean of H was calculated for a month if the daily means of H were available on at least 15 days in that month. If more than 30% of the stations have no monthly mean for a given month, the monthly mean for the entire NH is treated as missing data, which is the case for less than 2% of all months in the entire time series. The trend analysis was based on the time series of monthly anomalies of H, in which the monthly anomaly in each month was computed by subtracting the climatological monthly mean H in the corresponding month from the monthly mean H.

We also extracted temperature from each of the selected soundings at the surface and at 14 pressure levels including 925, 850, 700, 500, 400, 300, 250, 200, 150, 100, 70, 50, 30, and 20 hPa. Daily means, monthly means, and monthly anomalies at these pressure levels were calculated following the same procedure as for H. Tropospheric temperature (T_{TRO}) is represented by the mean of temperature at 850, 700, 500, 400, and 300 hPa, while lower stratospheric temperature (T_{STR}) is represented by the mean of temperature at 100 and 70 hPa. If any monthly value is unavailable at one of the corresponding pressure levels, T_{TRO} (or T_{STR}) in that month was treated as missing data.

While the IGRA2 radiosonde data provide a long-term historical record for climatic studies of tropopause height, temporal inhomogeneity in raw radiosonde data might cause biases in time series of tropopause height and affect trend analysis. Therefore, we also examined the homogenized radiosonde observations from the RAOBCORE and RICH data [version 1.7; (*26*, *27*)]. The version of the RICH data used is RICH-obs. To identify the break points, the RAOBCORE data use background forecasts from the 40-year European Centre for Medium-Range Weather Forecasts (ECMWF) reanalysis [ERA-40, 1958–1978; (*45*)] and the interim ECMWF reanalysis [ERA-Interim, 1979 to date; (*46*)] as references, while for the RICH-obs (shorted as RICH) data, the breaks are detected by comparing to reference series generated from neighboring radiosonde series. Over 1980–2020, gridded monthly means of temperature at 13 pressure levels (850, 700, 500, 400, 300, 200, 150, 100, 70, 50, 30, 20, and 10 hPa) with a horizontal resolution of 10° × 10° are provided by RAOBCORE and RICH.

According to the method introduced by Reichler *et al.* (*47*), we computed the monthly mean of tropopause pressure based on monthly means of temperature profiles provided by RAOBCORE and RICH. Using the hydrostatic approximation and the gas equation, we converted tropopause pressure to tropopause height in virtue of monthly means of geopotential height and temperature at 37 pressure levels (from 1000 to 1 hPa), which is obtained from the fifth-generation ECMWF reanalysis (ERA5) data (*48*). The selection criteria for the available grids are similar to those for the IGRA2 stations (the details are provided later). Similarly, the monthly means of T_{TRO} and T_{STR} were calculated.

The satellite-based GPS RO data have provided continuous temperature and pressure measurements as a function of height in the upper troposphere and lower stratosphere with high accuracy, high vertical resolution, and global coverage since 2001 (*49*–*51*). We used the latest Wegener Center (WEGC) multisatellite GPS RO data, OPSv5.6, available from May 2001 to December 2020. WEGC OPSv5.6 provides global upper-air satellite data in high quality from multiple RO satellite missions (including CHAMP, GRACE, SAC-C, Formosat-3/COSMIC, and Metop) (*25*, *52*) and thus is widely used for climate studies (*14*, *53*, *54*). H was estimated from each temperature profile following the WMO lapse-rate tropopause definition (*55*). Monthly zonal-mean H data are extracted at 5° latitudinal intervals between 80°S and 80°N. The monthly anomaly for a month in each of 5° zones was computed as the difference between the monthly mean H in that month and the corresponding climatological monthly mean H over 2001–2020 in that zone. Note that, for a better comparison between the radiosonde (including IGRA2, RAOBCORE, and RICH) and GPS RO data, we used the mean of H over 2001–2020, instead of the mean H over 1980–2020, to compute monthly anomalies of radiosonde H in Fig. 1. To be consistent with H anomalies for investigation of H responses to the changes in T_{TRO} and T_{STR}, the same treatment was applied to T_{TRO} and T_{STR} in Fig. 4. However, in Figs. 2 and 3 where only the IGRA2 radiosonde data are involved, monthly anomalies of H, T_{TRO}, and T_{STR} were calculated based on the corresponding climatological means over 1980–2020.

Volcanic eruptions, ENSO, and QBO are important natural phenomena that affect interannual variability of the tropopause (*49*, *56*), as well as atmospheric temperature in the troposphere and lower stratosphere (*53*, *57*–*59*). As our focus is on the tropopause trend induced by anthropogenic forcing, we removed these three natural influences from the original time series (fig. S2) before doing the trend analysis. This was done by applying multiple linear regression on the monthly anomalies of the relevant properties (i.e., H, T_{TRO}, and T_{STR}) at each of the radiosonde stations for the IGRA2 data, at each of the grids for the RAOBCORE and RICH data, and in each of the zonal bands for the GPS RO data (the details are provided later).

In comparison with the GPS RO data, monthly anomalies in each of 5° latitudinal zones for the IGRA2 data over 20°N to 80°N were calculated by averaging the H anomalies at all stations falling into the corresponding zone. Monthly 10°-zonal anomalies were calculated as the cosine-weighted averages of zonal anomalies in the two subordinate 5° latitudinal zones. Monthly anomalies in each of 10° zones for the RAOBCORE and RICH data were calculated by averaging the H anomalies at all available 10° × 10° grids falling into the corresponding 10° zone. The monthly anomalies in the NH over 20°N to 80°N were calculated as the cosine-weighted averages of all the monthly 10°-zonal anomalies between 20°N and 80°N. Both averaged anomalies in the NH over 20°N to 80°N and 10°-zonal anomalies were used in the trend analysis. Before the final trend analysis, the anomalies were filtered with an 11-month running mean (the current month, the five previous months, and the five following months) to remove perturbations on smaller scales. The significance levels of trends and correlations were tested with the F test and t test, respectively.

Overall, the annual means of H in IGRA2 and GPS RO are in very good agreement (the differences less than 100 m), while the annual means of H in RAOBCORE and RICH are generally higher by 300 to 400 m.

The selection criteria for the radiosonde stations and RAOBCORE and RICH grids

Each of the selected radiosonde stations must satisfy the following criteria:

1) At the station, the end year of the records is later than 2016 (inclusive) and the total number of soundings is larger than 10000.

2) In at least 80% of the years, the station has valid annual means of all the studied variables, including H; temperature at 850, 700,

Downloaded from https://www.science.org at Universitaet Graz on December 06, 2021

500, 400, 300, 250, 200, 150, 100, and 70 hPa; and layer mean temperature of 850 to 300 and 100 to 70 hPa, over each of the two subperiods (1980–2000 and 2001–2020). An annual mean in a year is valid only if the monthly means are available in at least 8 months and every season contains at least one monthly mean in that year.

Each of the selected grids in RAOBCORE and RICH (1980–2020) must satisfy the following criteria:

In at least 80% of the years, each grid has valid annual means of all the studied variables, including H; temperature at 850, 700, 500, 400, 300, 200, 150, 100, and 70 hPa; and layer mean temperature of 850 to 300 and 100 to 70 hPa, over each of the two subperiods (1980–2000 and 2001–2020). An annual mean in a year is valid only if the monthly means are available in at least 8 months and every season contains at least one monthly mean in that year.

Removal of natural variability in the original time series of the relevant variables

Volcanic eruptions, ENSO, and QBO are important natural forcings for the variations in the studied variables H, T_{TRO}, and T_{STR}. To remove these naturally forced variations, we applied a multiple linear regression model to fit the anomalies varying with time (t) over 1980–2020 at each of the stations for the IGRA2 data and each of the grids for the RAOBCORE and RICH data, and over 2001–2020 in each of the 5° zones for the GPS RO data.

The two large volcanic eruptions of El Chichón in April 1982 and Mount Pinatubo in June 1991 have complex impacts on H, T_{TRO}, and T_{STR}, persisting for the following 2 to 3 years. Meanwhile, El Niño events can raise tropospheric temperatures (*57*). Therefore, we first removed the volcano-related anomalies by regressing the anomalies of H, T_{TRO}, and T_{STR} against a proxy time series for volcanic intensity, which is the Northern Hemispheric monthly mean stratospheric aerosol optical depth (SAOD) at 550 nm (*60*). Note that monthly anomalies of H, T_{TRO}, and T_{STR} respond to large volcanoes, ENSO, and QBO with lags of various lengths (generally less than 12 months) at different stations, grids, or latitudinal zones. Therefore, lag-correlation regression analyses (*57*) were applied.

Take H as an example. In step 1, for H at a station, at a grid, or in a latitudinal zone, we found the time lag at which the correlation between SAOD and H is the largest. Then, we regressed the monthly anomalies of H against the monthly SAOD at that lag (Eqs. 1 and 2).

In step 2, we searched for the time lags giving the highest correlations between H and the ENSO index, and between H and the QBO proxy. Then, we made multiple regression of monthly anomalies of H against the monthly ENSO index and QBO proxy at those lags (Eq. 3). In step 2, the data in the time series after the large volcanic eruptions of El Chichón (April 1982) and Mount Pinatubo (June 1991) over 3 years were ignored to avoid any confusion of these signals.

In summary, monthly anomalies of H over 1980–2020 at a station in IGRA2 or at a grid in RAOBCORE or RICH or over 2001–2020 in a latitudinal zone in GPS RO were fitted to the following equations

$$A(t) = \alpha_0 + c \times \mathrm{SAOD}(t + \tau 0) + \varepsilon(t) \quad (1)$$

$$B(t) = A(t) - c \times \mathrm{SAOD}(t + \tau 0) \quad (2)$$

$$B(t) = \alpha + \beta \times \mathrm{QBO}(t + \tau 1) + \gamma \times \mathrm{ENSO}(t + \tau 2) + \delta(t) \quad (3)$$

where α_0, α, c, β, and γ are constants. $\tau 0$, $\tau 1$, and $\tau 2$ are the time lags for SAOD, QBO, and ENSO, respectively. $A(t)$ is the original monthly anomalies. $\alpha + \delta(t)$ in Eq. 3 is the residual term, which represents the resultant time series of H after removing the effects of volcanic eruptions, ENSO, and QBO. We used the multivariate ENSO index (*61*) to describe the ENSO variation and took the 70 hPa zonal winds at Singapore (*62*) as a QBO proxy. Following Weber *et al.* (*40*), the Northern Hemispheric monthly mean SAOD data at 550 nm were obtained from Sato *et al.* (*63*) for the period before 1990 and from Mills *et al.* (*64*) for the period over January 1990 to November 2015 for better descriptions of the two large volcanic eruptions. The SAOD data after December 2015 are unavailable.

The same procedures were followed for T_{TRO} and T_{STR}. Because QBO-related variations in the tropospheric temperature are negligible (*21*), no QBO effect is considered in the analysis of T_{TRO}. Therefore, $\beta = 0$ in Eq. 3 if $A(t)$ is the time series of T_{TRO} anomalies. For a better comparison between the radiosonde and GPS RO data, we separately applied the multiple linear regression model over 1980–2000 and 2001–2020 on the original radiosonde time series in Fig. 1. To be consistent, for illustrating the responses of H to the changes in T_{TRO} and T_{STR}, the same treatment was applied to T_{TRO} and T_{STR} in Fig. 4. The Supplementary Materials (fig. S2) shows the IGRA2 time series for $A(t)$ (pink), $B(t)$ (yellow), and $\alpha + \delta(t)$ (blue) for H, T_{TRO}, and T_{STR}, respectively, in the NH over 20°N to 80°N when the multiple linear regression model was separately applied. Because Fig. 3 only involves the IGRA2 radiosonde data, the multiple linear regression model was applied to the entire time series over 1980–2020 in Fig. 3.

Correlation between the trend of *H* and that of atmospheric temperature

To examine how the trend in H may be related to that in T_{TRO}, and how the relationships may depend on the length of the data record, we statistically assessed the relationships between the two trends. For a given period, we calculated the H and T_{TRO} trends at each of 149 radiosonde stations in the NH and then calculated a correlation coefficient (r) between the two trends using the 149 pairs of the variables. As the trend estimates over any long-term period are sensitive to the start and end years of the period (*65*, *66*), we considered all possible periods of which the lengths are 10 years or longer (i.e., up to 41 years) from 1980 to 2020. This provides 528 values of r between the trend in H and that in T_{TRO}. Similarly, 528 values of r between the trend in H and that in T_{STR} can be calculated. While this is a large number of r estimates, they will be autocorrelated because of the overlapping periods of the 528 time series for each variable. To estimate the confidence level of the mean r, we used a bootstrap method (*34*). The actual time series of monthly anomalies from 1980 to 2020 were divided into eight segments, and each segment has 60 values for monthly anomalies (the last segment has 72 values), and thus, the autocorrelation information is retained in each of the eight segments. We resampled these segments randomly and generated a new 492-month time series. On the basis of this new time series, we repeated the same statistical procedure and obtained a new mean r. The correlation between the trend in H and that in T_{TRO} (or T_{STR}) presented in the new generated time series is attributable to the temporal autocorrelation effects. A distribution of the statistical mean r was built up after we repeated the procedure many times. Therefore, taking the effect of autocorrelation into

Downloaded from https://www.science.org at Universitaet Graz on December 06, 2021

account, the confidence level of the mean r for the actual time series was determined using the Monte Carlo method with 5000 repetitions in this study. Specifically, the confident intervals were calculated statistically based on the mean r from each of the 5000 repetitions and the associated SD (Fig. 3, A and C) (*34*).

To quantify response of H to temperature changes in the troposphere and stratosphere, we developed a multiple linear regression model for each of the 528 periods. In the model, the trends in T_{TRO} and T_{STR} are two predictors for the trend in H. The regression coefficients of the two predictors were determined from the model (Fig. 3, B and D).

SUPPLEMENTARY MATERIALS

Supplementary material for this article is available at https://science.org/doi/10.1126/sciadv.abi8065

REFERENCES AND NOTES

1. A. C. Boothe, C. R. Homeyer, Global large-scale stratosphere-troposphere exchange in modern reanalyses. *Atmos. Chem. Phys.* **17**, 5537–5559 (2017).
2. J. R. Holton, P. H. Haynes, M. E. McIntyre, A. R. Douglass, R. B. Rood, L. Pfister, Stratosphere-troposphere exchange. *Rev. Geophys.* **33**, 403–439 (1995).
3. W. J. Randel, D. J. Seidel, L. L. Pan, Observational characteristics of double tropopauses. *J. Geophys. Res.* **112**, D07309 (2007).
4. B. D. Santer, M. F. Wehner, T. M. L. Wigley, R. Sausen, G. A. Meehl, K. E. Taylor, C. Ammann, J. Arblaster, W. M. Washington, J. S. Boyle, W. Bruggemann, Contributions of anthropogenic and natural forcing to recent tropopause height changes. *Science* **301**, 479–483 (2003).
5. D. J. Seidel, W. J. Randel, Variability and trends in the global tropopause estimated from radiosonde data. *J. Geophys. Res.* **111**, D21101 (2006).
6. D. J. Seidel, R. J. Ross, J. K. Angell, G. C. Reid, Climatological characteristics of the tropical tropopause as revealed by radiosondes. *J. Geophys. Res.* **106**, 7857–7878 (2001).
7. B. D. Santer, R. Sausen, T. M. L. Wigley, J. S. Boyle, K. AchutaRao, C. Doutriaux, J. E. Hansen, G. A. Meehl, E. Roeckner, R. Ruedy, G. Schmidt, K. E. Taylor, Behavior of tropopause height and atmospheric temperature in models, reanalyses, and observations: Decadal changes. *J. Geophys. Res.* **108**, ACL 1-1–ACL 1-22 (2003).
8. B. D. Santer, T. M. L. Wigley, A. J. Simmons, P. W. Kallberg, G. A. Kelly, S. M. Uppala, C. Ammann, J. S. Boyle, W. Bruggemann, C. Doutriaux, M. Fiorino, C. Mears, G. A. Meehl, R. Sausen, K. E. Taylor, W. M. Washington, M. F. Wehner, F. J. Wentz, Identification of anthropogenic climate change using a second-generation reanalysis. *J. Geophys. Res.* **109**, D21104 (2004).
9. S.-W. Son, L. M. Polvani, D. W. Waugh, T. Birner, H. Akiyoshi, R. R. Garcia, A. Gettelman, D. A. Plummer, E. Rozanov, The impact of stratospheric ozone recovery on tropopause height trends. *J. Climate* **22**, 429–445 (2009).
10. A. C. Maycock, W. J. Randel, A. K. Steiner, A. Y. Karpechko, J. Christy, R. Saunders, D. W. J. Thompson, C.-Z. Zou, A. Chrysanthou, N. L. Abraham, H. Akiyoshi, A. T. Archibald, N. Butchart, M. Chipperfield, M. Dameris, M. Deushi, S. Dhomse, G. Di Genova, P. Joeckel, D. E. Kinnison, O. Kirner, F. Ladstädter, M. Michou, O. Morgenstern, F. O'Connor, L. Oman, G. Pitari, D. A. Plummer, L. E. Revell, E. Rozanov, A. Stenke, D. Visioni, Y. Yamashita, G. Zeng, Revisiting the mystery of recent stratospheric temperature trends. *Geophys. Res. Lett.* **45**, 9919–9933 (2018).
11. C. McLandress, T. G. Shepherd, A. I. Jonsson, T. von Clarmann, B. Funke, A method for merging nadir-sounding climate records, with an application to the global-mean stratospheric temperature data sets from SSU and AMSU. *Atmos. Chem. Phys.* **15**, 9271–9284 (2015).
12. R. Philipona, C. Mears, M. Fujiwara, P. Jeannet, P. Thorne, G. Bodeker, L. Haimberger, M. Hervo, C. Popp, G. Romanens, W. Steinbrecht, R. Stubi, R. Van Malderen, Radiosondes show that after decades of cooling, the lower stratosphere is now warming. *J. Geophys. Res. Atmos.* **123**, 12509–12522 (2018).
13. W. J. Randel, L. Polvani, F. Wu, D. E. Kinnison, C.-Z. Zou, C. Mears, Troposphere-stratosphere temperature trends derived from satellite data compared with ensemble simulations from WACCM. *J. Geophys. Res. Atmos.* **122**, 9651–9667 (2017).
14. A. K. Steiner, F. Ladstädter, W. J. Randel, A. C. Maycock, Q. Fu, C. Claud, H. Gleisner, L. Haimberger, S. -P. Ho, P. Keckhut, T. Leblanc, C. Mears, L. M. Polvani, B. D. Santer, T. Schmidt, V. Sofieva, R. Wing, C. -Z. Zou, Observed temperature changes in the troposphere and stratosphere from 1979 to 2018. *J. Climate* **33**, 8165–8194 (2020).
15. A. Dai, J. C. Fyfe, S.-P. Xie, X. Dai, Decadal modulation of global surface temperature by internal climate variability. *Nat. Clim. Chang.* **5**, 555–559 (2015).
16. J. C. Fyfe, G. A. Meehl, M. H. England, M. E. Mann, B. D. Santer, G. M. Flato, E. Hawkins, N. P. Gillett, S.-P. Xie, Y. Kosaka, N. C. Swart, Making sense of the early-2000s warming slowdown. *Nat. Clim. Chang.* **6**, 224–228 (2016).
17. H. Gleisner, P. Thejll, B. Christiansen, J. K. Nielsen, Recent global warming hiatus dominated by low-latitude temperature trends in surface and troposphere data. *Geophys. Res. Lett.* **42**, 510–517 (2015).
18. Y. Kosaka, S. -P. Xie, Recent global-warming hiatus tied to equatorial Pacific surface cooling. *Nature* **501**, 403–407 (2013).
19. L. Dong, M. J. McPhaden, The role of external forcing and internal variability in regulating global mean surface temperatures on decadal timescales. *Environ. Res. Lett.* **12**, 034011 (2017).
20. S. Hu, A. V. Fedorov, The extreme El Niño of 2015-2016 and the end of global warming hiatus. *Geophys. Res. Lett.* **44**, 3816–3824 (2017).
21. M. Shagngguan, W. Wang, S. Jin, Variability of temperature and ozone in the upper troposphere and lower stratosphere from multi-satellite observations and reanalysis data. *Atmos. Chem. Phys.* **19**, 6659–6679 (2019).
22. R. Sausen, B. D. Santer, Use of changes in tropopause height to detect human influences on climate. *Meteorol. Z.* **12**, 131–136 (2003).
23. P. Pisoft, P. Sacha, L. M. Polvani, J. A. Añel, L. de la Torre, R. Eichinger, U. Foelsche, P. Huszar, C. Jacobi, J. Karlicky, A. Kuchar, J. Miksovsky, M. Zak, H. E. Rieder, Stratospheric contraction caused by increasing greenhouse gases. *Environ. Res. Lett.* **16**, 064038 (2021).
24. I. Durre, R. S. Vose, X. Yin, S. Applequist, J. Arnfield, Integrated Global Radiosonde Archive (IGRA) version 2, NOAA/National Centers for Environmental Information, **10**, V5X63X0Q (2016); https://doi.org/10.7289/V5X63K0Q.
25. EOPAC Team, GNSS Radio Occultation Record (OPS 5.6 2001–2020), Wegener Center, University of Graz, Austria (2021); https://doi.org/10.25364/WEGC/OPS5.6:2021.1.
26. L. Haimberger, Homogenization of radiosonde temperature time series using innovation statistics. *J. Climate* **20**, 1377–1403 (2007).
27. L. Haimberger, C. Tavolato, S. Sperka, Homogenization of the global radiosonde temperature dataset through combined comparison with reanalysis background series and neighboring stations. *J. Climate* **25**, 8108–8131 (2012).
28. E. J. Highwood, B. J. Hoskins, P. Berrisford, Properties of the Arctic tropopause. *Q. J. R. Meteorol. Soc.* **126**, 1515–1532 (2000).
29. Q. Fu, C. M. Johanson, J. M. Wallace, T. Reichler, Enhanced mid-latitude tropospheric warming in satellite measurements. *Science* **312**, 1179 (2006).
30. D. J. Seidel, W. J. Randel, Recent widening of the tropical belt: Evidence from tropopause observations. *J. Geophys. Res.* **112**, D20113 (2007).
31. P. W. Staten, J. Lu, K. M. Grise, S. M. Davis, T. Birner, Re-examining tropical expansion. *Nat. Clim. Chang.* **8**, 768–775 (2018).
32. T. Schmidt, J. Wickert, G. Beyerle, S. Heise, Global tropopause height trends estimated from GPS radio occultation data. *Geophys. Res. Lett.* **35**, L11806 (2008).
33. B. J. Hoskins, M. E. McIntyre, A. W. Robertson, On the use and significance of isentropic potential vorticity maps. *Q. J. R. Meteorol. Soc.* **111**, 877–946 (1985).
34. B. Efron, Bootstrap methods: Another look at the jackknife. *Ann. Stat.* **7**, 1–26 (1979).
35. V. Aquila, W. H. Swartz, D. W. Waugh, P. R. Colarco, S. Pawson, L. M. Polvani, R. S. Stolarski, Isolating the roles of different forcing agents in global stratospheric temperature changes using model integrations with incrementally added single forcings. *J. Geophys. Res. Atmos.* **121**, 8067–8082 (2016).
36. J. Liu, D. W. Tarasick, V. E. Fioletov, C. McLinden, T. Zhao, S. Gong, C. Sioris, J. J. Jin, G. Liu, O. Moeini, A global ozone climatology from ozone soundings via trajectory mapping: A stratospheric perspective. *Atmos. Chem. Phys.* **13**, 11441–11464 (2013).
37. E. C. Weatherhead, S. B. Andersen, The search for signs of recovery of the ozone layer. *Nature* **441**, 39–45 (2006).
38. J. R. Ziemke, S. Chandra, Development of a climate record of tropospheric and stratospheric column ozone from satellite remote sensing: Evidence of an early recovery of global stratospheric ozone. *Atmos. Chem. Phys.* **12**, 5737–5753 (2012).
39. World Meteorological Organization (WMO), Executive Summary: Scientific assessment of ozone depletion: 2018, World Meteorological Organization, Global Ozone Research and Monitoring Project—Report No. 58, 67 pp., Geneva, Switzerland.
40. M. Weber, M. Coldewey-Egbers, V. E. Fioletov, S. M. Frith, J. D. Wild, J. P. Burrows, C. S. Long, D. Loyola, Total ozone trends from 1979 to 2016 derived from five merged observational datasets—The emergence into ozone recovery. *Atmos. Chem. Phys.* **18**, 2097–2117 (2018).
41. Y. Zhang, J. M. Wallace, D. S. Battisti, ENSO-like interdecadal variability: 1900-93. *J. Climate* **10**, 1004–1020 (1997).
42. I. Durre, R. S. Vose, D. B. Wuertz, Overview of the Integrated Global Radiosonde Archive. *J. Climate* **19**, 53–68 (2006).
43. World Meteorological Organization (WMO), Meteorology—A three-dimensional science: Second session of the Commission for Aerology [WMO Bulletin IV(4), WMO, Geneva, 1957], pp. 134–138.

Downloaded from https://www.science.org at Universitaet Graz on December 06, 2021

44. G. Zängl, K. P. Hoinka, The tropopause in the polar regions. *J. Climate* **14**, 3117–3139 (2001).
45. S. M. Uppala, P. W. Kållberg, A. J. Simmons, U. Andrae, V. Da Costa Bechtold, M. Fiorino, J. K. Gibson, J. Haseler, A. Hernandez, G. A. Kelly, X. Li, K. Onogi, S. Saarinen, N. Sokka, R. P. Allan, E. Andersson, K. Arpe, M. A. Balmaseda, A. C. M. Beljaars, L. Van De Berg, J. Bidlot, N. Bormann, S. Caires, F. Chevallier, A. Dethof, M. Dragosavac, M. Fisher, M. Fuentes, S. Hagemann, E. Hólm, B. J. Hoskins, L. Isaksen, P. A. E. M. Janssen, R. Jenne, A. P. McNally, J.-F. Mahfouf, J.-J. Morcrette, N. A. Rayner, R. W. Saunders, P. Simon, A. Sterl, K. E. Trenberth, A. Untch, D. Vasiljevic, P. Viterbo, J. Woollen, The ERA-40 re-analysis. *Q. J. R. Meteorol. Soc.* **131**, 2961–3012 (2005).
46. D. P. Dee, S. M. Uppala, A. J. Simmons, P. Berrisford, P. Poli, S. Kobayashi, U. Andrae, M. A. Balmaseda, G. Balsamo, P. Bauer, P. Bechtold, A. C. M. Beljaars, L. van de Berg, J. Bidlot, N. Bormann, C. Delsol, R. Dragani, M. Fuentes, A. J. Geer, L. Haimberger, S. B. Healy, H. Hersbach, E. Hólm, L. Isaksen, P. Kållberg, M. Köhler, M. Matricardi, A. P. McNally, B. M. Monge-Sanz, J.-J. Morcrette, B.-K. Park, C. Peubey, P. de Rosnay, C. Tavolato, J.-N. Thépaut, F. Vitart, The ERA-Interim reanalysis: Configuration and performance of the data assimilation system. *Q. J. R. Meteorol. Soc.* **137**, 553–597 (2011).
47. T. Reichler, M. Dameris, R. Sausen, Determining the tropopause height from gridded data. *Geophys. Res. Lett.* **30**, 2042 (2003).
48. H. Hersbach, B. Bell, P. Berrisford, S. Hirahara, A. Horányi, J. Muñoz-Sabater, J. Nicolas, C. Peubey, R. Radu, D. Schepers, A. Simmons, C. Soci, S. Abdalla, X. Abellan, G. Balsamo, P. Bechtold, G. Biavati, J. Bidlot, M. Bonavita, G. De Chiara, P. Dahlgren, D. Dee, M. Diamantakis, R. Dragani, J. Flemming, R. Forbes, M. Fuentes, A. Geer, L. Haimberger, S. Healy, R. J. Hogan, E. Hólm, M. Janisková, S. Keeley, P. Laloyaux, P. Lopez, C. Lupu, G. Radnoti, P. de Rosnay, I. Rozum, F. Vamborg, S. Villaume, J.-N. Thépaut, The ERA5 global reanalysis. *Q. J. R. Meteorol. Soc.* **146**, 1999–2049 (2020).
49. T. Rieckh, B. Scherllin-Pirscher, F. Ladstädter, U. Foelsche, Characteristics of tropopause parameters as observed with GPS radio occultation. *Atmos. Meas. Tech.* **7**, 3947–3958 (2014).
50. B. Scherllin-Pirscher, A. K. Steiner, R. A. Anthes, M. J. Alexander, S. P. Alexander, R. Biondi, T. Birner, J. Kim, W. J. Randel, S.-W. Son, T. Tsuda, Z. Zeng, Tropical temperature variability in the UTLS: New insights from GPS radio occultation observations. *J. Climate* **34**, 2813–2838 (2021).
51. S.-W. Son, N. F. Tandon, L. M. Polvani, The fine-scale structure of the global tropopause derived from COSMIC GPS radio occultation measurements. *J. Geophys. Res.* **116**, D20113 (2011).
52. B. Angerer, F. Ladstädter, B. Scherllin-Pirscher, M. Schwaerz, A. K. Steiner, U. Foelsche, G. Kirchengast, Quality aspects of the Wegener Center multi-satellite GPS radio occultation record OPSv5.6. *Atmos. Meas. Tech.* **10**, 4845–4863 (2017).
53. A. K. Steiner, B. C. Lackner, F. Ladstädter, B. Scherllin-Pirscher, U. Foelsche, G. Kirchengast, GPS radio occultation for climate monitoring and change detection. *Radio Sci.* **46**, RS0D24 (2011).
54. A. K. Steiner, F. Ladstädter, C. O. Ao, H. Gleisner, S.-P. Ho, D. Hunt, T. Schmidt, U. Foelsche, G. Kirchengast, Y.-H. Kuo, K. B. Lauritsen, A. J. Mannucci, J. K. Nielsen, W. Schreiner, M. Schwärz, S. Sokolovskiy, S. Syndergaard, J. Wickert, Consistency and structural uncertainty of multi-mission GPS radio occultation records. *Atmos. Meas. Tech.* **13**, 2547–2575 (2020).
55. H. Wilhelmsen, F. Ladstädter, T. Schmidt, A. K. Steiner, Double tropopauses and the tropical belt connected to ENSO. *Geophys. Res. Lett.* **47**, e2020GL089027 (2020).
56. W. J. Randel, F. Wu, D. J. Gaffen, Interannual variability of the tropical tropopause derived from radiosonde data and NCEP reanalyses. *J. Geophys. Res.* **105**, 15509–15523 (2000).
57. G. Gu, R. F. Adler, Precipitation and temperature variations on the interannual time scale: Assessing the impact of ENSO and volcanic eruptions. *J. Climate* **24**, 2258–2270 (2011).
58. B. Scherllin-Pirscher, C. Deser, S. -P. Ho, C. Chou, W. J. Randel, Y. -H. Kuo, The vertical and spatial structure of ENSO in the upper troposphere and lower stratosphere from GPS radio occultation measurements. *Geophys. Res. Lett.* **39**, L20801 (2012).
59. H. Wilhelmsen, F. Ladstädter, B. Scherllin-Pirscher, A. K. Steiner, Atmospheric QBO and ENSO indices with high vertical resolution from GNSS radio occultation temperature measurements. *Atmos. Meas. Tech.* **11**, 1333–1346 (2018).
60. J. -P. Vernier, L. W. Thomason, J. -P. Pommereau, A. Bourassa, J. Pelon, A. Garnier, A. Hauchecorne, L. Blanot, C. Trepte, D. Degenstein, F. Vargas, Major influence of tropical volcanic eruptions on the stratospheric aerosol layer during the last decade. *Geophys. Res. Lett.* **38**, L12807 (2011).
61. K. Wolter, M. S. Timlin, El Nino/Southern Oscillation behaviour since 1871 as diagnosed in an extended multivariate ENSO index (MEI.ext). *Int. J. Climatol.* **31**, 1074–1087 (2011).
62. B. Naujokat, An update of the observed quasi-biennial oscillation of the stratospheric winds over the tropics. *J. Atmos. Sci.* **43**, 1873–1877 (1986).
63. M. Sato, J. E. Hansen, M. P. McCormick, J. B. Pollack, Stratospheric aerosol optical depths, 1850–1990. *J. Geophys. Res.* **98**, 22987–22994 (1993).
64. M. J. Mills, A. Schmidt, R. Easter, S. Solomon, D. E. Kinnison, S. J. Ghan, R. R. Neely III, D. R. Marsh, A. Conley, C. G. Bardeen, A. Gettelman, Global volcanic aerosol properties derived from emissions, 1990–2014, using CESM1(WACCM). *J. Geophys. Res. Atmos.* **121**, 2332–2348 (2016).
65. B. D. Santer, S. Solomon, G. Pallotta, C. Mears, S. Po-Chedley, Q. Fu, F. Wentz, C.-Z. Zou, J. Painter, I. Cvijanovic, C. Bonfils, Comparing tropospheric warming in climate models and satellite data. *J. Climate* **30**, 373–392 (2017).
66. B. D. Santer, S. Solomon, F. J. Wentz, Q. Fu, S. Po-Chedley, C. Mears, J. F. Painter, C. Bonfils, Tropospheric warming over the past two decades. *Sci. Rep.* **7**, 2336 (2017).
67. W. J. Randel, R. R. Garcia, N. Calvo, D. Marsh, ENSO influence on zonal mean temperature and ozone in the tropical lower stratosphere. *Geophys. Res. Lett.* **36**, L15822 (2009).

Acknowledgments: We thank the National Oceanic and Atmospheric Administration (NOAA) National Centers for Environmental Information (NCEI) for providing the IGRA radiosonde data. We are grateful to the WEGC EOPAC team for providing the WEGC GNSS RO OPSv5.6 data. We thank the comments and suggestions from the editor and three anonymous reviewers, which greatly help us improve this paper. We also thank colleagues and friends for valuable discussions and suggestions. **Funding:** This work was funded by the Chinese Ministry of Science and Technology National Key R&D Program of China (grant nos. 2019YFA0606803 and 2016YFA0600204). The National Center for Atmospheric Research is sponsored by the U.S. National Science Foundation. This work was partially supported by the COSMIC NSF-NASA Cooperative Agreement (grant no. 1522830), by the Canadian Space Agency (grant no. 17SUSOARTO), and by the Austrian Science Fund (FWF) under research grants P27724-NBL (VERTICLIM) and W1256-G15 (Doctoral Programme Climate Change: Uncertainties, Thresholds, and Coping Strategies). **Author contributions:** J.L. and L.M. conceived the study. L.M. developed the methodology and conducted data analysis under the supervision of J.L. W.J.R. provided critical guidance and advice. A.K.S., D.W.T., and L.W. contributed significantly to the work overall. A.K.S., H.W., and L.H. provided the GPS, RICH, and RAOBCORE data and guided application and interpretation of the data. J.L. and L.M. wrote the manuscript with valuable input from all coauthors. **Competing interests:** The authors declare that they have no competing interests. **Data and materials availability:** The radiosonde observations are openly provided by the National Oceanic and Atmospheric Administration (NOAA) National Centers for Environmental Information (NCEI), available online at https://ncdc.noaa.gov/. WEGC GNSS RO OPSv5.6 data are supported by the WEGC EOPAC team and are available online (see https://doi.org/10.25364/WEGC/OPS5.6:2021.1/). RAOBCORE/RICH data were downloaded from https://srvx1.img.univie.ac.at/webdata/haimberger/v1.7/. All data needed to evaluate the conclusions in the paper are present in the paper and/or the Supplementary Materials.

Submitted 31 March 2021
Accepted 17 September 2021
Published 5 November 2021
10.1126/sciadv.abi8065

Downloaded from https://www.science.org at Universitaet Graz on December 06, 2021

ScienceAdvances

Continuous rise of the tropopause in the Northern Hemisphere over 1980–2020

Lingyun MengJane LiuDavid W. TarasickWilliam J. RandelAndrea K. SteinerHallgeir WilhelmsenLei WangLeopold Haimberger

Sci. Adv., 7 (45), eabi8065. • DOI: 10.1126/sciadv.abi8065

View the article online
https://www.science.org/doi/10.1126/sciadv.abi8065
Permissions
https://www.science.org/help/reprints-and-permissions

Downloaded from https://www.science.org at Universitaet Graz on December 06, 2021

Use of think article is subject to the Terms of service

Science Advances (ISSN) is published by the American Association for the Advancement of Science. 1200 New York Avenue NW, Washington, DC 20005. The title *Science Advances* is a registered trademark of AAAS.
Copyright © 2021 The Authors, some rights reserved; exclusive licensee American Association for the Advancement of Science. No claim to original U.S. Government Works. Distributed under a Creative Commons Attribution NonCommercial License 4.0 (CC BY-NC).

Science Advances
AAAS

Supplementary Materials for

Continuous rise of the tropopause in the Northern Hemisphere over 1980–2020

Lingyun Meng, Jane Liu*, David W. Tarasick, William J. Randel*, Andrea K. Steiner, Hallgeir Wilhelmsen, Lei Wang, Leopold Haimberger

*Corresponding author. Email: janejj.liu@utoronto.ca (J.L.); randel@ucar.edu (W.J.R.)

Published 5 November 2021, *Sci. Adv.* **7**, eabi8065 (2021)
DOI: 10.1126/sciadv.abi8065

This PDF file includes:

Figs. S1 to S5
Tables S1 and S2
References

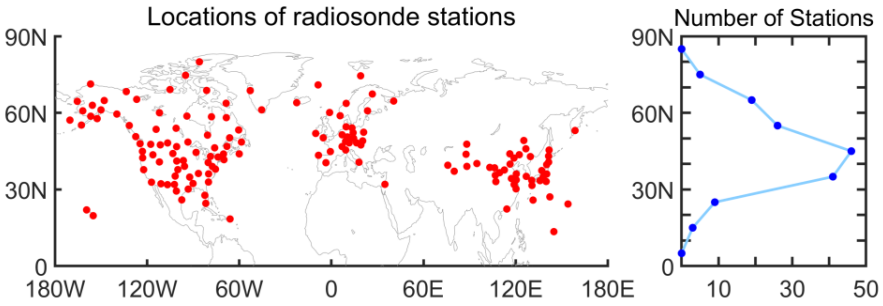


Fig. S1. Distribution of the radiosonde stations. Locations of the radiosonde stations used in this study and the number of stations in each 10° latitudinal band.

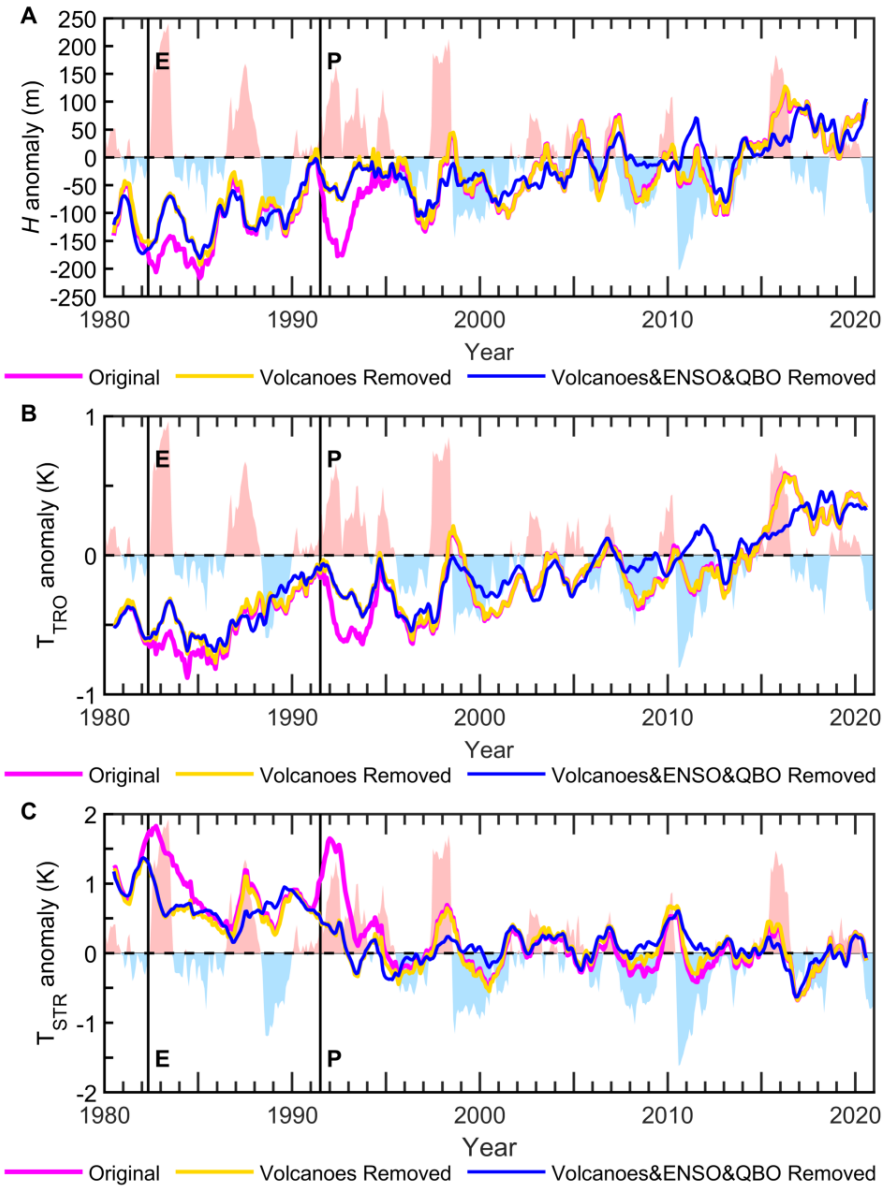


Fig. S2. The original and natural variability-removed time series of H, T_{TRO}, and T_{STR} in the IGRA2 radiosonde data. Time series of the 11-month running mean of monthly anomalies of H **(A)**, T_{TRO} **(B)**, and T_{STR} **(C)** in the original time series (pink line), as well as in the volcanic-effect-removed (yellow line), and volcanic-ENSO-QBO-effect-removed (blue line) time series in the Northern Hemisphere over 20°N to 80°N from 1980 to 2020. The two vertical black lines respectively indicate the large volcanic eruptions of El Chichón (April 1982) and Mount Pinatubo (June 1991). The shaded areas indicate the variations in the ENSO index over 1980-2020 with negative phases in light blue and positive phases in light pink. Note that the atmospheric response is lagging the ENSO index by about three months (*53, 58, 67*).

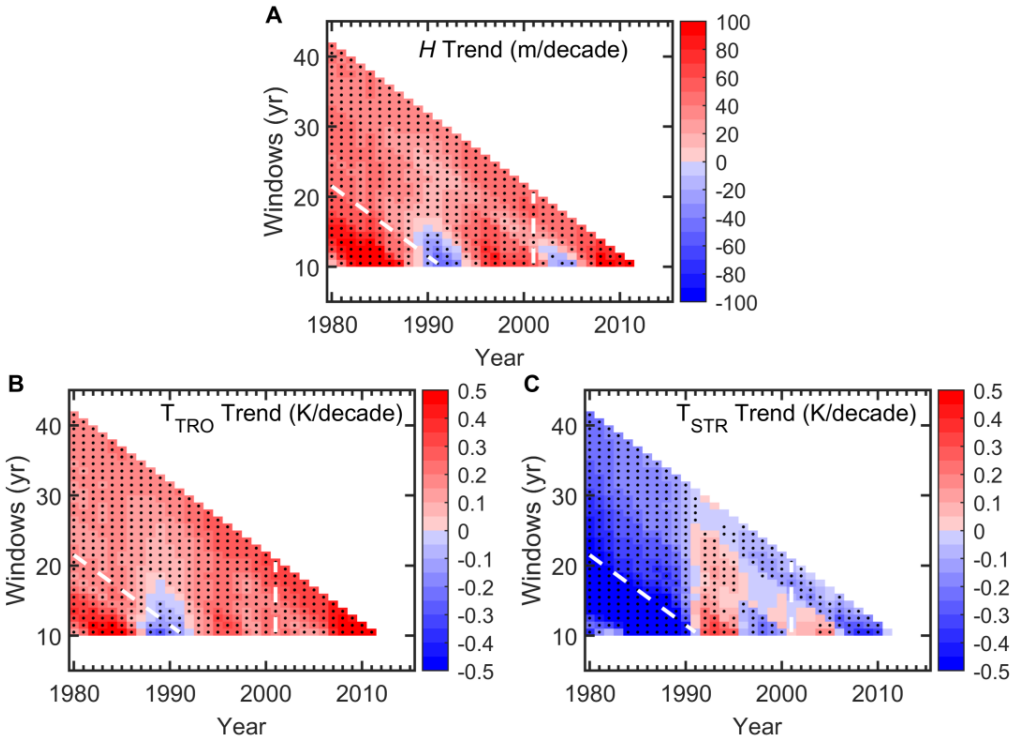


Fig. S3. Running windows for linear trends in H (A), T_{TRO} (B), and T_{STR} (C) over 1980-2020 in the IGRA2 radiosonde data. The x-axis indicates the start year, and the y-axis indicates the number of years since the start year. The inclined white line indicates all linear trends ending in 2000, while the vertical white line indicates all linear trends starting in 2001. Trends that are statistically significant at the 95% confidence level are indicated by black dots. Note that running windows with lengths less than 10 years are not considered and thus not shown.

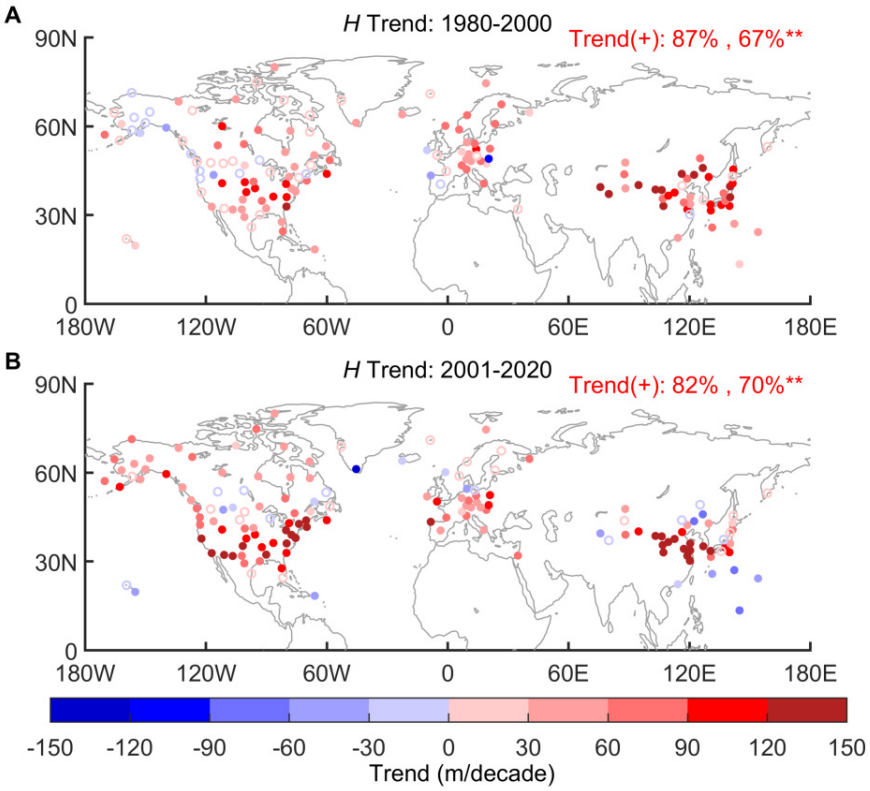


Fig. S4. The spatial distribution of the trend in *H* over 1980-2000 (A) and 2001-2020 (B) in the IGRA2 radiosonde data. Dots (circles) indicate statistically significant (insignificant) trends at the 95% confidence level. The red numbers in (A) and (B) indicate the percentage of stations with positive trends and with significant positive trends at the 95% confidence level indicated by double asterisks.

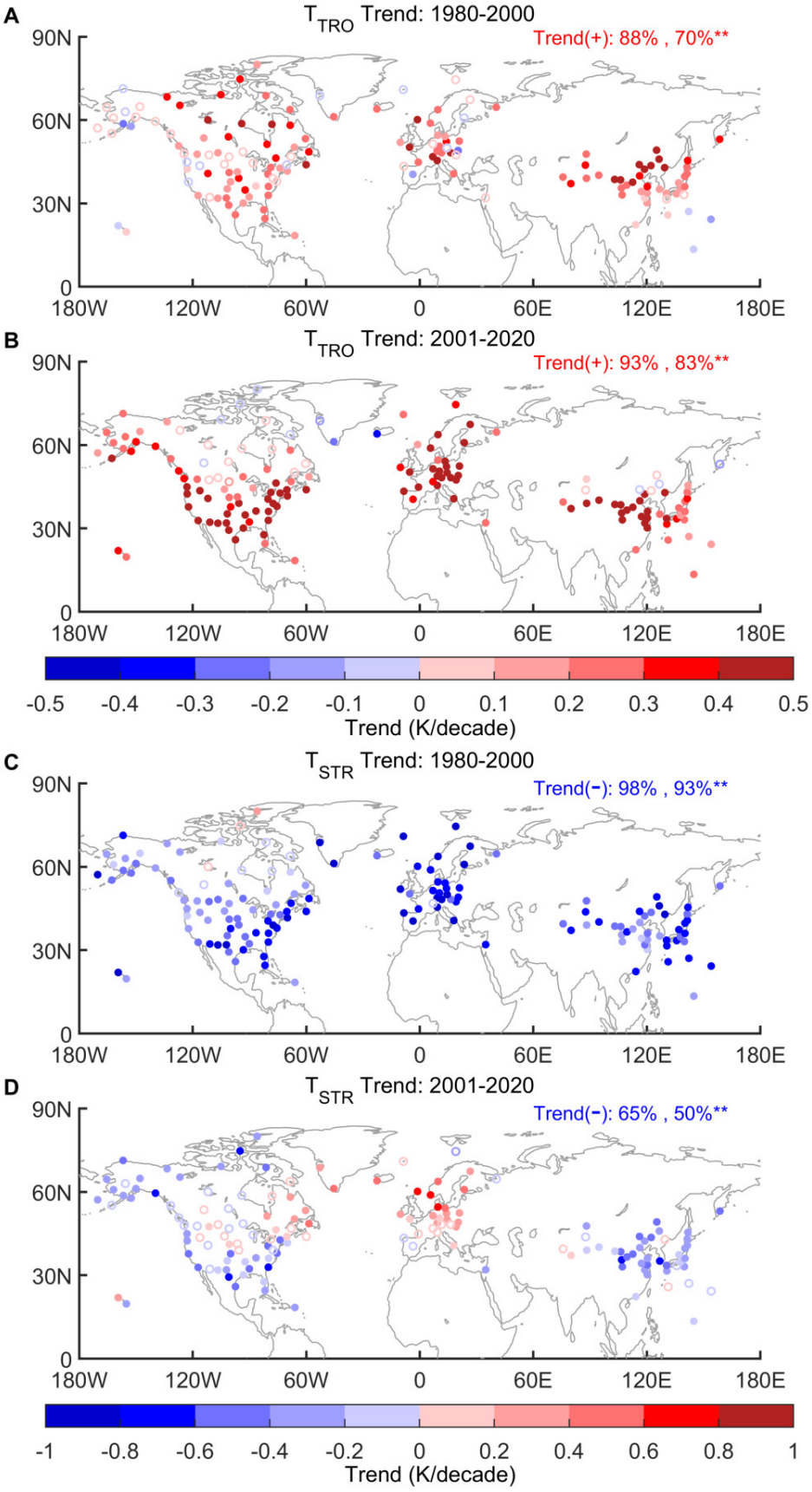

A
T_TRO Trend: 1980-2000
Trend(+): 88% , 70%**
B
T_TRO Trend: 2001-2020
Trend(+): 93% , 83%**
-0.5 -0.4 -0.3 -0.2 -0.1 0 0.1 0.2 0.3 0.4 0.5
Trend (K/decade)
C
T_STR Trend: 1980-2000
Trend(-): 98% , 93%**
D
T_STR Trend: 2001-2020
Trend(-): 65% , 50%**
-1 -0.8 -0.6 -0.4 -0.2 0 0.2 0.4 0.6 0.8 1
Trend (K/decade)
90N
60N
30N
0
180W 120W 60W 0 60E 120E 180E

Fig. S5. The spatial distribution of the trend in T_{TRO} (A and B) and T_{STR} (C and D) over 1980-2000 and 2001-2020 in the IGRA2 radiosonde data. Dots (circles) indicate statistically significant (insignificant) trends at the 95% confidence level. The numbers in red (blue) in a subplot indicate the percentage of stations with positive (negative) trends, and with significant positive (negative) trends at the 95% confidence level indicated by double asterisks.

Table S1. Information on the radiosonde stations selected for this study. The information includes latitude, longitude, the World Meteorological Organization Identification Number (ID), country, and the total number of missing monthly data of tropopause height over 1980-2020.

Station	Latitude	Longitude	ID	Country	Missing Data
WEATHER FORECAST OFFICE	13.48	144.79	91212	GQ	44
PR SAN JUAN/INT.	18.43	-65.99	78526	RQ	15
HI HILO HI	19.72	-155.06	91285	US	8
HI LIHUE	21.99	-159.35	91165	US	11
KOWLOON	22.33	114.17	45004	HK	25
MINAMITORISHIMA	24.29	153.98	47991	JA	35
FL KEY WEST/INT.	24.55	-81.79	72201	US	37
MINAMIDAITOJIMA	25.83	131.23	47945	JA	48
TX BROWNSVILLE/INT.	25.92	-97.42	72250	US	26
CHICHIJIMA	27.09	142.19	47971	JA	50
FL TAMPA BAY AREA	27.71	-82.4	72210	US	10
TX DEL RIO/INT.	29.37	-100.92	72261	US	2
LA LAKE CHARLES/MUN.	30.13	-93.22	72240	US	8
HANGZHOU	30.23	120.17	58457	CH	61
KAGOSHIMA	31.56	130.55	47827	JA	31
TX SANTA TERESA	31.87	-106.7	72364	US	5
NANJING	31.93	118.9	58238	CH	26
TX MIDLAND/MIDLAND REG. AIRTERM	31.94	-102.19	72265	US	4
BET DAGAN	32	34.82	40179	IS	33
AZ TUCSON	32.23	-110.96	72274	US	3
MS JACKSON/ALLEN C. THOMPSON FIEL	32.32	-90.08	72235	US	2
CA SAN DIEGO/MIRAMAR	32.83	-117.12	72293	US	1
SC CHARLESTON/MUN.	32.9	-80.03	72208	US	11
HANZHONG	33.07	107.03	57127	CH	39
HACHIJOJIMA	33.12	139.78	47678	JA	24
SHIONOMISAKI	33.45	135.76	47778	JA	25
FUKUOKA	33.58	130.38	47807	JA	6
SHEYANG	33.75	120.3	58150	CH	23
XUZHOU	34.28	117.15	58027	CH	28
HAMAMATSU AB	34.75	137.7	47681	JA	25
AR LITTLE ROCK/ADAMS FLD	34.84	-92.26	72340	US	0
GWANGJU AB	35.12	126.8	47158	KS	20
TX AMARILLO/INTL.	35.23	-101.71	72363	US	2
PINGLIANG	35.55	106.67	53915	CH	20
TATENO	36.06	140.13	47646	JA	6
QINGDAO	36.07	120.33	54857	CH	25
NC GREENSBORO/G.-HIGH PT.	36.1	-79.94	72317	US	4
TN NASHVILLE/OLD HICKORY	36.25	-86.56	72327	US	1
YAN AN	36.57	109.45	53845	CH	20
HOTAN	37.13	79.93	51828	CH	21
WAJIMA	37.39	136.9	47600	JA	7
TAIYUAN	37.62	112.58	53772	CH	22
CA OAKLAND/METROP. OAKLAND INT.	37.74	-122.22	72493	US	3
KS DODGE CITY/MUN.	37.76	-99.97	72451	US	0
VA WALLOPS ISLAND	37.93	-75.48	72402	US	17
YINCHUAN	38.47	106.2	53614	CH	17
MINQIN	38.63	103.08	52681	CH	21
VA STERLING	38.98	-77.49	72403	US	7
RUOQIANG	39.03	88.17	51777	CH	21
KS TOPEKA/MUN.	39.07	-95.63	72456	US	0
KASHI	39.48	75.75	51709	CH	25
AKITA	39.72	140.1	47582	JA	4
BEIJING	39.93	116.28	54511	CH	38
DUNHUANG	40.15	94.68	52418	CH	19
MADRID/BARAJAS RS	40.47	-3.58	8221	SP	24
PA PITTSBURGH	40.53	-80.22	72520	US	2
BRINDISI RDS	40.66	17.96	16320	IT	55

MISAWA AB	40.71	141.37	47580	JA	13
UT SALT LAKE CITY/INTNL UT.	40.77	-111.96	72572	US	4
NE NORTH PLATTE/LEE BIRD	41.13	-100.7	72562	US	1
NE VALLEY	41.32	-96.37	72558	US	3
MA CHATHAM	41.66	-69.96	74494	US	6
CHIFENG	42.3	118.83	54218	CH	63
OR MEDFORD/MEDFORD-JACKSON COUNTY	42.38	-122.88	72597	US	1
NY ALBANY	42.69	-73.83	72518	US	5
YANJI	42.87	129.5	54292	CH	60
NY BUFFALO/GREATER BUFFALO INT.	42.94	-78.72	72528	US	0
SAPPORO	43.06	141.33	47412	JA	19
LA CORUNA	43.37	-8.42	8001	SP	33
ID BOISE/MUN.	43.57	-116.21	72681	US	5
TONGLIAO	43.6	122.27	54135	CH	48
WU LU MU QI	43.78	87.62	51463	CH	57
ME GRAY	43.89	-70.26	74389	US	0
SABLE ISLAND	43.93	-60.01	71600	CA	24
XILIN HOT	43.95	116.12	54102	CH	40
SD RAPID CITY WFO	44.07	-103.21	72662	US	5
WI GREEN BAY/A.-STRAUBEL	44.5	-88.11	72645	US	8
BORDEAUX MERIGNAC	44.83	-0.69	7510	FR	14
OR SALEM/MCNARY	44.91	-123.01	72694	US	3
WAKKANAI	45.42	141.68	47401	JA	10
MILANO LINATE RDS	45.46	9.28	16080	IT	4
HARBIN	45.93	126.57	50953	CH	30
MANIWAKI UA	46.3	-76.01	71722	CA	3
ND BISMARCK/MUN.	46.77	-100.76	72764	US	8
PAYERNE	46.81	6.94	6610	SZ	20
ME CARIBOU/MUN.	46.87	-68.01	72712	US	0
BUDAPEST/PESTSZENTLORINC	47.43	19.18	12843	HU	37
MT GREAT FALLS	47.46	-111.38	72776	US	1
WA SPOKANE	47.68	-117.63	72786	US	3
ALTAY	47.73	88.08	51076	CH	15
WA QUILLAYUTE	47.93	-124.56	72797	US	4
MT GLASGOW/INT.	48.21	-106.63	72768	US	4
MUENCHEN-OBERSCHLEISSHEIM	48.24	11.55	10868	GM	3
WIEN/HOHE WARTE	48.25	16.36	11035	AU	24
MN INT.FALLS/FALLS INT. MN.	48.56	-93.4	72747	US	7
STEPHENVILLE UA	48.57	-58.57	71815	CA	47
STUTTGART/SCHNARRENBERG	48.83	9.2	10739	GM	4
POPRAD-GANOVCE	49.03	20.32	11952	LO	7
NENJIANG	49.17	125.23	50557	CH	26
PRAHA-LIBUS	50.01	14.45	11520	EZ	4
CAMBORNE	50.22	-5.33	3808	UK	9
SEPT-ILES UA	50.22	-66.25	71811	CA	3
MEININGEN	50.56	10.38	10548	GM	3
PORT HARDY UA	50.69	-127.38	71109	CA	11
MOOSONEE UA	51.27	-80.65	71836	CA	20
ESSEN-BREDENEY	51.41	6.97	10410	GM	3
VALENTIA OBSERVATORY	51.94	-10.24	3953	EI	15
LINDENBERG	52.22	14.12	10393	GM	3
LEGIONOWO	52.41	20.96	12374	PL	9
PETROPAVLOVSK-KAMCHATSKIJ	53.08	158.58	32540	RS	42
GOOSE UA	53.3	-60.37	71816	CA	7
EDMONTON STONY PLAIN	53.55	-114.11	71119	CA	3
THE PAS UA	53.97	-101.1	71867	CA	3
GREIFSWALD	54.1	13.41	10184	GM	5
SCHLESWIG	54.53	9.55	10035	GM	19
AK ANNETTE ISLAND	55.04	-131.58	70398	US	11
AK COLD BAY	55.2	-162.72	70316	US	12
AK ST. PAUL ISLANDS	57.15	-170.22	70308	US	22
AK KODIAK	57.74	-152.49	70350	US	1
KUUJJUAQ	58.12	-68.42	71906	CA	9
INUKJUAK UA	58.47	-78.08	71907	CA	12
AK KING SALMON	58.68	-156.67	70326	US	10
CHURCHILL A UA	58.73	-94.07	71913	CA	21

STAVANGER/SOLA	58.87	5.67	1415	NO	13
AK YAKUTAT	59.52	-139.67	70361	US	8
FORT SMITH UA	60.03	-111.93	71934	CA	6
LERWICK	60.14	-1.18	3005	UK	24
AK BETHEL/BETHEL AIRPORT	60.79	-161.84	70219	US	11
JOKIOINEN OBSERVATORY	60.81	23.5	2963	FI	12
AK ANCHORAGE/INT.	61.16	-149.99	70273	US	0
MITTARFIK NARSARSUAQ	61.17	-45.42	4270	GL	11
AK MCGRATH	62.96	-155.6	70231	US	26
ORLAND III	63.71	9.61	1241	NO	31
IQALUIT UA	63.75	-68.55	71909	CA	9
KEFLAVIKURFLUGVOLLUR	63.98	-22.6	4018	IC	15
AK NOME	64.51	-165.43	70200	US	8
ARHANGEL SK	64.62	40.51	22543	RS	34
AK FAIRBANKS/INT.	64.82	-147.88	70261	US	0
NORMAN WELLS UA	65.28	-126.75	71043	CA	8
SODANKYLA ARCTIC RESEARCH CENT	67.37	26.63	2836	FI	8
INUVIK UA	68.32	-133.52	71957	CA	4
AASIAAT (EGEDESMINDE)	68.71	-52.85	4220	GL	23
HALL BEACH UA	68.77	-81.22	71081	CA	5
CAMBRIDGE BAY UA	69.13	-105.07	71925	CA	1
JAN MAYEN	70.94	-8.67	1001	JN	22
AK BARROW/W. POST W. ROGERS	71.29	-156.78	70026	US	23
BJORNOYA	74.5	19	1028	SV	9
RESOLUTE UA	74.7	-94.97	71924	CA	5
EUREKA UA	79.98	-85.93	71917	CA	3

Acronyms

AMO Atlantic Multidecadal Oscillation.

BDC Brewer–Dobson Circulation.

COSMIC Constellation Observing System for Meteorology, Ionosphere, and Climate.

CPTP Cold Point Tropopause.

DJF December–January–February.

DKCC Doctoral Programme Climate Change.

DMI Danish Meteorological Institute.

DT Double Tropopause.

ECMWF European Centre for Medium-Range Weather Forecasts.

El Niño The warm phase of the El Niño–Southern Oscillation.

ENSO El Niño–Southern Oscillation.

EOF Empirical Orthogonal Function.

ERA ECMWF Re-Analysis.

ERA5 ECMWF Re-Analysis Version 5.

FU Berlin Freie Universität Berlin.

FWF Austrian Science Fund (Fonds zur Förderung der wissenschaftlichen Forschung).

GloSSAC Global Space-based Stratospheric Aerosol Climatology.

GMM Gaussian mixture model.

GNSS Global Navigation Satellite System.

GPS Global Positioning System.

IGRA Integrated Global Radiosonde Archive.

IGRA2 Integrated Global Radiosonde Archive Version 2.

IPCC Intergovernmental Panel on Climate Change.

JJA June–July–August.

La Niña The cold phase of the El Niño–Southern Oscillation.

LEO Low Earth Orbit.

LRTP Lapse Rate Tropopause.

MAM March–April–May.

multivariate linear regression A mathematical method to statistically decompose e.g. a time series into multiple components.

NASA National Aeronautics and Space Administration.

NH Northern Hemisphere.

Niño 3 region A region in the Pacific between 5° N–5° S and 150° W–90° W.

Niño 3.4 Index A El Niño–Southern Oscillation index create by monthly mean Sea Surface Temperature (SST) anomalies in the Niño 3.4 region.

Niño 3.4 region A region in the Pacific between 5° N–5° S and 170° W–120° W.

Niño 4 region A region in the Pacific between 5° N–5° S and 160° E–150° W.

NOAA National Oceanic and Atmospheric Administration.

NumFOCUS Organization with the mission "to promote open practices in research, data, and scientific computing by serving as a fiscal sponsor for open source projects and organizing community-driven educational programs.".

OLR Outgoing Longwave Radiation.

ONI Oceanic Niño Index.

OPSv5.6 Occultation Processing System version 5.6.

PC Principal Component.

PCA Principal Component Analysis.

PDF Probability Density Function.

PDO Pacific Decadal Oscillation.

QBO Quasi-Biennial Oscillation.

QC Quality Control.

RAOB Radiosonde Observation.

RO Radio Occultation.

SciPy ecosystem A collection of open source software for scientific computing in Python, funded by NumFOCUS.

SH Southern Hemisphere.

SOI Southern Oscillation Index.

SON September–October–November.

SST Sea Surface Temperature.

STE Stratosphere-Troposphere Exchange.

STJ Subtropical Jet Stream.

TEL Tropical Edge Latitude.

TIL Tropopause Inversion Layer.

Trade winds Consistently westward blowing winds at Equator.

TTL Tropical Tropopause Layer.

UCAR University Corporation for Atmospheric Research.

UTLS Upper Troposphere–Lower Stratosphere [region].

WC Walker Circulation.

WEGC Wegener Center for Climate and Global Change [University of Graz].

WMO World Meteorological Organization.

ZLRTP Zero Lapse Rate Tropopause.

List of Figures

2.1. Monthly mean temperature profiles from RO at different latitude intervals for different seasons. . . . 11
2.2. Cross-section of the general global circulation patterns including the STJ. . . . 12
2.3. Illustration of the general global circulation. . . . 13
2.4. STJ shown on the NH. . . . 14
2.5. Global aspect of STE. . . . 14
2.6. Illustration of the QBO wind patterns. . . . 16
2.7. Disruption in the QBO pattern. . . . 17
2.8. Phase space diagram of the two first time components from the EOF analysis on QBO winds. . . . 18
2.9. SST anomalies during El Niño and La Niña. . . . 19
2.10. Schematic illustration of the ENSO and the WC during the neutral phase. . . . 20
2.11. Schematic illustration of the ENSO and the WC during the warm phase, El Niño. . . . 20
2.12. Schematic illustration of the ENSO and the WC during the cold phase, La Niña. . . . 21

3.1. An illustration of a Radio Occultation satellite constellation. . . . 24
3.2. Monthly mean winds, QBO winds, since 1953. . . . 27
3.3. The ENSO regions in the Pacific. . . . 28
3.4. Monthly mean SST anomaly time series between 2000 and 2021 in the Niño 3.4 region. . . . 29
3.5. The solar F10.7 index since 1948. . . . 30

4.1. EOF analysis example: Two time series used as input. . . . 32
4.2. EOF analysis example: A new set of unit vectors. . . . 33
4.3. EOF analysis example: The time series that correspond to the new unit vectors in Figure 4.2. . . . 34
4.4. EOF analysis example: Reconstructed data using the 1st PC only. 34
4.5. Joy plot of the mean altitude of the CPTP at every 5° zonal band using individual RO temperature profiles. . . . 37
4.6. A scan of the WMO (1957) LRTP definition. . . . 39
4.7. Joy plot of the mean altitude of the LRTP at 5° zonal bands using individual RO temperature profiles. . . . 41

4.8. Trends of the Lapse Rate Tropopause (LRTP) for 5° zonal bands, using RO data from September 2001 to the end of 2020. 44
4.9. Trends of the LRTP temperature for 5° zonal bands, using RO data from 2002–2017, for DJF and JJA. 44
4.10. Trends of the altitude and temperature at the LRTP in the tropics using individual RO temperature profiles from September 2001 to 2020 45
4.11. Joy plot of the altitude of the LRTP at 5° zonal bands using monthly mean RO temperature profiles. 46
4.12. Monthly averaged temperature profiles from RO measurements showing a "jump" in the LRTP altitude. 47
4.13. Trends of the temperature at the LRTP at 5° zonal bands from individual and mean RO temperature profiles. 48
4.14. Trends of the altitude and temperature at the LRTP in the tropics using individual and mean RO temperature profiles. 49
4.15. A cross section of all the 1st and the 2nd LRTPs using individual RO temperature profiles in February 2012 by latitude and altitude. 50
4.16. Cross correlation between the monthly mean DT rates on the NH and monthly mean temperature anomalies at each $5° \times 5°$ grid point for different altitudes levels. 51
4.17. Cross correlation between the monthly mean DT rates on the SH and monthly mean temperature anomalies at each $5° \times 5°$ grid point for different altitudes levels. 52
4.18. Trends of the CPTP altitude and of the ZLRTP altitude in the tropics using individual RO temperature profiles. 53
4.19. Trends of the Cold Point Tropopause (CPTP) altitude and the Zero Lapse Rate Tropopause (ZLRTP) altitude at 5° zonal bands. . . . 54
4.20. Joy plot of the mean altitude of the ZLRTP at 5° zonal bands from individual RO temperature profiles. 54
4.21. Two temperature profiles and the corresponding $\frac{d\theta}{dz}$ profiles. 56
4.22. TTL thickness from the altitude at the ZLRTP minus the altitude at the $\frac{d\theta}{dz}$ minimum peak. 57
4.23. TTL thickness from the altitude at 70 hPa subtracted from the altitude at 150 hPa. 58
4.24. Trends of the TTL thickness from pressure levels at 5° zonal bands including the altitude at the lower and the upper pressure levels. . 59
4.25. TTL thickness from the altitude at the N^2 peak above the ZLRTP minus the altitude at the N^2 minimum peak below the ZLRTP. . . 60
4.26. The Probability Density Function of the altitude of the 1st and the 2nd LRTP during February 2012. 61
4.27. A cross section of all the 1st and the 2nd LRTPs detected in February 2012 including the contours of the multivariate normal distributions found to identify each cluster. 62
4.28. Time series of the width of the tropical belt from three methods. . 63

4.29. PDFs of spatial distribution of the 1st LRTPs based on RO measurements from the 3 first months of 2013, using the altitude of the 1st LRTPs only. 64
4.30. PDFs of spatial distribution of the RO measurements from the 3 first months of 2013 using the altitude of both the 1st and the 2nd LRTPs. 65
4.31. Mean temperature profiles based on the 10 closest individual temperature profiles. 66
4.32. Example of weights given to points by their spatial density. 67
4.33. Scatter plots illustrating removal of LRTPs anomalies by three different percentiles. 67

Paper I: Atmospheric QBO and ENSO indices with high vertical resolution from GNSS radio occultation temperature measurements 73

1. Zonal monthly mean temperature anomalies from GNSS RO from 20° S to 20° N and 2 to 35 km. 75
2. The first four EOFs computed from M1 76
3. The first four PCs computed from M1 77
4. The first and second EOFs computed from M2, shown for selected altitude levels from the stratosphere to the troposphere 78
5. PC1s and PC2s from M2 for each altitude level 79
6. Explained variance ratio for M1 and M2. 79
7. Correlations between derived indices (PCs) from M1 with conventional variability indices 80
8. Correlations between the first PCs and the second PCs derived from M2 with known variability indices 81
9. Phase space diagrams are shown for the RO time period September 2001 to February 2017 82
10. Reconstructed temperature fields from the first principal components which explain maximum variability 82
11. The residual temperature field for M1 and M2 showing the difference of the input minus the reconstructed fields 83

Paper II: Quantifying Stratospheric Temperature Signals and Climate Imprints From Post-2000 Volcanic Eruptions 87

1. Altitude time pattern of the aerosol concentration. 89
2. Altitude time cross section of the volcanic aerosol reconstructed temperature (mean 30° N to 30° S; top) as well as the latitude time cross section at 18km (bottom). 92
3. Altitude-latitude cross section of the linear trend for the time series from 2002 to 2016 considering only natural variability indices (left), and natural variability indices together with the volcanic aerosols (center); trend difference (right). 93

Paper III: Double Tropopauses and the Tropical Belt Connected to ENSO 97
1. Global spatial distribution of DTs from the years 2001 to 2018 by season: (a) December–January–February (DJF), (b) March–April–May (MAM), (c) June–July–August (JJA), and (d) September–October–November (SON). 100
2. Monthly time series of DT percentages split into (a) 5°zonal bands, (b) 5°meridional bands, and (c) monthly mean anomalies of the meridional bands in panel (b). 100
3. Global spatial distribution of DTs during (a) DJF La Niña, (b) DJF El Niño, and (c) difference between DJF La Niña and DJF El Niño (i.e., a minus b). 101
4. Narrowing of the tropical edge, with DTs and temperature profiles during DJF El Niño and DJF La Niña. 102

Paper IV: Continuous rise of the tropopause in the Northern Hemisphere over 1980–2020 107
1. Variations in zonal mean tropopause height over the Northern Hemisphere (NH) and derived trends from the IGRA2, RAOBCORE, and RICH data over the time period 1980–2020 and GPS RO satellite data over 2001–2020. 108
2. Vertical profile of the correlation between H and temperature at a given altitude. 109
3. Histograms of correlation and regression slope between trends of H and T_{TRO} and between trends of H and T_{STR}. 110
4. Time series of tropospheric temperature (T_{TRO}) and lower stratospheric temperature (T_{STR}) in the NH over the time period 1980–2020. 111

Supplementary Materials for Paper IV 117
1. Distribution of the radiosonde stations. 118
2. The original and natural variability-removed time series of H, T_{TRO}, and T_{STR} in the Integrated Global Radiosonde Archive Version 2 (IGRA2). 119
3. Running windows for linear trends in H (A), T_{TRO} (B), and T_{STR} (C) over 1980–2020 in the IGRA2 radiosonde data. 120
4. The spatial distribution of the trend in H over 1980–2000 (A) and 2001–2020 (B) in the IGRA2 radiosonde data. 121
5. The spatial distribution of the trend in T_{TRO} (A and B) and T_{STR} (C and D) over 1980–2000 and 2001–2020 in the IGRA2 radiosonde data. 122

List of Tables

Paper II: Quantifying Stratospheric Temperature Signals and Climate Imprints From Post-2000 Volcanic Eruptions **87**
1. Eruptions Between 2002 and 2017 With a Minimum VEI of 4. . . . 88

Paper IV: Continuous rise of the tropopause in the Northern Hemisphere over 1980–2020 **107**
1. Trends in tropopause height (H), tropospheric temperature (T_{TRO}), and stratospheric temperature (T_{STR}). 109

Supplementary Materials for Paper IV **117**
1. Information on the radiosonde stations selected for this study. . . . 124

Bibliography

Añel, J., J. C. Antuña, L. de la Torre, J. M. Castanheira, and L. Gimeno (2008). "Climatological features of global multiple tropopause events". *J. Geophys. Res.* 113, D00B08. DOI: 10.1029/2007JD009697.

Angerer, B., F. Ladstädter, B. Scherllin-Pirscher, M. Schwärz, A. K. Steiner, U. Foelsche, and G. Kirchengast (2017). "Quality aspects of the WEGC multi-satellite GPS radio occultation record OPSv5.6". *Atmos. Meas. Tech.* 10, pp. 4845–4863. DOI: 10.5194/amt-10-4845-2017.

Anstey, J. A., T. P. Banyard, N. Butchart, L. Coy, P. A. Newman, S. Osprey, and C. J. Wright (2021). "Prospect of Increased Disruption to the QBO in a Changing Climate". *Geophys. Res. Lett.* 48.15, e2021GL093058. DOI: 10.1029/2021GL093058.

Anstey, J. A. and T. G. Shepherd (2014). "High-latitude influence of the quasi-biennial oscillation". *Q. J. R. Meteor. Soc.* 140. DOI: 10.1002/qj.2132.

Anthes, R. A. (2011). "Exploring Earth's atmosphere with radio occultation: contributions to weather, climate, and space weather". *Atmos. Meas. Tech.* 4, pp. 1077–1103. DOI: 10.5194/amt-4-1077-2011.

Aquila, V., L. D. Oman, R. Stolarski, A. R. Douglass, and P. A. Newman (2013). "The Response of Ozone and Nitrogen Dioxide to the Eruption of Mt. Pinatubo at Southern and Northern Midlatitudes". *J. Atmos. Sci.* 70.3, pp. 894–900. DOI: 10.1175/jas-d-12-0143.1.

Baldwin, M. P., L. J. Gray, T. J. Dunkerton, K. Hamilton, P. H. Haynes, W. J. Randel, J. R. Holton, M. J. Alexander, I. Hirota, T. Horinouchi, D. B. A. Jones, J. S. Kinnersley, C. Marquardt, K. Sato, and M. Takahashi (2001). "The Quasi-Biennial Oscillation". *Rev. Geophys.* 39.2, pp. 179–229. DOI: 10.1029/1999rg000073.

Bell, B., H. Hersbach, A. Simmons, P. Berrisford, P. Dahlgren, A. Horányi, J. Muñoz-Sabater, J. Nicolas, R. Radu, D. Schepers, C. Soci, S. Villaume, J.-R. Bidlot, L. Haimberger, J. Woollen, C. Buontempo, and J.-N. Thépautt (2021). "The ERA5 global reanalysis: Preliminary extension to 1950". *Q. J. R. Meteor. Soc.* 147.741, pp. 4186–4227. DOI: 10.1002/qj.4174.

Biondi, R., W. J. Randel, S.-P. Ho, T. Neubert, and S. Syndergaard (2012). "Thermal structure of intense convective clouds derived from GPS radio occultations". *Atmos. Chem. Phys.* 12.12, pp. 5309–5318. DOI: 10.5194/acp-12-5309-2012.

Biondi, R., A. K. Steiner, G. Kirchengast, H. Brenot, and T. Rieckh (2017). "Supporting the detection and monitoring of volcanic clouds: A promising new application of Global Navigation Satellite System radio occultation". *Adv. Space Res.* 60.12, pp. 2707–2722. DOI: 10.1016/j.asr.2017.06.039.

Birner, T., S. M. Davis, and D. J. Seidel (2014). "The changing width of Earth's tropical belt". *Phys. Today* 67 (12), pp. 38–44. DOI: 10.1063/PT.3.2620.

Birner, T., A. Dörnbrack, and U. Schumann (2002). "How sharp is the tropopause at midlatitudes?" *Geophys. Res. Lett.* 29.14. DOI: 10.1029/2002GL015142.

Birner, T., D. Sankey, and T. G. Shepherd (2006). "The tropopause inversion layer in models and analyses". *Geophys. Res. Lett.* 33. DOI: 10.1029/2006GL026549.

Bischoff, S. A., P. O. Canziani, and A. E. Yuchechen (2007). "The tropopause at southern extratropical latitudes: Argentine operational rawinsonde climatology". *Int. J. Climatol.* 27.2, pp. 189–209. DOI: 10.1002/joc.1385.

Blunden, J. and D. S. Arndt (Aug. 2016). "State of the Climate in 2015". *Bull. Amer. Meteor. Soc.* 97.8, Si–S275. ISSN: 0003-0007, 1520-0477. DOI: 10.1175/2016BAMSStateoftheClimate.1.

Boothe, A. C. and C. R. Homeyer (2017). "Global large-scale stratosphere–troposphere exchange in modern reanalyses". *Atmos. Chem. Phys.* 17.9, pp. 5537–5559. DOI: 10.5194/acp-17-5537-2017.

Bourassa, A. E., A. Robock, W. J. Randel, T. Deshler, L. A. Rieger, N. D. Lloyd, E. J. (Llewellyn, and D. A. Degenstein (2012). "Large Volcanic Aerosol Load in the Stratosphere Linked to Asian Monsoon Transport". *Science* 337, pp. 78–81. DOI: 10.1126/science.1219371.

Butchart, N. (2014). "The Brewer-Dobson circulation". *Rev. Geophys.* 52, pp. 157–184. DOI: 10.1002/2013RG000448.

Castanheira, J. M. and L. Gimeno (2011). "Association of double tropopause events with baroclinic waves". *J. Geophys. Res.* 116, D19113. DOI: 10.1029/2011JD016163.

Castanheira, J. M., T. R. Peevey, C. A. F. Marques, and M. A. Olsen (2012). "Relationships between Brewer–Dobson circulation, double tropopauses, ozone and stratospheric water vapour". *Atmos. Chem. Phys.* 12, pp. 10195–10208. DOI: 10.5194/acp-12-10195-2012.

Christiansen, B., S. Yang, and M. S. Madsen (Oct. 2016). "Do strong warm ENSO events control the phase of the stratospheric QBO?" *Geophys. Res. Lett.* 43.19, pp. 10489–10495. ISSN: 00948276. DOI: 10.1002/2016GL070751.

Covington, A. E. (June 1969). "Solar Radio Emission at 10.7 cm, 1947–1968". *J. Royal Astron. Soc. Canada* 63, pp. 125–132. URL: https://ui.adsabs.harvard.edu/abs/1969JRASC..63..125C.

Coy, L., P. A. Newman, S. Pawson, and L. R. Lait (Aug. 2017). "Dynamics of the Disrupted 2015/16 Quasi-Biennial Oscillation". *J. Climate* 30.15, pp. 5661–5674. ISSN: 0894-8755, 1520-0442. DOI: 10.1175/JCLI-D-16-0663.1.

Davis, N. and T. Birner (2017). "On the Discrepancies in Tropical Belt Expansion between Reanalyses and Climate Models and among Tropical Belt Width Metrics". *J. Climate* 30.4, pp. 1211–1231. DOI: 10.1175/JCLI-D-16-0371.1.

Davis, S. M. and K. H. Rosenlof (2012). "A multidiagnostic intercomparison of tropical-width time series using reanalyses and satellite observations". *J. Climate* 25, pp. 1061–1078. DOI: 10.1175/JCLI-D-11-00127.1.

Dee, D. P., S. M. Uppala, A. J. Simmons, P. Berrisford, P. Poli, S. Kobayashi, U. Andrae, M. A. Balmaseda, G. Balsamo, P. Bauer, P. Bechtold, A. C. M. Beljaars, L. van de Berg, J. Bidlot, N. Bormann, C. Delsol, R. Dragani, M. Fuentes, A. J. Geer, L. Haimberger, S. B. Healy, H. Hersbach, E. V. Hólm, L. Isaksen, P. Kållberg, M. Köhler, M. Matricardi, A. P. McNally, B. M. Monge-Sanz, J.-J. Morcrette, B.-K. Park, C. Peubey, P. de Rosnay, C. Tavolato, J.-N. Thépaut, and F. Vitart (2011). "The ERA-Interim reanalysis: configuration and performance of the data assimilation system". *Q. J. R. Meteor. Soc.* 137.656, pp. 553–597. DOI: 10.1002/qj.828.

Diallo, M., M. Riese, T. Birner, P. Konopka, R. Müller, M. I. Hegglin, M. L. Santee, M. Baldwin, B. Legras, and F. Ploeger (2018). "Response of stratospheric water vapor and ozone to the unusual timing of El Niño and the QBO disruption in 2015–2016". *Atmos. Chem. Phys.* 18.17, pp. 13055–13073. DOI: 10.5194/acp-18-13055-2018.

Domeisen, D. I., C. I. Garfinkel, and A. H. Butler (2019). "The Teleconnection of El Niño Southern Oscillation to the Stratosphere". *Rev. Geophys.* 57.1, pp. 5–47. DOI: 10.1029/2018rg000596.

Dunkerton, T. J. (2016). "The quasi-biennial oscillation of 2015–2016: Hiccup or death spiral?" *Geophys. Res. Lett.* 43.19, pp. 10547–10552. DOI: 10.1002/2016GL070921.

– (Aug. 2017). "Nearly identical cycles of the quasi-biennial oscillation in the equatorial lower stratosphere". *J. Geophys. Res.: Atmos* 122.16, pp. 8467–8493. ISSN: 2169897X. DOI: 10.1002/2017JD026542.

Dunkerton, T. J. and D. P. Delisi (Feb. 1985). "Climatology of the Equatorial Lower Stratosphere". *J. Atmos. Sci.* 42.4, pp. 376–396. ISSN: 0022-4928, 1520-0469. DOI: 10.1175/1520-0469(1985)042<0376:COTELS>2.0.CO;2.

Ern, M., Q. T. Trinh, P. Preusse, J. C. Gille, M. G. Mlynczak, J. M. Russell III, and M. Riese (2018). "GRACILE: a comprehensive climatology of atmospheric gravity wave parameters based on satellite limb soundings". *Earth Sys. Sci. Data* 10.2, pp. 857–892. DOI: 10.5194/essd-10-857-2018.

Fernández, N. C., R. R. García, R. G. Herrera, D. G. Puyol, L. G. Presa, E. H. Martín, and P. R. Rodríguez (2004). "Analysis of the ENSO signal in tropospheric and stratospheric temperatures observed by MSU, 1979–2000". *J. Climate* 17.20, pp. 3934–3946.

Ferraro, A. J., E. J. Highwood, and A. J. Charlton-Perez (2011). "Stratospheric heating by potential geoengineering aerosols". *Geophys. Res. Lett.* 38. DOI: 10.1029/2011GL049761.

Flury, T., D. L. Wu, and W. G. Read (2013). "Variability in the speed of the Brewer–Dobson circulation as observed by Aura/MLS". *Atmos. Chem. Phys.* 13.9, pp. 4563–4575. DOI: 10.5194/acp-13-4563-2013.

Foelsche, U., B. Scherllin-Pirscher, F. Ladstädter, A. K. Steiner, and G. Kirchengast (2011). "Refractivity and temperature climate records from multiple radio occultation satellites consistent within 0.05 %". *Atmos. Meas. Tech.* 4, pp. 2007–2018. DOI: 10.5194/amt-4-2007-2011.

Free, M. and J. Lanzante (2009). "Effect of Volcanic Eruptions on the Vertical Temperature Profile in Radiosonde Data and Climate Models". *J. Climate* 22.11, pp. 2925–2939. DOI: 10.1175/2008jcli2562.1.

Free, M. and D. J. Seidel (2009). "Observed El Niño–Southern Oscillation temperature signal in the stratosphere". *J. Geophys. Res.* 114, D23108. DOI: 10.1029/2009JD012420.

Fueglistaler, S., A. E. Dessler, T. J. Dunkerton, I. Folkins, Q. Fu, and P. W. Mote (2009). "Tropical tropopause layer". *Rev. Geophys.* 47, RG1004. DOI: 10.1029/2008RG000267.

Fujiwara, M., J. S. Wright, G. L. Manney, L. J. Gray, J. Anstey, T. Birner, S. Davis, E. P. Gerber, V. L. Harvey, M. I. Hegglin, C. R. Homeyer, J. A. Knox, K. Krüger, A. Lambert, C. S. Long, P. Martineau, A. Molod, B. M. Monge-Sanz, M. L. Santee, S. Tegtmeier, S. Chabrillat, D. G. H. Tan, D. R. Jackson, S. Polavarapu, G. P. Compo, R. Dragani, W. Ebisuzaki, Y. Harada, C. Kobayashi, W. McCarty, K. Onogi, S. Pawson, A. Simmons, K. Wargan, J. S. Whitaker, and C.-Z. Zou (2017). "Introduction to the SPARC Reanalysis Intercomparison Project (S-RIP) and overview of the reanalysis systems". *Atmos. Chem. Phys.* 17.2, pp. 1417–1452. DOI: 10.5194/acp-17-1417-2017.

Gao, P., X. Xu, and X. Zhang (Apr. 2017). "On the relationship between the QBO/ENSO and atmospheric temperature using COSMIC radio occultation data". *J. Atmos. Solar-Terr. Phys.* 156, pp. 103–110. ISSN: 13646826. DOI: 10.1016/j.jastp.2017.03.008.

Geller, M. A., T. Zhou, and W. Yuan (Aug. 2016). "The QBO, gravity waves forced by tropical convection, and ENSO". *J. Geophys. Res.: Atmos* 121.15, pp. 8886–8895. ISSN: 2169-8996. DOI: 10.1002/2015JD024125.

Gettelman, A. and P. Forster (2002). "A climatology of the tropical tropopause layer". *J. Meteor. Soc. Japan* 80.4B, pp. 911–924.

Gettelman, A., W. J. Randel, S. Massie, F. Wu, W. G. Read, and J. M. Russell III (2001). "El Niño as a natural experiment for studying the tropical tropopause region". *J. Climate* 14, pp. 3375–3392.

Global Volcanism Program (2013). *Volcanoes of the World, v. 4.3.4*. Ed. by E. Venzke. Smithsonian Institution, Downloaded 08 Nov 2018. URL: https://doi.org/10.5479/si.gvp.votw4-2013.

Hannachi, A., I. T. Jolliffe, and D. B. Stephenson (July 2007). "Empirical orthogonal functions and related techniques in atmospheric science: A review". *Int. J. Climatol.* 27.9, pp. 1119–1152. ISSN: 08998418, 10970088. DOI: 10.1002/joc.1499.

Hersbach, H. et al. (2020). "The ERA5 global reanalysis". *Q. J. R. Meteor. Soc.* 146.730, pp. 1999–2049. DOI: 10.1002/qj.3803.

Highwood, E. J. and B. J. Hoskins (1998). "The tropical tropopause". *Q. J. R. Meteor. Soc.* 124.549, pp. 1579–1604. DOI: 10.1002/qj.49712454911.

Hoffmann, L., X. Xue, and M. J. Alexander (2013). "A global view of stratospheric gravity wave hotspots located with Atmospheric Infrared Sounder observations". *J. Geophys. Res.: Atmos* 118.2, pp. 416–434. DOI: 10.1029/2012JD018658.

Hoinka, K. P. (Dec. 1997). "The tropopause: discovery, definition and demarcation". *Met. Z.* 6.6, pp. 281–303. DOI: 10.1127/metz/6/1997/281.

Holton, J. R., P. H. Haynes, M. E. McIntyre, A. R. Douglass, R. B. Rood, and L. Pfister (1995). "Stratosphere-troposphere exchange". *Rev. Geophys.* 33.4, pp. 403–439. DOI: 10.1029/95RG02097.

Homeyer, C. R., K. P. Bowman, and L. L. Pan (2010). "Extratropical tropopause transition layer characteristics from high-resolution sounding data". *J. Geophys. Res.* 115, D13108. DOI: 10.1029/2009JD013664.

Hommel, R., C. Timmreck, M. A. Giorgetta, and H. F. Graf (2015). "Quasi-biennial oscillation of the tropical stratospheric aerosol layer". *Atmos. Chem. Phys.* 15.10. DOI: 10.5194/acp-15-5557-2015.

IPCC (2021). *Climate Change 2021: The Physical Science Basis. Contribution of Working Group I to the Sixth Assessment Report of the Intergovernmental Panel on Climate Change*. Ed. by M.-D. V., P. Zhai, A. Pirani, S. L. Connors, C. Péan, S. Berger, N. Caud, Y. Chen, L. Goldfarb, M. I. Gomis, M. Huang, K. Leitzell, E. Lonnoy, J. B. R. Matthews, T. K. Maycock, T. Waterfield, O. Yelekçi, R. Yu, and B. Zhou. in press. Cambridge, United Kingdom and New York, NY, USA: Cambridge University Press.

Jolliffe, I. T. (2002). *Principal Component Analysis*. Springer Series in Statistics. Springer. ISBN: 978-0-387-95442-4. DOI: 10.1007/b98835.

Kedzierski, R. P., K. Matthes, and K. Bumke (Sept. 2016). "The tropical tropopause inversion layer: variability and modulation by equatorial waves". *Atmos. Chem. Phys.* 16.18, pp. 11617–11633. DOI: 10.5194/acp-16-11617-2016.

Kremser, S., L. W. Thomason, M. von Hobe, M. Hermann, T. Deshler, C. Timmreck, M. Toohey, A. Stenke, J. P. Schwarz, R. Weigel, S. Fueglistaler, F. J. Prata, J.-P. Vernier, H. Schlager, J. E. Barnes, J.-C. Antuña-Marrero, D. Fairlie, M. Palm, E. Mahieu, J. Notholt, M. Rex, C. Bingen, F. Vanhellemont, A. Bourassa, J. M. C. Plane, D. Klocke, S. A. Carn, L. Clarisse, T. Trickl, R. Neely, A. D. James, L. Rieger, J. C. Wilson, and B. Meland (2016). "Stratospheric aerosol—Observations, processes, and impact on climate". *Rev. Geophys.* 54.2, pp. 278–335. DOI: 10.1002/2015RG000511.

Kursinski, E. R., G. A. Hajj, J. T. Schofield, R. P. Linfield, and K. R. Hardy (1997). "Observing Earth's atmosphere with radio occultation measurements using the Global Positioning System". *J. Geophys. Res.* 102.D19, pp. 23429–23465. DOI: 10.1029/97JD01569.

Lackner, B. C., A. K. Steiner, G. Kirchengast, and G. C. Hegerl (2011). "Atmospheric Climate Change Detection by Radio Occultation Data Using a Fingerprinting Method". *J. Climate* 24, pp. 5275–5291. DOI: 10.1175/2011JCLI3966.1.

Lau, K.-M. and S. Yang (2015). "TROPICAL METEOROLOGY & CLIMATE | Walker Circulation". In: *Encyclopedia of Atmospheric Sciences (Second Edition)*. Ed. by G. R. North, J. Pyle, and F. Zhang. Second Edition. Oxford: Academic Press, pp. 177–181. ISBN: 978-0-12-382225-3. DOI: 10.1016/B978-0-12-382225-3.00450-3.

Leroy, S. S., J. A. Dykema, and J. G. Anderson (2006). "Climate benchmarking using GNSS occultation". In: *Atmosphere and Climate: Studies by Occultation Methods*. Ed. by U. Foelsche, G. Kirchengast, and A. K. Steiner. Berlin Heidelberg: Springer, pp. 287–301. DOI: 10.1007/3-540-34121-8_24.

Liu, C. and E. Barnes (2018). "Synoptic Formation of Double Tropopauses". *J. Geophys. Res.: Atmos* 123.2, pp. 693–707. DOI: 10.1002/2017JD027941.

Maher, P., M. E. Kelleher, P. G. Sansom, and J. Methven (Feb. 2020). "Is the subtropical jet shifting poleward?" *Climate Dyn.* 54.3, pp. 1741–1759. ISSN: 1432-0894. DOI: 10.1007/s00382-019-05084-6.

Manney, G. L., M. I. Hegglin, W. H. Daffer, M. J. Schwartz, M. L. Santee, and S. Pawson (2014). "Climatology of Upper Tropospheric–Lower Stratospheric (UTLS) Jets and Tropopauses in MERRA". *J. Climate* 27, pp. 3248–3271. DOI: 10.1175/JCLI-D-13-00243.1.

Manney, G. L., M. I. Hegglin, Z. D. Lawrence, K. Wargan, L. F. Millán, M. J. Schwartz, M. L. Santee, A. Lambert, S. Pawson, B. W. Knosp, R. A. Fuller, and W. H. Daffer (2017). "Reanalysis comparisons of upper tropospheric–lower stratospheric jets and multiple tropopauses". *Atmos. Chem. Phys.* 17.18, pp. 11541–11566. DOI: 10.5194/acp-17-11541-2017.

Mehta, S. K., M. Fujiwara, T. Tsuda, and J.-P. Vernier (2015). "Effect of recent minor volcanic eruptions on temperatures in the upper troposphere and lower stratosphere". *J. Atmos. Solar-Terr. Phys.* 129, pp. 99–110. DOI: 10.1016/j.jastp.2015.04.009.

Melbourne, W. G., E. S. Davis, C. B. Duncan, G. A. Hajj, K. R. Hardy, E. R. Kursinski, T. K. Meehan, L. E. Young, and T. P. Yunck (1994). *The application of spaceborne GPS to atmospheric limb sounding and global change monitoring*. Tech. rep. Pasadena, California, USA: Jet Propulsion Laboratory, NASA. 147 pp.

Meng, L., J. Liu, D. W. Tarasick, W. J. Randel, A. K. Steiner, H. Wilhelmsen, L. Wang, and L. Haimberger (2021). "Continuous rise of the tropopause in the Northern Hemisphere over 1980–2020". *Sci. Adv.* 7.45, eabi8065. DOI: 10.1126/sciadv.abi8065.

Naujokat, B. (Sept. 1986). "An Update of the Observed Quasi-Biennial Oscillation of the Stratospheric Winds over the Tropics". *J. Atmos. Sci.* 43.17, pp. 1873–1877. DOI: 10.1175/1520-0469(1986)043<1873:AUOTOQ>2.0.CO;2.

Newman, P. A., L. Coy, S. Pawson, and L. R. Lait (Aug. 2016). "The anomalous change in the QBO in 2015–2016". *Geophys. Res. Lett.* 43.16, 2016GL070373. ISSN: 1944-8007. DOI: 10.1002/2016GL070373.

Okazaki, I. and K. Heki (2012). "Atmospheric temperature changes by volcanic eruptions: GPS radio occultation observations in the 2010 Icelandic and 2011 Chilean cases". *J. Volcanol. Geotherm. Res.* 245–246, pp. 123–127. DOI: 10.1016/j.jvolgeores.2012.08.018.

Osprey, S. M., N. Butchart, J. R. Knight, A. A. Scaife, K. Hamilton, J. A. Anstey, V. Schenzinger, and C. Zhang (Sept. 2016). "An unexpected disruption of the atmospheric quasi-biennial oscillation". *Science* 353.6306, pp. 1424–1427. ISSN: 0036-8075, 1095-9203. DOI: 10.1126/science.aah4156.

Pan, L. L., W. J. Randel, J. C. Gille, W. D. Hall, B. Nardi, S. Massie, V. Yudin, R. Khosravi, P. Konopka, and D. Tarasick (2009). "Tropospheric intrusions associated with the secondary tropopause". *J. Geophys. Res.* 114, D10302. DOI: 10.1029/2008JD011374.

Parker, D. E., H. Wilson, P. D. Jones, J. R. Christy, and C. K. Folland (1996). "The impact of Mount Pinatubo on world-wide temperatures". *Int. J. Climatol.* 16.5, pp. 487–497. DOI: 10.1002/(SICI)1097-0088(199605)16:5<487::AID-JOC39>3.0.CO;2-J.

Peevey, T. R., J. C. Gille, C. R. Homeyer, and G. L. Manney (2014). "The double tropopause and its dynamical relationship to the tropopause inversion layer in storm track regions". *J. Geophys. Res.* 119.17, pp. 10194–10212. DOI: 10.1002/2014JD021808.

Peevey, T. R., J. C. Gille, C. E. Randall, and A. Kunz (2012). "Investigation of double tropopause spatial and temporal global variability utilizing High Resolution Dynamics Limb Sounder temperature observations". *J. Geophys. Res.* 117, D01105. DOI: 10.1029/2011JD016443.

Randel, W. J., R. R. Garcia, N. Calvo, and D. Marsh (2009). "ENSO influence on zonal mean temperature and ozone in the tropical lower stratosphere". *J. Geophys. Res.* 36, L15822. DOI: 10.1029/2009GL039343.

Randel, W. J. and E. J. Jensen (2013). "Physical processes in the tropical tropopause layer and their roles in a changing climate". *Nat. Geosci.* 6, pp. 169–176. DOI: 10.1038/ngeo1733.

Randel, W. J., D. J. Seidel, and L. L. Pan (2007). "Observational characteristics of double tropopauses". *J. Geophys. Res.* 112, D07309. DOI: 10.1029/2006JD007904.

Randel, W. J. and F. Wu (2015). "Variability of Zonal Mean Tropical Temperatures Derived from a Decade of GPS Radio Occultation Data". *J. Atmos. Sci.* 72, pp. 1261–1275. DOI: 10.1175/JAS-D-14-0216.1.

Randel, W. J., F. Wu, and W. R. Ríos (2003). "Thermal variability of the tropical tropopause region derived from GPS/MET observations". *J. Geophys. Res.: Atmos* 108.D1, ACL 7-1–ACL 7-12. DOI: 10.1029/2002JD002595.

Randel, W. J., F. Wu, R. Swinbank, J. Nash, and A. O'Neill (1999). "Global QBO circulation derived from UKMO stratospheric analyses". *J. Atmos. Sci.* 56.4, pp. 457–474.

Reid, G. C. (1994). "Seasonal and interannual temperature variations in the tropical stratosphere". *J. Geophys. Res.* 99.D9, pp. 18923–18932.

Reid, G. C. and K. S. Gage (1985). "Interannual variations in the height of the tropical tropopause". *J. Geophys. Res.* 90.D3, pp. 5629–5635. DOI: 10.1029/JD090iD03p05629.

Rieckh, T., B. Scherllin-Pirscher, F. Ladstädter, and U. Foelsche (2014). "Characteristics of tropopause parameters as observed with GPS radio occultation". *Atmos. Meas. Tech.* 7, pp. 3947–3958. DOI: 10.5194/amt-7-3947-2014.

Robock, A. (2000). "Volcanic eruptions and climate". *Rev. Geophys.* 38.2, pp. 191–219. DOI: 10.1029/1998rg000054.

Robock, A. (2015). "Climatic Impacts of Volcanic Eruptions". In: *The Encyclopedia of Volcanoes (Second Edition)*. Ed. by H. Sigurdsson. 2nd ed. Amsterdam: Academic Press, pp. 935–942. ISBN: 978-0-12-385938-9. DOI: 10.1016/B978-0-12-385938-9.00053-5.

Salby, M. L. (2012). *Physics of the Atmosphere and Climate*. 2nd ed. Cambridge University Press.

Santer, B. D., T. M. L. Wigley, C. Doutriaux, J. S. Boyle, J. E. Hansen, P. D. Jones, G. A. Meehl, E. Roeckner, S. Sengupta, and K. E. Taylor (2001). "Accounting for the effects of volcanoes and ENSO in comparisons of modeled and observed temperature trends". *J. Geophys. Res.* 106, pp. 28033–28059. DOI: 10.1029/2000JD000189.

Santer, B. D., S. Solomon, C. Bonfils, M. D. Zelinka, J. F. Painter, F. Beltran, J. C. Fyfe, G. Johannesson, C. Mears, D. A. Ridley, J.-P. Vernier, and F. J. Wentz (2015). "Observed multivariable signals of late 20th and early 21st century volcanic activity". *Geophys. Res. Lett.* 42.2, pp. 500–509. DOI: 10.1002/2014GL062366.

Sato, K., S. Tateno, S. Watanabe, and Y. Kawatani (2012). "Gravity Wave Characteristics in the Southern Hemisphere Revealed by a High-Resolution Middle-Atmosphere General Circulation Model". *J. Atmos. Sci.* 69.4, pp. 1378–1396. DOI: 10.1175/JAS-D-11-0101.1.

Scherllin-Pirscher, B., C. Deser, S.-P. Ho, C. Chou, W. Randel, and Y.-H. Kuo (2012). "The vertical and spatial structure of ENSO in the upper troposphere and lower stratosphere from GPS radio occultation measurements". *Geophys. Res. Lett.* 39, L20801. DOI: 10.1029/2012GL053071.

Scherllin-Pirscher, B., W. J. Randel, and J. Kim (Jan. 2017). "Tropical temperature variability and Kelvin-wave activity in the UTLS from GPS RO measurements". *Atmos. Chem. Phys.* 17.2, pp. 793–806. ISSN: 1680-7324. DOI: 10.5194/acp-17-793-2017.

Scherllin-Pirscher, B., A. K. Steiner, G. Kirchengast, Y.-H. Kuo, and U. Foelsche (2011). "Empirical analysis and modeling of errors of atmospheric profiles from GPS radio occultation". *Atmos. Meas. Tech.* 4, pp. 1875–1890. DOI: 10.5194/amt-4-1875-2011.

Schirber, S. (Feb. 2015). "Influence of ENSO on the QBO: Results from an ensemble of idealized simulations". *J. Geophys. Res.: Atmos* 120.3, pp. 1109–1122. DOI: 10.1002/2014JD022460.

Schmidt, T., G. Beyerle, S. Heise, J. Wickert, and M. Rothacher (2006). "A climatology of multiple tropopauses derived from GPS radio occultations with CHAMP and SAC-C". *Geophys. Res. Lett.* 33, L04808. DOI: 10.1029/2005GL024600.

Schmidt, T., S. Heise, J. Wickert, G. Beyerle, and C. Reigber (2005). "GPS radio occultation with CHAMP and SAC-C: global monitoring of thermal tropopause parameters". *Atmos. Chem. Phys.* 5.6, pp. 1473–1488. DOI: 10.5194/acp-5-1473-2005.

Schmidt, T., J. Wickert, G. Beyerle, and C. Reigber (2004). "Tropical tropopause parameters derived from GPS radio occultation measurements with CHAMP". *J. Geophys. Res.* 109, D13105. DOI: 10.1029/2004JD004566.

Schreiner, W., C. Rocken, S. Sokolovskiy, S. Syndergaard, and D. Hunt (2007). "Estimates of the precision of GPS radio occultations from the COSMIC/FORMOSAT-3 mission". *Geophys. Res. Lett.* 34, L04808. DOI: 10.1029/2006GL027557.

Schwärz, M., G. Kirchengast, B. Scherllin-Pirscher, J. Schwarz, F. Ladstädter, and B. Angerer (2016). *Multi-Mission Validation by Satellite Radio Occultation – Extension Project*. Final report for ESA/ESRIN No. 01/2016. University of Graz, Austria: WEGC. 164 pp.

Seidel, D. J., Q. Fu, W. J. Randel, and T. J. Reichler (2008). "Widening of the tropical belt in a changing climate". *Nature* 1, pp. 21–24. DOI: 10.1038/ngeo.2007.38.

Seidel, D. J. and W. J. Randel (2006). "Variability and trends in the global tropopause estimated from radiosonde data". *J. Geophys. Res.* 111, D21101. DOI: 10.1029/2006JD007363.

Seidel, D. J., R. J. Ross, J. K. Angell, and G. C. Reid (2001). "Climatological characteristics of the tropical tropopause as revealed by radiosondes". *J. Geophys. Res.* 106.D8, pp. 7857–7878. DOI: 10.1029/2000JD900837.

Son, S.-W., N. F. Tandon, and L. M. Polvani (2011). "The fine-scale structure of the global tropopause derived from COSMIC GPS radio occultation measurements". *J. Geophys. Res.* 116, D20113. DOI: 10.1029/2011JD016030.

Staten, P. W., K. M. Grise, S. M. Davis, K. B. Karnauskas, D. W. Waugh, A. C. Maycock, Q. Fu, K. Cook, O. Adam, I. R. Simpson, R. J. Allen, K. Rosenlof, G. Chen, C. C. Ummenhofer, X.-W. Quan, J. P. Kossin, N. A. Davis, and S.-W. Son (2020). "Tropical Widening: From Global Variations to Regional Impacts". *Bull. Amer. Meteor. Soc.* 101.6, E897–E904. DOI: 10.1175/BAMS-D-19-0047.1.

Staten, P. W., J. Lu, K. M. Grise, S. M. Davis, and T. Birner (2018). "Re-examining tropical expansion". *Nat. Clim. Change* 8.43, pp. 768–775. DOI: 10.1038/s41558-018-0246-2.

Steiner, A. K., B. C. Lackner, F. Ladstädter, B. Scherllin-Pirscher, U. Foelsche, and G. Kirchengast (2011). "GPS radio occultation for climate monitoring and change detection". *Radio Sci.* 46, RS0D24. DOI: 10.1029/2010RS004614.

Steiner, A. K., F. Ladstädter, C. O. Ao, H. Gleisner, S.-P. Ho, D. Hunt, T. Schmidt, U. Foelsche, G. Kirchengast, Y.-H. Kuo, K. B. Lauritsen, A. J. Mannucci, J. K. Nielsen, W. Schreiner, M. Schwärz, S. Sokolovskiy, S. Syndergaard, and J. Wickert (2020). "Consistency and structural uncertainty of multi-mission GPS radio occultation records". *Atmos. Meas. Tech.* 13.5, pp. 2547–2575. DOI: 10.5194/amt-13-2547-2020.

Stockdale, T., M. Balmasedaand, and L. Ferranti (2017). "The 2015/2016 El Niño and beyond". *ECMWF Newsletter*. DOI: 10.21957/m3c157. URL: https://www.ecmwf.int/node/18187.

Stocker, M., F. Ladstädter, H. Wilhelmsen, and A. K. Steiner (2019). "Quantifying Stratospheric Temperature Signals and Climate Imprints From Post-

2000 Volcanic Eruptions". *Geophys. Res. Lett.* 46.21, pp. 12486–12494. DOI: 10.1029/2019GL084396.

Stohl, A., P. Bonasoni, P. Cristofanelli, W. Collins, J. Feichter, A. Frank, C. Forster, E. Gerasopoulos, H. Gäggeler, P. James, T. Kentarchos, H. Kromp-Kolb, B. Krüger, C. Land, J. Meloen, A. Papayannis, A. Priller, P. Seibert, M. Sprenger, G. J. Roelofs, H. E. Scheel, C. Schnabel, P. Siegmund, L. Tobler, T. Trickl, H. Wernli, V. Wirth, P. Zanis, and C. Zerefos (2003). "Stratosphere-troposphere exchange: A review, and what we have learned from STACCATO". *J. Geophys. Res.* 108.D12. DOI: 10.1029/2002JD002490.

Sun, Y.-Y., J.-Y. Liu, H.-F. Tsai, C.-H. Lin, and Y.-H. Kuo (2014). "The Equatorial El Niño-Southern Oscillation Signatures Observed by FORMOSAT-3/COSMIC from July 2006 to January 2012". *Terr. Atmos. Ocean. Sci.* 25.4, pp. 545–558. ISSN: 1017-0839. DOI: 10.3319/TAO.2014.02.13.01(A).

Sunilkumar, S. V., M. Muhsin, M. V. Ratnam, K. Parameswaran, B. V. K. Murthy, and M. Emmanuel (Jan. 2017). "Boundaries of tropical tropopause layer (TTL): A new perspective based on thermal and stability profiles". *J. Geophys. Res.: Atmos* 122.2, pp. 741–754. DOI: 10.1002/2016JD025217.

Taguchi, M. (Sept. 2010). "Observed connection of the stratospheric quasi-biennial oscillation with El Niño-Southern Oscillation in radiosonde data". *J. Geophys. Res.* 115.D18120. DOI: 10.1029/2010JD014325.

Tapping, K. F. (2013). "The 10.7 cm solar radio flux (F10.7)". *Space Weather* 11.7, pp. 394–406. DOI: 10.1002/swe.20064.

Teng, W.-H., C.-Y. Huang, S.-P. Ho, Y.-H. Kuo, and X.-J. Zhou (2013). "Characteristics of global precipitable water in ENSO events revealed by COSMIC measurements". *J. Geophys. Res.* 118.15, pp. 8411–8425. DOI: 10.1002/jgrd.50371.

Thomason, L. W. (2017). *GloSSAC Level 3 netCDF file - Version 1 [Data set].* NASA Langley Atmospheric Science Data Center DAAC. URL: https://doi.org/10.5067/glossac-l3-v1.0.

Thomason, L. W., N. Ernest, L. Millán, L. Rieger, A. Bourassa, J.-P. Vernier, G. Manney, B. Luo, F. Arfeuille, and T. Peter (2018). "A global space-based stratospheric aerosol climatology: 1979–2016". *Earth Sys. Sci. Data* 10.1, pp. 469–492. DOI: 10.5194/essd-10-469-2018.

Timmreck, C. (2012). "Modeling the climatic effects of large explosive volcanic eruptions". *WIRes. Clim. Change* 6, pp. 545–564. DOI: 10.1002/wcc.192.

Trenberth, K. E. (1997). "The Definition of El Niño". *Bull. Amer. Meteor. Soc.* 78, pp. 2771–2777. DOI: 10.1175/1520-0477(1997)078<2771:TDOENO>2.0.CO;2.

Trenberth, K. E. and D. P. Stepaniak (Apr. 2001). "Indices of El Niño Evolution". *J. Climate* 14.8, pp. 1697–1701. ISSN: 0894-8755, 1520-0442. DOI: 10.1175/1520-0442(2001)014<1697:LIOENO>2.0.CO;2.

Trepte, C. R. and M. H. Hitchman (1992). "Tropical stratospheric circulation deduced from satellite aerosol data". *Nature* 355.6361, pp. 626–628. DOI: 10.1038/355626a0.

Tweedy, O. V., N. A. Kramarova, S. E. Strahan, P. A. Newman, L. Coy, W. J. Randel, M. Park, D. W. Waugh, and S. M. Frith (June 2017). "Response of

trace gases to the disrupted 2015?2016 quasi-biennial oscillation". *Atmos. Chem. Phys.* 17.11, pp. 6813–6823. ISSN: 1680-7324. DOI: 10.5194/acp-17-6813-2017.

Vergados, P., Z. J. Luo, K. Emanuel, and A. J. Mannucci (2014). "Observational tests of hurricane intensity estimations using GPS radio occultations". *J. Geophys. Res.: Atmos* 119.4, pp. 1936–1948. DOI: 10.1002/2013JD020934.

Vernier, J.-P., L. W. Thomason, J.-P. Pommereau, A. Bourassa, J. Pelon, A. Garnier, A. Hauchecorne, L. Blanot, C. Trepte, D. Degenstein, and F. Vargas (2011). "Major influence of tropical volcanic eruptions on the stratospheric aerosol layer during the last decade". *Geophys. Res. Lett.* 38.12. DOI: 10.1029/2011GL047563.

Wallace, J. M. and P. V. Hobbs (2006). *Atmospheric Science. An Introductory Survey*. 2nd ed. Elsevier. ISBN: 0-12-732951-X.

Wallace, J. M., R. L. Panetta, and J. Estberg (1993). "Representation of the equatorial stratospheric Quasi-Biennial Oscillation in EOF phase space". *J. Atmos. Sci.* 50.12, pp. 1751–1762.

Wang, K.-Y., S.-C. Lin, and L.-C. Lee (2009). "Immediate impact of the Mt Chaiten eruption on atmosphere from FORMOSAT-3/COSMIC constellation". *Geophys. Res. Lett.* 36.3, L03808. DOI: 10.1029/2008GL036802.

Wang, S. and L. M. Polvani (2011). "Double tropopause formation in idealized baroclinic life cycles: The key role of an initial tropopause inversion layer". *J. Geophys. Res.: Atmos* 116.D5. DOI: 10.1029/2010JD015118.

Wilhelmsen, H., F. Ladstädter, B. Scherllin-Pirscher, and A. K. Steiner (2018). "Atmospheric QBO and ENSO indices with high vertical resolution from GNSS radio occultation temperature measurements". *Atmos. Meas. Tech.* 11.3, pp. 1333–1346. DOI: 10.5194/amt-11-1333-2018.

Wilhelmsen, H., F. Ladstädter, T. Schmidt, and A. K. Steiner (2020). "Double Tropopauses and the Tropical Belt Connected to ENSO". *Geophys. Res. Lett.* 47.14, e2020GL089027. DOI: 10.1029/2020GL089027.

Wilks, D. S. (2006). *Statistical methods in the atmospheric sciences*. 2nd ed. Burlington, MA, USA, San Diego, California, USA, and London, UK: Elsevier. ISBN: 978-0-12-751966-1.

WMO (1957). *Meteorology – A three dimensional science: Second session of the commission for aerology*. WMO Bull. 4. Geneva: World Meteorological Organization (WMO), pp. 134–138.

Wolter, K. and M. S. Timlin (June 2011). "El Niño/Southern Oscillation behaviour since 1871 as diagnosed in an extended multivariate ENSO index (MEI.ext)". *Int. J. Climatol.* 31.7, pp. 1074–1087. ISSN: 08998418. DOI: 10.1002/joc.2336.

Xian, T. and C. R. Homeyer (2019). "Global tropopause altitudes in radiosondes and reanalyses". *Atmos. Chem. Phys.* 19.8, pp. 5661–5678. DOI: 10.5194/acp-19-5661-2019.

Xu, X., P. Gao, and X. Zhang (2014). "Global multiple tropopause features derived from COSMIC radio occultation data during 2007 to 2012". *J. Geophys. Res.* 119, pp. 8515–8534. DOI: 10.1002/2014JD021620.

Human-induced climate change reveals itself in many forms, one of which is long term changes in the atmospheric temperature. The atmospheric temperature is, however, also influenced by natural phenomena. This natural variability masks the underlying anthropogenic climate change.
The latest report of the Intergovernmental Panel on Climate Change clearly stated that the rise in temperature near the Earth's surface is caused by human activity. Higher up, in the Upper Troposphere–Lower Stratosphere (UTLS), the picture is more diffuse. There it is more difficult to detect the underlying trend emerging from natural variability.
This work aims at enhancing diagnostics of atmospheric temperature variability in order to reduce uncertainties, improve trend detection, and increase our understanding of the effects of atmospheric phenomena.
Radio Occultation (RO) observations are currently the only global measurements that properly resolve the vertical thermal structure. RO utilizes GPS signals to provide profiles of atmospheric parameters. These measurements are highly accurate in the UTLS and have a high vertical resolution.
In this thesis, I use RO observations to describe the variability in the UTLS as well as tropopause characteristics. Establishing vertically-resolved indices from RO temperature, the main modes of variability in the tropical UTLS are detected. These help to isolate the signals caused by volcanic aerosols and to detect stratospheric warming from even minor volcanic eruptions.
Moreover, analyzing double tropopauses reveals a connection to the El Niño– Southern Oscillation. A higher frequency of double tropopauses is observed during the cold La Niña phase as the tropical belt narrows, potentially enabling exchange of air between the troposphere and the stratosphere at lower latitudes than normal. Finally, a continuous rise of the tropopause over the Northern Hemisphere is detected, one of the fingerprints of climate change in the UTLS.

Der vom Menschen verursachte Klimawandel zeigt sich in vielen Formen, eine davon ist die langfristige Veränderung der atmosphärischen Temperatur. Diese wird jedoch auch durch natürliche Variabilität beeinflusst welche die anthropogene Klimaänderung überlagert.
Der jüngste IPCC Bericht stellt eindeutig fest, dass der Temperaturanstieg an der Erdoberfläche durch menschliche Aktivitäten verursacht wird. In der oberen Troposphäre und unteren Stratosphäre (UTLS) ist es jedoch schwieriger den zugrunde liegenden Trend von der natürlichen Variabilität zu trennen.
Ziel dieser Arbeit ist eine verbesserte Diagnostik der atmosphärischen Variabilität um Unsicherheiten zu verringern, die Trenddetektion zu verbessern und unser Verständnis von atmosphärischen Phänomenen zu erweitern.
Radio-Okkultationsbeobachtungen (RO) sind derzeit die einzigen globalen Messungen, die die vertikale thermische Struktur auflösen. RO nutzt GPS-Signale, um Profile atmosphärischer Parameter zu erstellen. Diese Messungen haben eine hohe Genauigkeit in der UTLS und eine hohe vertikale Auflösung.
In dieser Arbeit verwende ich RO, um die Variabilität in der UTLS und die Eigenschaften der Tropopause zu beschreiben. Durch die Erstellung vertikal aufgelöster Indizes aus der RO-Temperatur werden die Hauptmoden der Variabilität in der tropischen UTLS ermittelt. Diese helfen, durch vulkanische Aerosole verursachte Signale zu isolieren und die Erwärmung der Stratosphäre selbst bei kleineren Vulkanausbrüchen zu detektieren.
Darüber hinaus zeigt die Analyse von doppelten Tropopausen einen Zusammenhang mit der El-Niño-Südlichen Oszillation. Während der kalten La-Niña-Phase wird eine größere Häufigkeit von doppelten Tropopausen beobachtet, da sich der tropische Gürtel verengt, was einen Luftaustausch zwischen Troposphäre und Stratosphäre in niedrigeren Breiten ermöglicht. Schließlich wird ein kontinuierlicher Anstieg der Tropopause über der Nordhemisphäre festgestellt, einer der Fingerabdrücke des Klimawandels im UTLS.

SR 98 | 2023 Diagnostics of tropospheric and stratospheric variability from radio occultation observations
Wegener Center Verlag, University of Graz, Austria. ISBN 978-3-9504700-7-9